PHOTONIC SOURCES AND DETECTORS FOR QUANTUM INFORMATION PROTOCOLS: A TRILOGY IN EIGHT PARTS

BY

RADHIKA RANGARAJAN

DISSERTATION

Submitted in partial fulfillment of the requirements
for the degree of Doctor of Philosophy in Physics
in the Graduate College of the
University of Illinois at Urbana-Champaign, 2010

Urbana, Illinois

Doctoral Committee:

Professor James N. Eckstein, Chair
Professor Paul G. Kwiat, Director of Research
Associate Professor Peter M. Abbamonte
Assistant Professor Smitha Vishveshwara

Abstract

Quantum information processing (QIP) promises to revolutionize existing methods of manipulating data, via truly unique paradigms based on fundamental nonclassical physical phenomenon. However, the eventual success of optical QIP depends critically on the available technologies. Currently, creating multiple-photon states is extremely inefficient because almost no source thus far has been well optimized. Additionally, high-efficiency single-photon detectors can drastically improve multi-photon QIP (typical efficiencies are ~70%). In fact, it has been shown that scalable linear optical quantum computing is possible only if the product of the source and detector efficiencies exceeds ~67%. The research presented here focuses on developing optimized source and detector technologies for enabling scalable QIP.

The goal of our source research is to develop an ideal "*indistinguishable"* source of ultrabright polarization-entangled but spatially- and spectrally-*un*entangled photon pairs. We engineer such an ideal source by first designing spatio-spectrally unentangled photons using optimized and group-velocity matched spontaneous parametric down conversion (SPDC). Next, we generate polarization-entangled photons using the engineered SPDC. Here we present solutions to the various challenges encountered during the indistinguishable source development. We demonstrate high-fidelity ultrafast pulsed and cw-diode laser-pumped sources of polarization-entangled photons, as well as the first production of polarization-entanglement directly from the highly nonlinear biaxial crystal BiB_3O_6 (BiBO). We also discuss the first experimental confirmation of the emission-angle dependence of the downconversion polarization (the *Migdall* effect), and a novel scheme for polarization-dependent focusing.

The goal of our single-photon detector research is to develop a very high-efficiency detection system that can also resolve incident photon number, a feature absent from the typical detectors employed for QIP. We discuss the various cryogenic, optical and electronic challenges encountered en route to detector development and present details on detector characterization, ultra-short electronics design and photon-number-resolution studies.

The source and detector technologies developed here share a common goal: to enhance the efficiency of existing quantum protocols and pave the way for new ones. Here we discuss some of the possible benefits via a popular quantum protocol – teleportation – as well as a novel quantum communication technique – hyper-fingerprinting. Taken as a whole, this dissertation explores viable technological options for enhancing optical quantum information protocols, offers a perspective on the current status and limitations of existing technologies, and highlights the possibilities enabled by optimized photonic sources and detectors.

To Dagny Taggart — *for knowing that by the time the sun's exhausted, man would find a substitute*.

Acknowledgements

When I greeted the US at seventeen, moved from tropical warmth to a brutal mid-western winter, I learnt harsh life lessons from the minute I landed – tee-shirts and snow don't mix, all of the US doesn't look like New York (thanks Hollywood!), etc. Now, a few years later, I would like to thank all those people who helped me step into foreign lands in the pursuit of knowledge, and made it possible for me to endure these bitter winters, pursue fascinating ventures as well as a few idle thoughts, and of course buy a few-more-than-really-needed wool coats.

First and foremost, thanks to the brave lady who boarded me onto that first international flight – Raji. Mom, thank you for letting me go on this adventure! After all these years of formal schooling, you have taught me that the most important lesson in life is to have fun. Thank you for being my best friend, my moral support and my fashion guru. I had a privileged childhood thanks to all my family. Thanks to the smart man who nurtured in me a deep seated love for science, adventure, business and socializing - Ranga Rajan. Dad, you instilled in me a passion for books and travel that helps me remain a *poor* graduate student –thank you, I know I am richer for the experience! Thanks for the trips to "Landmark" (yes, I really needed *five* books every time – if it is any consolation to your bank account, it was all those books that led me down this path.). Thanks to my brother Raghav for being smarter and choosing some games in addition to the books. I always wondered why you had more toys than me – if only I had realized then how important it is to diversify my portfolio of assets. It was perhaps because you and dad "altered" my big beautiful doll that I am an experimentalist today, although there might have been better ways to teach the lesson – somehow once she could talk she was never as pretty. I guess this is as good time as any to apologize for wearing your tee-shirts to high school (and taking over your room/ things during every visit home). Somehow your stuff is always cooler. Thanks also for listening to my experimental woes these past few years and sending flashes of insight (and nicknames) my way. Above all, thanks for truly being my big brother and shielding me when needed the most.

Special thanks to Vasumathi Ramesh and Ramesh Kannan, who opened their homes and hearts to me. It was because of you that I could go to my dream high-schools, which were instrumental in making me *curiouser* and *curiouser*. Thanks to my little brother Raghuveer for all the fun we had painting Chennai red. Mohan – I don't know anyone else who has gone more out-of-their way in helping me – thank you (more so for having an excellent taste)!

The fact that I now have a reverse culture shock every time I visit my hometown is a good measure of how welcome I have felt in the US. This would be impossible without the first real cowboy I met in this country – Travis Dirks. You somehow knew we were meant to be more than just lab partners when we met (you did not say "lab partner") and I couldn't be happier that you were right. You inspire me constantly and have taught me quite a few valuable things in life (a personal favorite being "*western*" ethos, of course) – I am a better person because of you. Thanks for being my best friend and for encouraging all my whims and vagaries (I spy something blue). I am touched by the support and optimism you have shown me every step of the way. I look back fondly at the road we have traversed (the sunsets are getting prettier) and I am eager to go on many more adventures with you (someplace warmer please).

To Greg, Jana, Trent and Trace – thank you for embracing me as part of your family. Knowing that comfort food, encouragement, counsel and support were just a few hours away was a constant source of solace during graduate school.

Uthra Gopalakrishnan, aka Lucy – thank you for always being there for me. There are very few women who can simultaneously pull off chic and warm, and you have mastered that art. You set the bar for the fun times (as proved by my lost voice the day after we hang out!) and make the not-so-fun times bearable – thank you my dearest. Anusha Anantharaju, partner in crime (as in, *if* I were to commit a crime you'd be my partner and that's not just because you can tell me exactly how risky our venture would be) – thanks for taking me to the fourth dimension every time we talk (I don't know where everyone else is!). More than anything else thanks for being you (meeting you was by far the best thing that happened to me in grad school). Farah Zaman, you are somehow both the voice of fun and sanity – I would not have thought they mix well – thank you! Samyuktha Sishta, thanks for imparting that horrible sense of humor – no one else seems to get it, which only makes me miss you more. Without you I wouldn't know how to enjoy chick flicks or wake up at 3 am to talk math. Turns out these diverse skills have been crucial in surviving graduate school – so thank you, my dear. Samrat Chakrabarty, the elusive friend with whom I can reconnect in seconds after years – thanks for being a physicist at heart. We skipped school to study physics, thereby inventing a whole new genre of *cool nerds*. Thanks for those balmy afternoons with delicious home cooked meals and deep conversations that go nowhere. I am glad we can at least still share the latter. Guy *maybe* Tal, David *King* Layton, Aaron *diving* VanDevender, Victor *you-tell-me-why* Elarde thanks for being such amazing friends – grad school would not have been as exciting if not for you.

I am extremely grateful to the International Students Office at Purdue University for funding most of my undergraduate studies. Also, thanks to the 53% of Americans for funding my graduate studies with their hard earned tax dollars. Funding for the work presented here has been generously provided by the National Science Foundation, IARPA-funded Quantum Computing Concept Maturation Optical Quant

Special thanks to the many teachers who have sparked and nourished my interest in a wide range of subjects. I am especially grateful to Prof. Ian Shipsey for believing in me from my eighth day in this country (I am sure he would have believed me on the *first* day had I met him then) and, entrusting a freshman with research as well as teaching a junior level astronomy class. These past few years, I have had the pleasure of working with several former and current members of the Kwiat group – Evan, Nick, Joe, Julio, Mike G, Rachel, Gleb, Onur, Kevin M, Scott, Mike W, Aditya, Trent, Katie, Dickson, Stephan, Darcy and Kevin Z – be it fundamental physics or fun you-tube videos there was never a dull moment because you guys were around. Thanks for the discussions, the toasts and the laughs! Thanks especially to Kevin Z for sharing both the good and the bad of some of my main projects.

Graduate school is a long, intense and not-so-easy quest (some have even likened it to Frodo's mission in the Lord of the Rings). And I have been extremely fortunate to have a truly wonderful advisor (wizard) to guide me through it. Paul, you have been an excellent mentor – be it science or diverse soft skills – I have learnt quite a few valuable life lessons from you. I sincerely appreciate the freedom in pursuing various projects and the motivation in times of need. The conferences, group-dinners and barbeques were all icing on the cake. I am a better leader and scientist because of you – so long and thanks for all the fish!

Table of Contents

List of Tables

List of Figures

List of Abbreviations

APD	Avalanche photo diode
AR	Anti-reflection coatings
BSM	Bell state measurement
BBO	Beta barium borate
BiBO	Bismuth borate
BS	Beam splitter
CW	Continuous wave
DOF	Degree of freedom
GVM	Group-velocity matching
FWHM	Full width at half maximum
H	Horizontal polarization
HWP	Half-wave plate
JTPA	Joint two-photon amplitude
KTP	Potassium titanyl phosphate
L	Left circular polarization
LP	Linear polarizer
OQIP	Optical quantum information processing
PBS	Polarizing beam splitter
PMMA	Poly methyl methacrylate
R	Right circular polarization
SiO_2	Silicon dioxide
Si_3N_4	Silicon nitride
SPDC	Spontaneous parametric downconversion

SNR	Signal-to-noise ratio
SSPM	Solid-state photomultiplier
TF	Typical filtered source
TFF	Typical filtered focused source
UV	Ultraviolet
V	Vertical polarization
VLPC	Visible light photon counter

Chapter 1
Source and Detector Technologies

There once came a very strange cat –
To a land where laws were set.
Neither 'live nor dead,
With a half-clever head,
And commanded his state to spread.

-To the mascot of quantum mechanics, Schrodinger's cat.

Quantum information processing promises to revolutionize existing methods of manipulating data, via truly unique paradigms based on fundamental physical laws governed by quantum mechanics. The applications span many diverse fields, including computing [1], communication [2-3], cryptography [4], metrology [5], lithography [6], etc. Although still in its infancy, several platforms, including solid-state technology, superconductors, ions, and photons, currently appear viable for implementing quantum protocols. Photons, inherently quantum particles, are especially indispensible resources in quantum communication applications. However, the eventual success of optical quantum information processing (OQIP) depends critically on the available technologies. Photons produced via the nonlinear process of spontaneous parametric downconversion (SPDC) have now been used in a vast array of experiments, from fundamental tests of quantum mechanics, to quantum cryptography and teleportation, to implementing small quantum algorithms. However, almost no source to date has been well optimized. For instance, creating states with multiple photons is typically very inefficient, e.g., in order to prepare a particular state with six photons, one must wait until three pairs are emitted simultaneously, a very low probability occurrence. In addition to requiring better sources, nearly every facet of multi-photon OQIP, especially optical quantum computing [1] and long-distance quantum communication [2-3], would be nearly impossible without high-efficiency single-photon detectors: the probability P for detecting n photons scales with the detector efficiency ε as $P(n) = \varepsilon^n$. For example, when simultaneously detecting 6 photons (currently the world record in any OQIP experiment [7]), a 90%-efficient detector is 130 times better than a 40%-efficient one! Conventional single-photon detectors, like avalanche photodiodes (APDs) and photo-multiplier tubes, are presently limited to < 70% intrinsic detector efficiency. In fact scalable linear optical quantum computing is possible only if the product of the source and detector efficiencies exceed 2/3 [8]. The research presented in this dissertation focuses on developing enabling technologies for scalable OQIP, at both the source and the detector front. While optimizing quantum technology has been the primary goal, fundamental physics, is also explored to fully understand and solve challenges along the way. Taken as a whole, this dissertation explores viable technological options for enhancing optical quantum information protocols, and offers a perspective on the current status and limitations of photonic sources and detectors.

The research presented comprises two independent topics – source technology (Chapters 2-6) and detector technology (Chapters 7-8) – with a common goal: to enhance the efficiency of existing quantum protocols and pave the way for new ones (Chapter 9). This chapter overviews the entire scope of our research by introducing existing challenges, to motivate the need for engineering ideal photonic-qubit sources and optimizing high-efficiency photon-number resolving detectors. Chapter 2 explains our specific approach to engineering an ideal source. Chapters 3-5 present solutions to challenges encountered during the source development: Chapter 3 discusses techniques for creating ultra-bright, high-fidelity sources of polarization-entangled photons from a variety of pump lasers, Chapter 4 explores and demonstrates the first experimental confirmation of the emission-angle dependence of the downconversion polarization, the Migdall effect, and Chapter 5 describes polarization-dependent focusing using a birefringent crystal and derives a theoretical explanation to explain the experimental intricacies. Chapter 6 summarizes source development by proposing a different approach to engineering an ideal source. In Chapters 7-8 we turn our attention to discuss our research on high-efficiency single-photon detectors, which have the ability to resolve photon number, i.e., to identify the exact number of photons per detection event, not present in conventional APDs: Chapter 7 describes our efforts to optimize overall system detection efficiency, Chapter 8 discusses details on detector characterization, including ultra-short electronics development and photon-number-resolution studies. Lastly, in Chapter 9 we present an outlook for the improved source and detector technologies by highlighting their advantages in a popular quantum protocol – teleportation – as well as in a novel quantum communication technique – hyper-fingerprinting.

1.1 Introduction to Sources

Two vital physical phenomena underlie the famed *quantum advantage* in most if not all of quantum information processing – quantum superpositions and interference [9]. Quantum superpositions – including entanglement – give quantum applications the power of *parallelism*, e.g., the ability to simultaneously evaluate a function $f(x)$ for many different inputs x. Interference, on the other hand, makes quantum parallelism truly useful; it allows for information about more than one value of the function $f(x)$ to be extracted from superposition states like $\sum_{x} |x, f(x)\rangle$. Thus, interference is a required component and manifests ubiquitously in linear optical quantum computing and quantum communication (for example, see [10]). To develop an ideal source of photonic qubits, one needs to understand the archetypical interferometer in OQIP, the Hong-Ou-Mandel (HOM) interferometer.

1.1.1 The Hong-Ou-Mandel Interferometer

The traditional HOM interferometer [11], shown in Figure 1-1a, combines two photons at a beam splitter. Detectors situated at the two output ports, spatial modes *c* and *d*, can then be counted in coincidence. The "magic" happens when the two photons are truly *indistinguishable*[1] – they then always arrive at the *same* detector, i.e., both photons take path *c* or both take *d*! Such a "photon bunching" [12] effect occurs because the Feynman paths corresponding to the "both-reflected" and the "both-transmitted" cases

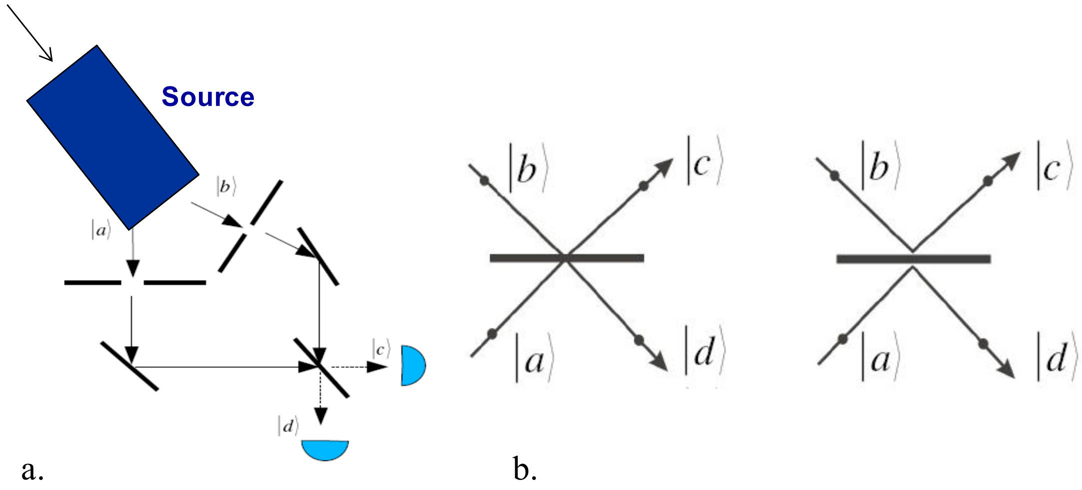

Figure 1-1: **a**. The Hong-Ou-Mandel interferometer consists of combining two photons, often generated by the same source, at a 50-50 beam splitter. **b.** If the Feynman paths corresponding to the "both-transmitted" and "both-reflected" processes are indistinguishable, then there is a destructive interference between these processes, leading to a dip in the coincidences between detectors in mode *c* and *d*.

---

[1] In the context of the Hong-Ou-Mandel, the term "indistinguishable" has a slightly different connotation than its use in quantum statistics, where photons, being bosons, would always be considered indistinguishable. Typically, in quantum statistics the photons are labeled by the particle numbers and differences in degrees of freedom are not explicitly written. However, here two photons are considered distinguishable if they have different degrees of freedom, e.g., frequencies or arrival times. Also, note that we do not explicitly symmetrize their wave functions by labeling the particle numbers; this is acceptable because i) there is no frequency transformation at the beam splitter and ii) to propagate the state, we use the creation operators, which has symmetrization built into the notation.

(see Figure 1-1b) are indistinguishable, so that the coincidence probability, $\left|\frac{1}{\sqrt{2}}\frac{1}{\sqrt{2}}+\frac{i}{\sqrt{2}}\frac{i}{\sqrt{2}}\right|^2=0$[2]. In fact, a characteristic HOM *dip* in coincidences, shown in Figure 1-2, can be seen by varying a parameter that controls the distinguishability between the two photons, e.g., their relative arrival times at the beam splitter.

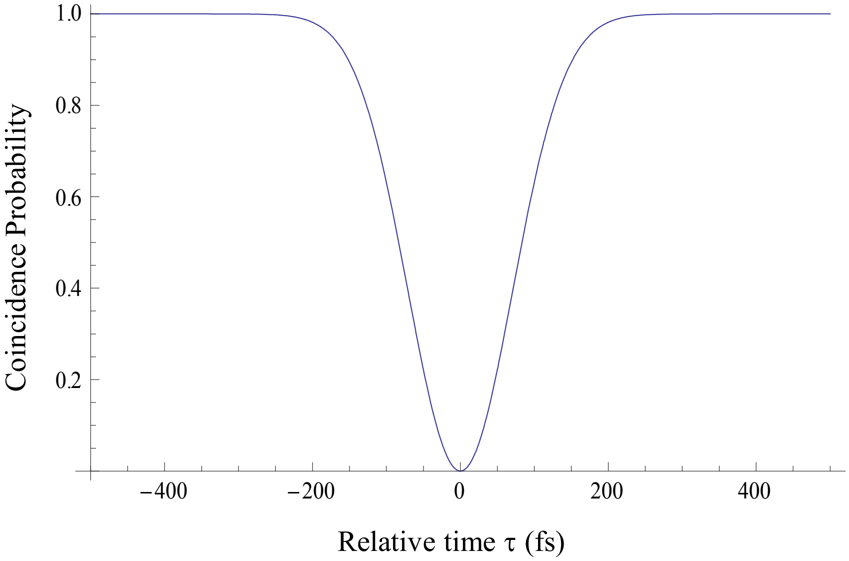

Figure 1-2: The predicted characteristic HOM dip [11] in the coincidence probability for indistinguishable photons as the relative delay τ between the two photons, and hence, the distinguishability, is varied. The plotted curve is for Gaussian beams with a coherence time ~100 fs.

The detailed general theory explaining this effect can be found in [11]. However, we can glean a quick insight into the origin of the HOM curve for the special case considered here. The coincidence probability that a photon in spatial mode *c* is detected at time *t* and a photon in *d* is detected at $t+\tau$ is given by the fourth-order correlation function [13]

$$P_{cd}(\tau)\propto\left\langle\psi\left|\hat{E}_c^{(-)}(t)\hat{E}_d^{(-)}(t+\tau)\hat{E}_d^{(+)}(t+\tau)\hat{E}_c^{(+)}(t)\right|\psi\right\rangle. \qquad 1.1$$

---

[2] The factor "*i*" comes from a π/2 phase shift between the transmitted and the reflected modes of each photon. More generally, $(\varphi_{r1}-\varphi_{t1})+(\varphi_{r2}-\varphi_{t2})=\pi$, where φ_{r1} (φ_{r2}) refers to the phase acquired from reflection by the first (second) photon and φ_{t1} (φ_{t2}) to the phase acquired from transmission by the first (second) photon. We have also assumed perfect 50-50 beam splitters and long detection times compared to the correlation times.

Here $\left|\psi\right\rangle$ is the input state at the beam splitter and $\widehat{E}^{(\pm)}$ are the positive- and negative-frequency parts of the field operator, which can be written as

$$\begin{aligned} \widehat{E}_c^{(+)}(t) &= \left|E_0\right|\left(\frac{\hat{a}^\dagger(t)}{\sqrt{2}}+\frac{i\hat{b}^\dagger(t)}{\sqrt{2}}\right), \\ \widehat{E}_d^{(+)}(t) &= \left|E_0\right|\left(\frac{ia^\dagger(t)}{\sqrt{2}}+\frac{\hat{b}^\dagger(t)}{\sqrt{2}}\right), \end{aligned} \qquad 1.2$$

where $\hat{a}^\dagger$ and $\hat{b}^\dagger$ are the photon creation operators for the input modes and $\widehat{E}^{(-)}$ is the hermitian conjugate of $\widehat{E}^{(+)}$. If there is only one photon in each of the input beams, then the coincidence probability (expanded using Eqns. 1.1-1.2) reduces to only four non-zero terms:

$$P_{cd}(\tau)=\frac{\left|E_0\right|^4}{4}\left(\begin{array}{l} \left\langle \hat{a}^\dagger(t)\hat{b}^\dagger(t+\tau)\hat{b}(t+\tau)\hat{a}(t)\right\rangle+\left\langle \hat{b}^\dagger(t)\hat{a}^\dagger(t+\tau)\hat{a}(t+\tau)\hat{b}(t)\right\rangle \\ -\left\langle \hat{a}^\dagger(t)\hat{b}^\dagger(t+\tau)\hat{a}(t+\tau)\hat{b}(t)\right\rangle-\left\langle \hat{b}^\dagger(t)\hat{a}^\dagger(t+\tau)\hat{b}(t+\tau)\hat{a}(t)\right\rangle \end{array}\right) \qquad 1.3$$

The first two terms arise from the "both-reflected" and the "both-transmitted" amplitudes. Thus, $\left\langle \hat{a}^\dagger(t)\hat{b}^\dagger(t+\tau)\hat{b}(t+\tau)\hat{a}(t)\right\rangle=\left\langle \hat{b}^\dagger(t)\hat{a}^\dagger(t+\tau)\hat{a}(t+\tau)\hat{b}(t)\right\rangle=1$. The last two terms correspond to the interference between the transmitted-reflected and reflected-transmitted amplitudes, resulting from mixing the two photons at the beam splitter, and are the true quantum interference contributions to the coincidence probability. By modeling the randomly produced SPDC photons as a Gaussian distribution of bandwidth $\Delta\omega$, exhibiting cross correlations between the field amplitudes [13], we can write[3]

$$\left\langle \hat{a}^\dagger(t)\hat{b}^\dagger(t+\tau)\hat{a}(t+\tau)\hat{b}(t)\right\rangle=\left\langle \hat{a}^\dagger(t)\hat{b}(t)\right\rangle\left\langle \hat{b}^\dagger(t+\tau)\hat{a}(t+\tau)\right\rangle=e^{-(\Delta\omega\tau)^2} \quad . \qquad 1.4$$

Thus, the coincidence probability becomes

$$P_{cd}(\tau)\propto\frac{\left|E_0\right|^4}{2}\left(1-e^{-(\Delta\omega\tau)^2}\right), \qquad 1.5$$

explaining the dip in the coincidence rate at $\tau = 0$. The width of the dip is determined by the photon coherence times, which are inversely proportional to $\Delta\omega$. Note that the HOM dip, a purely quantum-

---

[3] Eqn. 1.4 can be derived using the Fourier transform $g(\tau)$ of the spectral function ϕ, where $g(\tau)=G(\tau)/G(0)$ and $G(\tau)=\int_0^\infty \phi\left(\frac{\omega_0}{2}+\omega,\frac{\omega_0}{2}-\omega\right)e^{-i\omega\tau}d\omega$. When the spectral function is Gaussian, $g(\tau)=e^{-(\Delta\omega\tau)^2/2}$.

mechanical feature[4], relies on a fourth-order interference effect, i.e., a single photon does *not* interfere with itself, as occurs in second-order interferometers such as a Michelson. In fact, the HOM effect is insensitive to the relative phase in the two arms and truly a two-photon interference phenomenon. When the two incident photons are completely distinguishable, e.g., by their arrival times, they no longer interfere with each other, and therefore, they *can* be detected in coincidence. Thus, indistinguishability is critical to observe HOM interference between two independent photons[5].

Need for an Indistinguishable Photon-Pair Source: For most linear-optics QI applications, including quantum computation and communication protocols such as teleportation, a HOM measurement has to be performed between photons originating from *different* sources. Figure 1-3 shows such an "event-ready" HOM consisting of two independent sources, each of which generates a pair of photons. One photon from each source is combined at a beam splitter, while detection of the remaining two trigger photons initiates coincidence counting. Here, mere indistinguishability between the two photons at the beam splitter does not suffice; any "*which-process*" information carried by a partner trigger photon essentially makes the interfering processes distinguishable. Thus, in OQIP the ability of multiple independently-generated single photons to interfere can be reduced, or even completely suppressed, if the photon pairs emitted from a single source are correlated with each other (e.g., in frequency) [15]. Photon state distinguishability increases the error rate of quantum protocols, e.g., logic gates [1], by limiting the visibility of the HOM interference underlying these protocols. Currently, most experiments solve this problem by *discarding* most of the correlated photons to reduce any distinguishing information. However, filtering also significantly reduces the incident photon flux, thereby drastically lowering the overall efficiency of the quantum protocol at hand. A better solution is to generate photons in a pure state, i.e., photons with no correlations to their heralding triggers. To understand this, let us first review conventional OQIP sources and the origin of these unwanted correlations.

---

[4] For classical fields, the coincidence probability can be shown to be proportional to $\left(1-\frac{e^{-(\Delta\omega\tau)^2}}{2}\right)$. Thus, classically the coincidence probability never reaches zero and can be reduced to only ½ of its maximum value.

[5] As an aside, note that photon-number resolving detectors not only facilitate easy confirmation of photon bunching but can also drastically improve the protocol, since one can then directly detect two photons in a single port [14].

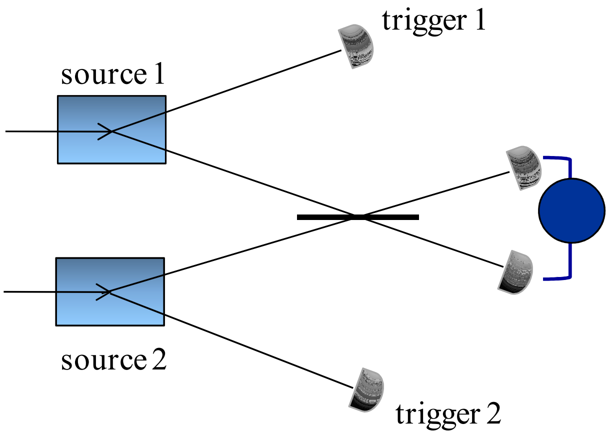

Figure 1-3: Typical HOM interference between two independent (SPDC) sources. For perfect interference the two control photons need to be indistinguishable; moreover, this means they cannot be correlated with their partner trigger photons.

1.1.2 Typical SPDC Sources

Single photons for OQIP may be generated on-demand by individual quantum emitters, such as quantum dots [16] and diamond vacancy centers [17] or they may be heralded from photon pairs generated through a spontaneous parametric process, i.e., downconversion (SPDC) [18] and four-wave mixing [19]. While the former solid-state technologies appear promising, efficiently collecting the photons has been problematic, and interfering photons from two such emitters has hardly been addressed. Thus far, the most commonly employed technique for generating photons for OQIP is SPDC. The full derivation of SPDC requires the quantization of the electric field and can be found in several textbooks (e.g., see [20]). In brief, SPDC utilizes the nonlinear response of the dielectric polarization P (dipole moment per unit volume) to an applied electric field E, found in some crystals:

$$P(t) = \chi^{(1)}E(t) + \chi^{(2)}E^2(t) + \chi^{(3)}E^3(t) + ... \qquad 1.6$$

A pump photon incident on a dielectric having a $\chi^{(2)}$ nonlinearity[6], e.g., a Beta Barium Borate (BBO) crystal, spontaneously splits into two daughter photons, the *signal* and the *idler* (with respective frequencies ω_s and ω_i, and wave vectors $\vec{k_s}$ and $\vec{k_i}$). Efficient SPDC requires momentum conservation $\overrightarrow{k_p} = \overrightarrow{k_s} + \overrightarrow{k_i}$, known as phasematching, and energy conservation $\omega_p = \omega_s + \omega_i$, where ω_p refers to the pump frequency and $\overrightarrow{k_p}$ to the pump momentum wave vector. There are two different ways to achieve

---

[6] SPDC is typically observed in materials with large χ^2 because downconversion involves the transformation of a single photon into two photons, i.e., it is a very weak effect.

spontaneous downconversion: in type-I phase matching, an extraordinary[7] polarized pump photon splits into two ordinary polarized daughter photons, while in type-II an extraordinary pump photon splits into one ordinary and one extraordinary photon[8]. The key point to note here is that the phasematching and energy conservation constraints in SPDC processes imply that for typical source designs the resulting photon pairs are highly correlated in spatial modes and frequencies.

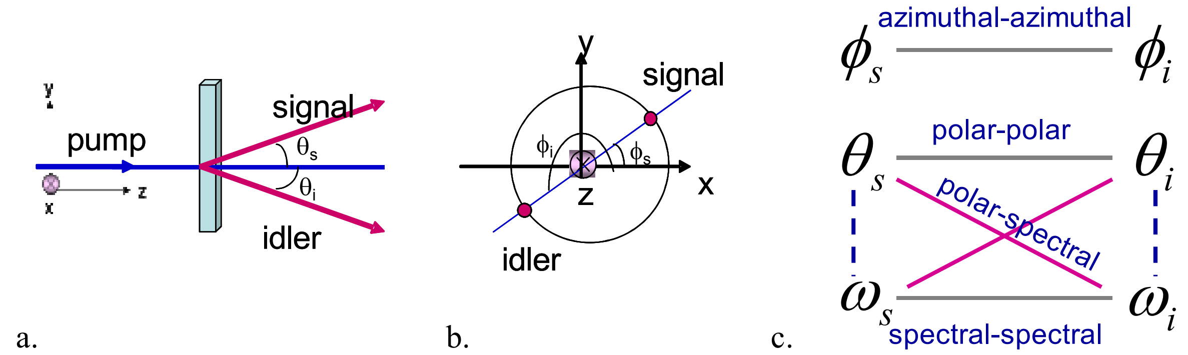

Figure 1-4: Basic source geometry of SPDC from a χ^2 crystal. **a**. Side view of the SPDC crystal, showing the emission polar angles θ_s and θ_i . **b**. Looking-into-the-pump view, showing the emission azimuthal angles ϕ_s and ϕ_i . **c**. Dominant correlations in a typical type-I SPDC source.

Correlations in typical SPDC sources: The signal and idler downconversion photons from a typical SPDC crystal usually exhibit several different types of correlations. Figure 1-4 shows the typical SPDC source geometry, which defines the polar and azimuthal downconversion emission angles. Correlations can exist in the spectral ω and angular orientation (both polar θ and azimuthal ϕ) of the downconversion beams. Figure 1-4c shows the dominant correlations that typically exist between the signal and the idler photons for a type-I downconversion source. Internal or *intra-photon* correlations, denoted by the vertical dashed lines, exist between the frequency and polar emission angle of the *same* photon. Intra-photon correlations, e.g., the lower frequency components of the downconversion photons emerge at wider angles, can be thought of as being similar to a chirp in a classical field. External or *inter-photon* correlations also exist between the signal and the idler, and are denoted by solid lines in Figure 1-4c. These constitute azimuthal-azimuthal, spectral-spectral, polar-polar and mixed spectral-polar

---

[7] Birefringent materials have different indices of refraction depending on the propagation direction and the polarization of the light. Uniaxial crystals have a single axis of anisotropy called the *optic axis*, which together with the wave vector of the incident light define the *principal plane*. Light rays whose polarization is perpendicular to the principal plane are called *ordinary (o)*, whereas *extraordinary (e)* rays are polarized in the principal plane. The refractive index of the o-beam does not depend on the propagation direction, whereas it does for the e-beam.

[8] These statements are for a negative uniaxial crystals, where n_o (the index of ordinary polarization) > n_e (the index of estraordinary polarization). For positive uniaxial crystals ($n_o < n_e$), type-I phasematched downconversion us an $o \rightarrow e+e$ process, while type-II phasematching gives $o \rightarrow o+e$.

entanglement between the signal and the idler [21]. The origin of some of these correlations can be easily seen from the phasematching conditions — energy conservation results in spectral-spectral correlations (energy entanglement), momentum conservation dictates that the photons be emitted on opposite sides of the cone, which leads to azimuthal-azimuthal correlations, etc. Figure 1-5a shows a numerical simulation of the actual spectral-spectral correlations that exist in a typical type-I SPDC source[9]. Energy conservation renders the signal and idler photons distinguishable because measuring the signal's frequency automatically determines that of the idler. The typical solution to deal with this is to use extremely narrowband spectral filters, F_1 and F_2 in Figure 1-5b, on the signal and idler beams in order to retain only the indistinguishable part of the joint two-photon spectrum. This is achieved, unfortunately, at the cost of a considerable reduction in source brightness. The resulting spectrum, Figure 1-5c, is mostly indistinguishable; however, the majority of the incident photons have been discarded leading to extremely low count rates. The spatial angular correlations are similarly suppressed by coupling into single-mode optical fibers (which essentially act as extremely narrow spatial filters). Mathematically, it is a factorable the joint spectrum $f(\omega_s,\omega_i)$, i.e, $f(\omega_s,\omega_i)=h(\omega_s)g(\omega_i)$ for any two independent functions h and g, that corresponds to an indistinguishable signal and idler pair. Figure 1-6 shows the tradeoff between

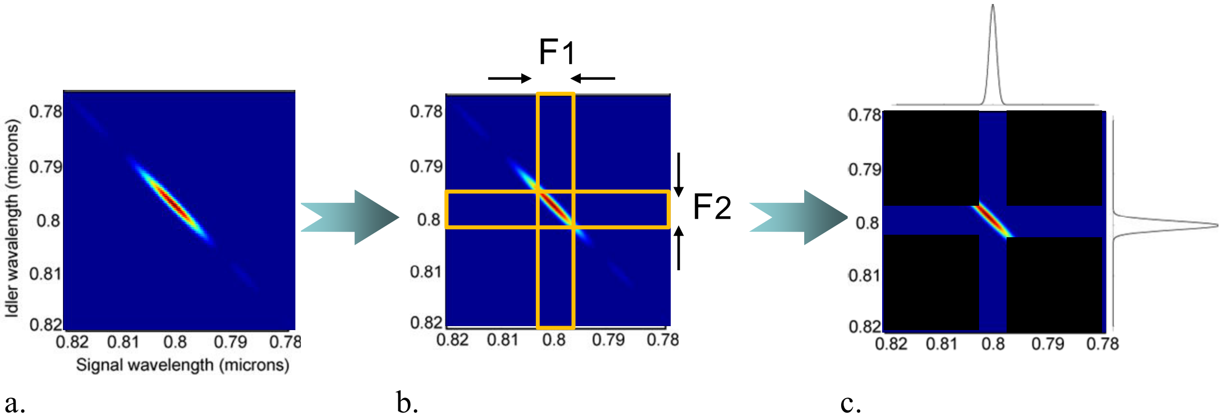

Figure 1-5: **a**. Joint spectral intensity (JSI) plot showing the predicted spectral-spectral correlations between the signal and idler in a typical type-I SPDC source. **b**. Narrowband filters, F_1 and F_2, are typically used to eliminate correlations and make the signal and idler indistinguishable. **c**. Resulting JSI after using filters.

---

[9] These numerical simulations were performed by our theory collaborator, Alfred U'Ren at National Autonomous University of Mexico.

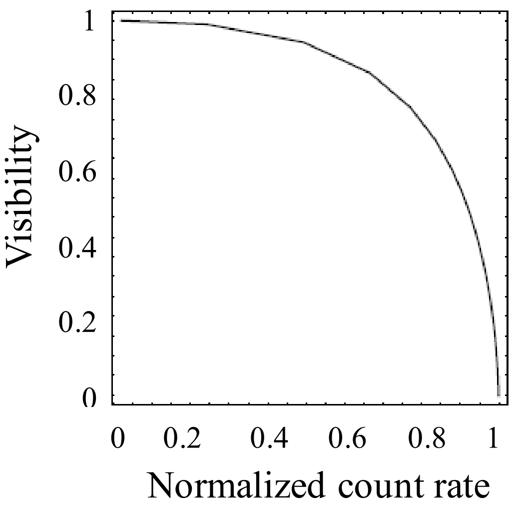

Figure 1-6: Tradeoff between interference visibility and count rates in a HOM (based on [22]).

interferometric visibility[10] (used to quantify the fringe contrast in any interferometer) and photon-count rates when employing filters in a typical HOM interferometer [23]. This becomes a crucial issue for experiments relying on simultaneous generation of two or more photon pairs. An enhancement of r in the single-crystal photon-pair brightness becomes an enhancement of r^2 for a dual-crystal, four-photon source, and r^N for an N-crystal, $2N$-photon source. Sources leading to enhancement values in the hundreds, compared to typical sources, could represent a significant step towards practical OQIP implementations.

1.1.3 Overview: Engineering an Ideal Source for Quantum Information

The ideal source generates *truly indistinguishable* photons — photons that are indistinguishable and further do not carry any *which-source* information — so that high-visibility interference can be obtained without any filtering. Photon pairs from such an ideal source would exhibit no correlations and thus will *not* be entangled in any relevant DOF. Figure 1-7 shows an example of a desired uncorrelated joint two-photon spectrum from an ideal indistinguishable source. The dominant SPDC correlations are in frequency and directions; consequently, we need to engineer photons that are unentangled in spatial and spectral modes. Nevertheless, we still need usable entanglement, the fundamental resource for OQIP, in one DOF. In type-I SPDC, the daughter photons have identical polarization. A proven method of

---

[10] $\text{Visibility} = \dfrac{Max - Min}{Max + Min}$, where Max (Min) refers to the photon count rate at the maximum (minimum) fringe intensity.

generating polarization entanglement uses two orthogonally oriented type-I SPDC crystals [24]. Using two engineered crystals, each designed to generate truly indistinguishable uncorrelated photons, we can create polarization entanglement with spatio-spectral *un*entanglement. The research presented here aims at engineering such an ideal photon-pair source for OQIP. Throughout this dissertation, we refer to such a source as an *indistinguishable-photon source* or, alternatively, as an *unentangled source*.

Various other groups are investigating the generation of indistinguishable photons by directly controlling the state of the emitted photon pairs at the point of production. These approaches include shaping the pump and downconversion beams using diffraction gratings [25], applying additional phasematching constraints [26], or controlling pumping geometry and natural material dispersion [27-28]. Similarly, the spectral structure of photon pairs created via spontaneous four-wave mixing in micro-structured fibers can be manipulated by fabricating optical fibers with designed dispersion [29]. However, all of these methods have thus far been limited to studying only the spectral correlations. The angular correlations, such as azimuthal-azimuthal and polar-polar, including the mixed correlations, have been ignored, mostly because of the complexity involved in analyzing the full spatio-spectral structure of the downconversion photons. Additionally, none of these methods address the task of including polarization entanglement, a required resource for OQIP. Our approach to an indistinguishable-photon source is based on theory developed by our collaborator, Alfred U'Ren; it consists of imposing group-velocity matching and optimizing the phasematching parameters for non-collinear, degenerate type-I SPDC to achieve maximum unentanglement in both frequency and spatial modes [21]. Further, we engineer polarization-entangled, using these spectrally and spatially unentangled photons to obtain a truly indistinguishable-photon source for OQIP.

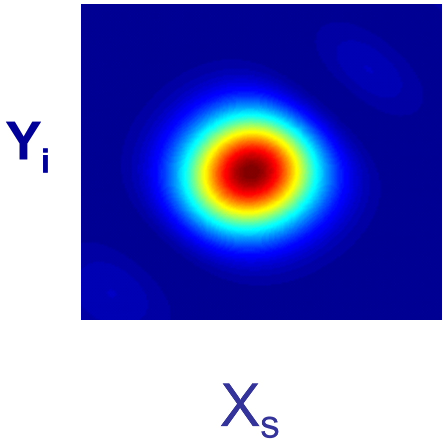

Figure 1-7: Joint two-photon spectrum of the ideal source. X_s and Y_i represent any relevant DOF, such as, frequency or emission angle of the signal (*s*) and the idler (*i*) .

1.2 Introduction to Detectors

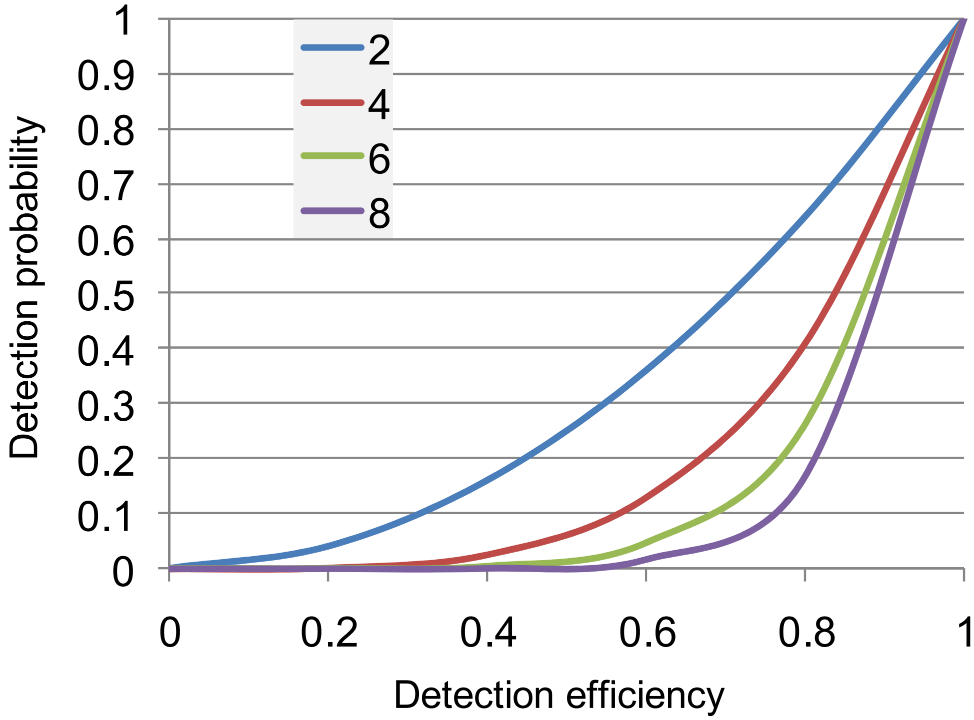

Figure 1-8: Graph showing the net detection probability, for a given detector efficiency, for two (blue), four (red), six (green) and eight (violet) incident photons.

The challenging task of optimally engineering photon detectors with near-perfect efficiency, and capable of distinguishing the number of photons, has enormous potential pay-offs in optical metrology in general, and particularly in OQIP. Every example of multi-photon OQIP will benefit from high-efficiency detection, and some applications such as optical quantum computing are nearly impossible to achieve without efficiencies exceeding 90-95%. Figure 1-8 shows that the probability P for detecting n photons scales with the detector efficiency ε as $P(n) = \varepsilon^n$. Thus, when detecting 6 photons, the current world record [7], a 90% efficiency is 130-times better than a 40% efficiency. Conventional single-photon detectors, like APDs and photo-multiplier tubes, are presently limited to < 70% intrinsic detector efficiency, and are often more likely to be in the 40-50% range. Further, they lack the crucial ability to resolve photon number, i.e., to distinguish between 1 and 2 photons, or more generally, between n and n+1. Detectors with this capability are also critical for realizing efficient heralded sources of single photons [30], and enabling the preparation of many-photon entangled states, which could be of great utility in other quantum information schemes, such as quantum lithography and ultrasensitive super-resolution interferometry [31]. In addition, photon-number resolution (PNR) enhances several applications as well, including optical (and quantum optical) metrology and virtually every quantum communication protocol, including quantum cryptography, teleportation, and quantum repeaters. Limitations of existing photon-counting detectors – quantum efficiency (QE), spectral response, dark counts, dead time, multiphoton response, etc. – leave much room for improvement. This research focuses on developing an ultrafast no-dead-time high-efficiency photon-number resolving detection system using two related types of solid-state detectors: visible light photon counters (VLPCs) and solid-state photomultipliers (SSPMs).

1.2.1 Overview: Optimizing Efficiency and Photon-Number Resolution

Visible light photon counters (VLPCs) and solid-state photomultipliers (SSPMs) feature both the coveted traits — high QE [32-33] and multi-photon counting capability [34]. Both these structurally similar solid-state detectors operate at ~6 K, but they are optimized for different wavelength regimes. Single-photon detectors generate a small electrical signal (usually in terms of a current or voltage pulse) upon absorption of a single photon. In a typical semiconductor device, a single-photon absorption event generates a single electron-hole pair, which is not sufficient to overcome the intrinsic thermal noise of electronics that follow. Therefore, all single-photon detectors require an internal gain mechanism to substantially amplify this initial electron-hole pair. VLPCs and SSPMs have a unique gain mechanism compared to other known single-photon detectors. In contrast to conventional APDs, which rely on excitations between valence and conduction bands, VLPCs utilize impact-ionization of impurity atoms as the gain mechanism to amplify carriers generated by a single-photon absorption event [6]. The VLPC design was a modification of the original detector, the SSPM [35] invented at Rockwell[11], intended to significantly enhance the QE at visible wavelengths while suppressing dark count rate. The absolute QE of SSPMs was first tested in the context of quantum optics experiments by Kwiat et al. [32, 36]. The noise, QE and multi-photon detection capabilities of VLPCs were characterized by Kim et al. [33-34]. The unique design of VLPCs and SSPMs leads to a very high quantum efficiency — the VLPCs have predicted *intrinsic* quantum efficiency of 94 ± 5% (at 694 nm) [33] (and SSPMs have 96% ± 3% (at 660 nm) [32-33]), good time resolution (pulse width ~1 ns, with timing jitter of ~200 ps), low multiplication noise (excess noise factor ENF ~1.03), and photon-number resolving (PNR) capability.

Despite these demonstrated strengths, several areas remain where significant development in VLPC technology has been necessary: the systems used are not particularly robust or easy to use; they have yet to achieve the expected 95% net-system detection efficiency, which in turn affects the reliability for

---

[11] Rockwell, after being absorbed by Boeing, is now part of DRS Technologies.

photon-number resolution. For both VLPCs and SSPMs, the actual measured detection efficiencies were limited to less than 88% due to losses in the coupling optics [33, 36]. In-coupling optical fibers and reflection losses at the detector surface are the two main contributors to optical loss. Other factors that degrade the detector performance include sensitivity to infrared background radiation, electronic noise and pulse-recognition issues. To add to the challenge, the devices themselves are not widely available – most of the ones we currently have access to are essentially "rejects" from the FermiLab D0 project. They have a significant variation in their intrinsic gain, resulting in a wide range of performance characteristics, ranging from mostly inoperative to a few good devices. Thus, VLPC detector development has included various challenges, including optical, cryogenic and electronic. This dissertation will address all of these issues, and describe our approach to create a more robust, low background, efficiency-optimized photon-number-resolving detection system.

1.3 Outlook

The source and detector approaches investigated in this dissertation could have profound implications for OQIP protocols. For example, if operating as envisioned, not only would they signify a 10^5–fold brightness enhancement for quantum teleportation, but they would also facilitate a 50% increase in the inherent efficiency of the protocol. Akin to most technological improvements, they also enable advancements in new areas – in our proposed hyper-fingerprinting technique one can communicate seven messages using a single hyper-entangled [37] qubit. Moreover, the technologies can be incorporated into a variety of quantum information science applications, including novel single- and multi-photon sources, Gbit/s quantum random number generators, and a long-awaited definite test of quantum nonlocality – a 'loophole-free' test of Bell's inequality [38]. We envision that both an ultra-bright source of indistinguishable photons and high-efficiency photon-number resolving detectors will greatly enhance the capability of OQIP and, increase it scalability as well as enabling the practical use of downconversion photons in many more non-OQIP applications.

Chapter 2

Engineering Indistinguishable Photons

No good fish goes anywhere without a porpoise.
-Lewis Carroll

Our approach to engineering indistinguishable polarization-entangled photon pairs consists of two parts. First, we engineer unentanglement in spatial mode and frequency from a single SPDC crystal. Then we use standard techniques to generate polarization entanglement between these spatio-spectrally engineered photons. We start with a theoretical analysis of the spatio-spectral correlations present in photon pairs produced by type-I, non-collinear spontaneous parametric downconversion. In order for the photon pairs to be completely uncorrelated with each other, the joint two-photon amplitude (JTPA), which describes the signal-idler relationship, needs to be fully factorable in all its variables, i.e., there should be no term in the full analytical expression of the JTPA that contains two or more independent variables. We derive a set of conditions for full factorability between the signal and idler modes [21] by making certain assumptions about the pump and first-order approximations of the downconversion modes. In this chapter, we first present the set of conditions needed to minimize these correlations to create an indistinguishable source and then discuss experimental tests of such an engineered source. Finally, we elaborate on the two-crystal scheme, the standard method of generating polarization-entangled photons, which we will implement using the engineered crystals to create a truly indistinguishable source for OQIP.

2.1 The Method: Group-Velocity Matching[12]

JTPA Analysis: Here we present a brief outline of the JTPA analysis and derivation of the factorability conditions. For a full derivation of the complete theory see [21]. Mathematically, the two-photon downconversion state can be written in terms of creation operators acting on the vacuum state as

$$|\Psi\rangle = \int d\mathbf{k_s} \int d\mathbf{k}_i f(\mathbf{k}_s, \mathbf{k}_i) \hat{a}_s^+(\mathbf{k}_s) \hat{a}_i^+(\mathbf{k}_i) |vac\rangle , \qquad 2.1$$

where **k** refers to the momentum wave vectors and the subscripts *s* and *i* stand for signal and idler, respectively. The joint two-photon amplitude *f* depends on the phase-matching conditions and SPDC parameters shown in Figure 2-1, including the crystal length *L*, pump beam waist w_0, position of beam waist x_0 measured relative to the crystal center, and pump spectral bandwidth σ.

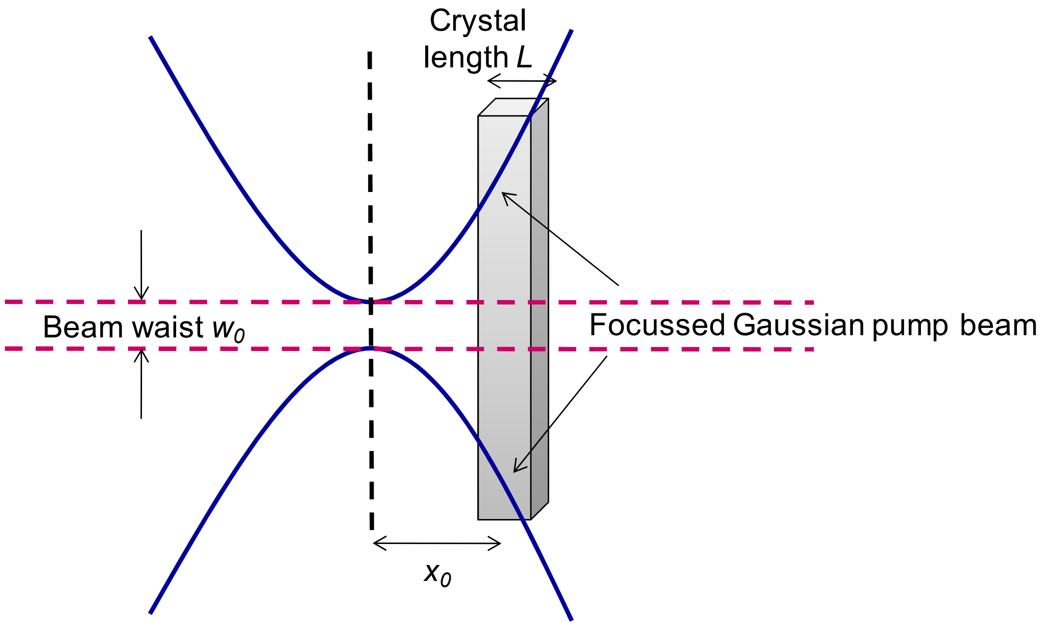

Figure 2-1: SPDC parameters — crystal length L, pump beam waist w_0, and position of beam waist x_0 measured relative to the crystal center.

---

[12] The theory for this work was done primarily by our collaborators, Alfred U'Ren and Luis Vincent at the National Autonomous University of Mexico. As indicated below, a number of the theoretical curves and plots are drawn from their work. My contribution has been in proposing ideas, suggesting further calculations, confirming some of the numerical results using my programs, providing realistic parameters, finding errors, and experimentally testing the predictions.

By modeling the pump as a Gaussian beam with bandwidth σ around a central frequency w_{p0}, and with a beam waist *w₀* located at x_0, the JTPA can be expressed as

$$f(\vec{k}_s,\vec{k}_i)=\sqrt{\frac{\hbar\omega}{\epsilon_0 n(\vec{k}_s)^2}}\sqrt{\frac{\hbar\omega}{\epsilon_0 n(\vec{k}_i)^2}}\alpha(\omega_s+\omega_i)\phi(\vec{k}_s,\vec{k}_i)\,, \qquad 2.2$$

in terms of the indices of refraction $n\left(\vec{k}_s\right)$ and $n\left(\vec{k}_i\right)$, the pump envelope function $\alpha\left(\omega_s+\omega_i\right)$, and the phasematching function $\phi\left(\vec{k}_s,\vec{k}_i\right)$:

$$\phi(\vec{k}_s,\vec{k}_i)=\exp\left(i\frac{|\underline{k}_\perp|^2}{2k_p}x_0\right)\exp\left[i\frac{1}{2}L(\Delta k+k_{\perp y}\tan\rho_0)\right]\exp\left(-\frac{1}{4}w_0^2\,|\underline{k}_\perp|^2\right)\mathrm{sinc}\left(\frac{L\Delta k}{2}\right). \qquad 2.3$$

Here, an underlined symbol indicates a two-dimensional transverse vector in terms of the Cartesian components of the signal and idler wave vectors:

$$\begin{aligned}&\underline{k}_\perp\equiv(k_{sx}+k_{ix},k_{sy}+k_{iy})\ ,\\&\Delta k\equiv k_p-\frac{|\underline{k}_\perp|^2}{2k_p}-k_{sz}-k_{iz}+\underline{k}_{\perp y}\tan\rho_0.\end{aligned} \qquad 2.4$$

Δk and $\underline{k}_\perp$ are the longitudinal and transverse phase mismatches, and ρ_0 is the Poynting vector walkoff angle of the pump beam. To consider the full spatial and spectral dependence of the JTPA, the wave vectors in Eqn. 2.2 can be rewritten in spherical coordinates, i.e., $f(\mathbf{k}_s,\mathbf{k}_i)\rightarrow f(\omega_s,\theta_s,\phi_s;\omega_i,\theta_i,\phi_i)$, where θ and ϕ are the downconversion polar and azimuthal angles, respectively. To find an optimum region in the six-variable parameter space of the JTPA, the $sinc(x)$ in Eqn.2.3 can be approximated[13] as $e^{-\gamma x^2}$, with $\gamma=0.193$ selected so that the two functions have identical full width at half maximum (FWHM). Next, the resulting Gaussian JTPA can be expanded into a first-order Taylor series in the six variables $\{\omega_s,\theta_s,\phi_s,\omega_i,\theta_i,\phi_i\}$ around central values for each of these variables, to derive relationships between the correlations in different degrees of freedom. Mathematically, the JTPA becomes factorable when mixed terms are set to zero. Thus, we can finally obtain a set of conditions, in addition to phasematching ($\Delta k=0$ in Eqn. 2.4), that the various tunable parameters, i.e., *σ, w₀, L,* have to fulfill to generate a factorable JTPA. These conditions are listed in Table 2.1, while Table 2.2 summarizes all the variable definitions appearing in the five conditions for JTPA factorability.

---

[13] For justification see [39] and [40].

Condition 1	$k_s' = k_p' \cos\theta_s$
Condition 2	$k_i' = k_p' \cos\theta_i$
Condition 3	$\frac{w_0^2}{0.193L^2} = -\tan\theta_s \tan\theta_i$
Condition 4	$\sigma >> \frac{2}{0.193L\left(k_p' - k_s'\cos\theta_s\right)}$
Condition 5	$\theta_{max}^2 (w_0^2 + 0.193\rho L^2) \lesssim \frac{1}{4k^2}$

Table 2-1: Conditions for factorizing the JTPA to eliminate spatial and spectral correlations.

Variable	**Definition**
L	Crystal length
w_0	Pump beam waist
σ	Pump bandwidth
θ_s (θ_i)	Central signal (idler) emission angle inside the crystal
θ_{max}	Maximum spread of angles around the central signal and idler directions
k'	Group velocity inside the crystal, i.e., derivative of wave vector k with respect to ω.
ρ_0	Walkoff angle

Table 2-2: Definition of variables in the conditions for full JTPA factorization.

Factorability Conditions: Conditions 1-2 refer to vector group-velocity matching (GVM): specifically, the longitudinal component of the signal and idler group velocities is made equal to the pump group velocity. In the case of degenerate SPDC these two conditions become a single condition. Condition 3 refers to a constraint on the physical dimensions of the source (crystal length and pump beam radius at the beam waist), together with the propagation angles. Similar to other techniques (see Section 1.1.3) for factorable photon-pair generation [22, 25-27, 29], our scheme requires a broadband pump, with a bandwidth exceeding the threshold presented in condition 4. When the threshold bandwidth is exceeded, the joint amplitude of the two-photon state is determined by the longitudinal and transverse phasematching properties, independent of the pump bandwidth.

Physically, engineering of the JTPA can be understood as follows: In the frequency domain, the strong spectral correlation imposed by a monochromatic pump via energy conservation is relaxed by using a broad bandwidth pump. In the spatial domain, for a plane wave ($w_0 \longrightarrow \infty$) the transverse phase matching becomes a delta function, and for small emission angles, the polar-polar and azimuthal-azimuthal angles of the signal and the idler are perfectly correlated. However, by reducing w_0 via strong focusing, transverse momentum correlations can be weakened permitting the generation of effectively factorable states. Moreover, the additional degree of symmetry, group-velocity matching, provides a method to minimize correlations and leads to a factorable JTPA. The crystal properties and SPDC parameters determine the group velocities of the pump, signal and idler. For a given crystal and fixed central wavelengths, the group velocities can be varied by changing the downconversion emission angle. Figure 2-2 shows the change in the spectral correlations, which vary from anti-correlated to correlated, for different signal and idler group velocities corresponding to different downconversion emission angles. The factorable uncorrelated spectrum corresponding to the ~16° external downconversion emission angle results when the group-velocity of the signal and the idler match that of the pump's.

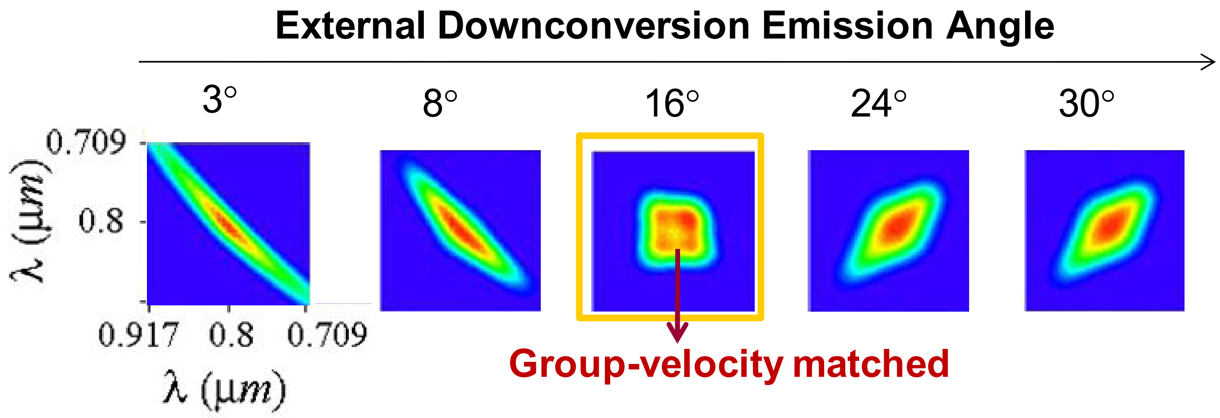

Figure 2-2: Effect of varying the downconversion emission angle on the spectral correlations.

2.2 Theoretical Results for Spatio-Spectral Unentanglement

The Engineered Crystal: Figure 2-3 shows the dominant external correlations that exist in a typical source, where the propagation angles involved are similar to those ubiquitously used in SPDC polarization-entanglement experiments (specifically, we consider for this source an internal propagation

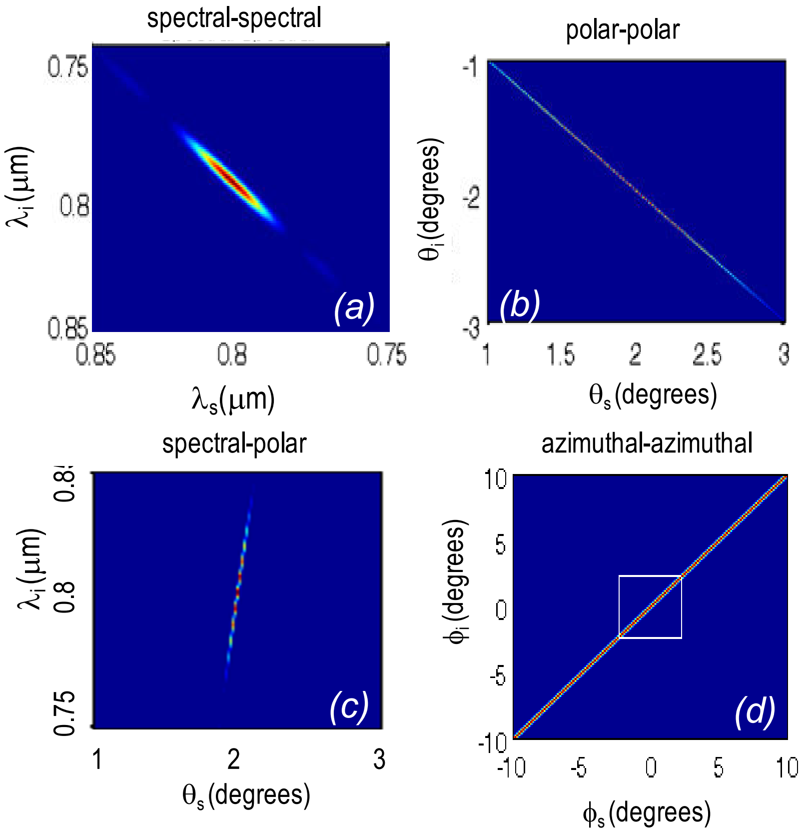

Figure 2-3: External correlations in a typical unfiltered source (plots of the joint intensity *f*). These plots show the a. spectral-spectral correlations, b. polar-polar correlations, c. spectral-polar correlations and d. azimuthal-azimuthal correlations. Typical azimuthal collection is ≤ ~2°, shown by the white solid lines.

angle[14] of ~2°). We can engineer a type-I degenerate[15] SPDC source that emits spatio-spectrally uncorrelated photons using the five conditions as listed in table 2.1. Let us consider a β-barium borate (BBO) crystal pumped by a train of ultrashort pulses centered at 405 nm, generating frequency-degenerate SPDC photon pairs, centered at 810 nm. The internal emission angle at which vector group-velocity matching occurs (computed from conditions 1 and 2 above) is $\theta_{s0} = -\theta_{i0} = 9.96^{\circ}$, which corresponds to ~16° external propagation angle. For this emission angle, and for the selected central emission frequency, the required crystal-cut angle required to attain phasematching is $\theta_{\mathrm{pm}} = 40.7^{\circ}$ (we

---

[14] *Internal* refers to the emission angle inside the crystal. The external emission angle, outside the crystal, is greater because of refraction, and is related to the internal angle by Snell's law.

[15] For type-I processes, simultaneous group-velocity matching and phase matching is possible only for the degenerate case.

also assume an azimuthal cut angle of $\phi_{\text{pm}} = 30^{\circ}$, for which the effective non-linearity is near its maximum[16]). The optimal crystal length can be shown to be $L = 300\ \mu m$ [21], based on the overlap of the crystal with the fiber-collection modes; condition 3 then results in a required pump-beam radius of $w_0 = 23.15\ \mu m$. The fulfillment of conditions $1-4$ results in a two-photon state that is essentially

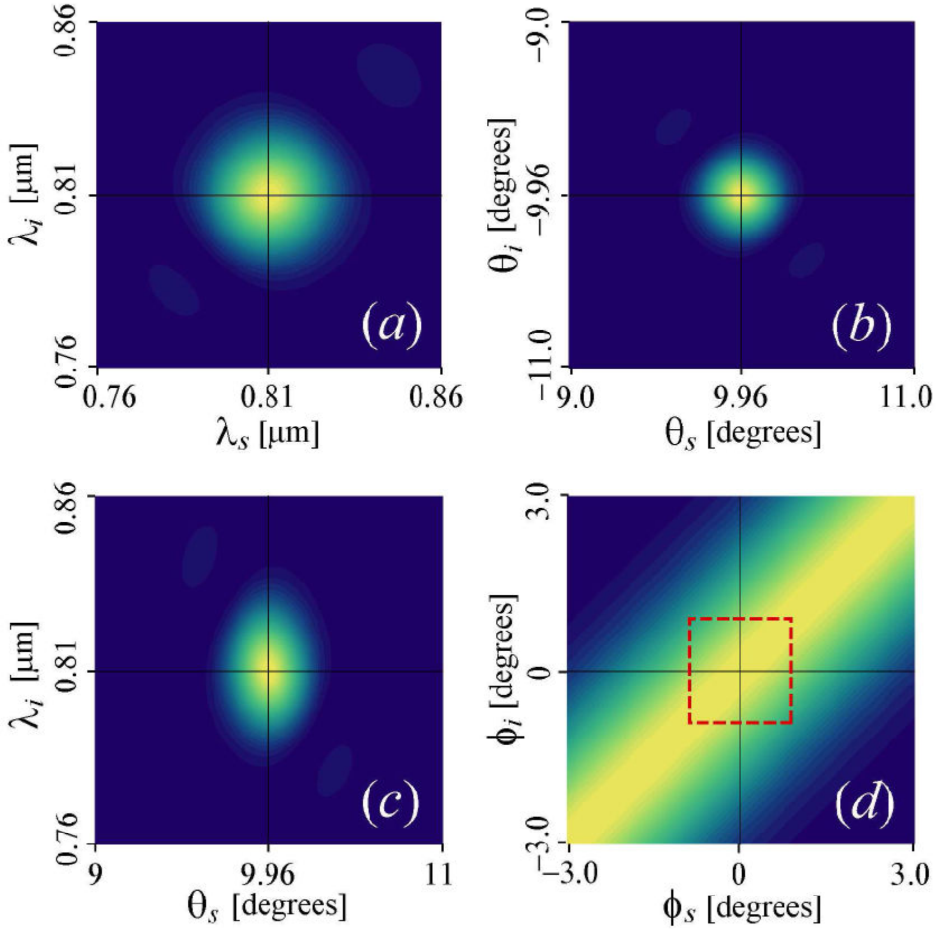

Figure 2-4: External correlations in the engineered source (plots of the joint intensity *f*). These plots show the a. spectral-spectral (non-)correlations, b. polar-polar (non-)correlations, c. spectral-polar (non-)correlations and d. azimuthal-azimuthal correlations. Azimuthal correlations can be suppressed by limiting collection to ≤ 1°, as shown by the red dotted lines [21].

---

[16] The effective nonlinearity d_{eff}^{eoo} is determined by the crystal optic axis angle specifications θ and ϕ [41]. The definitions of the crystal cut angles, and consequently their relationship to d_{eff}^{eoo} varies between different textbooks and manufacturers. E.g., Newlight Photonics, who supplied our BBO crystals, defines θ and ϕ such that $d_{eff}^{eoo} = d_{31}\ \sin\theta + \left(d_{11}\cos 3\varphi - d_{22}\sin 3\varphi\right)\cos\theta$, where d_{11}, d_{22} and d_{31} are the respective nonlinear susceptibility tensor coefficients. The optimized engineered crystal has an effective nonlinearity of ~1.64 pm/V, compared to ~1.92 pm/V for the typical case.

factorable in the spectral and polar-angle degrees of freedom. This can be seen from Figure 2-4, where we present plots of correlations between particular pairs of variables for the signal and idler photons. Figure 2-4a shows spectral $\omega_s - \omega_i$ correlations; Figure 2-4b shows polar angle $\theta_s - \theta_i$ correlations; Figure 2-4c shows mixed spectral-spatial $\omega_i - \theta_s$ correlations; Figure 2-4d shows azimuthal angle $\phi_s - \phi_i$ correlations. Note that while the analysis leading to the conditions for factorability relied on a power series expansion, the plots in Figure 2-4 were computed including the spectral and angular dependence of k vectors to all orders. As predicted, spectral, polar angle, and mixed spectral-polar angle correlations are essentially suppressed. Azimuthal correlations cannot be made to completely vanish; however, by restricting the directions of propagation which are allowed to reach the detectors, these correlations may be essentially suppressed. This is illustrated by the red dotted lines in Figure 2-4d, which correspond to limiting azimuthal angle ranges to $|\delta\phi_s|, |\delta\phi_i| \leq 1°$. Note that mixed spectral-polar angle correlations $\omega_i - \theta_s$ are similar to those shown in Figure 2-4c. Correlations between azimuthal angle variables and polar angle/frequency (not shown) are, for this particular source, essentially negligible.

Detailed comparison with typical sources: To evaluate the advantages of the engineering scheme, we compare three particular sources. First, we consider the engineered GVM source just presented, requiring large signal/idler propagation angles (~ 9.96° internal). We also consider two variations of a *typical* source (with internal propagation angles of ~2°): i). TF ("typical filtered") — a typical source for which the fiber-coupled signal and idler modes are spectrally filtered to render the photon pairs nearly-factorable, and ii). TFF ("typical filtered focused") — in addition to the spectral filtering, the pump beam is focused to the same degree as for the engineered source. For our comparison, TF and TFF involve the same pump and emission frequencies as the engineered source, i.e., 405 nm and 810 nm, respectively. All three sources are characterized by a crystal length $L = 300\ \mu m$ and a pump power of 1 mW. For the typical source, the smaller 2° emission angle requires a crystal cut angle of $\theta_{\mathrm{pm}} = 29.3^{\circ}$. For each source configuration the pump bandwidth is selected as $\lambda_{pump} = 2\overline{\Delta\lambda}$, where $\overline{\Delta\lambda}$ refers to the threshold bandwidth, expressed in nm, corresponding to the threshold value from our condition 5 in Table 2.1. A larger pump bandwidth could lead to a greater degree of factorability, though in practice the available laser bandwidth may be limited. Now we can compare these three sources in terms of source brightness and degree of factorability.

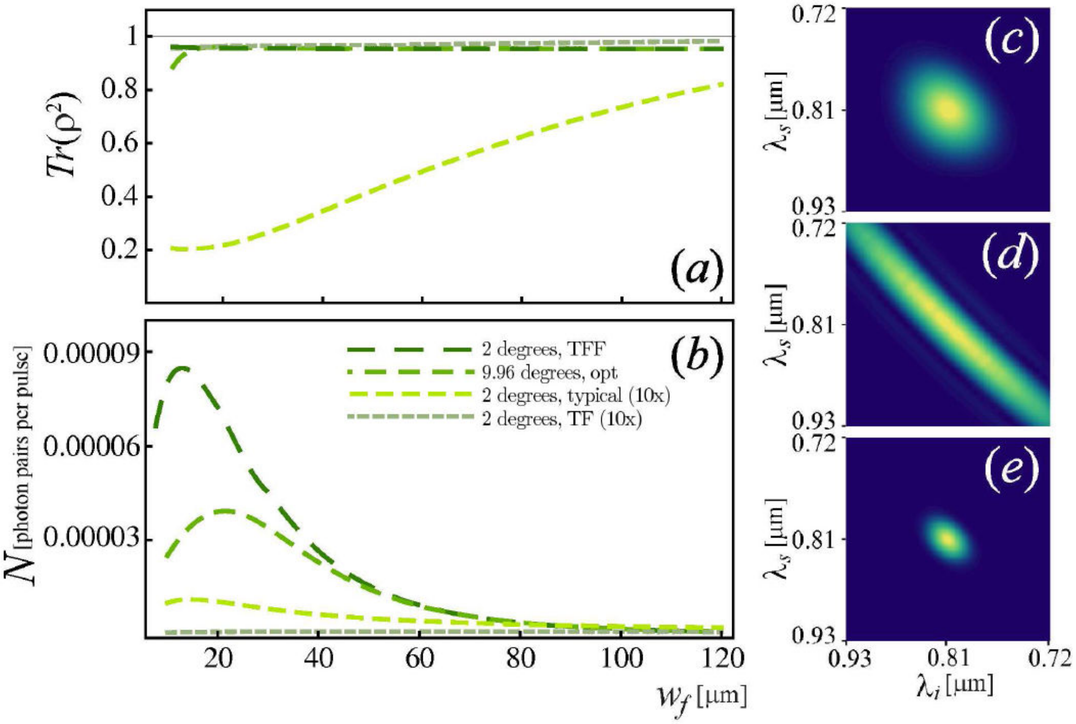

Figure 2-5: **a**. Purity for single heralded photon in the signal mode vs. fiber-collection mode radius w_f, for three sources of interest: i) optimized source, ii) 'typical' source and iii) 'typical' source rendered factorable through filtering. **b**. Brightness (number of fiber-coupled photon pairs per pump pulse, assume 1.25 x10^{-11} J energy per pump pulse) as a function of w_f for the three sources. Coupled joint spectra $f(\omega_s,\omega_i)$, plotted for the optimum value of w_f for the three sources: **c**. engineered, **d**. typical, and **e**. typical filtered (TF) sources. Figure is from [21]. TFF refers to the typical filtered source with the pump focused.

The degree of entanglement present can be characterized by the heralded single-photon purity, i.e., $Tr(\rho_s^2)$ where ρ_s is the density operator for the heralded single photon in the signal mode. Another crucial source attribute is the source brightness N, defined as the number of photon pairs that could be coupled into a single-mode fiber for a single pump pulse. These two quantities, $Tr(\rho_s^2)$ and N, can be used to compare the three sources considered. For the ideal source we expect $Tr(\rho_s^2)=1$ and N to be maximized. Also, for a given pump beam radius w_0, the degree of focusing given by w_f, the fiber-collection mode radius on the output face of the crystal, needs to be optimized to maximize the resulting brightness. Figure 2-5a and b show the expected heralded single-photon purity and the source brightness as a function of w_f, for the optimized phasematching parameters. Figure 2-5c–e show the fiber-coupled joint spectra for the three sources considered here (TF, TFF and engineered), where for each case the optimum fiber-collection mode radius has been selected. The engineered source leads to a brightness of ~4 × 10^{-5} fiber-coupled photon pairs per pump pulse (assuming a pulse energy of 1.25 x 10^{-11} J), together with a purity of 0.96, for pump bandwidth of 28.8 nm[17]. In contrast, the typical source leads to a comparatively low single-photon purity, which in the vicinity of the maximum expected brightness, reaches values of only 0.2. Figure 2-5c and d show that while the engineered source leads to a nearly factorable joint spectrum, the typical source exhibits strong spectral correlations. Spectral filtering imposes factorability on the typical source. However, this is achieved at the cost of a significant reduction of the two-photon flux. Thus, the engineered source leads to a 500-fold brightness enhancement compared to the TF source, as shown in Figure 2-5b. The TFF source, the typical filtered source with an optimized pump focus and fiber collection, however, has similar purity and brightness advantages as the engineered source, indicating that the majority of the benefits arise from optimizing the pump focus and downconversion collection. Table 2.3 summarizes the optimized SPDC parameters for the three different sources used in these comparisons.

SPDC Parameter/ Source	**Engineered**	**TF**	**TFF**
Crystal length L	300 μm	300 μm	300 μm
Internal downconversion emission angle $\theta_s = \theta_i$	9.96°	2°	2°
Crystal cut angle θ_{pm}	40.7°	29.3°	29.3°
405-nm pump bandwidth $\Delta\lambda_{pump}$	28.8 nm	10.5 nm	10.5 nm
Energy per pump pulse	1.25x 10^{-11} J	1.25x 10^{-11} J	1.25x 10^{-11} J
Pump beam waist w_0 at the center of the crystal	23.15 μm	1mm	23.15 μm
Fiber collection mode radius w_f	21.46 μm	N/A	11.36 μm
Spectral filter bandwidth	None used	15.3 nm	17.5 nm
Source Purity $Tr\left(\rho_s^2\right)$	0.96	0.96	0.96
Source Brightness N	4x10^{-5}	8x10^{-8}	8x10^{-5}

Table 2-3: Optimized SPDC parameters for the engineered, typical filtered (TF) and typical filtered focused (TFF) sources, assuming BBO crystals and $405\text{ nm} \rightarrow 810\text{ nm}+810\text{ nm}$ type-I SPDC.

2.3 Experimental Characterization

The spectral and spatial correlations present in the JTPA of any source can be characterized via several methods. The brute-force methods involve projecting the signal photon onto the relevant parameter subspace and measuring the corresponding idler's value, thereby recreating the JTPA. For example,

---

[17] The 28.8-nm bandwidth at 405 nm corresponds to a 81.3-nm bandwidth for an ultrafast titanium-sapphire laser centered at 810 nm, which gives rise to the 405-nm SPDC pump via second harmonic generation.

spectral-spectral plots of the joint two-photon intensity can be measured using a monochromator[18] in each of the signal and the idler arms. However, the proof of the pudding – the indistinguishability of the photons from a source – lies in direct testing via a two-source Hong-Ou-Mandel interferometer (Section 1.1.1). For such a test, we would interfere photons from two engineered sources; a high visibility would then be proof of their true indistinguishability. However, for such a test we would need *two* such sources that are synchronized with each other. Though this is our eventual goal, for preliminary characterization we revert to the brute-force methods to test the engineered source. Here we discuss two separate experimental characterizations of the engineered crystal, respectively measuring the spectral-spectral correlations and the spatial-spatial correlations, by obtaining the joint spectral/spatial intensity of the emitted SPDC photons.

The source: The engineered scheme discussed in Section 2.2 calls for a 300-μm BBO crystal pumped by a ~28-nm bandwidth pump at 405 nm. To create such a pump, we would have to frequency-double an ~80-nm bandwidth (~20-fs) Ti-Saph laser; such an extremely large bandwidth might lead to a host of complications, such as dispersion, chirp, etc. Therefore, we first measure the correlations in a typical source: a 600-μm BBO pumped with a ~4-nm bandwidth at 405 nm. Then, to test the applicability of our engineering techniques over a wider range, we use a quasi-optimal source: a 600-μm BBO pumped with the optimized (for a 600 μm crystal) 15-nm bandwidth at 405 nm.

2.3.1 Spectral-Spectral Correlations: Fourier Spectroscopy

Spectral-spectral correlations can be measured using monochromators in each arm, as mentioned above. In practice, however, there are two drawbacks to this approach –it requires *two* monochromators, and the coupled output light results in very low coincidence counts, thereby necessitating extremely long measurement times. Alternatively, we can infer the frequency correlations present in the source by analyzing in the temporal domain, which is the conjugate space of frequency. One way to do this would be to use long, dispersive fibers so that the different frequencies would separate temporally by more than the detector timing resolution [43]. However, with our current timing jitter of ~180 ps, we would need ~2 km of standard 810-nm fiber (with -125-ps/(nm-km) specified dispersion) to get a ~0.75-nm resolution. Unfortunately, the transmission (at 810-nm) through such a length of fiber is only ~10% (typical attenuation ~5dB/km) implying a coincidence coupling efficiency of only ~1%. Given the extremely low

---

[18] A monochromator is an optical device, usually employing a precision grating and slits, to transmit and mechanically select a narrow band of wavelengths of light chosen from a wider range of wavelengths available at the input.

coupling efficiency and other disadvantages (e.g., we would need a pulse picker[19]), we decided against this approach.

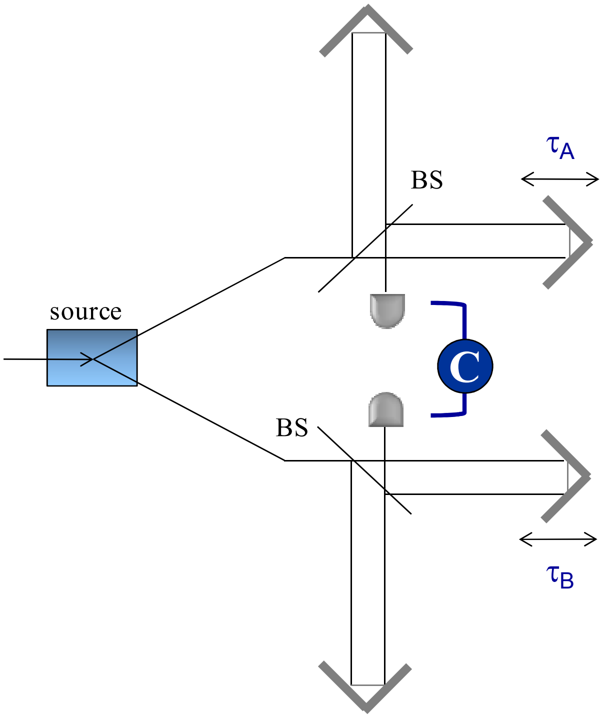

Figure 2-6: Simplified schematic of a Fourier spectrometer used to measure the JTI (based on [42]) using two separate interferometers (*C* stands for coincidence detection and *BS* refers to beam splitters).

A second newly demonstrated technique [42] relies on Fourier Spectroscopy, which maps out the two-photon joint *temporal* intensity (JTI). A Fourier transform of the JTI gives the required *joint spectral intensity* (JSI). The Fourier spectrometer works as follows: the signal and the idler are sent into separate interferometers (Figure 2-6). The signal (idler) interferometer introduces a relative delay τ_A (τ_B) between its two paths and the recombined light at the output of the interferometer is measured in coincidence. The coincidence probability $P_{AB}(\tau_A, \tau_B)$ as a function of the delays τ_A and τ_B maps out the JTI. To understand how the Fourier spectroscopy technique yields the joint intensity we can analyze the expected behavior in each interferometric arm; the detection probability for a photon of frequency ω is similar to that in a standard interferometer, namely $P = \frac{1}{2}(1+\cos\omega t)$. Figure 2-7 models the detection probability (in one arm) as a function of time for different input frequencies, as seen in a “white-light” interferometer.

---

[19] Our estimated downconversion bandwidth is ~42 nm; Given a fiber dispersion of ~0.25ns/nm implies that the pulse will spread ~10.5 ns. The Ti-Saph pump pulse separation is 12.5 ns. Thus, in order to avoid consecutive pulses from overlapping with each other, we need a pulse picker.

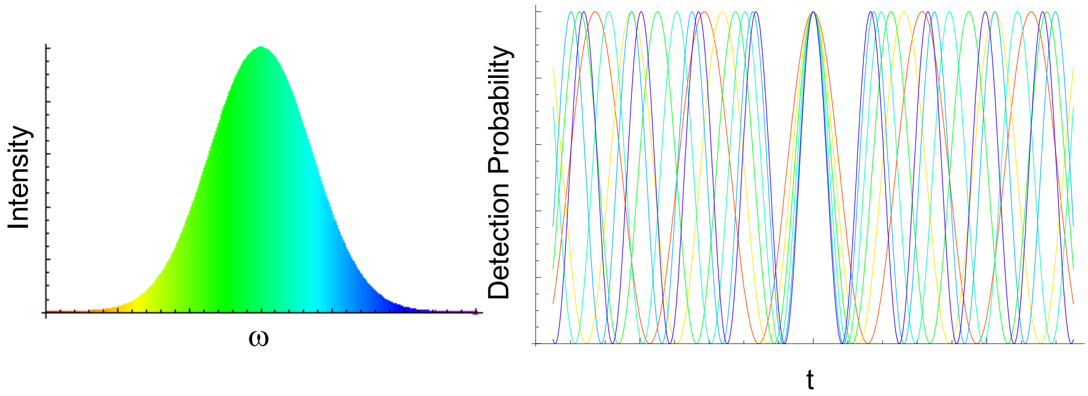

Figure 2-7: Expected behavior in a “white-light” interferometer. Left: Input intensity profile as a function of frequency. Right: Detection probability in one arm as a function of time and frequency.

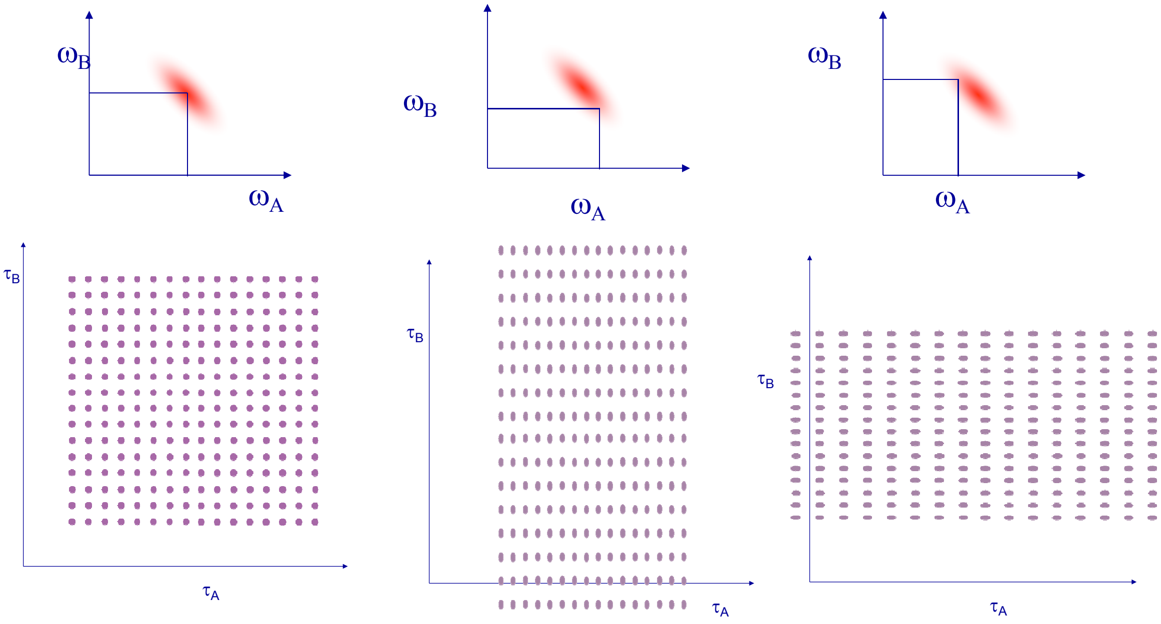

Figure 2-8: Rough schematic of expected coincidence Fourier interferogram $P(\tau_A,\tau_B)$ for three different sets of (ω_A,ω_B) selected from the joint spectral intensity: left: $\omega_A = \omega_B$, middle: $\omega_A > \omega_B$, right: $\omega_A < \omega_B$.

The joint coincidence probability for a source with an arbitrary spectrum takes the form [42]

$$P_{A,B}(\tau_A,\tau_B) \propto \frac{1}{4}\int d\omega_A \int d\omega_B \left\langle I(\omega_A) I(\omega_B)\right\rangle \left(1+\cos\omega_A\tau_A\right)\left(1+\cos\omega_B\tau_B\right), \qquad 2.5$$

where $\hat{I}(\omega_A)$ and $\hat{I}(\omega_B)$ are the spectral intensity operators in each arm and $\left\langle \hat{I}(\omega_A)\hat{I}(\omega_B)\right\rangle$ gives the joint spectral intensity. Figure 2-8 shows how the Fourier interferograms (plots of $P(\tau_A,\tau_B)$) vary with specific values of (ω_A,ω_B) for three different cases: $\omega_A=\omega_B$, $\omega_A>\omega_B$, and $\omega_A<\omega_B$. The Fourier interferogram for the entire joint spectral intensity, i.e., all available ω_A,ω_B, characteristic of typical SPDC sources is shown in Figure 2-9. The essence of the technique, then, is to measure the data on the right, and from that deduce the underlying spectral-spectral distribution (left).

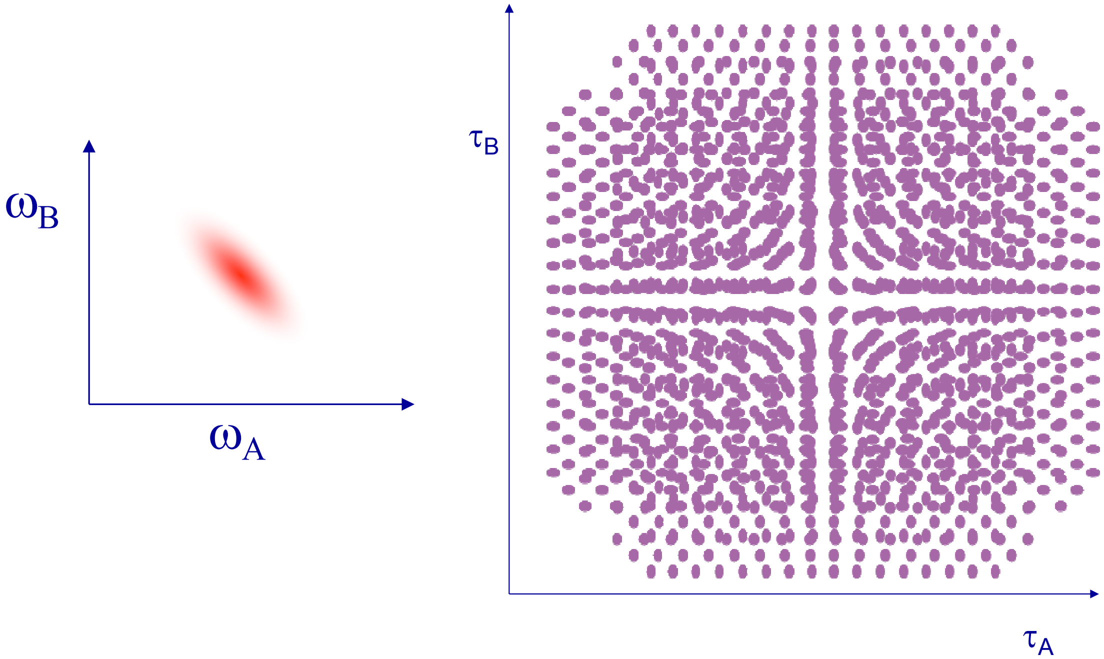

Figure 2-9: Schematic of expected coincidence Fourier interferogram $P(\tau_A,\tau_B)$ for the entire joint spectral intensity shown on the left.

Instead of using an interferometer with two spatially separated arms, we can use a pair of "common-path" Mach-Zehnder interferometers in order to ensure the stability of the interferometric setup over the entire two-dimensional scan. In such a *polarization* interferometer, shown in Figure 2-10a, the two interferometric arms are implemented as orthogonal polarizations. A half-wave plate (HWP) rotates the polarization of the generated photons to 45°, resulting in the two orthogonal polarizations H+V. The optical path difference arises in a birefringent crystal, where each of the polarizations sees a different refractive index and, thus, a different optical path length. The entire range of the temporal delay $+\tau_A$ to

$-\tau_A$ and $+\tau_B$ to $-\tau_B$ is implemented by a combination of a quartz plate, cut with a vertical optic axis and a pair of quartz wedges with horizontal optic axes. The quartz plate gives a positive fixed delay, and the wedges provide a variable negative delay. Finally, the two polarizations are interfered using a second HWP and a polarizing beam splitter (PBS) to analyze in the diagonal polarization basis.

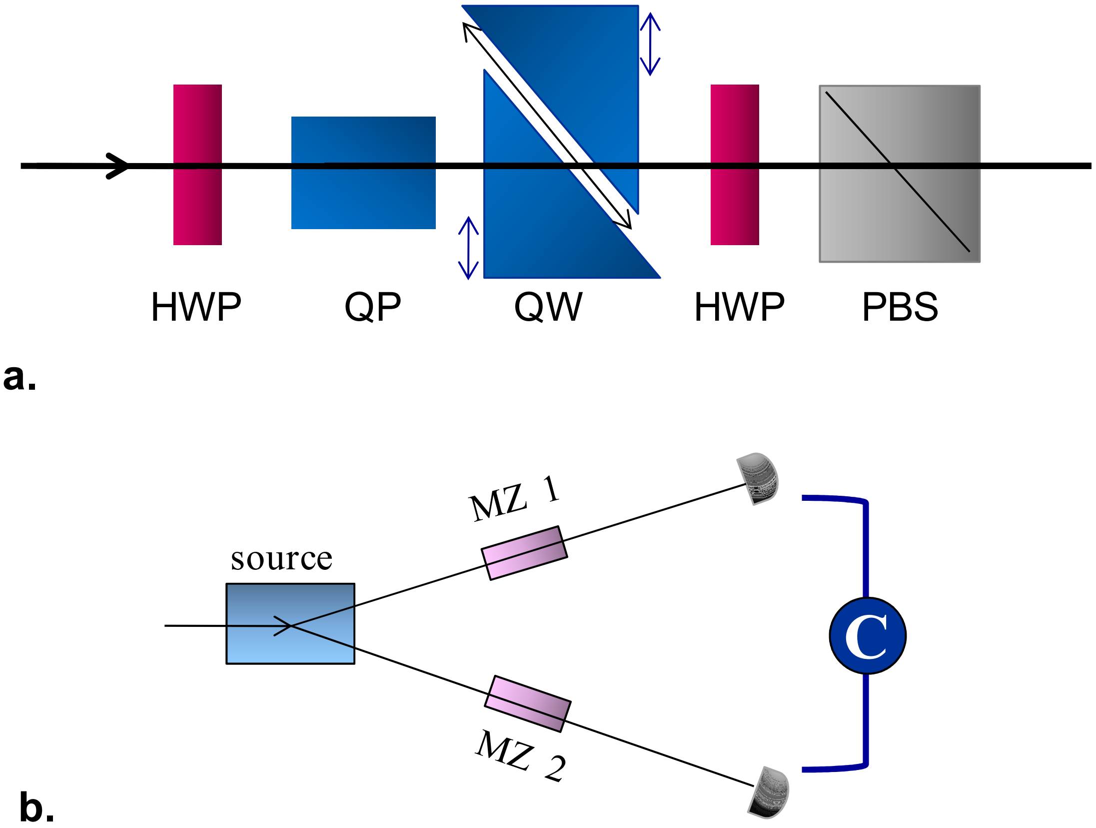

Figure 2-10: **a**. A common-path polarization Mach-Zehnder (MZ) interferometer (top view, so 'vertical' is out of the paper) implemented using half-wave plates (HWP), a birefringent quartz plate (QP), birefringent quartz wedges (QW) and a polarizing beam splitter (PBS). The blue arrows indicate the direction of the optic axis cut. **b**. Experimental setup for Fourier Spectroscopy.

The common path interferometers in each arm were implemented using two pairs of matched wedges, each with a side profile of 37.8 mm x 20 mm, wedged at 5° and horizontal optic axis. Each pair was mounted such that they had a thickness range of 4.38 – 7.07 mm (signal side) and 4.58 -7.08 mm (idler side). Additionally, quartz plates of varying thicknesses with vertical optic axes were used in the signal (idler) arms; combined with the wedges, these gave an effective temporal range of ~-200 fs to 200 fs.

Figure 2-11 shows the measured singles detection probability in the signal arms as one of the quartz wedges was scanned[20]. The singles in the idler arm behaved similarly.

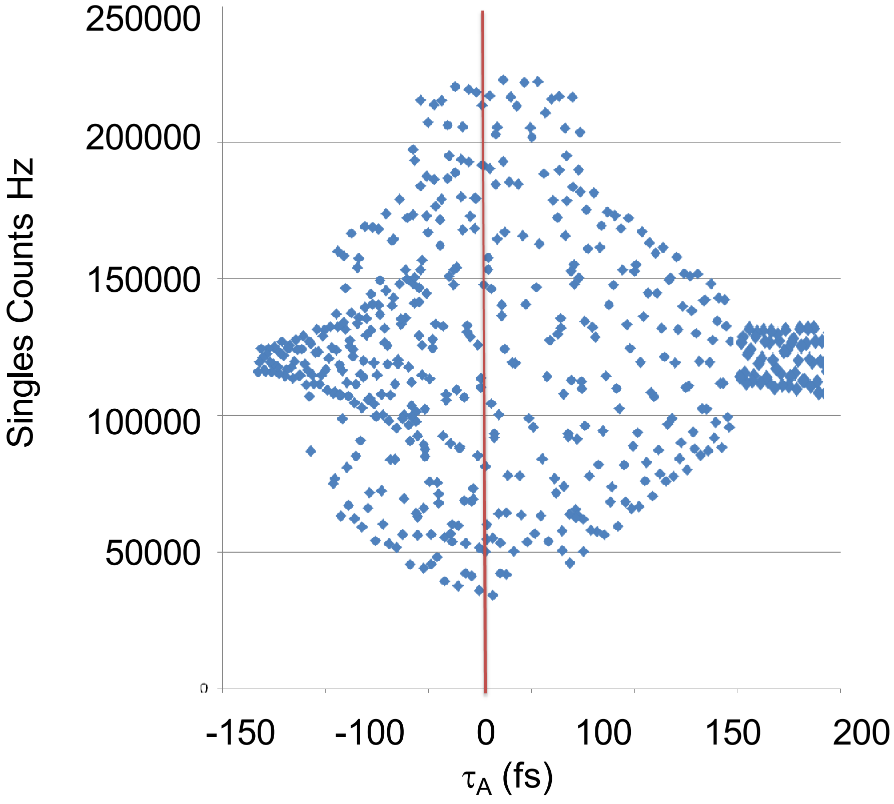

Figure 2-11: Measured singles counts in the signal arm using the common path interferometer.

Figure 2-12 shows an example of the expected JTI for a typical source and the resulting Fourier transform. The vertical and horizontal fringes in the JTI correspond to the interferometric fringes from a *single* arm; it is the diagonal fringes that contain information about the joint spectrum. Thus the JSI data can be found in the four "corners" of the Fourier transform plot – the yellow circle marks the desired JSI pattern, where the spectral correlations seen are that expected from a typical spectrally entangled source.

---

[20] We did not have the capability to scan the entire range in one setting – different combinations of quartz wedges were used to span the entire range. For example, a 6.8-mm quartz plate (vertical optic axis) combined with the wedges in the signal arm was used to scan from -8 fs to 76 fs. Similarly, a 15.85-mm quartz plate (vertical optic axis) and an effectively ~13.2-mm quartz plate (horizontal optic axis) were combined with the quartz wedges to scan from -141 fs to -57 fs. The data in Figure 2-11 is a compilation of several such measurements; therefore, any discontinuities that appear are an artifact of the measurement technique. This can be easily avoided by having optimal custom quartz wedges and plates to give the appropriate time range (discussed later in this Section).

In order to reproduce the JSI accurately, the coincidence probability needs be scanned over a significant temporal range (~ -250 to 250 fs) in each arm. However, with the available set of quartz plates and wedges we were only able to get a temporal range of ~-8 to 76 fs in the signal and -22 to 57 fs in the idler simultaneously, obtained using a 6.8 mm (6.4 mm) quartz plate in combination with the wedges in the signal (idler) arm. Figure 2-13 shows the interferogram measured using these sub-optimal temporal ranges for the 0.6-mm engineered crystal pumped using a ~4-nm bandwidth 405-nm frequency-doubled Ti-Saph laser focused to ~340 μm[21]. Thus, while we are able to make out some features in the diagonal "corners", we need a longer and more symmetric scanning range in order to obtain more accurate data. Quartz wedges each with a edge profile of 35x20 mm and wedged at 32°, combined with 15.85-mm quartz plates can readily give the desired scanning range of -250 to 250 fs. Thus, we have confirmed that Fourier spectroscopy is indeed a viable and easy technique to measure the JSI and characterize the spectral properties of the engineered source.

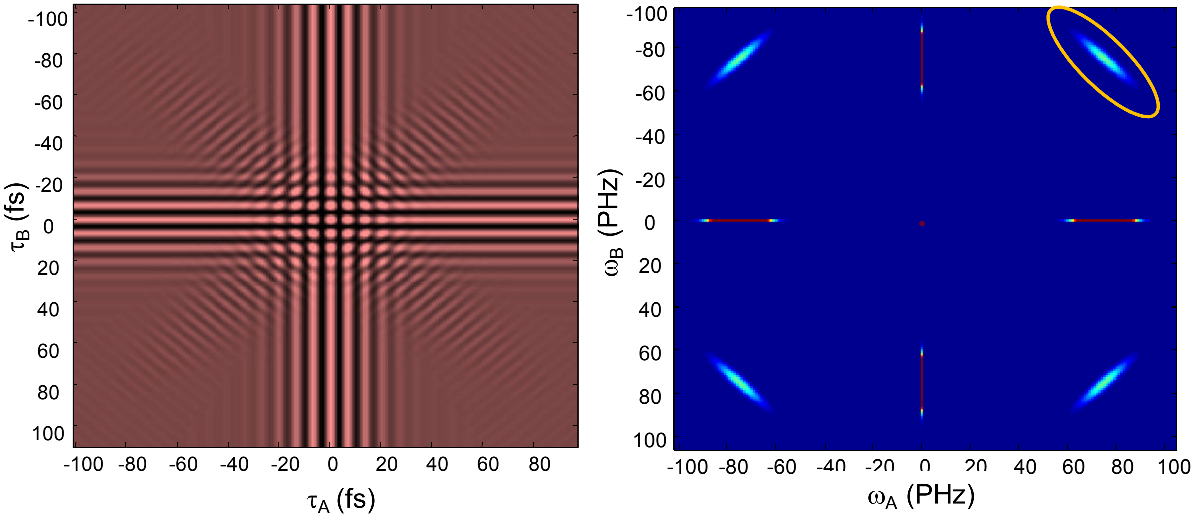

Figure 2-12: Left: Predicted coincidence interferogram as a function of optical path differences τ_A and τ_B gives the joint temporal intensity distribution. Right: The Fourier transform of the joint temporal intensity. The yellow oval marks the desired joint spectral intensity [42]. Note the vertical axis is flipped.

---

[21] The beam spot at the crystal was measured by using a "knife-edge" technique [44] – where the side of the crystal mount aperture itself was used as a "knife-edge".

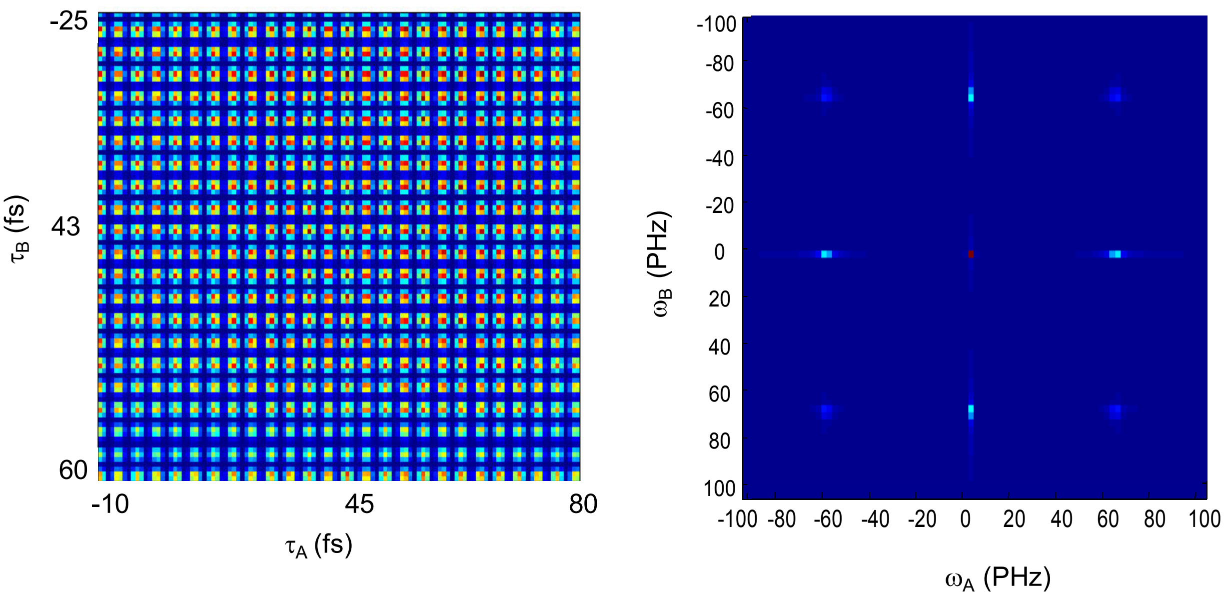

Figure 2-13: Experimentally measured coincidence interferogram (left) and its Fourier transform (right), for the suboptimal scanning ranges.

2.3.2 Spatial-Spatial Correlations

Spatial-spatial correlations are obtained in a more direct way – two small-aperture irises are scanned independently for the signal and the idler, and the coincidence probability is measured. Figure 2-14 shows the resulting two-photon joint spatial intensity for the typical source, spectrally filtered using 10-nm band-pass filters at 810 nm. These spatial correlations are measured by translating a narrow iris (~2-mm) in x and y and recording the corresponding coincidence counts, as shown in Figure 2-14. These measurements were taken with irises located ~58 cm from the engineered crystal (~16° external propagation angle), pumped using a ~4-nm bandwidth 405-nm frequency- doubled Ti-Saph laser focused to ~340 μm. The scan range corresponds to ~1° in both x and y directions, implying that for the measurements here $x = \theta$ (the downconversion polar angle) and $y \approx \phi$ (the downconversion azimuthal angle). Thus, these plots can be roughly compared to the typical (Figure 2-3) and the engineered source (Figure 2-4); since we have only included GVM as part of the optimization process, the angular correlations fall in between that of the typical and the engineered source as expected.

Ideal spatial-spatial correlations (required to faithfully reproduce the theoretical plots in Figure 2-3 and Figure 2-4) would involve collection using single-mode fibers and severe spectral filtering – collecting using signal and idler irises is equivalent to integrating over the angular aperture of the irises as well as over the frequencies. However, optimal scanning while simultaneously coupling into single-mode fibers can be experimentally challenging and requires long data acquisition times. On the other hand, collection with narrow irises can be modeled for comparison to experiment.

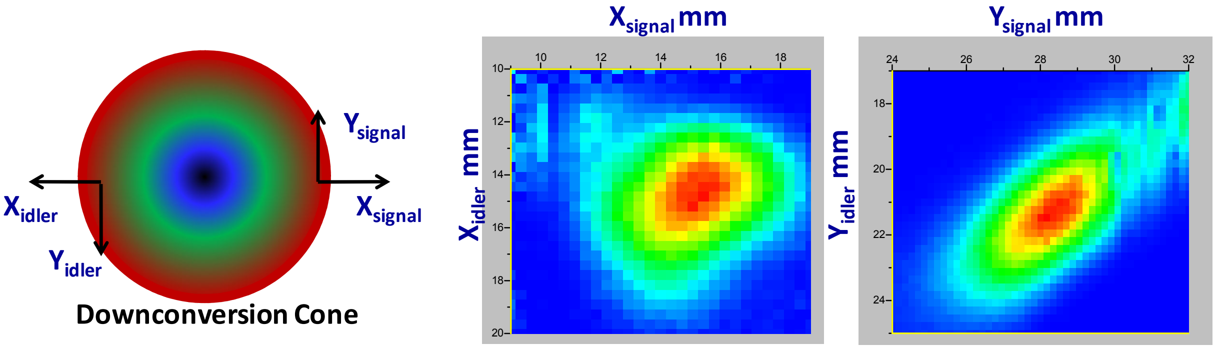

a. b. c.

Figure 2-14: a. Experimental setup to measure spatial correlations. a. ~2-mm irises (one for the signal, one for the idler) are scanned independently along *x* and *y* and the coincidence probability is measured. b. Measured two-photon joint spatial intensity along the *x*-*x* direction. c. Measured two-photon joint spatial intensity along the *y*-*y* direction.

2.3.3 Mixed Correlations

Mixed spatial-spectral correlations are harder to obtain using the Fourier spectroscopy method; a direct measurement would rely on using a monochromator on one arm and a scanning small-aperture iris on the other. Using similar techniques, the intra-photon correlations (correlations between different DOF within the same photon) can also be measured. In fact, one of the primary expected limitations of the engineered source is an intra-photon spatial chirp of ~0.82 mrad/THz) as shown in Figure 2-15. This limits the heralding efficiency, a key parameter of single-photon and other "trigger" sources, of the engineered

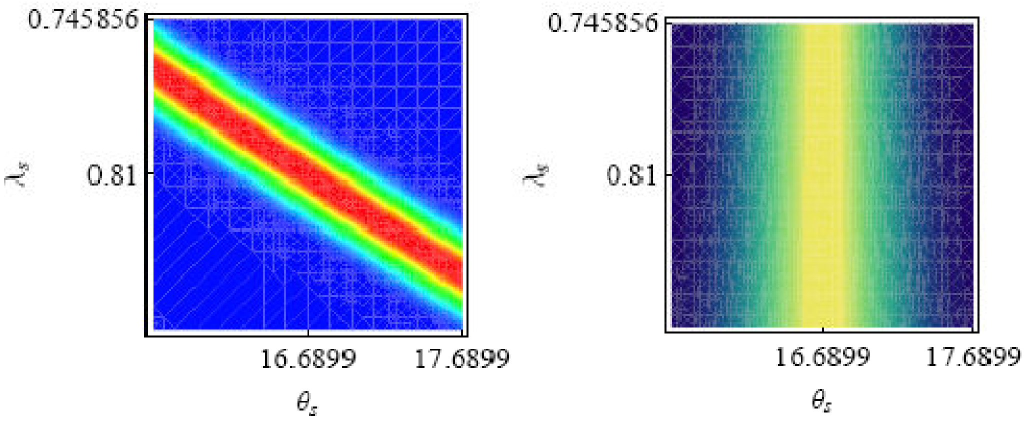

Figure 2-15: (Left): Predicted intra-photon chirp for the engineered optimized crystal. (Right): Modeled single-mode fiber collection. The product of the two plots gives the net expected fiber-coupled photons.

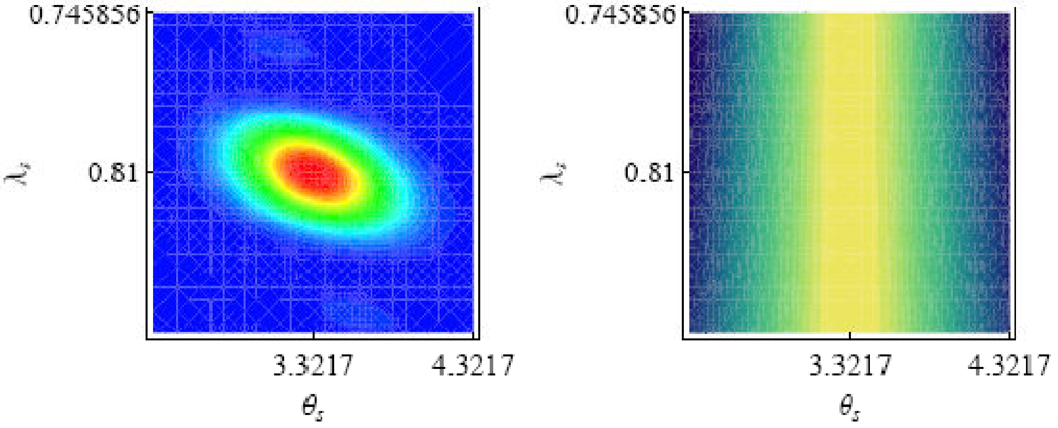

Figure 2-16: (Left): Predicted intra-photon chirp for the typical focused filtered source. (Right): Modeled single-mode fiber collection. The product of the two plots gives the net expected fiber-coupled photons.

GVM source to ~33%. In comparison, the heralding efficiency of the typical filtered source is ~43% and that of the typical focused filtered source is ~53% (the chirp for typical focused source is shown in Figure 2-16). It might be possible to eliminate such intra-photon chirp using diffraction gratings in each arm, thereby readily increasing the heralding efficiency of the source without sacrificing source purity.

2.4 Polarization Entanglement: The Two-Crystal Scheme

State Creation: Experimentally, polarization-entangled photon pairs can be generated via the nonlinear process of SPDC [18], using the *two-crystal scheme* [24] shown in Figure 2-17. Consider two thin, type-I phasematched, identical χ^2 crystals: the first crystal is oriented such that a vertical polarized pump photon down converts into horizontal photons, while the second crystal is oriented such that a horizontal polarized pump photon down converts into vertical photons. Entangled state states can be created by placing these two crystals adjacent to each other. When pumped by photons polarized at an angle $\theta_{p,}$ the downconversion processes in each crystal are coherent with one another, thereby generating arbitrary superposition states of horizontally (H) and vertically (V) polarized photons:

$$|\psi\rangle = \cos\theta_p |H_1H_2\rangle + e^{i\varphi}\sin\theta_p |V_1V_2\rangle \quad , \qquad 2.6$$

where the relative phase φ depends on the phase-matching conditions and crystal parameters. By pumping both crystals equally, i.e., $\theta_p = 45°$, we can generate a maximally entangled state, given by

$$|\psi\rangle = \frac{1}{\sqrt{2}}\left(|H_1H_2\rangle + e^{i\varphi}|V_1V_2\rangle\right) \ . \qquad 2.7$$

Such polarization-entangled *two-qubit*[22] states are valuable resources for OQIP, and the two-crystal scheme, specifically, is extensively employed as an OQIP source [45-46] .

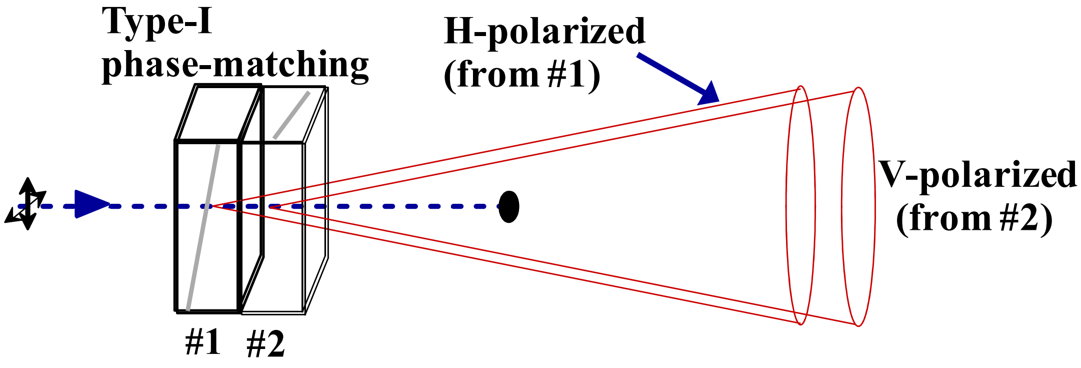

Figure 2-17: The two-crystal scheme, shown with the optic axes orientations and the corresponding downconversion photons from two orthogonally oriented type-I phase matched nonlinear crystals. If the downconversion cones overlap (accounting for the finite diameter of the pump beam, the cone opening angle and the length of the crystals), emitted photons will be entangled in polarization.

Quantum State Measures: To quantify the quality of the two-qubit polarization-entangled state created by our sources, we use several measures: fidelity, concurrence and tangle. Fidelity measures the amount of overlap between two states ρ_1 and ρ_2 [47]. In general,

$$F(\rho_1,\rho_2)=\left(Tr\left\{\sqrt{\sqrt{\rho_1}\rho_2\sqrt{\rho_1}}\right\}\right)^2, \qquad 2.1$$

which simplifies to $\left|\langle\psi_1|\psi_2\rangle\right|^2$ for pure states. While fidelity typically measures how well the generated state matches some desired state, concurrence and tangle quantify the non-classical properties of a quantum state [48]. The concurrence C for a mixed state ρ of two qubits is defined as

$$C(\rho)=max\ (0,\sqrt{\lambda_1}-\sqrt{\lambda_2}-\sqrt{\lambda_3}-\sqrt{\lambda_4}), \qquad 2.2$$

in which λ_i are the eigenvalues of $\rho(\sigma_y\otimes\sigma_y)\rho^*(\sigma_y\otimes\sigma_y)$ in decreasing order, and σ_y is the $\begin{pmatrix}0 & -i\\ i & 0\end{pmatrix}$ Pauli spin matrix. Tangle T can be computed from the concurrence:

---

[22] While a classical bit can be either a 1 or a 0, a quantum bit – *qubit* – can be in a superposition of all the basis states, in this case $|H\rangle$ or $|V\rangle$.

$$T \equiv C^2 . \qquad 2.3$$

Both concurrence and tangle vary from 0 (unentangled state) to 1 (maximally entangled state).

State Measurement: In general, quantum states cannot be "measured" easily. However, quantum state tomography [49], which uses several projective measurements in different bases, can be performed to reconstruct the quantum state of an ensemble of particles. To characterize the entangled state generated from the two-crystal source, we use 16 projective measurements in four different bases. By converting these projective measurements into probabilities, we can find the most likely state using a maximum-likelihood technique (an algorithm that finds the legitimate quantum state most likely to have resulted in the projective measurements). Further details on quantum state tomography for characterizing photonic qubits can be found in [49-50][23].

2.5 The Indistinguishable Source: The Path Forward

Our goal is to develop a bright, fiber-coupled, polarization-entangled but spatio-spectrally unentangled source. In Section 2.2, we discussed an optimal type-I SPDC crystal that produces spatio-spectrally unentangled photons. By incorporating two of these engineered crystals in the two-crystal scheme for polarization entanglement, we can accomplish our goal and create an indistinguishable photon-pair source. The idea is fairly straightforward —combine two technologies: the time-tested two-crystal polarization-entanglement method with the thoroughly analyzed *un*entanglement engineering design. In practice, however, we encounter several obstacles. In fact, there are three main challenges that need to be solved to engineer the ideal indistinguishable source: 1. temporal decoherence, 2. the *Migdall* effect, and 3. birefringent focusing. Each of these challenges arises because a particular requirement imposed by the *un*entanglement engineering design does not mesh optimally with the two-crystal scheme for polarization entanglement. The first issue, temporal decoherence, presents a challenge because the *unentanglement* design requires an ultrafast broad-bandwidth pump in order to minimize spectral correlations; however, using a broad bandwidth pump in the two-crystal scheme results in a highly decohered state with no discernable polarization entanglement. The next chapter discusses the origin of the temporal decoherence and its solution. The second challenge, the *Migdall effect* – the directional dependence of the downconversion polarization – becomes problematic only as a result of the large downconversion emission angle ~16° required by the GVM engineering scheme. Chapter 4 presents the first experimental confirmation of the Migdall effect, elaborates how it affects the engineering of the indistinguishable

---

[23] The tomography code is available online at http://research.physics.illinois.edu/QI/photonics/Tomography/.

source and, finally, presents ways to overcome it. The last problem, birefringent focusing/collection, stems from the optimization constraint imposed by the unentanglement conditions – the fiber collection-mode radius and the pump beam waist at the center of the SPDC crystal need to be specific values. Normally, this would not pose a big problem; controlling the focus of a Gaussian beam can be easily done with a lens; however, the two-crystal scheme for polarization entanglement relies on *two* crystals simultaneously pumped by orthogonal polarizations. Thus, the differently polarized beams have to focus at (and be collected from) slightly different longitudinal locations, which necessitates the capability to birefringently focus and collect photons. Chapter 5 discusses the complications that arise when we attempt to perform this seemingly simple manipulation. In fact, inconsistencies between our experiments and existing theory motivated us to develop a detailed theory elucidating the underlying behavior, and further, impelled us to develop a novel technique for birefringent focusing/collection. Hence, en route to engineering an ideal indistinguishable source we have solved a number of experimental and theoretical problems, developed a more affordable and convenient photonic qubit source, confirmed previously stated physical effects for the first time, and proposed novel techniques relying on basic concepts in physics. The next few chapters discuss each of these results in depth.

Chapter 3
Challenge 1: Temporal and Spatial Compensation[24]

"Evolve like a wave function. Breathe deep. Don't let any interaction collapse you or the environment decohere you."

-From the never-to-be released self-help series, Life Lessons from a Science Lab.

One of the foremost requirements to engineer indistinguishable photons is a broad bandwidth pump (Section 2.2), facilitated by an ultrafast femtosecond laser. The wide range of frequencies available in a broad bandwidth pump relaxes the strict limitation imposed by energy conservation, resulting in minimal spectral correlations in the engineered source. Thus, the pump bandwidth, along with the crystal length (which determines the range of pump frequencies that are phasematched for downconversion) need to be optimized to eliminate spectral correlations. However, decoherence in ultrafast entanglement sources causes a tradeoff between source brightness and fidelity, making it challenging to create an efficient high-fidelity entanglement source using these pumps. In fact, apart from needing ultrafast pulsed femtosecond pumps for engineering entangled-photon modes [21, 25, 51], these sources provide critical timing information and enable synchronization, making them essential for various quantum information processing protocols, including quantum teleportation [52-53] and optical quantum computing [7, 54]. Further, ultra-bright sources of entangled photons are required to scale up and facilitate practical OQIP. Therefore, sourced of ultrafast ultra-bright polarization-entangled photons would be a prized technology.

The predominant method for ultrafast entanglement generation has thus far been sources based on either type-II phasematching or type-I sources that require interferometric configurations [55-60]. Type-II sources are limited by fundamentally small solid angles over which entanglement persists. In contrast, type-I entanglement sources are advantageous because of their comparatively high brightness, stability and ease-of-alignment [24]. The brightness of all SPDC-based entanglement sources is limited in practice by decoherence, and fundamentally by the nonlinear dielectric tensor of the SPDC crystal used. In this chapter, we present ways to design ultra-bright type-I sources of entangled photons by combining

---

[24] Reproduced in part from R. Rangarajan, M. Goggin and P. G. Kwiat. Optimizing Type-I polarization-entangled photons. *Optics Express*. **17**, 18920 (2009). Copyright 2009 Optical Society of America, U.S.A.

multiple decoherence-compensation techniques. As it turns out, such decoherence mechanisms plague entanglement sources employing other broad bandwidth (or “non-monochromatic”) pumps, such a cw-diode lasers. Thus, we also discuss ways to generate high-fidelity polarization entanglement from diode lasers. Additionally, we demonstrate an ultrabright source by incorporating an unconventional highly nonlinear *biaxial* SPDC crystal, bismuth triborate (BiB_3O_6 , BiBO).

3.1 Decoherence Mechanisms and Brightness Limitations

The dominant decoherence mechanisms in polarization-entangled sources depend on the source specifications, which in turn depend on the particular application. For instance, given their simplicity, low costs and portability, cw-diode lasers appear attractive as pumps for applications such as quantum cryptography and investigating fundamental physics in undergraduate laboratories [61-62]. Such sources have nevertheless traditionally been limited by reduced entanglement with larger collection irises and increasing pump bandwidths. Here we consider the two main dephasing mechanisms that degrade type-I polarization entanglement: emission-angle dependent phase, and pump-frequency dependent phase, characteristic of low coherence-time pumps such as ultrafast and free-running diode lasers. The entanglement quality is typically recovered by strong filtering in the extra degree of freedom (e.g., narrow irises and spectral filters) thereby drastically reducing the collection efficiency [22, 27, 63]. However, using a spatial-phase compensation technique, one can drastically increase the brightness for type-I sources without sacrificing source fidelity. Specifically, by successfully correcting for the directional dependence of the relative phase between the different polarization components, the coincidence collection efficiency was increased by more than 50 times while maintaining a fidelity >97% for entangled sources pumped with monochromatic cw lasers [64]. Here, we extend this technique to both ultrafast-pumped and cw-diode laser-pumped entanglement sources, achieving brightness enhancements up to 400. As a result, we were able to achieve the highest fidelity reported for an ultrafast SPDC entanglement source.

In addition to the spatial decoherence just mentioned, downconversion sources pumped with ultrashort pulses are further plagued with decoherence arising from different pump-frequency components. One can use temporal precompensation techniques to mitigate this phenomenon [63]. In fact, they can also improve the fidelity of polarization-entangled photons generated using cw-diode lasers that contain a range of pump frequencies, characteristic of short coherence times, mode-hopping, etc. [61, 65-66]. Here, we present optimized solutions achieved by combining temporal and spatial compensation techniques to improve the fidelity and brightness from a variety of type-I polarization-entangled sources — ultrashort and cw-diode pumped, for both degenerate and, for the first time, non-degenerate entanglement[25]. We show that these techniques can be applied simultaneously, as long as one correctly accounts for the total effects of both the compensators. We have thus realized the highest entangled state fidelity[26] (99%) for a cw-diode laser-pumped degenerate source, as well as the highest reported entanglement concurrence[27] (98%, previously limited to 94% [63] for type-I sources) for a polarization-entanglement source pumped by an ultrashort pulsed laser.

Aside from these correctable decoherence effects, the downconversion efficiency in any experiment is *fundamentally* limited by the nonlinear dielectric properties of the SPDC crystal itself. For example, the uniaxial crystal barium borate (β-BaB_2O_4, or BBO, with effective nonlinear coefficient d_{eff} ~1.75 pm/V) has been almost ubiquitously employed for polarization-entanglement generation, although quasi-phasematching in materials such as periodically-poled potassium titanyl phosphate ($KTiOPO_4$, KTP, d_{eff}~ 3 pm/V) are becoming more popular [67]. Here we present the first direct entanglement results from the promising newly developed nonlinear optical crystal BiBO, which has exceptionally high nonlinearity (>3 pm/V), UV transparency, high damage threshold (comparable to BBO) and inertness to moisture (nonhygroscopic) [68-70]; moreover, as a biaxial crystal, BiBO offers versatile phasematching characteristics and broadband angle-tuning at room temperature [69]. Such a combination of properties makes this crystal highly attractive for frequency conversion in the UV, visible and IR; for example, BiBO is superior to BBO for second-harmonic-generation [71]. Nevertheless, while biaxial crystals such as BiBO may appear to be a better source material, their lack of the rotational symmetry present in traditionally used uniaxial crystals can significantly complicate the compensation techniques presented here, e.g., phasematching for a biaxial crystal depends on the azimuthal pump angle in addition to the polar pump angle. Here we show that, in spite of their increased complexity, such biaxial crystals can be used for a brighter source of polarization entanglement. Specifically, we numerically model and experimentally realize optimally compensated sources of high-quality (fidelity >99%) polarization-entangled photons using a pair of biaxial BiBO crystals. Further, our simulation code, available on our

---

[25] In degenerate SPDC, both the downconversion photons have the same central wavelengths. In nondegenerate downconversion, they are centered at different wavelengths. Energy conservation is obeyed in both cases.

[26] Fidelity between a pure state $|\psi\rangle$ and a mixed state ρ is defined as $F(|\psi\rangle,\rho)\equiv\langle\psi|\rho|\psi\rangle$.

[27] Concurrence C for a mixed state ρ of two qubits is defined as $C(\rho)=max\,(0,\sqrt{\lambda_1}-\sqrt{\lambda_2}-\sqrt{\lambda_3}-\sqrt{\lambda_4})$, in which λ_i are the eigenvalues of $\rho(\sigma_y\otimes\sigma_y)\rho^*(\sigma_y\otimes\sigma_y)$ in decreasing order, and σ_y is the $\begin{pmatrix}0 & -i\\ i & 0\end{pmatrix}$ Pauli spin matrix. Tangle is then the square of the concurrence.

website[28], can model type-I entanglement sources from a variety of nonlinear crystals with various phasematching parameters.

The remainder of the chapter is arranged as follows. In Section 3.2 we present experimental data and numerical simulations, first discussing spatial, then spectral-temporal, and finally, combined-compensation results, for both a cw-diode laser-pumped biaxial BiBO and an ultrafast-pumped BBO source. Theoretical details, including the principles of our numerical simulations, and specific calculations for designing the compensation crystals, are further discussed in Section 3.3.

3.2 **Compensating Decoherence**

We use the two-crystal geometry [24] with type-I phasematched SPDC, previously discussed in Section 2.4, to create a maximally polarization-entangled state:

$$\left|\psi\right\rangle = \frac{1}{\sqrt{2}}\left(\left|H_1H_2\right\rangle + e^{i\phi\left(\omega_p,\omega_s,\omega_i,\mathbf{k}_p,\mathbf{k}_s,\mathbf{k}_i\right)}\left|V_1V_2\right\rangle\right). \tag{3.1}$$

The relative phase ϕ is determined by phasematching constraints and depends on various parameters, such as crystal type and length, and pump (downconversion) frequency ω_p (ω_s , ω_i) and momentum vector $\mathbf{k}_p$ ($\mathbf{k}_s$, $\mathbf{k}_i$). Explicit calculations for ϕ are presented in Section 3.3. The coherence between the two downconversion amplitudes generated in the adjacent nonlinear crystals can be destroyed — decreasing the amount of polarization entanglement — by correlations between the polarization and other degrees of freedom; these then effectively yield distinguishing *which-crystal* information. In particular, due to birefringence and dispersion, downconversion photons emitted at varying angles and frequencies can acquire different relative phases. Collecting multiple such states through large-diameter irises and large-bandwidth spectral filters results in averaging over the phases, leading to effective *spatial* and *spectral-temporal* decoherence, respectively. Spatial decoherence can be eliminated by directing the downconversion photons through suitable birefringent compensating crystals that have the opposite phase characteristics as that of the downconversion crystals, a technique called spatial compensation [64]. Similarly, spectral-temporal decoherence can be countered by "precompensating" the pump by passing it through a birefringent crystal before the downconversion crystals [63], or by postcompensating the downconversion photons directly, though there are then other disadvantages, as we discuss below.

We first present results showing spatial and spectral-temporal decoherence independently, and then present the combined completely compensated systems. Experimentally, we use two distinct setups

---

[28] http://research.physics.illinois.edu/QI/photonics/phase_compensation.html

(shown in Figure 3-1b): in the first, two biaxial (BiBO) crystals are pumped by a 405-nm cw-diode laser; in the second, two uniaxial crystals (BBO) are pumped by a 90-fs 810-nm Ti-Saph laser that is frequency-doubled to obtain 405 nm. Both setups produce degenerate downconversion (405 nm → 810 nm + 810 nm); the BiBO crystals were also used to study nondegenerate downconversion (405 nm → 851 nm + 771 nm). In all cases, interference filters (10-nm FWHM) before the detectors were used to reduce background.

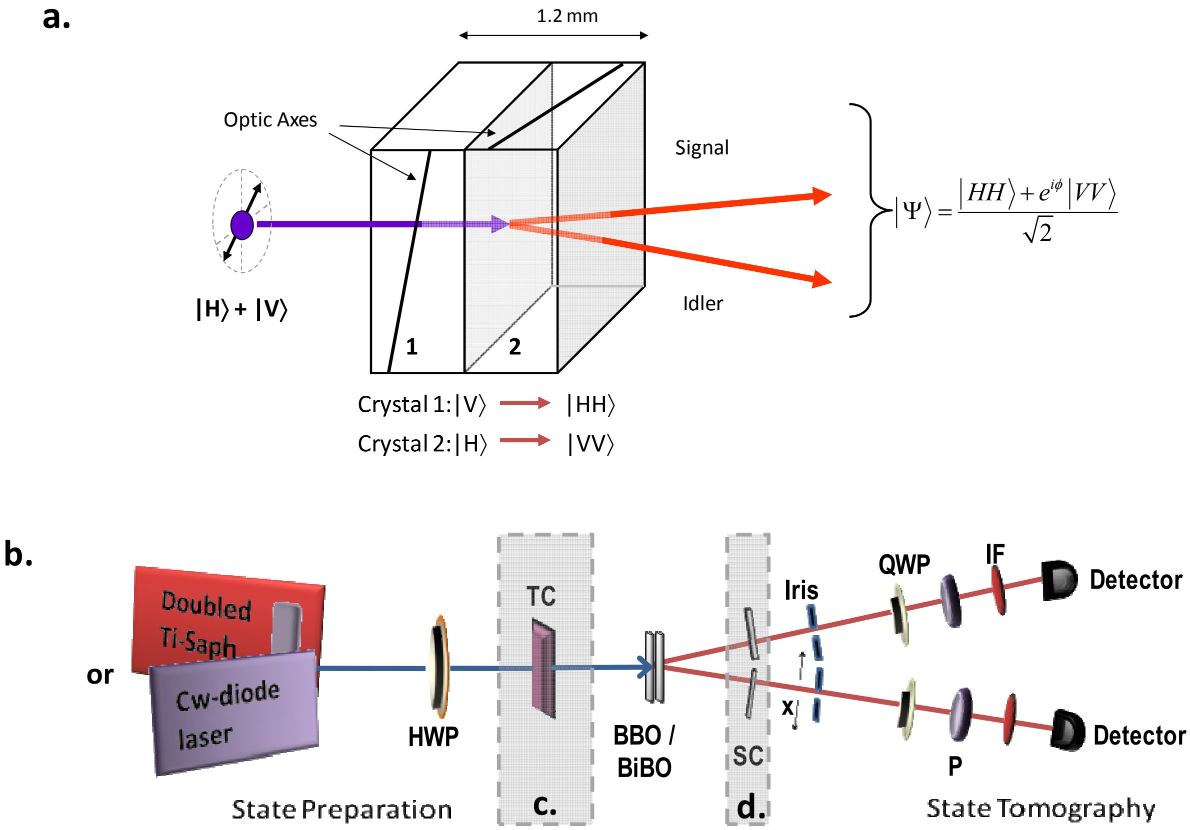

Figure 3-1: **a**. Schematic showing the optic axes orientations and the corresponding downconversion photons from two orthogonally oriented type-I phasematched nonlinear crystals used to produce polarization-entangled photons. **b**. Experimental setup to generate and analyze entangled photons. 405-nm light from a doubled ultra-short Ti-Saph laser or a cw-diode laser pumps either two BBO or two BiBO crystals. A half wave plate (HWP) prepares the pump state. Quarter waveplates (QWP) and polarizers (P) are used to analyze the downconverted state. 10-nm interference filters (IF) reduce background to the single-photon detectors. **c**. Quartz or BBO temporal compensators (TC) precompensate the pump for temporal walkoff. **d**. Birefringent spatial compensators (SC) compensate for angle-dependent phase variation.

3.2.1 Spatial Decoherence and Compensation Results

As discussed above, emission-angle dependent spatial decoherence can be countered by inserting two birefringent compensators, one in each downconversion arm[29]. Given the spatial-phase characteristics of the downconversion photons generated by a particular source, the optimal length of spatial compensation crystals can be calculated for any optic-axis cut. Such spatial compensation has been previously demonstrated only in uniaxial crystals (BBO) pumped with a monochromatic cw laser [64]. Here we extend this technique for the first time to spatially compensate an entangled source using biaxial crystals (BiBO), whose complex birefringent structure substantially complicates the necessary calculations of ϕ.

Our two 0.6-mm thick BiBO crystals are pumped by a 405-nm cw-diode laser. The crystals are cut at $\theta=151.7°$ and $\varphi=90°$ to produce degenerate downconversion (at 810 nm) into a cone with ~3° external opening half-angle. As shown in Figure 3-2a, the uncompensated source has a large phase gradient: ϕ varies by more than 20° per mm in the spatial dimension x transverse to the emission direction[30] (see Figure 3-1a), measured at the collection irises (~84 cm from the downconversion crystals)[31]. Thus, collecting the photons with moderate-size irises (e.g., 5-mm diameter) would greatly decohere the polarization entanglement. To counter this, we insert a birefringent spatial compensator (245-μm thick BBO crystal cut at 33.9°) into each downconversion arm. Our calculations (explained in detail in Section 3.3) predict a nearly ideal phasemap, and indeed our measured phasemap is essentially flat: the spatially compensated source has a residual phase below 0.05° over 1 mm, representing a 400-fold improvement for degenerate downconversion generated using biaxial BiBO. Figure 3-2b shows similar results for nondegenerate downconversion from 405 nm to 851 nm and 772 nm. Here we observe a 36-fold improvement over the uncompensated phasemap, limited by the suboptimal length of our available spatial compensators (245 μm, compared to the optimal lengths, i.e., 280 μm for the signal and 210 μm for the idler); in any event, the degree of compensation achieved precisely matches our theoretical prediction. Note that this is also the first nondegenerate source to be spatially compensated; the flexibility of the nondegenerate operation greatly increases the utility of SPDC sources, e.g., for coupling to atomic

---

[29] While it is possible to compensate for spatial decoherence using birefringent compensators in only one downconversion arm, other effects, such as induced temporal, transverse walkoff etc., need to be considered in this case.

[30] The phase slope in the y direction, transverse to the downconversion direction and x is negligible; the predicted phase slope ~-0.009°/mm because of the downconversion crystal. The predicted net y slope (along with the spatial compensators) is still only ~0.03°/mm, which our system is not very sensitive to. This agrees with our experimental results – as we collect over bigger irises, the tangle stays roughly constant.

[31] For these measurements both irises are scanned in opposite directions (i.e., away from the pump beam axis of symmetry).

transitions. For our second system (data not shown), using ultrafast (~90 fs) pumped 0.6-mm BBO cut at 29.3°, calculations indicate that the downconversion phase slope is ~17°/mm, which is nearly perfectly compensated using two 245-μm BBO crystals cut at 33.9° as spatial compensators.

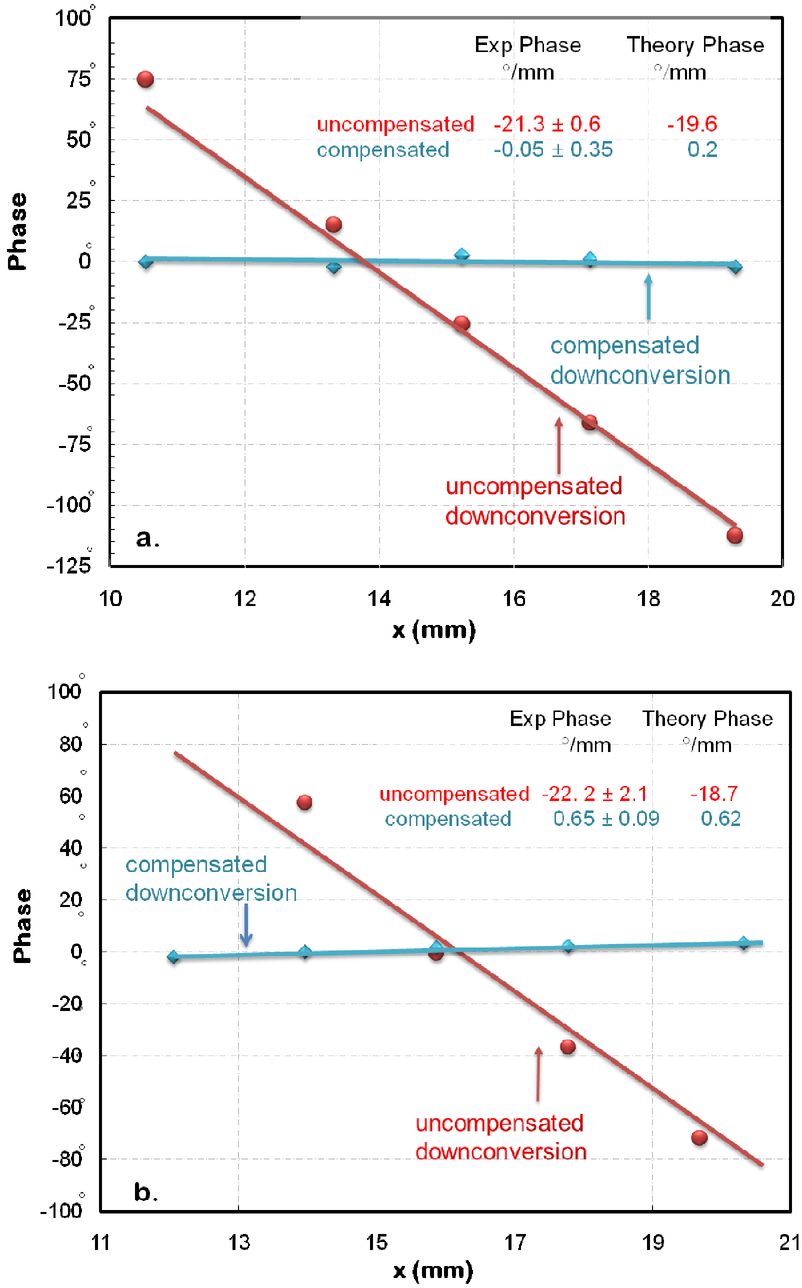

Figure 3-2: Experimentally measured phase gradients for uncompensated and compensated two-crystal geometry for **a**. degenerate downconversion (405 nm → 810 nm + 810 nm) and **b**. nondegenerate downconversion (405 nm → 851 nm + 771 nm) in BiBO pumped by a cw-diode laser. The x-axis represents the lateral position of the collection iris (see text for more details). The solid lines are the phase gradients predicted by our numerical simulation. The error (±0.05°) from the counting statistics is smaller than the data markers.

3.2.2 Spectral-Temporal Decoherence Results

Spectral decoherence arises due to frequency-dependence of the relative phase ϕ. It can be intuitively understood (especially in the case of a pulsed pump) in the temporal domain (hence the term *spectral-temporal* decoherence): different propagation speeds of the pump and downconversion photons within the crystals leads to temporal which-crystal information: the $|HH\rangle$ photons emitted in the first crystal are delayed by Δt compared to the $|VV\rangle$ photons generated in the second crystal. For nondegenerate downconversion, there may also be relative delays between photons generated in the *same* crystal. If any of these relative delays is comparable to or greater than the pump coherence time, entanglement quality will be reduced (for delays between photons from the same crystal, the downconversion coherence time becomes the relevant time scale[32]). Such spectral-temporal decoherence is extremely significant with an ultrafast pump. For example, dispersion over the ~4-nm pump bandwidth at 405 nm results in complete elimination of any polarization-entanglement when using 10-nm FWHM spectral filters. Specifically,

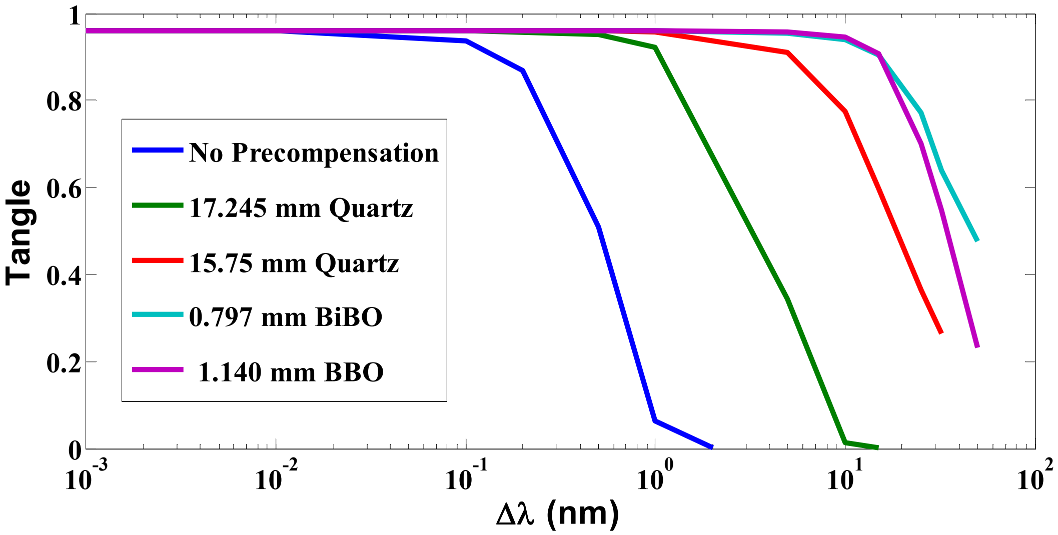

Figure 3-3: Predicted dependence of tangle on the precompensator material with increasing pump bandwidth. The plot shows that higher-order broadening effect become increasingly significant for broader pump bandwidth. The calculations[33] are for two 0.6- mm BiBO crystals pumped by a cw-diode laser.

---

[32] Note that in nondegenerate downconversion the signal walks off relative to the idler in each crystal – this in itself does not give rise to which-crystal information. It is the walkoff of the downconversion photons from the first crystal in the second crystal that causes distinguishability and the resulting decoherence.

[33] The specific precompensators chosen were optimized for a spatially compensated BiBO source (see Section 3.2.3 for a discussion on joint spatial and temporal compensation).

group velocity dispersion in the two 0.6-mm BBO crystals delays the $|HH\rangle$ downconversion photons generated in the first crystal by ~253 fs relative to the $|VV\rangle$ photons from the second crystal (including the pump pulse propagation time), much more than the ~90-fs pulse duration. We used 1.9 mm of BBO cut at 29.4° to optimally compensate for the 253-fs walkoff, recovering a high quality polarization-entangled state (98.9% fidelity). For our configuration (90-fs pump + 0.6-mm crystals), higher-order effects such as distinguishing dispersive *broadening* were calculated to be negligible; we were thus able to observe similar compensation results using 6.8-mm quartz precompensators instead, which yielded a 99.2% fidelity. However, as shown in Figure 3-3 higher-order broadening effects would become significant for shorter pulse widths and longer crystals. For instance, we calculate that if the pump bandwidth exceeds ~10 nm, first-order correction — only compensating for group velocity delays but not pulse spreading — will yield only a 90% fidelity. Thus, while any birefringent element of appropriate thickness could be used to precompensate for the temporal walkoff to first order, using the same material as in the downconversion source itself can better compensate for higher-order effects that can be significant for increased pump bandwidths.

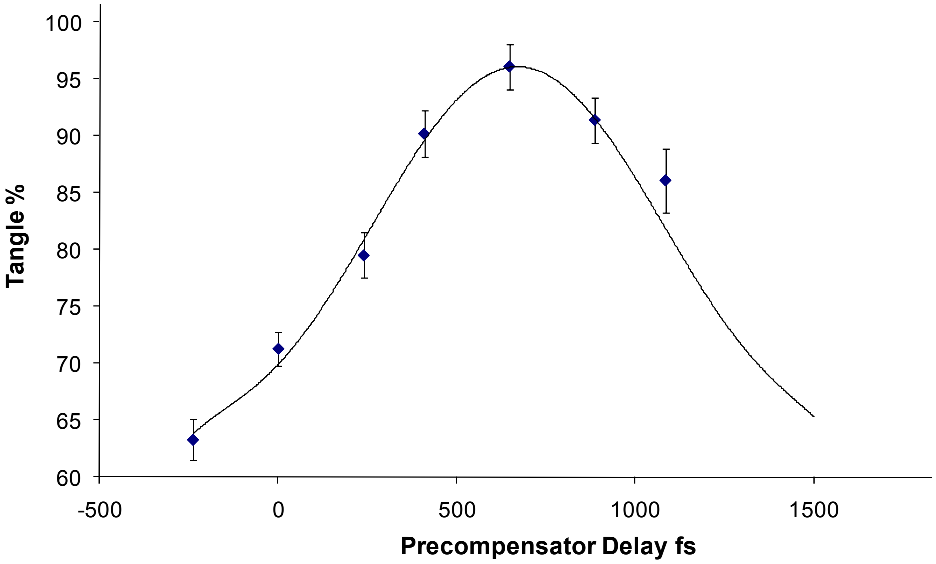

Figure 3-4: Effect of varying the delay between the H-and V- pump components on the polarization-entangled state generated from two 0.6-mm BiBO crystals, pumped with a cw-diode laser for degenerate downconversion (405 nm → 810 nm + 810 nm). The delay is varied by using precompensators (in this case quartz) of differing lengths. A 0-fs precompensator delay represents the case when no temporal precompensator is present in the system. Negative delays, achieved by rotating the precompensator's orientation by 90°, add to the problem of temporal walkoff instead of countering it. The solid line is the theoretical prediction based on the theory presented in Section 3.3. The center of the peak is determined by the crystal lengths, index dispersion, and pump central wavelength; the peak width varies inversely with pump bandwidth. Quantum state tomography is used to reconstruct the produced state. The error bars are a result of the maximum likelihood technique used in the state estimation [49].

Spectral-temporal effects are less critical for a cw-diode laser-pumped source, but optimal precompensators can still significantly improve the measured polarization entanglement. In our system a 0.5-nm bandwidth cw-diode laser pumps two 0.6-mm BiBO crystals phasematched for downconversion from 405 nm to 810 nm. The resulting ~600-fs delay between the $|HH\rangle$ downconversion photons born in the first crystal and the $|VV\rangle$ photons from the second crystal leads to an uncompensated tangle of only ~70%. ~16 mm of quartz[34] (cut with its optic axis perpendicular to the direction of propagation) can ideally compensate for this delay. Figure 3-4 shows the measured effect of varying the delay between the $|H\rangle$ and $|V\rangle$ pump components, achieved by varying the quartz precompensator thickness, on the tangle of the resulting two-photon polarization-entangled state.

3.2.3 Joint Spatial and Spectral-Temporal Compensation Results

Although both the decoherence effects – spatial and spectral-temporal – occur independently, the compensation for these *cannot* in general be independent. This is because the compensation crystals themselves can cause similar effects (see Section 3.3), e.g., the spatial compensators can cause their own temporal walkoff of the photons[35]. For example, the spatial compensators we used for the cw-diode laser-pumped BiBO source increase the net temporal walkoff from ~600 fs to ~640 fs; the latter can be compensated for with ~17.2 mm of quartz. Since it was readily available to demonstrate the (nearly) optimized spatially and temporally compensated BiBO source, a 15.85-mm thick quartz element was used instead as the temporal compensator. Quantum state tomography [72] was used to determine the reduced density matrix (i.e., only the polarization part) of the entangled two-photon state, for various iris sizes. From this we determined the associated two-qubit properties, such as fidelity with a maximally entangled state, and tangle. If the relative-phase variation with emission angle has truly been cancelled out, these metrics should be independent of the size of the collection irises, allowing for a quadratic increase in the brightness of the collected photon pairs with increasing iris diameters, while maintaining high-quality entangled states. Figure 3-5 shows the measured and predicted tangle as a function of iris size, for both the uncompensated and spatially compensated cases, for degenerate and nondegenerate downconversion in temporally compensated BiBO. In both cases, the compensated source shows much less reduction in tangle with iris size, as predicted. The maximum tangle is less than 1, matching the prediction, due to the suboptimal length of the available temporal precompensator. As shown in Figure 3-5, this effect is worse

---

[34] Given the relatively small pump bandwidth of the diode laser, higher-order effects are negligible. Thus, quartz can effectively compensate for the temporal delay.

[35] Similarly, if one were to temporally compensate the downconversion photons directly (instead of precompensating the collimated pump), the compensation elements could add spatial dephasing.

for nondegenerate pairs, because then both the spectral-temporal as well as the spatial compensators are non-ideal.

Downconversion from an ultrafast pump can be similarly compensated for spatial and spectral-temporal decoherence simultaneously. Accounting for the temporal walkoff in the spatial compensators, we used 6.4 mm of quartz to precompensate our optimized ultrafast-pumped BBO source. By

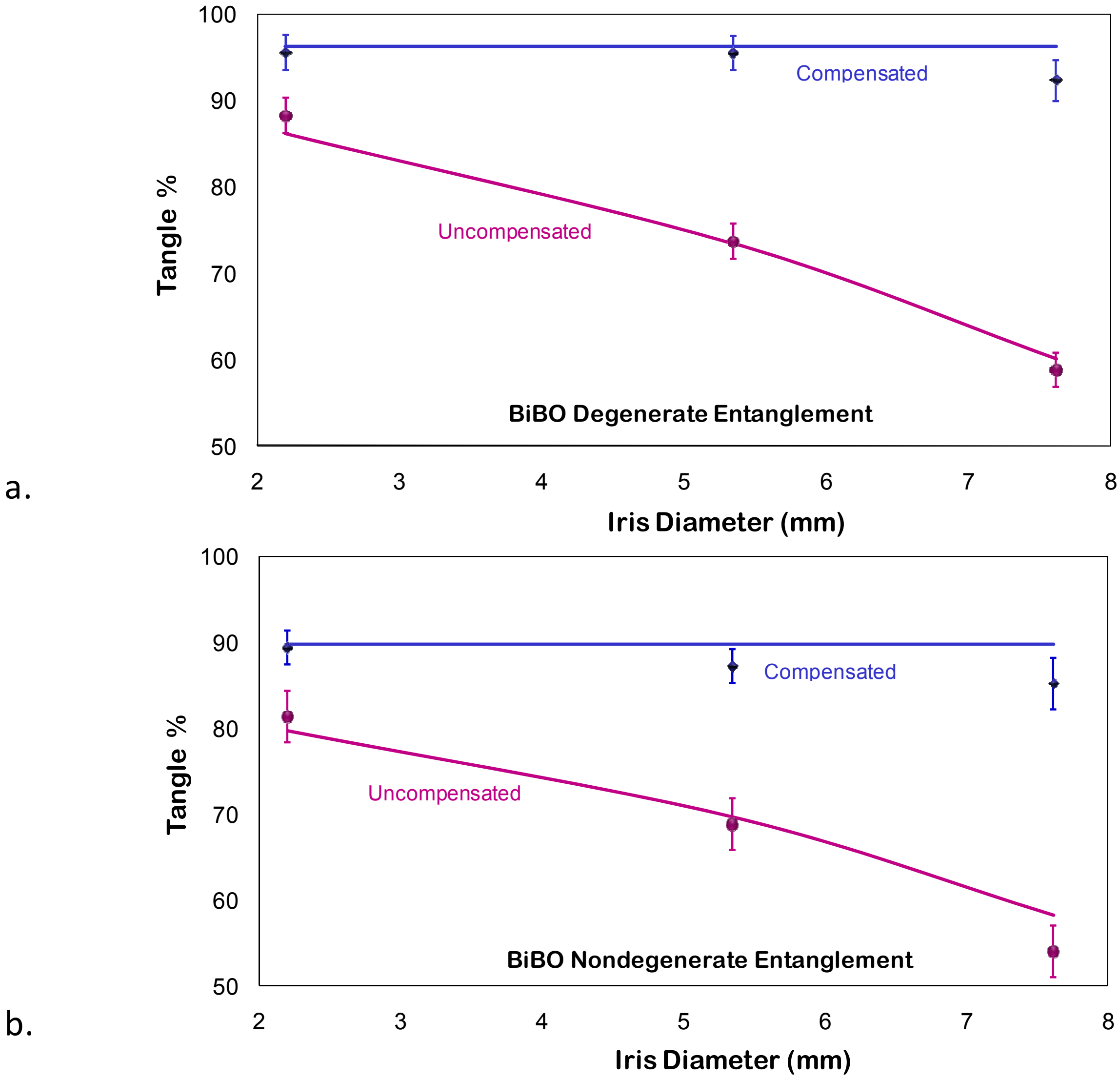

Figure 3-5: Spatial compensation results for temporally compensated cw-laser diode-pumped BiBO entanglement source. a. degenerate downconversion (405 nm → 810 nm) and b. nondegenerate downconversion (405 nm → 851 nm +772 nm). For this data, the collection irises were located ~84 cm from the downconversion source.

incorporating both spatial and temporal compensators, we obtained a tangle of 98% and fidelity of 99%, the highest reported thus far for type-I polarization entanglement generated using an ultrafast pump.

Figure 3-6 shows a plot of the density matrices obtained for all our jointly spatially and temporally compensated sources — ultrafast-pumped degenerate polarization entanglement from BBO (Figure 3-6a), and cw-diode laser-pumped degenerate (Figure 3-6b) and non-degenerate (Figure 3-6c) entanglement from BiBO. Table 3-1 directly compares the measured downconversion brightness between BiBO and BBO, when they are both pumped by the cw-diode laser. BiBO's higher nonlinearity results in a 3-fold brightness enhancement in the two-photon coincidence rate, supporting our hypothesis that it should be an inherently better source, once properly compensated.

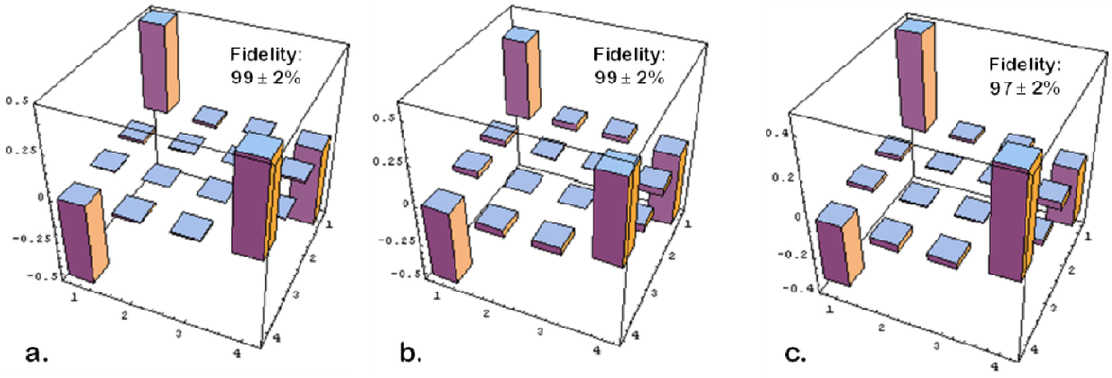

Figure 3-6: Density matrices of temporally and spatially compensated two-qubit polarization-entangled states produced by **a**. BBO pumped with 90-fs Ti-Saph, and **b**. degenerate and **c**. nondegenerate downconversion in BiBO pumped by cw-diode laser (with 0.5-nm bandwidth). Fidelities with the target maximally entangled state $\left(|HH\rangle - |VV\rangle\right)$ are shown.

Table 3-1: Comparative two-photon coincidence brightness between BBO and BiBO crystals

BBO (0.6mm)	**BiBO (0.6 mm)**
5400 coincidences/mW/s	13400 coincidences/mW/s
0.75% background	1.5% background

3.3 Theoretical Calculations and Compensation Design

Our code for numerically modeling various polarization-entanglement sources and designing compensation crystals can be found on our website: http://research.physics.illinois.edu/QI/photonics/phase_compensation.html. Appendix A outlines the algorithm that the overall simulation is based on. While the theory for spatial and temporal distinguishability can be completely analyzed by fully expanding the downconversion state's dependence on ω, θ, and φ, in the spirit of [21, 73], here we present specific calculations necessary to design ultrafast and diode-laser pumped-entanglement sources. To make the following discussions as brief as possible, we outline the theoretical framework and refer to [21, 73] for further details. To first order, spatial and spectral-temporal decoherence within the downconversion crystals themselves can be considered independent (our numerical simulations confirm this is a good approximation for the typical bandwidths and angles considered here) and hence, can be calculated separately (though as discussed above, the *compensators* for each will in general affect both).

3.3.1 Spatial Decoherence and Compensation Calculations

First, we calculate the emission-angle-dependent relative phase ϕ acquired by an entangled two-photon state generated by a monochromatic pump. Ordinary polarized[36] downconversion photons from the first crystal acquire an additional phase in the second crystal, where they are extraordinary polarized, both because of spatial walkoff and the fact that they have to traverse the additional (i.e., the second) crystal. The extraordinary phase Φ_e, ordinary phase Φ_o, and external phase Φ_Δ (accumulated by the extraordinary beam outside the crystals because it exits at a different location than does the ordinary beam, due to spatial walkoff) all contribute to the total relative spatial phase in Eqn. 3.1. Exact expressions for Φ_e, Φ_o, and Φ_Δ can be found in [64]. The downconversion photons born in the first crystal acquire a net phase in the second crystal, given by

$$\phi_{dc}\left(\hat{\mathbf{k}}_{s,i}\right)=\left(\Phi_e+\Phi_\Delta\right)_{s,i}, \qquad 3.2$$

making the final polarization-entangled state

$$\left|\psi_{\hat{\mathbf{k}}_{s,i}}\right\rangle=\frac{1}{\sqrt{2}}\left(\left|H_1H_2\right\rangle+e^{i\left(\phi_{dc}(\hat{\mathbf{k}}_s)+\phi_{dc}(\hat{\mathbf{k}}_i)\right)}\left|V_1V_2\right\rangle\right). \qquad 3.3$$

Multiple such states pass through a pair of finite-size collection irises; measuring these states together amounts to tracing over direction, producing the density matrix

$$\rho=\iint_{Iris}\left|\psi_{\hat{\mathbf{k}}_s}\right\rangle\left\langle\psi_{\hat{\mathbf{k}}_i}\right|d\hat{\mathbf{k}}_s d\hat{\mathbf{k}}_i; \qquad 3.4$$

In other words, averaging over the different relative phases leads to an effective decoherence. This can be compensated by appropriate birefringent crystals that impart an additional spatial phase opposite to that of the downconversion crystals. The polarization part of the final compensated state can be written in terms

---

[36] For ease of discussion we use the language of uniaxial crystals: ordinary and extraordinary polarization. For biaxial crystals, these terms are no longer an accurate description of polarization states. However, the terms can be used to refer to orthogonal linear polarizations with different velocities, usually labeled fast and slow, in the biaxial crystal [41].

of the downconversion phases ϕ_{dc} (Eqn. 3.2) and the phases ϕ_c due to the spatial compensation crystals in the downconversion arms, as

$$\left|\psi_{\hat{\mathbf{k}}_{s,i}}\right\rangle = \frac{1}{\sqrt{2}}\left(\left|H_1H_2\right\rangle + e^{i\left(\phi_{dc}(\hat{\mathbf{k}}_s)+\phi_{dc}(\hat{\mathbf{k}}_i)+\phi_c(\hat{\mathbf{k}}_s)+\phi_c(\hat{\mathbf{k}}_i)\right)}\left|V_1V_2\right\rangle\right). \tag{3.5}$$

When $\phi_{dc}\left(\hat{k}_s\right)+\phi_{dc}\left(\hat{k}_i\right)+\phi_c\left(\hat{k}_s\right)+\phi_c\left(\hat{k}_i\right)=0$ (or any constant phase), the polarization part of the state factors out of the integral in Eqn. 3.4, so that decoherence is suppressed [35]. Thus, spatial compensators allow increased brightness of the source, while maintaining high polarization-entanglement fidelity.

3.3.2 Spectral-Temporal Decoherence and Compensation Calculations

Spectral-temporal decoherence can be considered to arise because the emission times of the photons — specifically, *when* they exit the output face of the second crystal, relative to each other and/or relative to the time the pump photons entered the first crystal — depend on their frequencies and polarization because of dispersion and birefringence in the crystals. Assuming that the downconversion photons are emitted from the center of each crystal (see [74] for justification) the group-velocity dispersion effects which result in advancing or delaying the photons can be calculated as follows [63, 74]. The two-photon downconverted state from a single crystal can be written in the temporal domain in terms of creation operators acting on the vacuum state as

$$\left|\Psi\right\rangle = \int dt_s \int dt_i f(t_s,t_i)\hat{a}_s^+(t_s)\hat{a}_i^+(t_i)\left|vac\right\rangle, \tag{3.6}$$

where *f,* the joint two-photon amplitude (JTPA) which determines the signal-idler relationship, can be written for a pump with central frequency Ω_p and bandwidth σ_p in terms of the spectral detunings $\nu_{s,i} \equiv \omega_{s,i} - \Omega_p/2$ and the phasematching function Θ as

$$f\left(t_s,t_i\right) = \frac{e^{-i\Omega_p\frac{t_s+t_i}{2}}}{2\pi}\iint d\nu_s d\nu_i e^{-i(\nu_s t_s+\nu_i t_i)} e^{-\left(\frac{\nu_s+\nu_i}{\sigma_p}\right)^2}\Theta\left(\nu_s,\nu_i\right), \tag{3.7}$$

$$\Theta\left(\nu_s,\nu_i\right) = \mathrm{sinc}\left(\frac{d}{2}\left(D_+\left(\nu_s+\nu_i\right)+\frac{1}{4}D''\left(\nu_s-\nu_i\right)^2\right)\right) \text{ and} \tag{3.8}$$

$$D_+ = \frac{1}{V_g^{or}\left(\Omega_p/2\right)} - \frac{1}{V_g^{ex}\left(\Omega_p\right)}\ ,\ D'' = \left.\frac{d^2\mathbf{k}_s}{d\omega^2}\right|_{\Omega_p/2}. \tag{3.9}$$

Here D_+ gives the group velocity mismatch between the downconversion photons and the pump, and D'' represents the group velocity dispersion [74]. The net time delay between the downconversion photons emitted in the first crystal $t^1_{s,i}$ (second crystal $t^2_{s,i}$) relative to when the pump is incident on the face of the first crystal can be written in terms of the group velocity V_g^{ex} $\left(V_g^{or}\right)$ of the extraordinary (ordinary) photons and crystal thickness d as

$$\begin{aligned} t^1_{s,i} &= \frac{d}{2}\left(\frac{1}{V_g^{ex}(\omega_p)} + \frac{1}{V_g^{or}(\omega_{s,i})} + \frac{2}{V_g^{ex}(\omega_{s,i})}\right) \\ t^2_{s,i} &= \frac{d}{2}\left(\frac{2}{V_g^{or}(\omega_p)} + \frac{1}{V_g^{ex}(\omega_p)} + \frac{1}{V_g^{or}(\omega_{s,i})}\right) \end{aligned}. \qquad 3.10$$

For example, the first term in Eqn. 3.10 represents the propagation of the pump photon through the first half of the first crystal, the second term represents the propagation of the signal or idler photon through the rest of the first crystal, and the final term represents the downconversion propagation through the second crystal. The net delays between the downconverted states from each crystal can be calculated for both the signal and idler as

$$\Delta t_s^{dc} \equiv t_s^2 - t_s^1 = d\left(\frac{1}{V_g^{or}(\omega_p)} - \frac{1}{V_g^{ex}(\omega_s)}\right) \text{ and } \Delta t_i^{dc} \equiv t_i^2 - t_i^1 = d\left(\frac{1}{V_g^{or}(\omega_p)} - \frac{1}{V_g^{ex}(\omega_i)}\right). \qquad 3.11$$

After both crystals the two-photon state in the time domain becomes

$$|\psi\rangle = \frac{1}{\sqrt{2}}\left(f\left(t_s + \Delta t_s^{dc}, t_i + \Delta t_i^{dc}\right)|H,t_s\rangle_s |H,t_i\rangle_i + f\left(t_s,t_i\right)|V,t_s\rangle_s |V,t_i\rangle_i\right). \qquad 3.12$$

The downconversion polarization is now correlated with the time variable, leading to distinguishing which-crystal information. The effective density matrix associated with a polarization-entangled state can be obtained by tracing over the time variable and can be explicitly written as

$$\rho = \frac{1}{2}\left(|HH\rangle\langle HH| + |VV\rangle\langle VV| + v(\Delta t_s^{dc}, \Delta t_i^{dc})\,|HH\rangle\langle VV| + v^*(\Delta t_s^{dc}, \Delta t_i^{dc})\,|VV\rangle\langle HH|\right), \qquad 3.13$$

where $v(\Delta t_s^{dc}, \Delta t_i^{dc})$ is the self-convolution of the JTPA, defined as

$$v(\Delta t_s^{dc}, \Delta t_i^{dc}) \equiv \iint dt_s dt_i f\left(t_s + \Delta t_s^{dc}, t_i + \Delta t_i^{dc}\right) f^*\left(t_s, t_i\right). \qquad 3.14$$

Because $|HH\rangle$ and $|VV\rangle$ arrive at different times, the two-photon state is effectively decohered in the polarization basis. Mathematically, similar to spatial decoherence, such spectral-temporal decoherence can also be fully compensated for by introducing an appropriate birefringent element in the pump path. Ideally, the delay τ^{pc} introduced by a birefringent precompensator of length l^{pc} depends on the respective group velocities $V_{g,pc}^{ex}$ and $V_{g,pc}^{or}$ of the extraordinary and ordinary polarizations in the precompensator:

$$\tau^{pc} = l^{pc}\left(\frac{1}{V_{g,pc}^{or}(\omega_p)} - \frac{1}{V_{g,pc}^{ex}(\omega_p)}\right). \qquad 3.15$$

The temporal precompensater shifts the extraordinary and ordinary pump components temporally so as to eliminate emission-time distinguishability between $|HH\rangle$ and $|VV\rangle$ i.e., $\tau^{pc} = -\Delta t_{s,i}^{dc}$. When Δt_s^{dc} is significantly different from Δt_i^{dc} , which could be the case for downconversion at extremely nondegenerate wavelengths, then a post-downconversion crystal compensator is needed to completely compensate for the spectral-temporal decoherence[37]. Spatial compensators (length l^{sc}) placed in the path of the downconversion beams also contribute to the temporal delay, depending on the respective group velocities $V_{g,sc}^{ex}$ and $V_{g,sc}^{or}$ of the extraordinary and ordinary polarizations in the spatial compensators:

$$\tau_s^{sc} = l^{sc}\left(\frac{1}{V_{g,sc}^{or}(\omega_s)} - \frac{1}{V_{g,sc}^{ex}(\omega_s)}\right) \text{ and } \tau_i^{sc} = l^{sc}\left(\frac{1}{V_{g,sc}^{or}(\omega_i)} - \frac{1}{V_{g,sc}^{ex}(\omega_i)}\right).$$

3.16

The final state can be written in terms of the precompensator delay τ^{pc} and spatial compensator temporal delay $\tau_{s,i}^{sc}$ by replacing $v(\Delta t_s^{dc}, \Delta t_i^{dc})$ in Eqn. 3.13 with $v(\Delta t_s^{dc} - \tau^{pc} - \tau_s^{sc}, \Delta t_i^{dc} - \tau^{pc} - \tau_i^{sc})$. When $\tau^{pc} + \tau_{s,i}^{sc} = \tau_{s,i}^{dc}$, the temporal part of Eqn. 3.12 factorizes from the polarization part, i.e., $|HH\rangle$ and $|VV\rangle$ become completely indistinguishable and one effectively recovers perfect polarization entanglement. Note that we chose to precompensate the (presumed collimated) pump as opposed to postcompensating (the non-collimated signal and idler photons) for the emission-time distinguishability, because precompensating a collimated beam results in no additional spatial dependence; in other words, while we need to account for the temporal effects of the spatial compensators, the spatial effects of the temporal precompensator are negligible in this case. Spatial and temporal calculations for biaxial crystals can be carried out similarly, using the slow and fast polarizations instead of the extraordinary and ordinary. In our numerical simulation, we based our biaxial phasematching calculations on the classical analysis by Beouf *et al.* [75].

---

[37] Note that in this case spatial decoherence due to the temporal postcompensator must also be corrected in order to achieve complete joint spatial and spectral-temporal compensation.

3.3.3 Discussion of Temporal Decoherence in the Spectral Domain

The effects of emission-time distinguishability can be modeled and understood by comparing the difference to the pump coherence time as above; however, this simple model fails to directly explain why any effective decoherence occurs when a cw (but non-monochromatic) pump is used, since there is no pump timing to act as a relative which-crystal "clock". A more fundamental description in the spectral domain elucidates the underlying physics, including why narrowband spectral filters can minimize these unwanted correlations. In the spectral domain the joint two-photon amplitude can be expressed as [74]

$$f(\nu_s,\nu_i) = e^{-i\frac{d}{2}\left(D_+(\nu_s+\nu_i)+\frac{1}{4}D''(\nu_s-\nu_i)^2\right)}\mathrm{sinc}\left(\frac{d}{2}\left(D_+\left(\nu_s+\nu_i\right)+\frac{1}{4}D''\left(\nu_s-\nu_i\right)^2\right)\right),$$

3.17

where D_+, the group velocity mismatch between the downconversion photons and the pump, and D'', the group velocity dispersion are given by Eqn. 3.9 [74]. Each frequency component in the pump and the downconversion sees a different effective length of the crystals, depending on polarization, leading to an effective frequency-dependent relative phase ϕ in Eqn. 3.1. As with the emission-angle distinguishability discussed previously, averaging over the phases leads to an effective state decoherence. Since the extent to which frequency-polarization correlations matter depends on the pump bandwidth, such effects can become significant even for cw-diode lasers, which can have relatively large bandwidths (e.g., due to mode-hopping), requiring a precompensator to eliminate the spectral-temporal decoherence. The reason narrow bandwidth spectral filters can be used to recover the polarization entanglement — at the cost of collection efficiency — is that the measured JTPA is given by the convolution of the JTPA before the filters, shown in Eqn. 3.17, with the frequency response of the spectral filters. Spectral filters limit the collected bandwidth or equivalently, reduce the integration interval, and thus the amount of temporal decoherence. Extreme cases, e.g., ultrashort pulsed lasers (which necessarily have a very broad spectral bandwidth) require prohibitively narrow spectral filters to maintain high fidelity, making the source extremely inefficient without temporal precompensators.

3.4 Summary of Ultrafast and Ultrabright Techniques

Ultrabright sources of polarization-entangled photons are a critical resource for scalable optical quantum information processing. Type-I sources, especially those pumped by ultrafast-pulsed and cw-diode lasers, can be optimized by compensating for phase-decoherence mechanisms. Furthermore, the nonlinear downconversion crystals themselves can be upgraded, e.g., the brightness of polarization-entangled photons can be dramatically improved (a three-fold brightness improvement compared to BBO) by using BiBO, a highly nonlinear crystal. Here we have modeled and demonstrated for the first time high-fidelity (>99%) type-I polarization-entangled photons from BiBO. Further, we have combined for the first time two compensation techniques — spatial and spectral-temporal compensation — to counter the two limiting dephasing mechanisms, and report the highest fidelity (99%) maximally polarization-entangled state achieved using an ultrafast Ti-Saph laser. Our polarization-entanglement simulation code (freely available on our website[28]), experimentally tested and reported here, can predict state quality and design compensation crystals for a variety of type-I sources.

In summary, we have successfully overcome the first challenge presented by the broad bandwidth requirement needed for developing source of indistinguishable photons, by generating high-fidelity ultrafast ultra-bright polarization entangled photons. We did this by identifying the underlying decoherence mechanisms, simulating their effects and then compensating them. Thus, en route to engineering an ideal source for OQIP, we have developed solutions for other existing issues and found better alternatives to conventional SPDC crystals.

Chapter 4
Challenge 2: The Migdall Effect

You put your thumb straight up,
You put your index finger out,
You put your middle finger in,
And you rotate it all about.
You do the Hokey Pokey,
And you turn yourself around.
That's what it's all about.

- A Hokey Pokey-inspired explanation of the Migdall effect

The integration of the two-crystal scheme for producing polarization entanglement with the spatio-spectral unentanglement techniques, i.e., imposing group-velocity matching along with optimized phase matching, leads to a significant challenge: *the "Migdall effect"*. This effect, first discussed by Migdall, refers to an emission-angle dependence of the downconversion polarization [76]. The effect becomes especially significant in the engineered crystal (Section 2.2), due to the uncharacteristically large 16° external emission angle required for group-velocity and phase matching in BBO for degenerate downconversion from 405 nm to 810 nm. In this chapter we report the first experimental verification of the Migdall effect, for two different downconversion opening angles, and suggest ways to mitigate and even exploit the same for use in our engineering scheme.

4.1 Experimental Confirmation of the Migdall effect

Simultaneous group-velocity and phase matching in the engineered crystal results in a significantly larger emission half-angle of 16°, compared to the typical 3° cone [24]. Ideally, we might expect the downconversion polarization to be 90°, i.e., orthogonal to the incident pump polarization. As shown by Migdall [76], however, the polarizations of the downconverted photons actually vary with the emission angles, both with the cone opening half-angles as well as with the azimuthal angles (i.e., around the emission cone). Figure 4-1 shows the coordinate system defining these angles, along with a representation of the Migdall effect — how the downconversion polarization measured in the lab frame varies with the emission azimuthal angle for a given cone opening angle. The origin of the Migdall effect can be

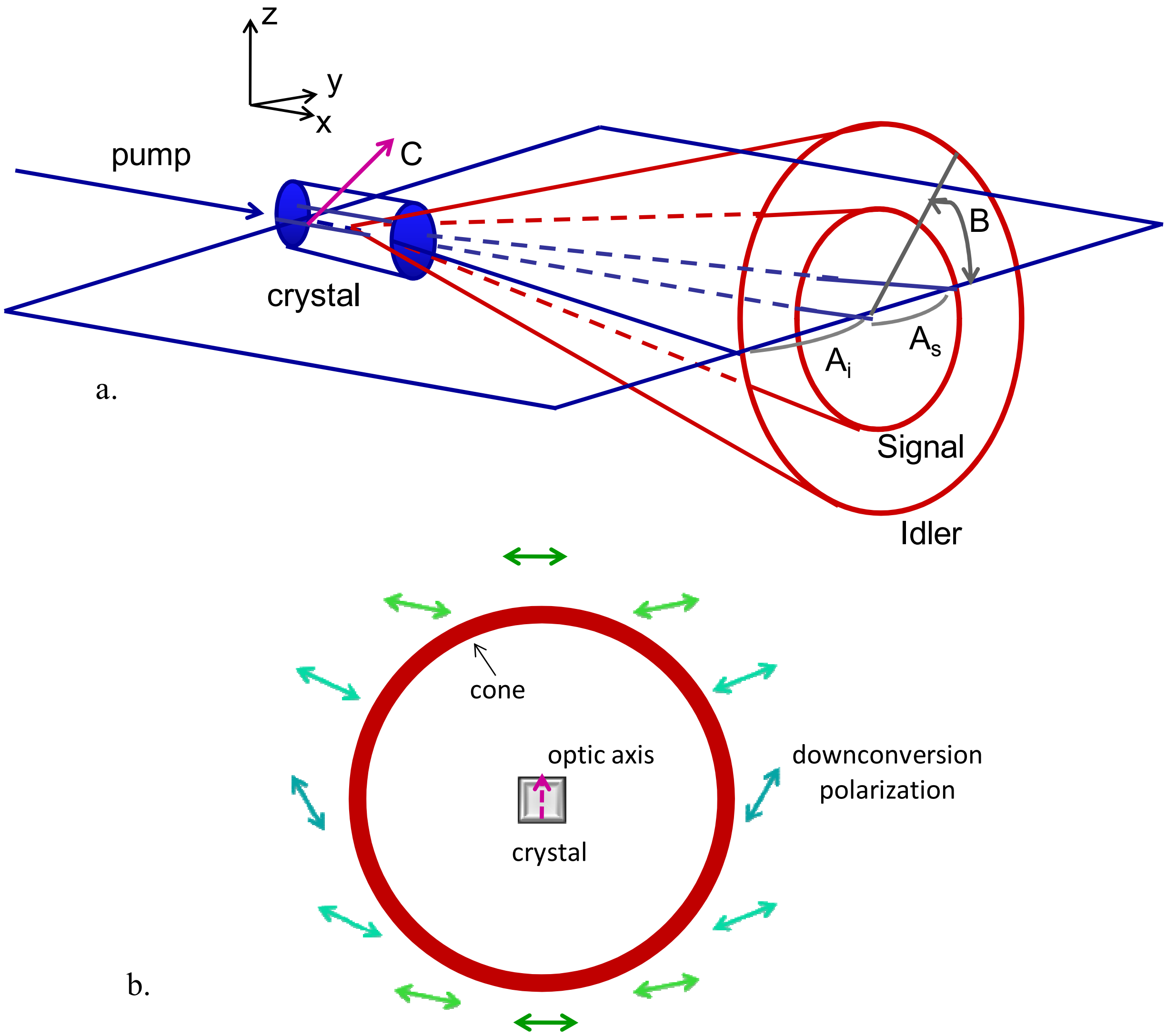

Figure 4-1: **a**. Schematic showing the crystal coordinate system with the pump beam, crystal optic axis ***C***, and signal and idler opening angles A_s and A_i respectively. The azimuthal angle B is referenced to the y direction and goes around the downconversion cone (based on [76]). **b**. A cartoon depiction of the Migdall effect: variation of the downconversion polarization at various points along the emission cone, shown end-on. The dotted central arrow indicates the projection of the optic axis (in the x-z plane) on to the z axis.

understood as follows. In type-I phasematching, the downconversion photons are *ordinary* polarized (assuming a negative uniaxial crystal, like BBO), i.e.,their polarization ***P*** is perpendicular to both their propagation direction **k** and the crystal optic axis **C** inclined at angle Θ with respect to the pump propagation direction, such that

$$\hat{\mathbf{P}}(A,B) = \hat{\mathbf{k}} \times \hat{\mathbf{C}}(\Theta)\ , \qquad 4.1$$

where A is the cone half-opening angle, B is the azimuthal emission angle and ***C*** is the direction of the optic axis. Since the downconversion propagation direction varies along the cone while the crystal optic axis is fixed, the downconversion polarization measured in the lab frame of reference depends on the emission direction, in spite of being ordinary polarized everywhere along the cone (see Figure 4-2a). As shown in [76], a particular coordinate transformation can be useful in determining the angular dependence of downconversion polarization. First, rotate the z axis by ϕ to give the $x'-y'-z'$ $(z'=z)$ frame, then we rotate about the y' axis by γ to give the $x''-y''-z''$ $(y''=y')$. Figure 4-2b shows the ϕ,γ,β coordinate system, in which the angle β defines the polarization of the downconversion photon propagating along the (A,B) direction, and

$$\begin{aligned}\phi &= \tan^{-1}\left[\tan A \cos B\right],\\ \gamma &= \sin^{-1}\left[\sin A \sin B\right].\end{aligned} \qquad 4.2$$

The output polarization angle β can be found from Eqn. 4.1 by transforming ***P*** and ***C*** into the new coordinate system [76], which yields

$$\beta = \tan^{-1}\left[\frac{-\cos\Theta\cos\phi\sin\gamma + \sin\Theta\cos\gamma}{\cos\Theta\sin\phi}\right]. \qquad 4.3$$

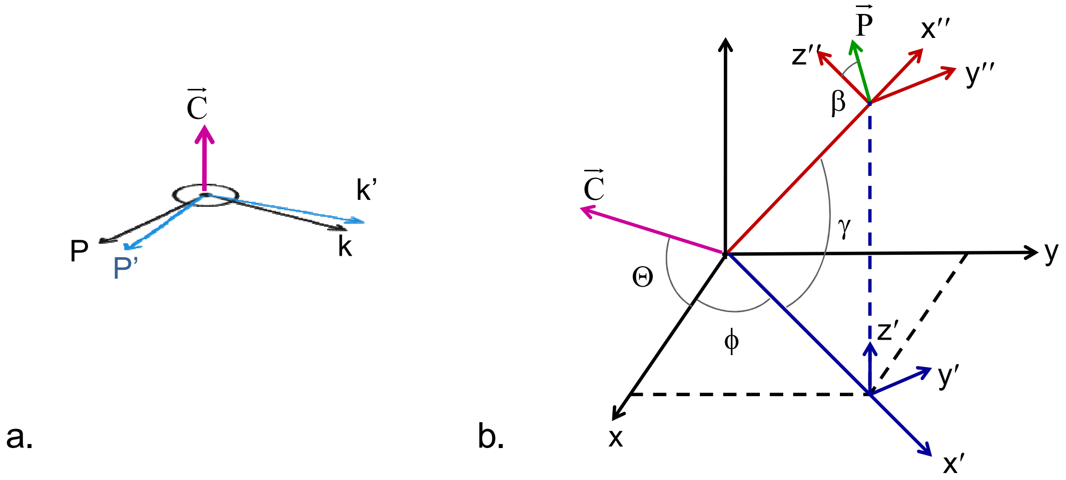

Figure 4-2: **a**. Schematic representation showing the origin of the Migdall effect. The downconversion photons are ordinary polarized, which is perpendicular to both the fixed crystal optic axis and the emission direction $\vec{k}$; thus when the emission direction changes $\left(\vec{k} \to \vec{k}'\right)$ so does the polarization $\left(\vec{P} \to \vec{P}'\right)$. **b.** ϕ,γ,β coordinate system and the crystal optic axis, cut at angle Θ in the $x-z$ plane. β is the angle between z'' and ***P*** in the $x''-z''$ plane (based on [76]).

Eqn. 4.3 implicitly gives the downconversion polarization dependence on both emission angles – the cone opening (A) and the azimuthal angle (B). Figure 4-3 shows this theoretical dependence along with the measured downconversion polarization from a single crystal, relative to the extraordinary pump polarization (defined to be 0°), as a function of the emission azimuthal angle, for both the typical 3° opening half-angle and the engineered 16° case. In the lab frame, downconversion photons are collected on opposite sides of the emission cone, conventionally at either 0° and 180°, or at 90° and 270° azimuthal angles. From Figure 4-3, the downconversion polarization at the latter azimuthal points is always the desired 90° regardless of the cone opening angle, making these the ideal collection spots on the cone (for the two-crystal entanglement source). The reason is that these collection points lie in the plane containing the crystal optic axis and the incident pump direction, making the polarization of the ordinary downconversion photons automatically orthogonal to the pump polarization in the lab frame. As we move away from these optimal collection angles, the downconversion polarization deviates from the ideal 90°, with the effect becoming appreciably larger for larger cone opening half-angles; the Migdall effect for a 16° downconversion cone exhibits up to a 12° deviation from the expected 90° polarization, compared to only a 3° maximum deviation for a 3° cone (Figure 4-3). Note that the extreme deviations do not occur at precisely at $B = 0°, 180°$.

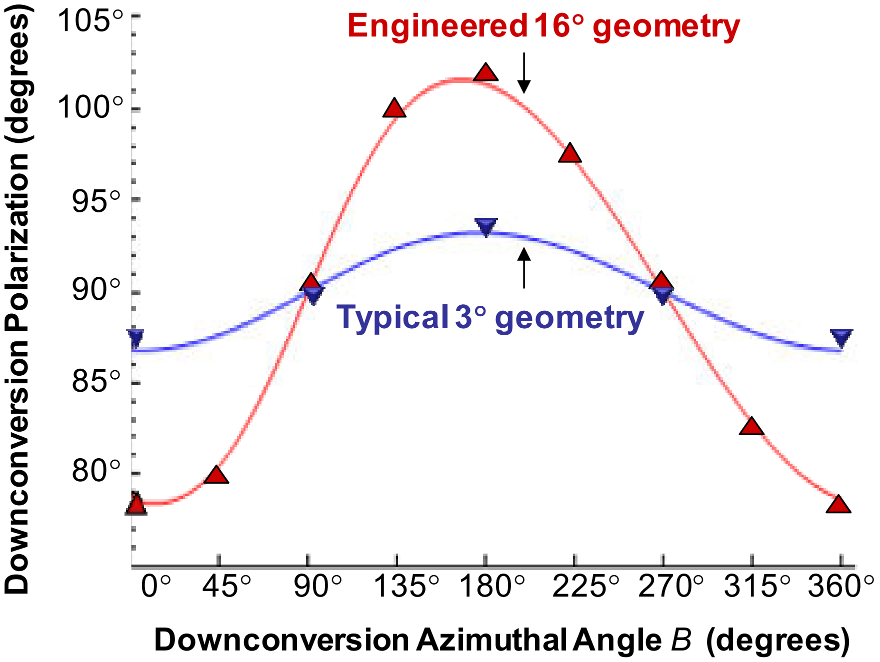

Figure 4-3: Experimental data (triangles) and theoretical predictions (solid lines) of the Migdall effect, showing the expected downconversion polarization vs. azimuthal collection angle for the 3° (blue) and 16° (red) cone opening half-angles. Polarization of the downconversion photons is measured relative to the pump polarization (0° in the lab frame).

4.2 Migdall Effect in the Two-crystal Scheme

The implications of the Migdall effect become significantly more important in the two-crystal scheme for polarization entanglement, which relies on two orthogonally oriented crystals, each pumped by orthogonal pump polarizations, $|V\rangle$ and $|H\rangle$, to generate nominally orthogonally polarized downconversion photons in the entangled state $|H\rangle|H\rangle + e^{i\phi}|V\rangle|V\rangle$. Here, we have to contend with the Migdall effect in each of the two crystals. In the lab frame, this results in specific azimuthal collection angles (Figure 4-4) for each of the crystals as follows. Assume that we collect signal photons at 0° and idler photons at 180° azimuthal angles, labeled according to the frame of crystal-1. Call the collected state $|S_1 I_1\rangle$. Similarly, for the second crystal we collect state $|S_2 I_2\rangle$ at 90° (signal) and 270° (idler), where now the angles are labeled with respect to the crystal-2 axes. In the lab frame, four photons[38] – crystal 1 and crystal 2 signal and idler – are emitted in a single plane (that also contains the pump beam direction). Note that in each crystal the signal and idler are always collected 180° apart because the photon pairs are emitted on opposite sides of the cone.

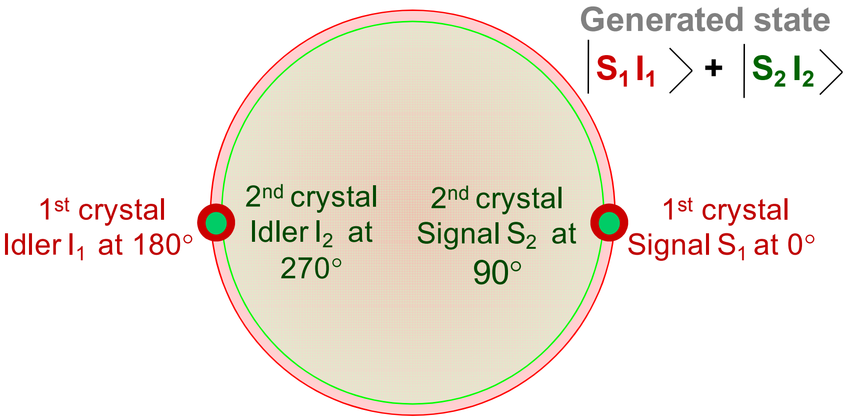

Figure 4-4: End-on view of the downconversion cones from the first (shown in red) and second (shown in green) crystal in the two-crystal scheme. The first (second) crystal is oriented such that a vertically (horizontally) polarized pump downconverts into horizontally (vertically) polarized photons. The figure shows the typical collection points in the lab frame (i.e., where the detectors are located) and the actual azimuthal angles, measured relative to the optic axis of each crystal, for the signal and idler photons generated in the two orthogonally oriented crystals.

---

[38] In reality we only have a single pair of emitted photons, but with equal amplitudes for it to have originated in either crystal.

In each crystal, the desired downconversion polarization is 90°_{p}[39], measured relative to the pump polarization in that crystal (defined to be 0°_{p} in that crystal). As seen from Figure 4-3, at the azimuthal collections angles 90° and 270°, the downconversion polarizations are always perpendicular to the pump. Hence, the polarizations of both the signal and the idler from the *second* crystal are the desired 90°_{p}, because these photons are collected at 90° (signal) and 270° (idler) azimuthal angles (measured with respect to the crystal's optic axis). However, for photons emitted from the first crystal, the Migdall effect for the 16°-engineered geometry results in 78°_{p} for the signal collected at 0° azimuthal angle and 102°_{p} for the idler collected at 180°. Note that because of the requisite orthogonal orientation of the crystals in the two-crystal scheme, collecting only at 90° and 270° from both crystals is not an option[40].

The Migdall effect in the two-crystal scheme has serious consequences on the generated entangled state. Since the pump polarization is defined in each crystal to be 0°_{p}, the *desired* downconversion polarization from each crystal is 90°_{p} (relative to that of the pump). Because the crystals are oriented orthogonal to each other, the ideal generated state can be written in the lab frame as the maximally entangled state $|\psi\rangle_{\max} = \left(|90°,90°\rangle + |0°,0°\rangle\right)/\sqrt{2}$, i.e., the relative downconversion polarizations from each crystal are ideally orthogonal. Due to the Migdall effect, however, the emitted two-photon state is instead $|\psi\rangle_{Migdall} = \left(|78°,102°\rangle + |0°,0°\rangle\right)/\sqrt{2}$. Now, the polarizations produced by the two crystals are no longer orthogonal to each other; more importantly, there is no basis in which they can be written as a maximally entangled state. The fidelity of $|\psi\rangle_{Migdall}$ with $|\psi\rangle_{\max}$ is only ~96% ; the predicted concurrence of $|\psi\rangle_{Migdall}$ is 90.8%, if there were *no* temporal decoherence[41]. Additionally, there is a significant component (~3%), quantified by the overlap between the downconversion states generated from the two

---

[39] The subscript p is used to indicate a polarization angle.

[40] Collection from both crystals at 90° and 270° azimuthal angles might be possible by inserting a wave plate *between* two crystals oriented with their optics axis *parallel* to each other. In both crystals, the horizontally polarized pump downconverts into vertically polarized photons and we collect at 90° and 270° azimuthal angles. The wave plate rotates the downconversion from the first crystal $|V\rangle|V\rangle \rightarrow |H\rangle|H\rangle$, thereby generating a maximally entangled state. Note that the wave plate must be chosen *not* to rotate the pump wavelength.

[41] In comparison, in the typical 3° half-opening angle geometry, the relative polarizations are 93.2° and 86.9° from the first crystal (collected at azimuthal angles 0° and 180°) due to the Migdall effect. Nevertheless, they are routinely employed in this configuration in the two-crystal scheme to produce high-fidelity maximally entangled state, implying that we are typically not sensitive to such minor imperfections.

crystals, that cannot be temporally compensated (Section 3.3.2), and therefore experiences unavoidable decoherence. The final predicted maximum concurrence is ~88%.

4.3 Exploiting the Migdall Effect to Generate a Maximally Entangled State

Here we show that we can actually intentionally *use* the Migdall effect and incorporate it in our engineered scheme to generate indistinguishable polarization-entangled photons. Our strategy[42] is to create a nearly maximally entangled state using the two-crystal scheme, by collecting at nontraditional azimuthal angles, i.e., locations where the relative polarizations between the downconversion photons generated from the two crystals *are* almost orthogonal. Figure 4-5a plots the relative polarization between the downconversion photons around the cone e.g., between the two signal photons. To generate maximally entangled states, we want the relative polarizations to be orthogonal. Further, this needs to be true at two opposite sides of the cone for both the signal and the idler, emitted exactly 180° apart. However, from Figure 4-5a we see that while there are azimuthal locations on the downconversion cone where the two output polarizations are perpendicular, this perpendicularity is not satisfied simultaneously on opposite sides of the cone, i.e., for both the signal at azimuthal angle B and the idler at $B+180$. For example, from Figure 4-5a we see that the two polarizations are exactly perpendicular at $B=93.6°$ but not so at $B=93.6°+180°$. A possible solution is to collect at azimuthal angles for which the deviation from orthogonality is minimized for both the signal and the idler on the downconversion cone. Such a strategy would maximize the overlap with the ideal maximally entangled state $\left|\psi\right\rangle_{\max}=\left(\left|90°,90°\right\rangle+\left|0°,0°\right\rangle\right)/\sqrt{2}$. Figure 4-5b plots the *deviation from perpendicularity* between the downconversion polarizations generated in the first and second crystals for the signal (at B) and the idler (at B+180°). From this figure, we see that the optimal collection angles are 105° (signal) and 285° (idler), for which the downconversion polarizations between the two crystals deviate from perpendicularity by only $\sim 3^{\circ}_{p}$. Hence, the downconversion polarization from the first crystal, where the Migdall effect was previously the most significant, becomes 93.4°_{p} $\left(\left|S_1\right\rangle\right)$ and 86.6°_{p} $\left(\left|I_1\right\rangle\right)$, and 0°_{p} $\left(\left|S_2\right\rangle\right)$ and 0°_{p} $\left(\left|I_2\right\rangle\right)$ for the second crystal, where we have relabeled the polarization angles[43]. Thus, instead of producing the ideal state

---

[42] Originally proposed by our theory collaborator Alfred U'Ren (National Autonomous University of Mexico).

[43] Collecting at unconventional azimuthal angles in the lab frame, e.g., 93.4° and 86.6°, would require a detection plane that is no longer parallel to the optical table, resulting in the need for complicated mounts and alignment. Therefore, instead of rotating the detection plane, we choose to rotate everything else, i.e., the pump

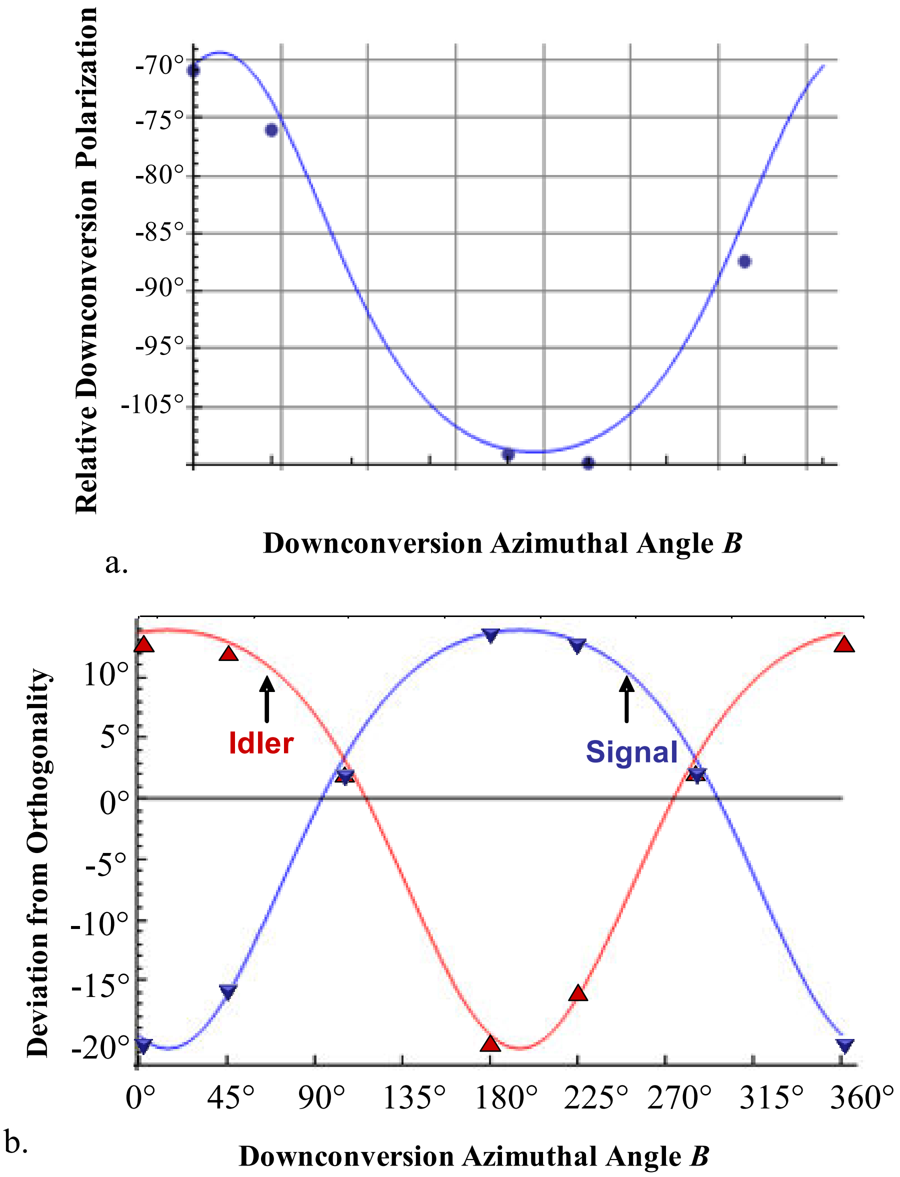

Figure 4-5: Experimental data (circles/triangles) and theoretical predictions[44] (solid line) for **a**. relative polarization between the downconversion photons – comparing either signals or idlers – from the first and second crystals in the two-crystal scheme, as a function of the location on the downconversion cone (i.e., collection) in the reference frame of the lab (ideally, this would be ± 90°); **b**. deviation from perpendicularity between the downconversion photons from the first and second crystals, plotted for both sides of the collection: signal (collected at B) and idler (at B +180°). The crossing indicates the optimal collection angles B_o=105° and 285°, for which the downconversion polarizations are the most orthogonal.

---

polarization, crystal optic axis and the analyzing polarizers. Thus, the downconversion polarizations are relabeled, i.e., $105^{\circ}_{p} \rightarrow 90^{\circ}_{p}$.

[44] The theory for these curves was obtained as follows: the downconversion polarization from the second crystal was calculated using exactly the same parameters used for the first crystal, except the optic axis, which was rotated by 90°. Thus, strictly speaking, what we now call the azimuthal coordinate in the lab frame is the azimuthal coordinate defined with respect to the first crystal.

$\left(|90°,90°\rangle + |0°,0°\rangle\right)/\sqrt{2}$ from the two crystals, we produce, after local corrections, $\left(|93.4°,86.6°\rangle + |0°,0°\rangle\right)/\sqrt{2}$,which has >99% predicted fidelity with a maximally entangled state and a concurrence above 98% (assuming no decoherence).

Collecting at the specified nontraditional azimuthal angles offers a viable solution to overcome the Migdall effect in order to generate a nearly maximally entangled state. However, in spite of our novel approach, experimentally producing a high-fidelity polarization-entangled state from the group velocity matched 16°-downconversion propagation SPDC crystals, thus far remains a challenge. The large 16° downconversion emission, combined with the unconventional collection angles, has led to a host of other related issues – extreme sensitivity to temporal and spatial compensation, polarization rotation, and as yet unsolved decoherence. For example, the GVM crystals have an extremely large spatial-phase slope (Section 3.3) of ~73°-per-mm compared to 15°-per-mm for the typical 3° downconversion propagation (at ~120 cm from the downconversion crystal). Thus, spatial decoherence alone theoretically limits the concurrence to ~66% (compared to 98% for the 3° cone) when collecting through 2-mm irises. Collecting at the unconventional Migdall angles actually worsens spatial decoherence, with a 78°-per-mm phase slope. This spatial decoherence can be countered using a 1.46-mm BBO compensator cut similar to the downconversion crystal[45]. However, such long crystals (the compensators are ~2.5 times the length of the SPDC crystals) can result in significant birefringent effects of their own, e.g., the total temporal walkoff (including the SPDC crystals) corresponds to ~535 fs, making this configuration extremely sensitive to temporal compensation. Experimentally, the highest concurrence obtained was only ~ 45% [46], possibly limited by several sources of decoherence in the two-crystal source, such as polarization rotation in the SPDC crystal, spatial walkoff, dispersion, etc. To overcome this, we pursue two options: characterize the JTPA of a *single* engineered source (discussed in Section 2.3), and avoid the two-crystal schemes entirely, by employing other methods for generating polarization entanglement (Chapter 6).

In summary, group-velocity engineering results in large downconversion cone opening angles, where the Migdall effect produces significant angular dependence of the emitted polarizations. Here, we have experimentally confirmed for the first time this important SPDC effect, and identified it as the dominant cause behind the generation of non-maximally entangled states from the 16°- GVM crystals. Thus, we have developed a strategy (collecting at nontraditional azimuthal angles) that uses the Migdall effect to

---

[45] Calculated using methods described Section 3.3.

[46] We did not use any spatial compensators; instead, spatial-phase coherence was controlled by collecting with very small irises (<0.5 mm), which resulted in very long collection times.

mitigate its impact on the engineered 2-crystal source. However, experimentally this led to a host of other related issues – extreme sensitivity to temporal and spatial compensation, polarization rotation and as yet unsolved decoherence. While these might be solvable, considering other challenges to our engineered source (such as birefringent focusing/collection, as discussed in the next chapter), a more elegant solution for generating polarization entanglement may be preferable, e.g., to bypass the Migdall effect (as well as the two-crystal scheme) entirely by using a double-pass through a single engineered crystal, as discussed in Section 6.1.

Chapter 5
Challenge 3: Birefringent Focusing

O-Ren Ishii: You didn't think it was gonna be that easy, did you?
The Bride: You know, for a second there, yeah, I kinda did.
O-Ren Ishii: Silly rabbit.
The Bride: Trix are...
O-Ren Ishii: ...for kids.
-From the movie Kill Bill: Vol 1(2003)

The third challenge involved in engineering an indistinguishable photon-pair source – birefringent focusing – arises from the requirement to optimize phasematching parameters in our system. Birefringent focusing refers to being able to focus different polarizations at different longitudinal spatial locations. The size and location of the pump beam waist[47] inside the downconversion crystal are key parameters that have to be optimized as part of engineering indistinguishable photons (Section 2.1). However, different orthogonal polarization components of the pump are extraordinary polarized in the two downconversion crystals. Therefore, birefringent focusing is required to optimally focus each of the orthogonally polarized pump components in the center of a particular crystal. The inverse problem, birefringent collection, is also important since the same is true for optimally collecting the downconversion photons from each crystal into single-mode fibers. Here we present the complexities involved in attempting birefringent focusing/collection using a simple lens and a birefringent crystal, present the results of a simplified theoretical calculation[48] that agrees with our experimental results and explain why this method does not work. Additionally, we propose a novel solution for achieving birefringent focusing.

5.1 Pump-beam focus optimization

As discussed in Section 2.1, the size and location of the pump beam waist inside the downconversion crystal are two key parameters that can be controlled to engineer indistinguishable downconversion photons. Figure 5-1 shows the effect of varying the focused pump beam-waist location z_0 (measured relative to the center of a *single* 0.6-mm group-velocity matched crystal) on the brightness and purity of the single-mode fiber-coupled SPDC photons. Thus, the pump beam has to be focused into the *center* of a

---

[47] For a Gaussian beam propagating in free space, the beam waist is the smallest value that the beam spot size takes.

[48] The full derivation will be added as an Appendix.

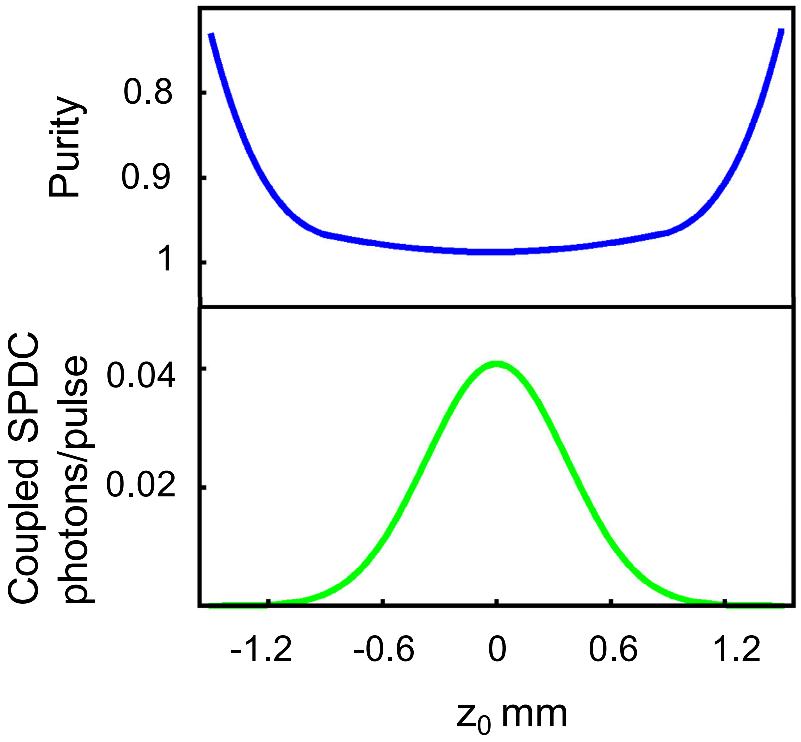

Figure 5-1: Simulated brightness and purity dependence of the coupled SPDC photons on the position of the (focused) pump beam waist z_0, measured relative to the center of the crystal (0.6-mm group-velocity matched crystals).

crystal to generate bright indistinguishable photons. For a single crystal, this is trivially accomplished with a lens of the appropriate focal length[49]. However, to generate polarization entangled photons we employ a two-crystal scheme (Section 2.4): downconversion pairs are generated with orthogonal polarizations in the two crystals, which are also pumped with orthogonal polarizations. The pump beam-waist's size and location need to be optimized, individually for each crystal, resulting in the need for birefringent focusing. Although the optimal pump beam waist is the same for both polarizations (since our approach is simply to optimize downconversion from each of the crystals), one of the pump polarizations has to be focused one crystal length away, as shown in Figure 5-2. The reverse problem of birefringent focusing, also shown in Figure 5-2, is similarly required since orthogonally-polarized downconversion photons have to be optimally collected into single-mode fibers from the center of each crystal.

---

[49] A simple formula to find the optimal focal length *f*, for a desired spot size w_0, wavelength λ and input pump beam diameter *D* is $f = \frac{\pi D w_0}{2\lambda}$.

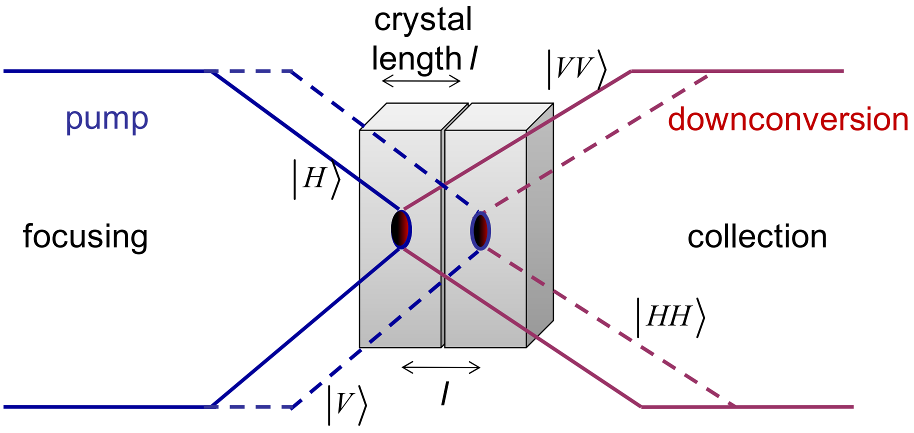

Figure 5-2: Schematic showing birefringent focusing (collection). The orthogonally polarized pump (downconversion) components need to be focused at (collected from) the center of two different crystals, separating the beam waists of the different polarizations by one crystal length.

5.2 Birefringent Focusing Using a Lens and a Birefringent Slab

The simplest approach to birefringent focusing is to employ a lens in combination with a birefringent slab to shift the focus of one of the polarizations, as shown in Figure 5-3; however, as will see this technique actually fails to achieve the desired effect, i.e., two displaced *round* focused spots with orthogonal polarizations. The distance between the beam waists is controlled by the thickness and the birefringence of the slab. To see this, first let us consider an optical setup consisting of a lens of focal length f followed by a simple *non*-birefringent slab with refractive index n and length d . For paraxial rays, the position of the focus can be derived using ray matrices (see e.g., [77]):

$$f_n = f + d\left(1 - \frac{1}{n}\right). \qquad 5.1$$

Thus, a glass slab results in an index-dependent longitudinal shift of the focus *away* from the lens. This is the idea underlying focusing/collection using a birefringent slab: the ordinary and extraordinary polarizations experience different indices of refractions (n_e and n_o, respectively) inside the birefringent crystal; since each has a different optical path length and hence focuses at a different location, we expect two spots with a longitudinal separation Δf between the two polarizations, given by

$$\Delta f = d\left(\frac{1}{n_o} - \frac{1}{n_e}\right). \qquad 5.2$$

For the simple case of a birefringent crystal cut with its optic axis perpendicular to the direction of propagation, we thus expect two beam waists: one for the ordinary-polarized light and the other for the extraordinary-polarized light. However, in practice we observe *one focused and one elongated* spot (with a range of beam waists)! In the rest of this section, we explain the origin of the three spots for the specific case of the optic axis cut perpendicular to the propagation direction, which has been studied before [77]. Further, we theoretically derive and experimentally confirm for the first time the more complicated general case of birefringent focusing for an *arbitrary* optic axis cut.

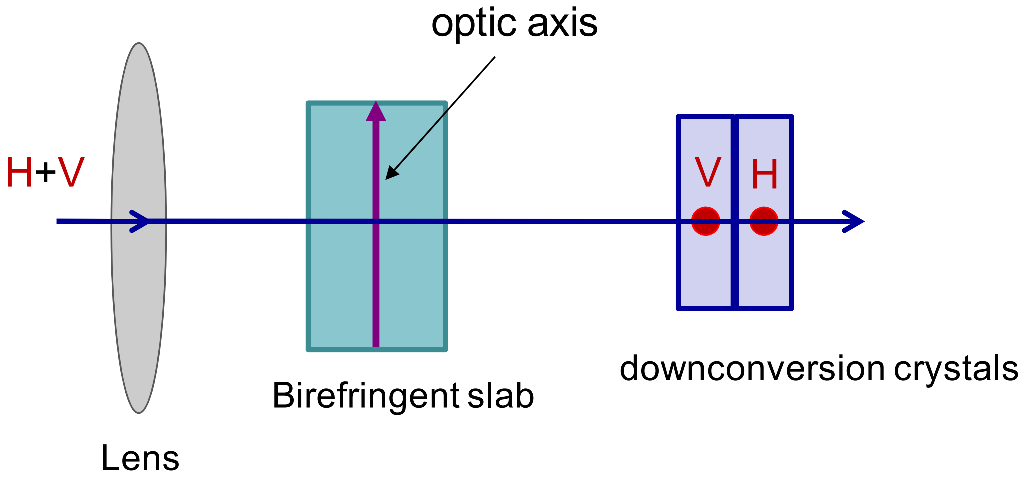

Figure 5-3: Expected results for birefringent focusing scheme using a lens and a birefringent slab.

5.3 Origin of Three Focused Spots

When focusing using a lens and a birefringent crystal, the ordinary polarized light behaves as expected, resulting in a longitudinal focus shift given by Eqn. 5.1, with $n = n_o$. However, the extraordinary polarized ray results in an elongated blurred focus with beam waists at the two extremities. To see this, we consider the two extreme rays: the horizontally incident and the vertically incident components of the extraordinary rays shown in Figure 5-4. These rays experience different longitudinal shifts because they experience different effective refractive indices inside the crystal [77]. In any uniaxial birefringent crystal, the refractive index of the extraordinary beam depends on its propagation direction relative to the optic axis

$$\frac{1}{n_e^2(\Theta_a)} = \frac{\cos^2\Theta_a}{n_o^2} + \frac{\sin^2\Theta_a}{n_e^2} , \qquad 5.3$$

where Θ_a refers to the angle between the wave vector of the extraordinary ray and the optic axis of the

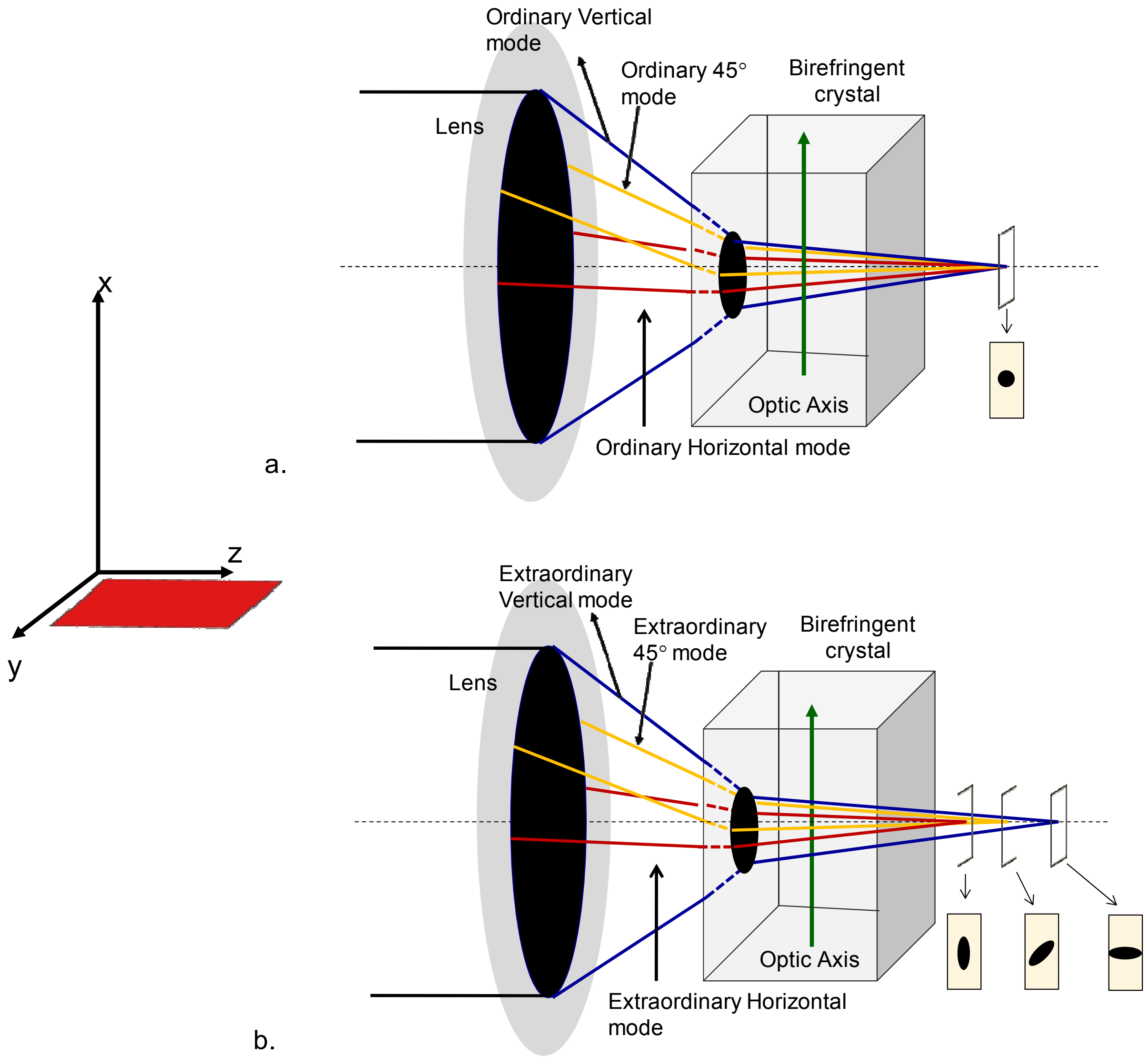

Figure 5-4: Schematic showing the focusing of the ordinary (**a**) and extraordinary (**b**) polarization, using a lens and a birefringent crystal with the optic axis cut at 90°, for rays in the horizontal (red), vertical (blue) and 45° plane of incidence (yellow). **a**. The ordinary beam results in a symmetric focused spot for all spatial modes. **b.** The extraordinary beam results in an elongated blurred spot; the extreme spots are caused by the extraordinary ray in the horizontal plane and the extraordinary ray in the vertical plane. The extraordinary horizontal components (in the y-z plane) always see the same index, n_e, whereas the vertical components (x-z plane) experience an angle-dependent index. A ray in between the two extreme cases, e.g., the in the 45° plane focuses in between. Note that the extraordinary polarization results in a blurred elongated spot due to the incident-direction dependence of the refractive index and spatial walkoff of the vertical components.

crystal. When the crystal's optic axis is cut at 90°, the plane of incidence of the horizontally incident extraordinary rays is always perpendicular to the optic axis of the crystal and thus $n_e(\Theta_a) = n_{e.}$ However, the plane of incidence of the vertically incident extraordinary rays is parallel to the optic axis of the crystal and thus, their refractive index varies according to their propagation direction, as given by Eqn. 5.3 [77]. Additionally, the vertically incident extraordinary rays experience Poynting vector walkoff because they are not perpendicular to the optic axis. Thus, the beam waists of the extraordinary rays are *elliptical* spots, which occur at two distinguishable locations depending on their plane of incidence (i.e., vertically or horizontally), shown in Figure 5-4. Together with the ordinary ray, this results in a total of three beam waists and an extended blurred focus. Park et al. [77], analyze only the specific case of a perpendicular optic axis cut. The case of birefringent focusing using a uniaxial crystal cut at an arbitrary angle is more complicated. In this case, the refractive index varies with propagation direction for both the horizontal and vertical components of the extraordinary rays, and their walk offs occurs in different directions. A simplified derivation for the arbitrary optic axis cut is presented in Appendix B. In the next section we discuss the theoretical predictions and present experimental results for such a general case.

5.4 **Theory for Arbitrary Crystal Cut Angle**

To derive the polarization-dependent beam-waist location for a birefringent crystal with the optic axis at an arbitrary angle, we consider three independent cases: ordinary polarization, extraordinary polarization in the vertical plane, and finally, extraordinary polarization in the horizontal plane.

5.4.1 Ordinary Polarization

The simplest case is that of ordinary polarization, for which the birefringent crystal behaves identically to a regular glass slab. These rays experience a constant refractive index n_o in the birefringent slab of thickness d and are focused to an image point by the lens with focal length f. Using Eqn. 5.1 the shift in the focus of the ordinary polarization Δf_o, caused by the birefringent slab, can be written as:

$$\Delta f_o = d\left(1-\frac{1}{n_o}\right). \qquad 5.4$$

5.4.2 Extraordinary Polarization

For extraordinary polarization, the effective refractive index depends on the angle Φ between the direction of propagation in the medium, and the crystal cut, i.e., the orientation of the optic axis. The effective angle-dependent refractive index $n(\Phi)$, can be written using Eqn. 5.3, as

$$n_e(\Phi) = \frac{n_o n_e}{\sqrt{n_o^2 \sin^2(\Phi) + n_e^2 \cos^2(\Phi)}} \quad . \qquad 5.5$$

Since these rays are extraordinary, the actual direction of energy propagation is given by the Poynting vector, which walks off from the wave vector inside a birefringent medium by:

$$\rho(\Phi) = \arctan\left(\left(\frac{n_{\mathrm{o}}}{n_{\mathrm{e}}}\right)^2 \tan(\Phi)\right) - \Phi \quad . \qquad 5.6$$

Φ is the wave-vector direction inside the crystal. Hence, to find the beam-waist location for extraordinary polarization, we first solve for the angle of refraction and then calculate the walkoff inside the crystal. Note that the walkoff plane will be incident-direction dependent, thus the horizontal and vertical components focus at different *x,y and z* locations. The simplified theoretical derivation is shown in Appendix B. Using these calculations, the average beam-waist location for extraordinary polarization in the vertical and horizontal plane can then be estimated (theory results shown in Figure 5-5d) and compared to the experimental results.

5.5 Experimental Results for Focusing via a Birefringent Slab

The experimental setup consisted of a 50-cm focusing lens and a 39.8-mm calcite crystal cut with its optic axis at 45° to the surface normal. The beam widths were measured using a knife-edge technique [44] at different points along the *z* axis. The extraordinary and ordinary components of the incident beam were isolated with a polarizer. The beam waists of the extraordinary components in the vertical and horizontal planes were measured by using different planes for the knife-edge scans – for the vertical (horizontal) component the scans were parallel to the *y* (*x*) axis (shown in Figure 5-4)[50]. Figure 5-5 shows the beam-waist measurement data for the three cases: ordinary polarization, extraordinary polarization in the vertical and the horizontal planes. The beam widths were measured at different positions z along the beam after the lens and the calcite crystal. The beam waists, computed from the Gaussian fits (red lines) are located at 34.61 ± 0.07 mm for the ordinary polarization, 27.33 ± 0.12 mm for the extraordinary polarization in the horizontal plane, and 34.14 ± 0.20 mm for the extraordinary polarization in the vertical plane. We thus measure the location of the foci for the extremes of extraordinary polarized beams (i.e., incident in the vertical vs. the horizontal plane) to be separated by 6.81 ± 0.23 mm, matching the theoretical prediction of 6.72 mm extremely well.

---

[50] Note that the vertical and horizontal components of the extraordinary were not really "isolated", i.e., both the knife-edge scans were done on the "entire" extraordinary beam. By rotating the plane in which the knife-edge is scanned we are able to deduce the location at which the beam waist (i.e., the smallest beam width) occurs for these respective components.

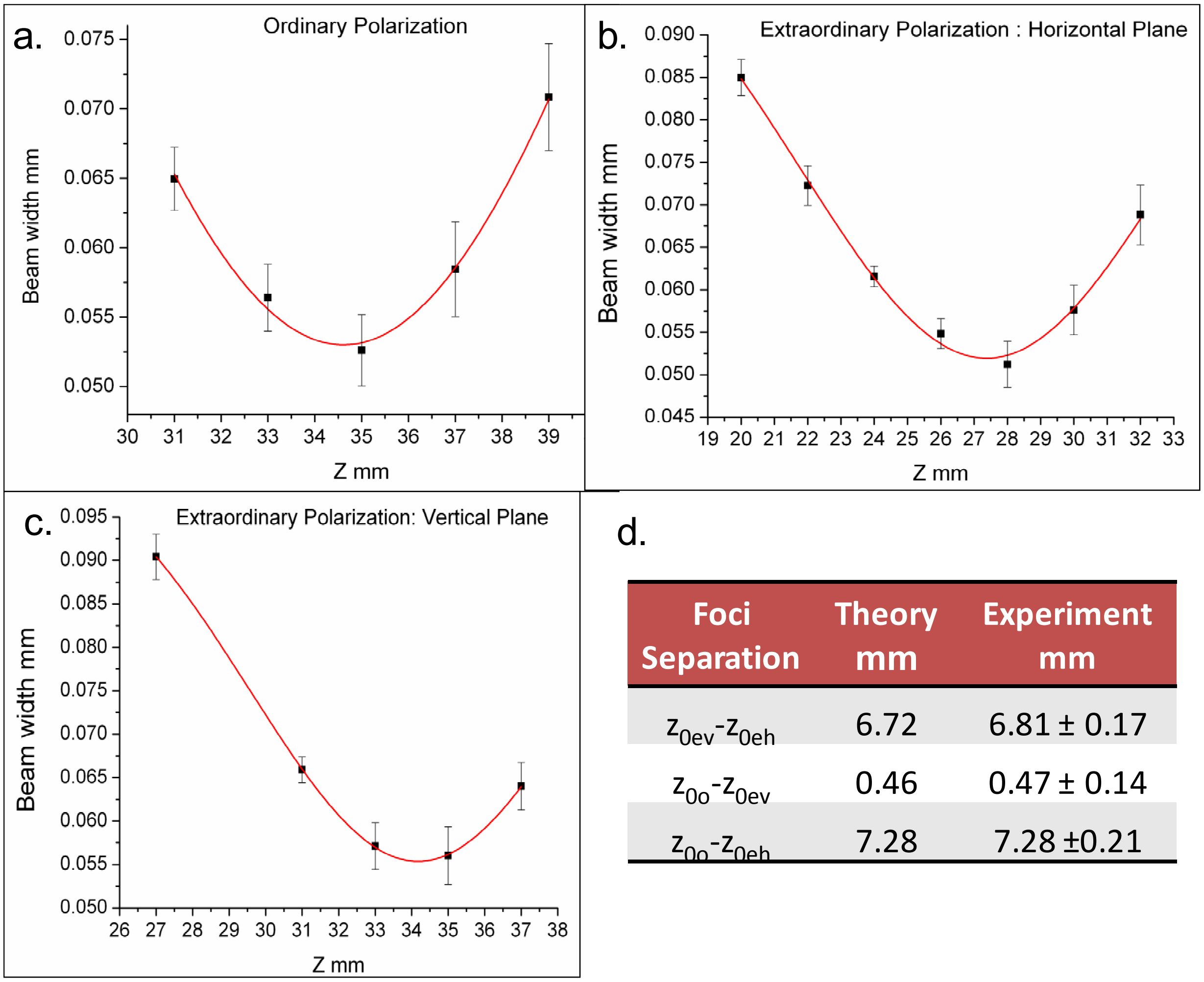

Foci Separation	Theory mm	Experiment mm
z_{0ev}-z_{0eh}	6.72	6.81 ± 0.17
z_{0o}-z_{0ev}	0.46	0.47 ± 0.14
z_{0o}-z_{0eh}	7.28	7.28 ±0.21

Figure 5-5: Beam-width measurements at different points *z* along the focused beam after a calcite crystal (39.8-mm long) for **a**. ordinary polarization, **b**. extraordinary polarization in the horizontal plane, and **c**. extraordinary polarization in the vertical plane. **d**. Summary of the expected theoretical and measured experimental values for the separation of the different beam waists. Here the beam waist occurs at z_{0o} for the ordinary, z_{0ev} for the extraordinary vertical and z_{0eh} for the extraordinary horizontal rays.

5.6 Interferometric Birefringent Focusing

Birefringent focusing using a birefringent slab results in an elongated blurred spot even for the simple case of a perpendicular optic axis cut. As a result, the extraordinary polarization cannot be focused into a round Gaussian-shaped beam, with a specific beam-waist size in the center of a particular crystal, i.e., focusing through a birefringent slab does not offer a viable option for our engineering scheme[51], in which we need to be able to control the beam-waist size and location for each polarization. However, the

---

[51] The birefringent effects on a pump beam waist will occur because of the SPDC crystal itself – i.e., the crystal will cause the extraordinary polarization to walkoff and shift the focus depending on the incident angle. However, because we employ extremely thin crystals for SPDC (~0.6 mm), these effects are negligible.

underlying idea behind this method, having a polarization-dependent optical path length, can be implemented in other ways. For instance, one can use a lens followed by an unbalanced interferometer, e.g., a Mach-Zender, as shown in Figure 5-6a. Here, a polarizing beam splitter (PBS) directs the different polarizations into different spatial arms, one longer than the other. The foci of the two different polarizations are thus controlled by the difference in the optical path lengths between the two arms. In the Mach-Zender shown in Figure 5-6a, the vertically polarized beam takes the longer path and thus focuses before the horizontally polarized beam. The disadvantage in using most interferometers, including the Mach-Zender, is that they are extremely sensitive to any differential differences between the two arms; in order to preserve the coherence between the two arms, they require interferometric stability at the sub-wavelength scale.

A special type of a stable interferometer, called the Sagnac (Figure 5-6b), circumvents the stability problem by using the same spatial path for the two arms. Here, the clockwise and counter-clockwise directions constitute the two arms. Thus, any noise becomes common-mode making the interferometer extremely stable. Birefringent focusing can be achieved by placing a focusing lens displaced from the midpoint of the path. As shown in Figure 5-6b, horizontally polarized light takes the counterclockwise path, sees the lens first and hence, focuses before the vertical polarization. The distance between the two foci $\Delta f = 2x$, with x corresponding to the distance of the lens from the center.

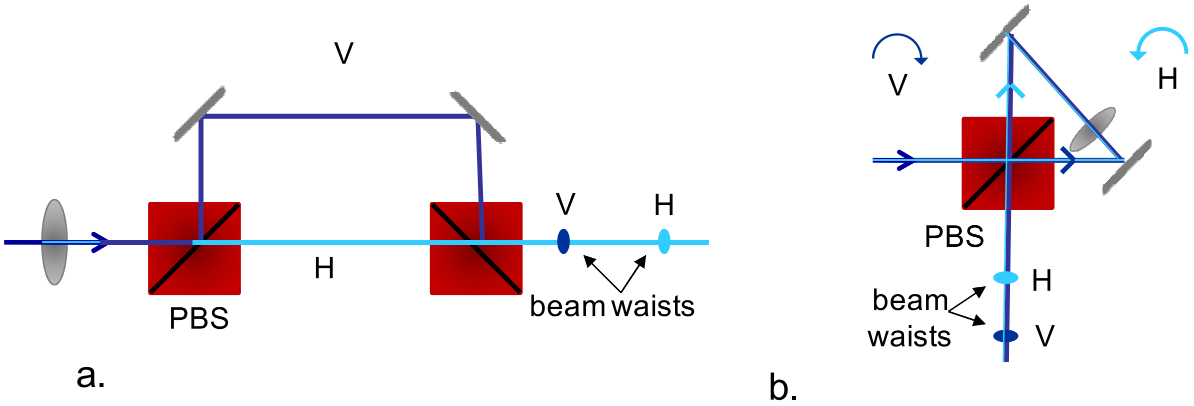

Figure 5-6: a. A Mach-Zender-like setup to achieve birefringent focusing. A polarizing beam splitter (PBS) is used to separate the two polarizations, and the foci separation is given by the path-length difference between the two arms. b. A Sagnac-based implementation of birefringent focusing. A PBS is used to direct the orthogonal polarizations into clockwise and anti-clockwise paths. A focusing lens is placed offset from the center of the two path. In the figure, the horizontal polarization sees the lens first, and thus is focused before the vertically polarized beam.

Apart from its simplicity, the Sagnac method of birefringent focusing has an additional benefit: the foci of two orthogonally-polarized beams can not only be separated longitudinally, i.e., along the pump direction, but can also be given a relative transverse shift[52]. As shown in Figure 5-7, a lateral shift $\Delta f_{\perp}$ between the two beam waists can be introduced by shifting one of the mirrors in the Sagnac by y . In this simple configuration, the mirrors and the PBS are oriented at 45° to the incident beams and thus, from basic trigonometry,

$$\Delta f_{\perp} = \sqrt{2y^2} \; . \tag{5.7}$$

The birefringent shifts of interest are typically small; thus, effects arising from the beams being off-axis to the lens are negligible; in any event, if we are only interested in lateral and no longitudinal shifts, the lens can be placed before the PBS, thereby eliminating any such higher-order effects.

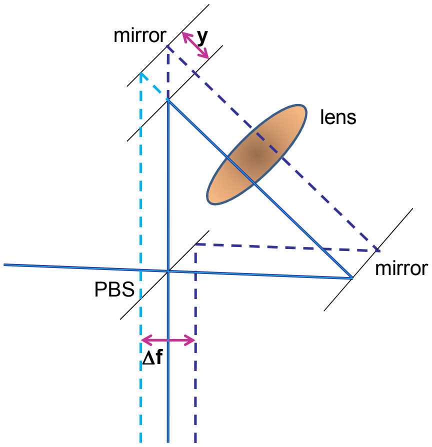

Figure 5-7: Birefringent lateral shift of the focus by moving one of the mirrors by y.

In summary, we have studied two different ways to achieve birefringent focusing, with the end goal of optimizing the differently polarized pump beam waist in each of the engineered crystals in the indistinguishable source. While we have derived the theory and experimentally confirmed the first method of birefringent focusing that uses a birefringent crystal, the complications arising from spatial walkoff effects preclude its use in the engineered source. The second Sagnac-based source presents a viable simple alternative to achieve birefringent focusing, and appears especially attractive given the additional control in the lateral dimension. However, to engineer the indistinguishable source we need to optimize collection as well as focusing. Given that the downconversion beams are non-collinear, we

---

[52] The beam waists of the different polarizations need not be laterally shifted for the engineered indistinguishable source. However, having this extra degree of control could be of use in other applications.

would need to use three such Sagnac interferometers– one for the pump and one for each of the downconversion arms.

Chapter 6
The Engineered Source: Outlook

When I am working on a problem I never think about beauty. I only think about how to solve the problem. But when I have finished, if the solution is not beautiful, I know it is wrong.

- Buckminster Fuller (1895-1983)

A known devil is better than an unknown angel.

- Old saying

To get a measure of the complications introduced by the three challenges (Chapters 3-5) in engineering the indistinguishable-photon source, let us list the proposed remedies: first, we need a temporal compensator[53] to eliminate spectral-temporal decoherence caused by an ultrashort femtosecond pump; second, we collect at unconventional cone angles to reduce the Migdall effect; and finally, we add *three* interferometers, albeit Sagnacs, to optimize pump focus and downconversion collection. *All* of these steps are required rather than simply inserting some narrow bandwidth filters, the conventional way of dealing with the correlations. Thus, while we have identified, understood and solved three huge challenges to engineering an indistinguishable photon source, we chose to take a giant step back and reconsider our overall approach. Engineering indistinguishable photons from one crystal, for the most part, is a matter of math – we identify the crystal cut angle for which simultaneous phase and group-velocity matching occurs, and, ideally, this produces uncorrelated photons. Most of the complications arise from incorporating these group-velocity matched engineered crystals in the two-crystal scheme for polarization entanglement. Of course, we prefer the convenience and the familiarity of the two-crystal scheme, given our extensive experience with this system, but at this point an alternate approach to generating polarization entangled photons warrants further investigation. In this chapter, we analyze the *rail-cross* scheme as a potential approach to generate polarization-entangled spatio-spectrally unentangled photons using the engineered crystal. Additionally, we compare the typical-filtered and focused (TFF) crystal (see Section 2.2), to the group-velocity matched case, as a possible source of indistinguishable photons.

---

[53] Spatial compensation is not of much help when coupling into single-mode fibers, which, at least initially, is required to confirm the theory of the engineered indistinguishable source.

6.1 **The Rail Cross Arrangement**

The rail cross scheme, shown in Figure 6-1, uses a single SPDC crystal and a double-pass pump arrangement to generate type-I polarization-entangled photons. An extraordinary polarized pump, e.g., horizontally polarized, is incident on a negative uniaxial χ^2 crystal, with an amplitude to produce SPDC photons in the $|VV\rangle_1$ state. The pump is then reflected back through the crystal, with an amplitude to produce a pair in the $|VV\rangle_2$ state. The subscript on the downconversion state indicates the pump pass, i.e., 1st or 2nd, that generated it. The $|VV\rangle_1$ spatial modes are also reflected back through the crystal, such that they overlap with the $|VV\rangle_2$ spatial modes [78]. However, the $|VV\rangle_1$ photons first pass through quarter-wave plates (QWP) in each arm, are reflected back and pass through the QWPs again; the wave plates are oriented such that after both these passes, $|VV\rangle_1$ becomes $|HH\rangle_1$. The optical path lengths L_s, L_i and L_p of the signal, idler and pump between the crystal and the respective mirrors are matched so that the arrival times of all three are matched at the crystal. The downconversion states from both the pump passes are thus interferometrically combined and when they are coherent with each other [54], they constitute the polarization-entangled state $|HH\rangle_1 + e^{i\Delta\phi}|VV\rangle_2$, where $\Delta\phi = \phi_s + \phi_i - \phi_p$, and ϕ_s, ϕ_i and ϕ_p denote the phases acquired by the signal, idler and pump in propagating to their respective mirrors and back, e.g., $\phi_p = 2\pi L_p / \lambda_p$. The rail cross has been demonstrated with the typical ~3° SPDC emission angles [78-79], and also used to stimulate type-II polarization entanglement [80] and control spectral correlations [56]; in the latter experiment a visibility >98% was achieved with only minimal spectral filtering. Note that interferometric stability between the first and second passes is a key requirement for high-fidelity polarization-entangled states, i.e., the path lengths L_s, L_i and L_p should be stable to within ~10 nm.

The spatio-spectrally engineered crystal (Section 2.2) can be employed in a rail cross arrangement to create an indistinguishable polarization-entangled photon-pair source. We can analyze the impact of the three main effects which complicated the two-crystal approach – temporal decoherence, the Migdall

---

[54] The pairs from the first and second passes will be indistinguishable if $L_s - L_i << L_s^c = L_i^c$, i.e., the path lengths of the signal and the idler should be well within the coherence lengths of the downconversion photons L_c, and if $L_p - L_s \approx L_p - L_i < L_p^c$, i.e., the path length of the pump should be small compared to its coherence length L_p^c. Note that in the retro-reflection geometry the path lengths L_s, L_i and L_p correspond to *twice* the distance between the crystal and the corresponding mirrors.

effect and birefringent focusing – in the rail cross arrangement. The first effect, temporal decoherence, can be accounted and compensated for using the methods discussed in Section 3.3.2. The temporal delay Δt between $|HH\rangle_1$ and $|VV\rangle_2$ is the overall difference in the arrival times between the downconversion states generated from the first and second pump pass. However, here the path lengths L_s, L_i and L_p can

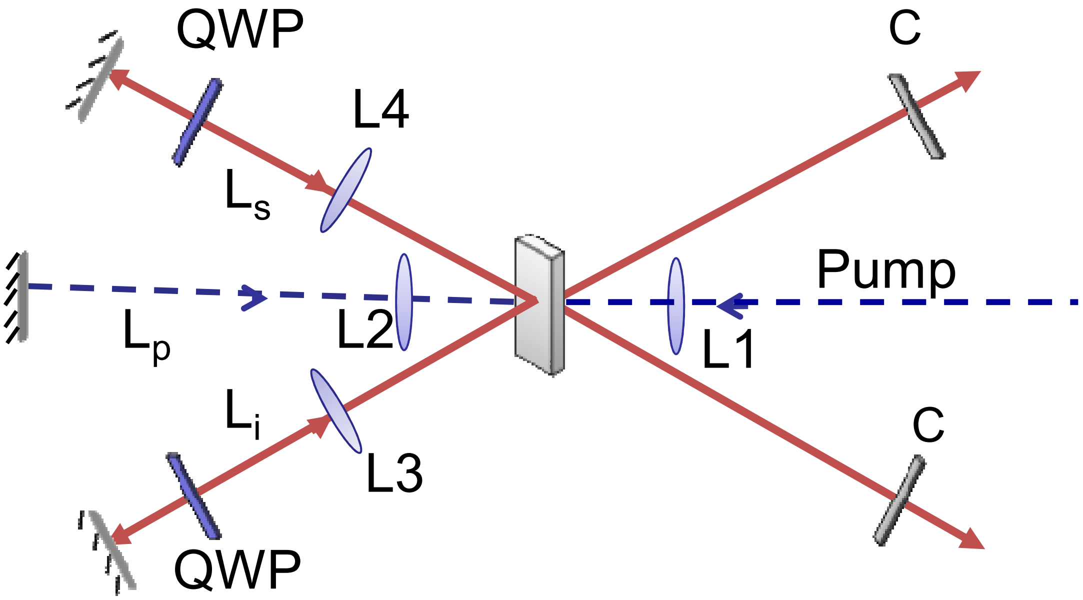

Figure 6-1: The rail cross arrangement to generate type-I polarization-entangled photons (after [79]). The first pass of a horizontally polarized pump produces the state $|VV\rangle_1$, where the subscript indicates the pump pass that generated the state. The pump is then retro-reflected back into the crystal and produces $|VV\rangle_2$. $|VV\rangle_1$ is also reflected back into the crystal and after doubling-passing through QWPs becomes $|HH\rangle_1$. The two downconversion paths are coherently superposed to produce the entangled state $|HH\rangle_1 + |VV\rangle_2$. The path lengths L_s, L_i, L_p are matched such that $|HH\rangle_1$ and $|VV\rangle_2$ exit the crystal at the same time. Compensators C in each downconversion arm compensate for the spatial (Poynting) walkoff. Lens L1 and L2 are used to optimally focus the pump for both the passes and are located one focal length away from the center of the crystal. Lens L3 and L4 are used to collimate and refocus back into the crystal the first pass downconversion modes, such that $|HH\rangle_1$ and $|VV\rangle_2$ can be optimally collected into single mode fibers. L3 and L4 are located one focal length away from the center of the crystal.

be matched[55] such that $\left|HH\right\rangle_1$ and $\left|VV\right\rangle_2$ are perfectly temporally compensated. The temporal walkoff can be split into three parts[56]: the walkoff Δt_1 of $\left|VV\right\rangle_1$ relative to the pump during the first pass, the walkoff Δt_2 of $\left|HH\right\rangle_1$ relative to the pump after they are both reflected back into the crystal, and finally the walkoff Δt_3 of $\left|VV\right\rangle_2$ relative to $\left|HH\right\rangle_1$. The total temporal delay Δt can thus be written be written in terms of the crystal length *l*, the propagation times of the horizontally polarized pump t_H^p, and the vertically and horizontally polarized downconversion states, t_V^{dc} and t_H^{dc}, respectively, as

$$\Delta t_1 = t_H^p\left(l/2\right) - t_V^{dc}\left(l/2\right) \tag{6.1}$$

$$\Delta t_2 = t_H^p\left(l/2\right) - t_H^{dc}\left(l/2\right) \tag{6.2}$$

$$\Delta t_3 = t_V^{dc}\left(l/2\right) - t_H^{dc}\left(l/2\right) \tag{6.3}$$

Instead of tweaking L_s, L_i and L_p to control the temporal walkoff, another birefringent crystal could be used to compensate for this delay. Thus, spatial and temporal compensators can be designed using calculations similar to Section 3.3.2.

Additionally, *spatial walkoff*[57] (not to be confused with spatial-phase decoherence) needs to be accounted for in the engineered double-pass scheme[58]. Spatial walkoff, also referred to as the Poynting vector walkoff (discussed in Chapter 5), would result in only a partial spatial overlap of $\left|HH\right\rangle_1$ and $\left|VV\right\rangle_2$. The amount of spatial walkoff ρ can be given in terms of the optic axis cut angle θ , and extraordinary and ordinary index of refraction n_e and n_o, respectively, by [41]:

$$\rho = \theta - \arctan\left[\left(\frac{n_o}{n_e}\right)^2 \tan\theta\right]\operatorname{sgn}\left(n_0 - n_e\right). \tag{6.4}$$

---

[55] For example, a temporal delay of 100 fs corresponds to ~33 μm *path length* in free space.

[56] The downconversion photons are assumed to be born in the center of the crystal. See Section 3.3 for more details.

[57] In birefringent materials, for extraordinary beams, the Poynting vector and the phase-velocity are in different directions. This is referred to as spatial walkoff, Poynting vector walkoff or birefringent walkoff. Note that ordinary polarization does not experience spatial walkoff.

[58] Spatial walkoff becomes significant in the engineered crystals mostly because of the pump beam waist optimization requirement. For 0.6-mm crystals, the optimized pump beam waist is ~45 μm. Spatial walkoff would have complicated the two-crystal scheme in the Migdall-collection-angle experiment discussed in Chapter 4 as well; however, because we had not yet optimized the pump beam waist, the experiment was not sensitive to spatial walkoff.

For an engineered crystal $\rho = 4.3°$ for the pump ($\rho = 4.1°$ for the downconversion) corresponding to a transverse walkoff of ~46 µm (~43 µm) in a 0.6-mm crystal. Figure 6-2a-b shows a simplified schematic of the spatial walkoff of the extraordinary beam for each pass. Birefringent compensators *C* that are

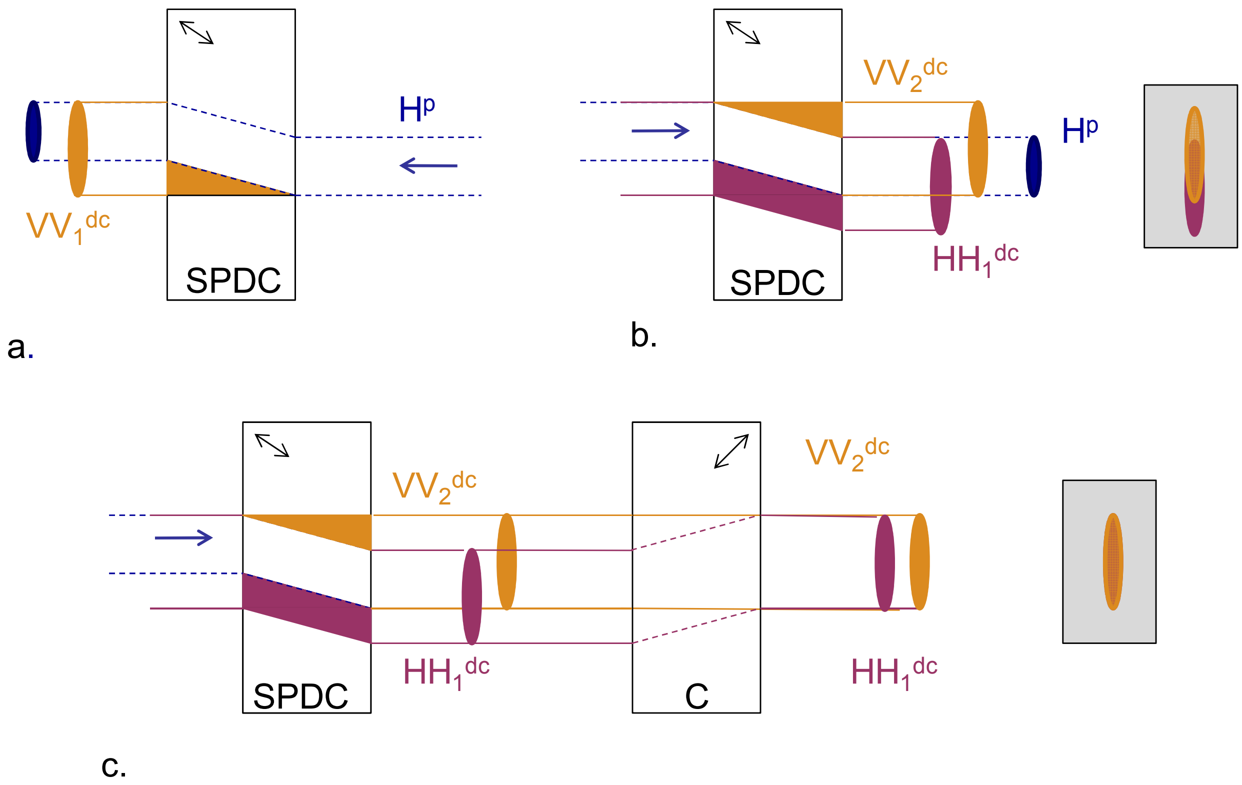

Figure 6-2: Poynting-vector walkoff and compensation in the rail cross arrangement. a. The extraordinary pump (blue) walks off during the first pass. The generated downconversion states $|VV\rangle_1$ (orange) are ordinary polarized and thus do not walk off; however, they are created along the entire length of the crystal, leading to an elliptical spot after the crystal. b. After reflection and rotation by the quarter-wave plates, the first-pass downconversion photons $|HH\rangle_1$ (purple) are extraordinary polarized and, consequently, now exhibit walk off along with the pump (although to a slightly lesser degree due to the different refractive indices at the longer wavelengths). The second-pass downconversion photons $|VV\rangle_2$ (orange), however, do not exhibit walkoff, though again they are elliptical spots after the crystal. Thus, there is only a partial spatial overlap (~50% for 0.6-mm GVM SPDC crystals). c. The Poynting-vector walkoff can be compensated using a birefringent element *C* identical to the SDPC crystal to reverse the $|HH\rangle_1$ and obtain complete spatial overlap[59]. The double-sided arrows (black) indicate the optic axis orientation in the SPDC and compensator crystals.

---

[59] We have neglected the fact that the downconversion amplitude is coherently enhanced as the beams propagate through the crystals (~stimulated downconversion), which may lead the output ellipses to have a non-uniform probability density (e.g., lower at the top and the bottom of the ellipse). This effect would affect the calculated overlap somewhat.

identical to the SPDC crystal[60], placed in each of the second-pass downconversion arms (Figure 6-2c) completely compensate for the spatial walkoff that otherwise results in partial spatial-mode overlap between $\left|HH\right\rangle_1$ and $\left|VV\right\rangle_2$ (~50% for the 0.6-mm engineered crystals). The spatial walkoff compensators can be easily designed using Eqn. 6.4. Note that the temporal walkoff in the compensators have to be accounted for and can be compensated by adjusting the appropriate path lengths [61].

The second main effect, the directional dependence of the downconversion polarization – the Migdall effect – *ceases to be a problem* when we employ the rail cross arrangement for polarization entanglement. At the chosen wavelengths $405\text{ nm}\rightarrow 810\text{ nm}+810\text{ nm}$ the large 16° downconversion cone emission angle is still required for group-velocity matching in the engineered (BBO) crystal a. However, since the downconversion occurs only in one crystal and always with the same polarization, e.g., $\left|H\right\rangle \rightarrow \left|VV\right\rangle$, the azimuthal collection angles can be chosen such that the downconversion polarization is perpendicular to that of the pump in the lab frame, i.e., we can always collect at the 90° and 270° points on the emission cone (Section 4.2). Thus, we do not need to collect at unconventional angles in order to overcome the Migdall effect

There is also no need for the third requirement, birefringent focusing. The engineering scheme calls for optimizing the pump beam waist. However, because the pump is always the same polarization in both the passes, birefringent focusing is unnecessary. The pump can be focused at the center of the crystal, for *both* passes, using a simple combination of two lenses, as shown in Figure 6-1. Lens L1 focuses the pump at the center of the crystal during the first pass. Lens L2 collimates the beam on its first pass. The mirror reflects the pump back through L2, which now focuses the pump back at the center of the crystal. Similarly, birefringent collection is no longer needed. Lens L3 and L4 (Figure 6-1) are used to collimate the first pass downconversion modes and, upon reflection by their respective mirrors, refocus them back into the crystal. L1, L2, L3 and L4 are all located one focal length away from the center of the crystal. The downconversion photons, in spite of the different polarizations, can be optimally collected by simple lenses in each arm because both $\left|HH\right\rangle_1$ and $\left|VV\right\rangle_2$ originate in the same crystal. Thus, the rail cross arrangement appears superior to the two-crystal scheme for engineering indistinguishable photons, specifically because it eliminates two of the three main challenges. Temporal compensation is still needed, but can be easily employed in the rail cross scheme without any additional compensators. Admittedly, there are known challenges with the rail-cross arrangement that are not present with the two-

---

[60] The compensation crystals are chosen to be identical to the SPDC for convenience. A number of other choices exist by making a tradeoff between optic-axis angle and thickness.

[61] Collection using single-mode fibers obviates the need for any *spatial-phase* compensators (although they can be designed using the methods of Section 3.3) which would otherwise be required for free-space collection.

crystal scheme, the biggest being the need for interferometric stability. Thus, although there might be new, unexpected challenges that complicate the rail cross arrangement, it promises to be a viable route to engineering an ideal indistinguishable source for OQIP.

6.2 **The Typical Filtered-Focused Source**

At the outset of our source research, we compared the engineered group-velocity matched crystal (~16° external emission angles) to the typically filtered TF SPDC source (~3°emission angles) and found a 500-fold brightness enhancement (see Section 2.2). However, apart from having matched group velocities, three key phasematching parameters – pump bandwidth, pump beam focus (and the associated downconversion collection mode radius), and crystal length – need to be optimized. A broad pump bandwidth, beyond a certain threshold, is required to minimize the spectral correlations. Similarly, a focused pump beam minimizes spatial correlations. Thus, during the course of the source development, in order to isolate the benefits arising from optimizing *only* the pump focus (and because of the various challenges that resulted from the large-angle group-velocity matched crystal), we decided to compare the engineered crystal to a TF source *but with the pump beam focus similar to the engineered case* – the TFF source. Table 6-1, a part reproduction of Table 2-3, compares the engineered with the TFF source, highlighting the parameters that resulted in the three challenges discussed in Chapters 3-5. Note that in spite of the two-fold brightness increase in the TFF source, we continued to pursue the engineered crystal for the indistinguishable source because of possibly higher *heralding* efficiencies (discussed in Section 2.3.3), which might be obtained by fixing the intra-photon chirp (e.g., see Figures 2.14-2.15). However, in light of the complications arising from the large emission angle, here we briefly revisit the TFF crystal as a possible contender for engineering the indistinguishable source.

First and foremost, note that as a result of the smaller emission angles, the Migdall effect is much smaller in the TFF crystal. Additionally, the secondary problems associated with the larger emission angles, such as larger spatial-phase decoherence and temporal walkoff, extreme sensitivity to compensation, greater spatial walkoff, etc., become less severe. Temporal compensation is still required. However, for the engineered crystal the extremely large bandwidth (~29 nm) might limit the source fidelity (as shown in Figure 3-3) because of significant higher order effects, such as pulse broadening from dispersion, even when the compensation crystals are of the same material as the downconversion crystals. On the other hand, such higher order effects are minimized for the smaller ~10.5-nm pump bandwidth employed in the TFF; experimentally, the smaller bandwidth is also much easier to work with. Lastly, note that birefringent focusing/collection is still required for the TFF source in the case of the two-crystal scheme. For easy comparison, the crystal length of the TFF is not optimized. The smaller emission angles should allow for longer crystals (when employing single-mode fiber collection the optimized crystal length is determined partly by the overlap of the fiber collection modes inside the crystal), thereby resulting in an additional brightness improvement. Longer crystals also require a shorter pump bandwidth. Thus, the TFF source has room for further optimization (see [81] for a similar discussion).

SPDC Parameter/ Source	**Engineered**	**TFF**
Crystal length L	300 μm	300 μm
Internal downconversion emission angle $\theta_s = \theta_i$	**9.96°**	**2°**
Crystal cut angle θ_{pm}	40.7°	29.3°
405-nm pump bandwidth $\Delta\lambda_{pump}$	**28.8 nm**	**10.5 nm**
Energy per pump pulse	1.25x 10^{-11} J	1.25x 10^{-11} J
Pump beam waist w_0 **at the center of the crystal**	**23.15 μm**	**23.15 μm**
Fiber collection mode radius w_f	**21.46 μm**	**11.36 μm**
Spectral filter bandwidth	None used	17.5 nm
Source Purity $Tr\left(\rho_s^2\right)$	0.96	0.96
Source Brightness N	4x10^{-5}	8x10^{-5}
Heralding efficiency	?	53%

Table 6-1: Comparison of the engineered source to the TFF source.

In summary, we have discussed four possible methods to engineer the indistinguishable source: two brighter SPDC sources – the group-velocity matched engineered crystal or the typical filtered focused crystal – in combination with two schemes for generating polarization entanglement – the two-crystal or the interferometric rail-cross arrangement. The deciding factors for the best route to the indistinguishable source are heralding efficiencies, and the tradeoff between the various experimental challenges analyzed here, including temporal/spatial decoherence, emission-angle dependence of the downconversion polarization, optimized focusing/collection and spatial walkoff. Currently, the engineered group-velocity matched crystals employed in a rail-cross arrangement appears to the most promising option (given that the heralding efficiencies might be drastically better than the typical focused crystal once the intra-photon chirp has been eliminated). However, the optimization of a typical SPDC source using the approach presented here might be limited (either fundamentally or because of experimental challenges), in which case other engineering options, such as crystal superlattices [82] or four-wave mixing in micro-structured fibers [29], could be pursued.

Detector Nemesis - The Rise of Efficiencies

Mission Maximize overall detection efficiency of photon-number resolving detectors to >90%

Avatars

VLPC - Visible Light Photon Counter

SSPM - Solid State Photo Multiplier

Attributes

VLPC	SSPM
λ: 380 – 780 nm	λ: 0.38– 1; 2- 20 μm
~95 % inferred efficiency [1]	~95 % inferred efficiency [2]
Photon-number resolution	Photon-number resolution

The Story

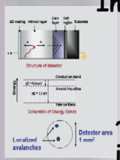

Intrinsic silicon with lightly doped Arsenic (As) gain region

~2% sensitivity to infra-red photons requires 6K operation

Rewards

Loophole-free test of Bells' inequality

Scalable optical quantum computation

Evil Photon Diva

The Enemy

The Diva steals the signal photons for herself...
and tosses fake IR photons to throw you off!

Boards

Choose between different cryo measurement systems !

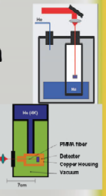

Level 1: Coupling Fibers

Your goal is to minimize background and losses in the coupling fibers.

Battle:

- Blackbody radiation
- Fresnel Reflection
- Attenuation

Level 2: Detector Surface

Vanquish the loss at very surface of the detectors.

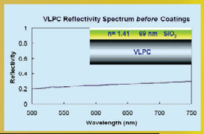

Level 3: Electronics

You have come this far - but now get ready for the Big Boss.

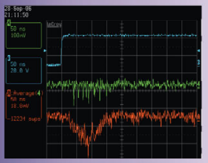

Conquer the land of low-noise ultrafast electronics and free the high-efficieny photon-number resolving detectors !

Good Cryo-queen

The Queen

Helps you battle IR imposters

Brave photon seeker - Goku

Play the game now!

Chapter 7
Building Single-Photon Detection Systems

"The human brain is a differential amplifier."

- Also from the never-to-be released self-help series, Life Lessons from a Science Lab.

The holy grail of photodetection would be a highly efficient photon-number resolving detector that is fast, accurate, easily available and affordable. The ultimate goal of our detector development project is to achieve as many of these desired features as possible using VLPCs and SSPMs. Both these solid-state detectors feature photon-number resolving (PNR) capability and high *intrinsic* quantum efficiency (>95%) but their actual measured efficiencies were limited to <88% due to in-coupling losses [32-35]. Thus, our primary goal is to develop a detection system optimized for *overall* detection efficiency and low-error PNR. Unfortunately, VLPCs and SSPMs are currently *not* off-the-shelf products– the VLPC chips need to be custom fabricated[62]. A new fabrication run would cost ~$100,000, but would provide more than enough detectors for the entire OQIP community. However, even if one had access to readily available chips, extensive system development (as shown in this chapter) is required in order to make them usable. Hence, our second goal is to develop a robust plug-and-play system that would significantly reduce the resources (currently averaging at one full-time graduate student for several years) required to use VLPCs. Here, we discuss the development of a photodetection system that would provide four of the six features of the ultimate photodetector – high-efficiency, PNR, low-error probability and high-speed – and might eventually become easily available as well (at least for the OQIP community).

VLPCs and SSPMs operate optimally at ~7K and produce a very small ultrafast electrical pulse (~150 μV in 1 ns), presenting non-trivial cryogenic, electronic and optical considerations. To develop an optimized detection system, we improve several factors that can degrade detector performance: in-coupling optical fibers losses, reflection losses at the detector surface, infrared background radiation, cryogenic behavior of the detection system, and finally, electronic noise and ultrafast-pulse recognition. In this chapter, we consider each of these issues in turn, after discussing the basic detector operating mechanism.

---

[62] To the best of our knowledge, the VLPCs are currently made by only one company – DRS Technologies, Inc. Our current supply of VLPCs, supplied by Fermilab, are "rejects" (where the mode of failure is unknown and can range from suboptimal operation to complete nonfunctionality). The SSPMs were originally developed by Rockwell, Inc around 1987 (and eventually redesigned as the VLPCs); it is unlikely that any more SSPMs will be produced.

7.1 Detector Operation Principle

The desirable VLPC and SSPM properties arise from their unique gain mechanism. In contrast to conventional APDs, which rely on excitations between valence and conduction bands, these detectors utilize impact-ionization of impurity atoms as the gain mechanism to amplify carriers generated by a single-photon absorption event. Both detectors have an intrinsic silicon layer and a lightly doped arsenic gain layer (the impurity region), as shown in Figure 7-1a-b. The device structure in VLPCs is optimized for operation in the visible spectrum (thicker undoped absorption layer), while the SSPMs are sensitive from the visible to beyond 20 μm (thicker doped gain layer). Figure 7-1c shows the energy band diagram of the arsenic-doped gain region. Since the impurities require only ~50 meV to be ionized, the devices must be cryogenically cooled to ~7 K in order to prevent thermal excitations of these atoms. At these operating temperatures, the electrons from the As impurity atoms are frozen out, and the device behaves as an insulator. An electron-hole pair is generated when a photon is absorbed. Due to the applied field (the bias voltage), the electron drifts toward the surface while the hole drifts toward the gain region. The electric field decreases deep in the gain region and the hole slows down, but has enough kinetic energy to impact-ionize an As atom. The released electron in the conduction band drifts towards the surface, impact-ionizing more As atoms to create an avalanche. The electrons generated in this process (~30,000) are quickly swept to the surface, generating an external current pulse in the timescale <1 ns. The avalanche process leaves ionized As impurities which relax through a much slower (~1 μs) hopping conduction mechanism. The local region cannot support another avalanche event until the impurity-band holes fully relax (~ 3.5 ms). This disparity in time constants for electrons and impurity-band holes plays a critical role in the noise properties of this detector. The positive space charge, left behind as the avalanche grows, slows down the avalanche, leading to a well-defined avalanche size and thus very low multiplication noise (the variance in the number of electrons released per avalanche). Each avalanche is localized to a filament that is typically much smaller (~ 4 μm) than the device diameter (~ 1mm), leaving the rest of the device open for detection (Figure 7-1d). Further, only one initial carrier (the hole) triggers an avalanche in these devices, resulting again in low multiplication noise. Thus, for incident photon fluxes below ~30 per pulse, the output signal amplitude is directly proportional to the number of photons absorbed (in contrast with standard APDs, which produce a single avalanche irrespective of the number of incident photons), enabling PNR capability. The excess noise factor (ENF), a measure of multiplication noise[63], of these devices is <1.03, near the theoretical limit of 1. APDs and PMTs have a lowest achievable ENF of 2 and 1.2, respectively. The theoretical maximum of the number of resolved photons is given by $N_{\max} = (ENF - 1)^{-1}$, limiting $N_{\max}$ for APDs, PMTs, and VLPCs/SSPMs to 2, 5, and 30, respectively [83]. Note that the probability of the initial hole (generated when the photon is absorbed) impact-ionizing the first electron critically affects the QE of the device.

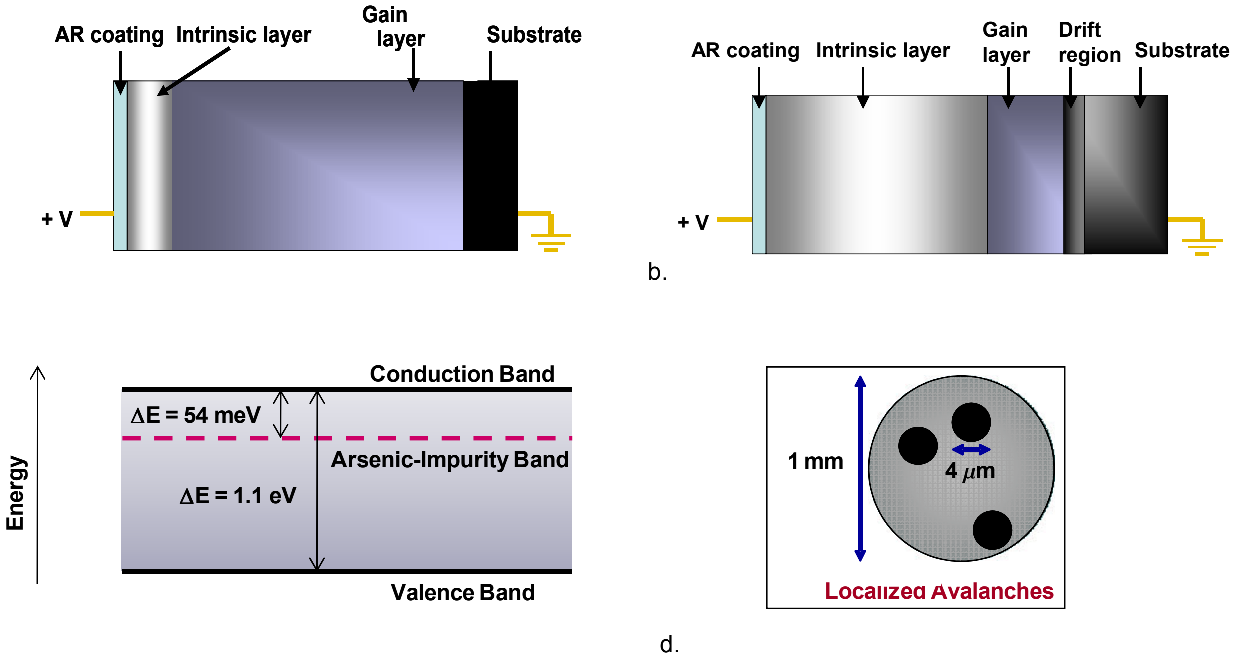

Figure 7-1: **a**. SSPM device structure **b**. VLPC device structure. **c**. Energy band diagram of the gain region for both SSPMs and VLPCs. **d**. Detector top view, showing localized one-photon avalanches relative to the entire active area (not to scale).

7.2 Coupling Fiber Optimization

Background and loss are the two main issues we encounter while trying to couple the photons of interest. Spurious background is an especially serious issue – even the VLPCs are ~2% sensitive to infrared (IR) radiation up to ~28 µm; the SSPMs peak in their sensitivity at ~500 nm and ~ 24 µm (QE estimated > 90%) and have a minimum ~ 1 µm. Based on the device geometry, roughly 10^{14} room-

---

[63] $ENF \equiv \frac{\langle M^2 \rangle}{\langle M \rangle^2}$ where M describes the number of carriers generated as result of the multiplication gain. Note that the theoretical limit $ENF = 1$ can be achieved in an ideal noise-free avalanche mechanism, where every photon absorption event results in exactly M carriers.

temperature photons would strike an unblocked detector surface every second. Given that the detectors saturate at ~10 MHz[64], severe background filtering is required; moreover, any filter has to be very cold to inhibit its intrinsic blackbody radiation emission. For this purpose, we use polymethyl methacrylate (PMMA) optical fibers (or blocks) that have very high attenuation above ~750 nm. Regardless, it can be quite difficult to cool PMMA; contributing factors include geometrical issues limiting thermal conduction, the vacuum in the cryostat's sample space (if applicable), and the remarkable insulating properties of the PMMA itself.

The second issue, loss in the optical fibers, is less daunting. The fibers have undesirable absorption and reflection losses at the detection wavelengths. Typical loss due to Fresnel reflections at each fiber interface is 4%. Anti-reflection (AR) coatings for the two fiber ends have to be optimized at different temperatures (300K and 6K). We have had our fibers custom-coated[65], measuring <1% reflection at 710 nm at both temperatures, and verified that the coatings withstand thermal cycling[66]. The typical attenuation at 710 nm for PMMA fibers is ~0.9 dB/m. Figure 7-2 shows the measured spectral response of a 1.8-mm PMMA fiber, which has a ~96% transmission at 710 nm; sources of loss could include imperfect fiber-ends (e.g., due to suboptimal polishing), or reflection losses greater than the estimated 4% Fresnel loss. Hence, transmission losses still remain but depend on the actual setup being used (discussed in Section 7.4), due to the differing fiber lengths. In order to keep transmission above 90% (95%) [99%], one must keep the PMMA fiber length below 50 cm (24 cm) [4.8 cm].

The attenuation in typical glass fibers is extremely low (~ 0.006 dB/m); however, glass does not offer any of the required infrared filtering. While most of the fiber-coupled results presented here, uses 1-mm diameter PMMA fibers, we also tested two novel approaches to filter the infrared background. The first uses a regular glass fiber that is single mode at 1550 nm to efficiently transmit in the visible spectrum while simultaneously blocking most of the IR photons. The expected number of modes at any wavelength λ for a given core diameter of the fiber D can be given by

---

[64] We can estimate the device saturation rate by treating the VLPCs as a detector with ~x "pixels", where x = detector area (=0.79 mm^2)/avalanche area (=12 μm^2) = 65,800, and each recovers in ~ 3.5 ms. Such a rough calculation gives a saturation rate of ~18 MHz.

[65] AR-coating plastic fibers require a special low-temperature process, not typically offered at most optical coating companies. Our fibers were coated by Evaporated Coatings Inc (ECI) using ECI process #6468EP, which incorporates Electron Beam, Ion Assist.

[66] Our tests for thermal cycling typically consists of first slowly cooling the test piece to ~ 77K (using liquid nitrogen) and slowly warming it back up to room temperature; this process is then repeated at least 15 times. Most thermal cycling effects typically begin to occur by 10th cycle. Also, the majority of thermal contraction typically occurs by 100 K; thus, testing at 77 K suffices in most cases. In some cases, the thermal stability at and cycling to 4 K is also tested. For AR coatings, the reflectivity was measured at room temperature, at 4 K and monitored during the entire cycling process.

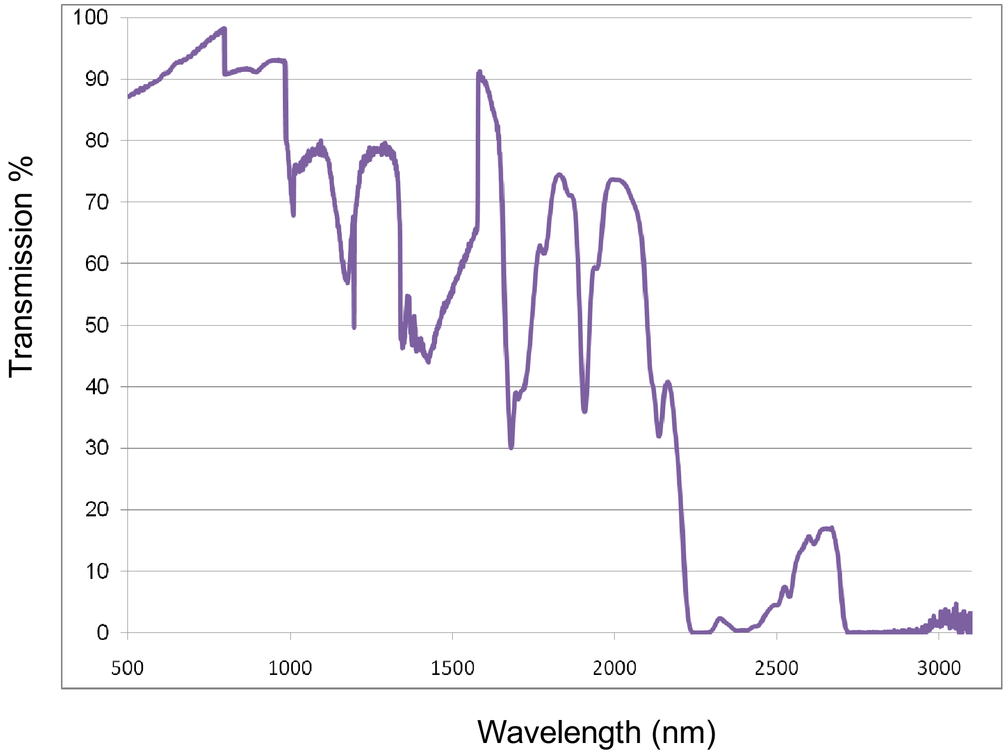

Figure 7-2: Measured transmission as a function of wavelength for a 1.8-mm PMMA fiber[67] after subtracting the theoretically calculated Fresnel reflection loss.

$$N_m = 0.5\frac{\pi D^2}{\lambda^2}\left(n_f^2 - n_c^2\right), \qquad 6.5$$

where n_f refractive index of the fiber core and n_c is refractive index of the fiber cladding; less than 6 modes for wavelengths above 2000 nm is expected when using a 1550 nm single-mode fiber. We have been able to successfully couple 94 ± 1.5 % of 676-nm multimode fiber-coupled light into a 1550-nm optical fiber, limited only by reflection losses. Preliminary tests indicate the results to be cryogenically stable for jacketed off-the-shelf 1550-nm fiber. The second approach couples a low-loss multimode glass fiber (to maximize transmission efficiency) with a minimal length of plastic fiber (to filter IR photons). We have fabricated a glass-plastic couple using Devcon 5-minute epoxy, found to be mechanically stable at cryogenic temperatures. Optically, we found the coupling to be limited by reflection losses. Although the glass-plastic method seems promising, proper fabrication of these is an acquired skill[68]; with better designing and further cryogenic testing, these might be a viable option.

---

[67] This measurement was performed by Onur Hosten.

[68] We use heat-shrink tubing for mechanical stability between the glass and plastic fibers while applying the epoxy. Extreme care must be taken to not get any epoxy or heat-shrink tubing on the fiber ends, to keep the fiber

The glass multimode and single-mode fibers have another inherent advantage; blackbody contributions should be reduced somewhat by using such narrower fibers, which have a smaller surface area. Table 7.1 shows the expected decrease in blackbody emission as the fiber diameter is reduced. A five-orders of magnitude decrease in the background counts can be expected by simply incorporating 1550-nm single-mode fibers. Note that these simplified calculations assume that the fibers are not cooled (i.e., they are at room temperature) and also neglect any spectral filtering inherent to the plastic or single-mode fibers. Both these effects are expected to decrease the blackbody estimates.

Type of Fiber	**Fiber Diameter**	**Expected blackbody counts Hz**
PMMA	1 mm	$\sim 10^{14}$
PMMA	0.5 mm	$\sim 10^{12}$
Glass Multimode	64 μm	$\sim 10^{11}$
Glass 1550 nm Single-mode	10 μm	$\sim 10^{9}$

Table 7-1: Expected blackbody contributions as a function of fiber diameter.

Some of the cryogenic setups require optical-fiber vacuum feedthroughs. There are two main ways to implement this. The first, quick and easy method is recommended for initial tests when the optical fibers and the vacuum-compatible part housing the feedthrough (e.g., aluminum cryostat windows) are easily replaceable. Here we drill holes in the housing that are just big enough to fit the fibers. The fibers are carefully fed through the drilled holes. Then the feedthrough can be made vacuum safe (tested up to 10^{-6} mbar) by using Devcon 5-minute epoxy (recommended only if the temperature at the feedthrough exceeds ~100 K) or Stycast (while Stycast works well at cryogenic and room temperatures, the effort involved might not be justified unless the operating temperature is <100 K) on both sides of the housing around the drilled holes and the fed-through fibers. A glimpse into the dark art of epoxy perfection can be gleaned from [84] and [85][69]. The second method, recommended for more permanent and professional-quality vacuum feedthroughs, is replace the metal ferrule in a standard Swagelok connector with machined Teflon, as discussed in [86].

---

ends fixed during the entire fabrication process and to not melt the plastic fiber while heating the heat-shrink tubing. Also, note that index-matching fluids freeze at cryogenic temperatures, making them useless for our purposes. Thus, ultimately both the glass and plastic fibers must be AR coated.

[69] Note that not all 5-minute epoxies are created equal – Devcon 5 Minute® epoxy (Stock#8040-00-264-6816:#8040-01-067-6126) is cryogenically stable to thermal cycling than most others that were tested.

7.3 **Detector Reflectivity**

Due to the high refractive index of silicon, the Fresnel reflection at the detector surface is about 30%. High-reflectivity spherical refocusing mirrors have been used in the past to mitigate this issue [33], but losses due to secondary reflection at the detector surface can still be quite high. Thus, AR-coatings for the detectors are essential. However, due to the limited availability of these detectors, AR-coating at the desired wavelength is not always an option during fabrication. Our VLPCs came with a 69-nm layer of silicon dioxide (SiO_2), resulting in ~23% reflection at 710 nm. We custom re-coated our VLPCs, using in-house fabrication facilities, to optimize the detector performance at 710 nm. Because removing the existing SiO_2 layer using wet etching techniques could damage the detector surface, we chose to add an additional multilayer AR-coating on top of the existing SiO_2 layer. An additional 250 nm of SiO_2 followed by 89 nm of silicon nitride (Si_3N_4), both deposited by plasma-enhanced chemical vapor deposition (PECVD), resulted in $< 0.5\%$ total reflection at the design wavelength of 710 nm. Figure 7-3 shows the structure and the measured reflectivity spectrum of the VLPCs before and after the in-house coatings. More details on AR coating the VLPCs, including programs for modeling the coatings, can be found in Appendix C. Using such techniques, both the SSPMs and VLPCs can be optimized for high-efficiency single-photon detection at any wavelength within the sensitivity range of the detectors.

Unfortunately, these in-house coatings were observed to peel after repeated thermal cycling (after ~ 7 cycles), due to the quality of optical coatings obtained via typical processes such as PECVD and thermal evaporation; in particular, these processes tend introduce strain into the coating, which increases the likelihood of de-adhesion under temperature-induced expansion and contraction. This can be solved by using a stress-free coating process, such as reactive low-voltage ion plating RLVIP [87][70] . To test the cryogenic stability of such coatings, we (slowly) cool the coated detectors to ~ 4 K (by dunking them in a liquid Helium Dewar) and (slowly) warm them back up to room temperature; this process is then repeated at least 15 times. The room temperature reflectivity is measured at the beginning and end of each thermal cycle; additionally, a high-resolution magnified image of the detector surface is obtained for comparison between thermal cycles. We found no discernable pulling or performance degradation after 20 cycles. Ideally, optimal AR coatings would be directly incorporated during fabrication.

---

[70] Note that thermal evaporated do not result in cryogenically-stable AR coatings. Unfortunately, RLVIP is not currently offered at most vendors. We used INO, located in Quebec, Canada for our RLVIP coatings.

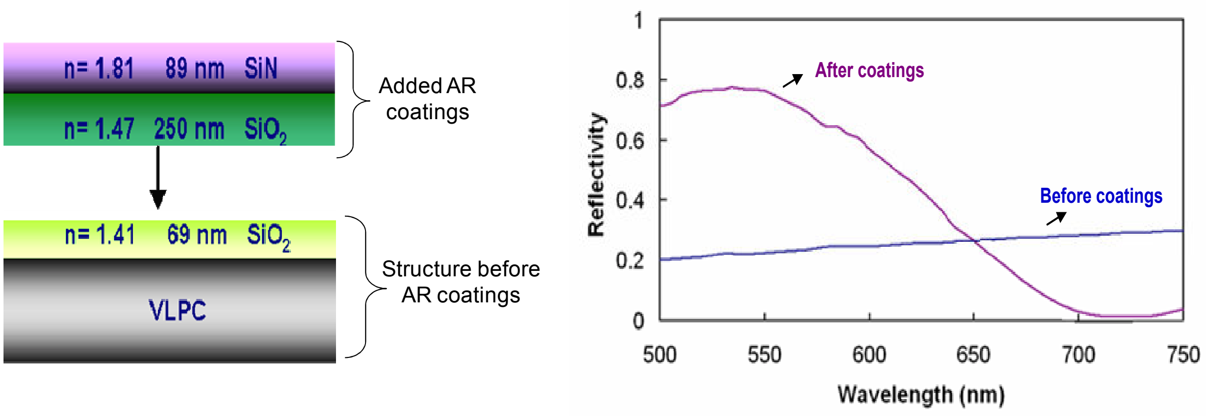

a. b.

Figure 7-3: **a**. Structure of VLPCs as supplied, and with the added AR coatings. Here *n* is the refractive index of the layer. **b**. Measured reflectivity spectrum of VLPCs before and after applying custom in-house AR-coatings optimized for 710 nm.

7.4 Measurement Systems

Despite the small sensitivity (~2%) of a VLPC to IR photons, a large number of thermal photons in this range can still cause huge dark counts. The suppression of these dark counts is a critical aspect of developing a VLPC system. Over the course of this research, we have developed and worked with four cryostats – some designed and built from the scratch – for free-space and fiber-coupled operation. While building any cryogenic measurement system, the materials chosen and component design need to be based on their cryogenic behavior such as heat transfer, thermal contraction and heat capacity[71]. Each system, presented here in chronological order, has its characteristic pros and cons that inspired the design of the next version. Our very first system, cryostat 1, shown in Figure 7-4a, consists of a short-dunking probe in a custom dual-neck Dewar. The Dewar is based on a previously used single-neck design [32], modified so that liquid helium can be conveniently refilled, using the second Dewar opening, without disrupting device operation. The detectors, mounted at the end of a 22.5-cm long dunking probe, are suspended above the liquid helium in cold helium vapor; their operating temperature can be grossly controlled by adjusting their distance relative to the liquid helium, and finely controlled via slightly heating the detectors. Incoming light is coupled in via ~23-cm long 1-mm diameter optical PMMA fibers. The dual-neck Dewar setup possses at least two attractive features: vapor cooling and minimal liquid-helium consumption. However, there are three main disadvantages: the Dewar requires considerable setup times (resulting from the need to pre-cool the thermally-insulating vapor jacket), difficulty in maintaining

---

[71] For an excellent reference for designing and building cryogenic measurement systems, see [85] .

a constant device temperature[72], the dunking-probe design precludes any free-space measurements (needed to decouple fiber effects[73]), and most importantly, the ~23-cm long optical fibers have an associated intrinsic ~4% transmission loss.

To reduce the fiber-transmission loss, we developed the second cryogenic setup (cryostat 2 shown in Figure 7-4b) in which the detectors sit in a copper sample holder at the end of the cold finger of an optical constant-flow cryostat[74] (Janis ST-100). Optical windows facilitate easy free-space coupling. Light can also be directly coupled in via vacuum optical-fiber feedthroughs. The resulting shorter fibers (~ 6 cm) reduce the transmission loss to < 1% while still retaining excellent filtering of the IR photons (transmission is < -4 dB/mm for wavelengths >1 μm), facilitating a net in-coupling efficiency > 97% (at 710 nm, assuming AR-coated fibers and detectors). Although it had several benefits, including both fiber-coupled and free-space configurations, and served as the initial test bed for detectors, this cryostat was ultimately limited by its low cooling power. The detectors, optical fibers, and wires were suspended in vacuum and could be cooled only by direct thermal contact with the cold finger. Moreover, the temperature of the cold finger varies along its length (it is coldest (~4K) at the bottom where liquid-helium collects), thereby drastically limiting the available cooling power of the cryostat.

To combine the benefits of the first two designs, namely vapor cooling and short optical-fiber design switchable to free-space, we briefly investigated a third cryostat design: the Janis STVP-100 (cryostat 3), a sample-in-vapor version of the constant-flow optical cryostat STP-100. The STVP-100, shown in Figure 7-4c, vaporized liquid helium collected at the bottom of the cryostat, thereby releasing cold helium vapors that cooled the sample space. The sample space was thermally isolated by a vacuum shroud between the room-temperature cryostat walls, and a radiation shield (with a small optical window for in-coupling light). Unfortunately, we encountered two major hurdles with the STVP-100 system – fiber coupling required *two* replaceable vacuum optical-fiber feedthroughs (one at the cryostat outside wall and one at

---

[72] As the liquid helium vaporizes, the distance between the probe and the liquid-helium level increases, and therefore the temperature of the detectors in the probe rises. The probe then needs to be moved closer to the liquid helium to recover the original colder temperature. In retrospect, a constant liquid-helium flow version of this cryostat (where instead of using the second neck for intermittent refilling of helium, we maintain a constant influx of helium) would provide a much more stable thermal operation. However, this being our very first cryostat, we had not yet acquired a thorough insight of cryogenic systems. Thus, while this appeared to be an issue (albeit minor), it is indeed very much solvable.

[73] For example, previously observed optical degradation of the fibers was attributed to thermal cycling [32].

[74] The sample is in vacuum and cooling occurs solely through conduction via thermal grease. Hence, cooling to 6K in this setup was a challenge, solved by designing a sample holder to maximize surface area and by reducing the heat load through the electronic wires. Cooling in the dual-neck system occurs via cold He vapor, so neither sample- nor fiber-cooling is an issue, whereas fiber transmission losses are.

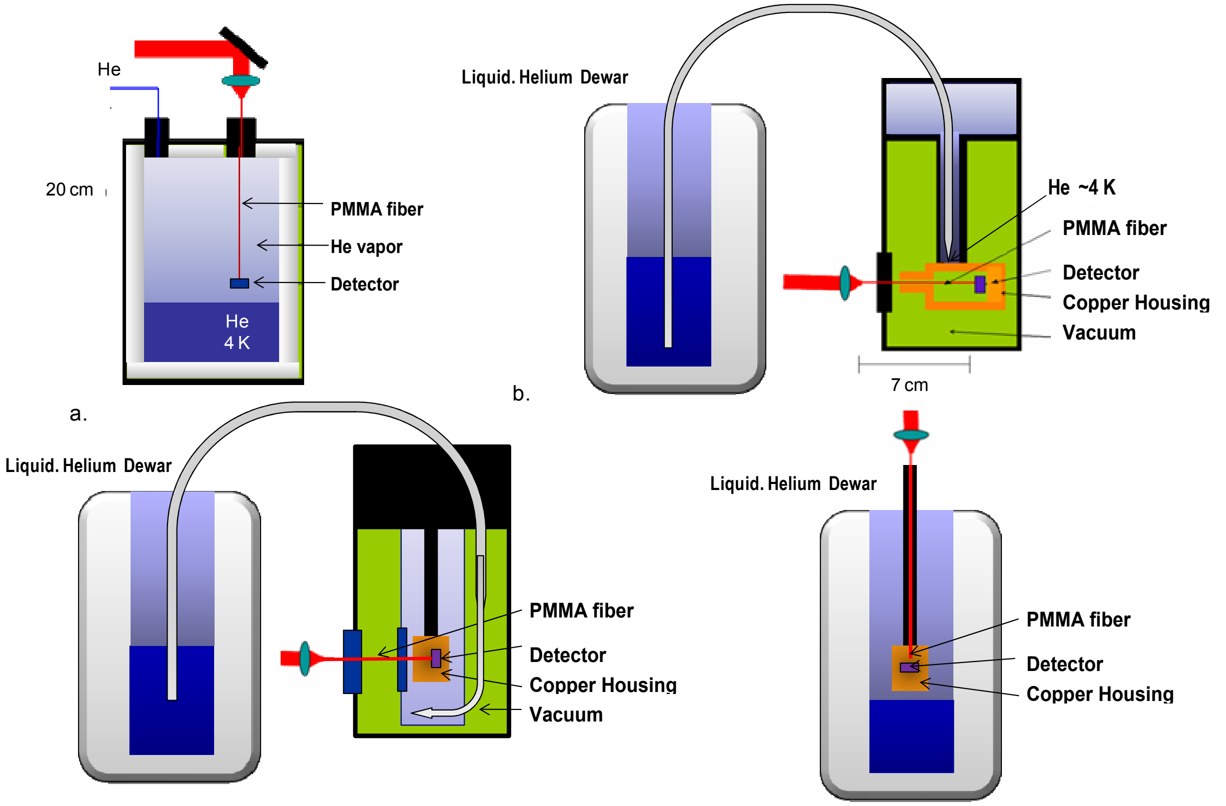

Figure 7-4: **a**. Cryostat 1: a dual-neck Dewar in which light is coupled into the detectors via one input and helium is filled via the other, obviating the need to temperature cycle the detector (it is believed that temperature cycling of the PMMA coupling fiber resulted in damage, reducing the transmission by ~10% [33, 36]). **b**. Cryostat 2: a constant-flow cryostat with the sample in vacuum (Janis STP 100). The detectors are attached to the sample holder at the end of the cold finger. Focused light goes through a cold PMMA block mounted in front of the detectors or is coupled in through optical PMMA fibers via a vacuum feedthrough in the cryostat window. **c**. Cryostat 3: a constant-flow cryostat with the sample in vapor (Janis STVP 100). The detectors are attached to the sample holder, which is cooled from the bottom by helium vapors. Light is coupled in through optical fibers via vacuum feedthroughs in the cryostat and radiation -shield windows. **d**. Cryostat 4: a dunking-probe immersed in a liquid-helium storage Dewar. The detectors are attached to the sample holder at the end of the dunking probe. Light is coupled in via optical fibers.

the radiation shield), and the detector layout prevented accurate measurement of the detector temperature[75]. Experimentally, the detector dark counts turned out to be much higher than in the sample-

---

[75] Given the strong cooling power of the helium vapors, the temperature sensor has to not only be at the same height and position as the detectors but should also be exposed to same vapor flux. The temperature sensor needs to be thermally *anchored* to the sample for an ideal temperature measurement, which, given that the only accessible side of the detector is its detecting side for VLPCs and SSPMs, is prohibitively hard. As a side note, an accurate measurement of the detector temperature, which is optimal for convenience and completeness sake, is not always a *necessity*. In almost all of the VLPC and SSPM measurements (in ours as well as other groups), a rough measurement of the operating temperature facilitated by a temperature sensor placed as close as possible indicates

in-vapor version (indicating that the detectors were not cold enough [76]), even when the STVP-100 was operating at full cooling power and the detectors were completely covered.

Motivated to have at least one system with complete thermal control and minimal thermal effects, we designed our fourth cryostat: a fiber-based long dunking-probe designed to be simply inserted into a typical ~60-l liquid-helium storage Dewar. The ease of operation, low cost, low background, complete design control (compared to the store-bought Janis cryostats), and temperature stability are superior to the other designs. The main disadvantage in this system is that ~120-cm long fibers are required. The corresponding transmission losses here could be minimized by using narrower multimode glass fibers or the glass-plastic hybrid fiber as mentioned previously (Section 7.2).

Out of the four developed systems, the free-space version of cryostat 2 (Figure 7-4b) and the dunking-probe of cryostat 4 (Figure 7-4c) have thus far yielded the best performance. As mentioned above, they both have characteristic pros and cons, which we take advantage of to directly study the effects of several interdependent factors. Thus, most of the results presented here are based on one of these two cryostats.

7.5 **Read-out Electronics**

The electronic characteristics of the device output pulse can lead to further complications. A single-photon detection event results in only a ~150-mV pulse, even after 60 dB of external amplification. Moreover, the pulse is ultra-short, with a full-width at half-maximum (FWHM) of only ~1.5 ns (after a 300-MHz amplifier). Thus, the system is therefore very sensitive to electrical noise. Most of our setups are designed to use the VLPCs in their original ceramic packaging, which uses patterned gold pads that are wire-bonded to a particular detector on a chip containing eight detectors. Electrical contacts to these gold pads are made via springy "pogo" pins (Everett Charles Tech A-S-R)[77]. Coaxial cables are ideal to minimize pick-up noise; however, care must be taken to minimize heat load in low-cooling-power

---

that the device is within operating range. The optimal temperature for a particular system can be fine-tuned based on operating characteristics such as dark counts and efficiency. Since the temperature measurements are completely determined by the design of sample holder and the thermodynamics of the particular cryostat, the optimal operating temperatures do not always agree between different systems, i.e., optimal temperature of cryostat 2 is 8 K while for cryostat 1 it is 7 K; the optimal desired temperature setting must therefore be individually determined at least once for each system.

[76] Cooling the detectors further would have required a complete redesign of the sample holder and the in-coupling fibers – the detectors would have to be closer to the vaporizer , thereby not only requiring longer fibers but also a novel fiber-holder design given the space constraints of the cryostat and the minimum bending radius of the fibers.

[77] Most materials lose their springiness at cryogenic temperatures and/or with thermal cycling; an exception is beryllium copper. The Everett Charles pogo pins were chosen especially because both their plunger and the spring are made from beryllium copper, ensuring even contact resistance at all temperatures over several uses. Out of all the different materials and parts we have experimented with in the entire setup, these pins are one of the few components that were found to be insensitive to thermal cycling and other cryogenic effects.

cryostats such as the cryostat 2. In this regard, we found mini-conformable coax cables to be the best choice. Specifically, the Belden 1674A with a nominal diameter of 1.19 mm and outer tin-coated copper

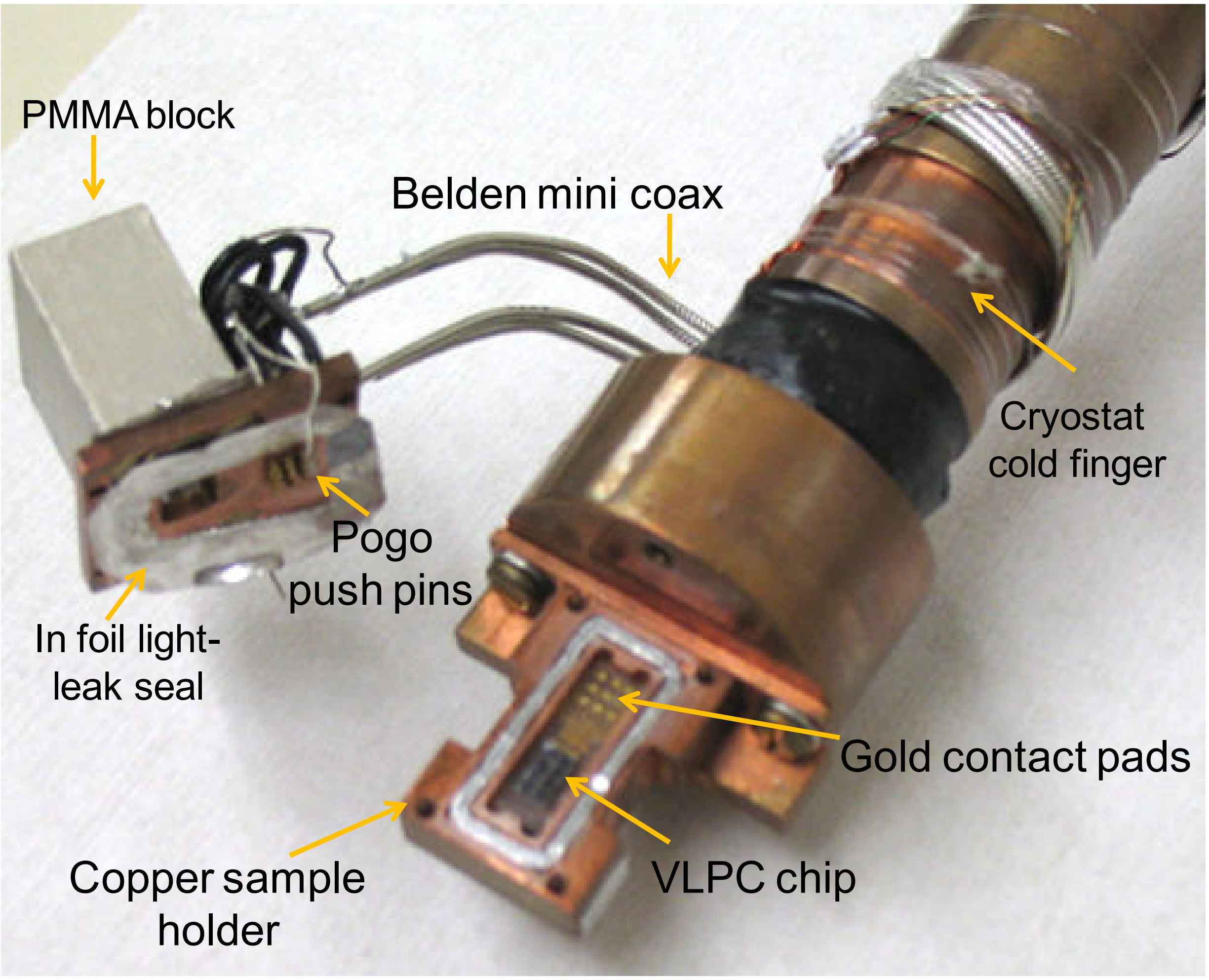

Figure 7-5: Photograph showing a close-up view of the VLPC sample holder and connecting wires in the free-space setup of the constant-flow-cryostat. The sample holder design for the other cryostats is based on this design as well. The top piece containing the PMMA block is mechanically screwed into the base sample holder containing the VLPCs. An indium-foil seal is used to prevent any stray background light from entering into copper sample holder.

conductor had suitable electrical (i.e., good shielding) and thermal properties (minimal heat load and possibility of conductive cooling of the outer conductor braid). However, the Belden 1672A is not an ideal initial choice for setups requiring much longer transmission lines, e.g., the dunking probe setup in cryostat 4, because of its high attenuation (~1.25dB/m)[78]. Therefore, for the long dunking probe in

---

[78] Alternatively, one could use the coax cable with a cryogenic preamplifier.

cryostat 4, we use a twisted pair of phosphor bronze cryogenic wires[79]; these are unfortunately slightly more sensitive to pick-up noise than the coaxial cables.

The cryostats themselves provide an additional layer of electronic shielding – they are electrically grounded[80] and therefore act as Faraday cages. However, this does not help shield against any pick-up noise coupled into the system through the temperature-sensor wires present both inside and outside the cryostat. By far, the best solution we found for this problem is to use commercially available noise-filter adapters on the temperature sensor and heater connections. For custom-built cryostats, we recommend standard D-sub connectors for the temperature sensor wires, especially because of the variety and availability of quite effective D-Sub filters (e.g, the 243A100y0X Conec filter used in cryostat 4). For the typical military connectors prevalent in off-the-shelf optical cryostats, such as cryostats 2-3, finding typical commercial filter adapters can be extremely challenging. An excellent alternative is to use silicone filter inserts (EESeal) that are made to retrofit into most connectors[81].

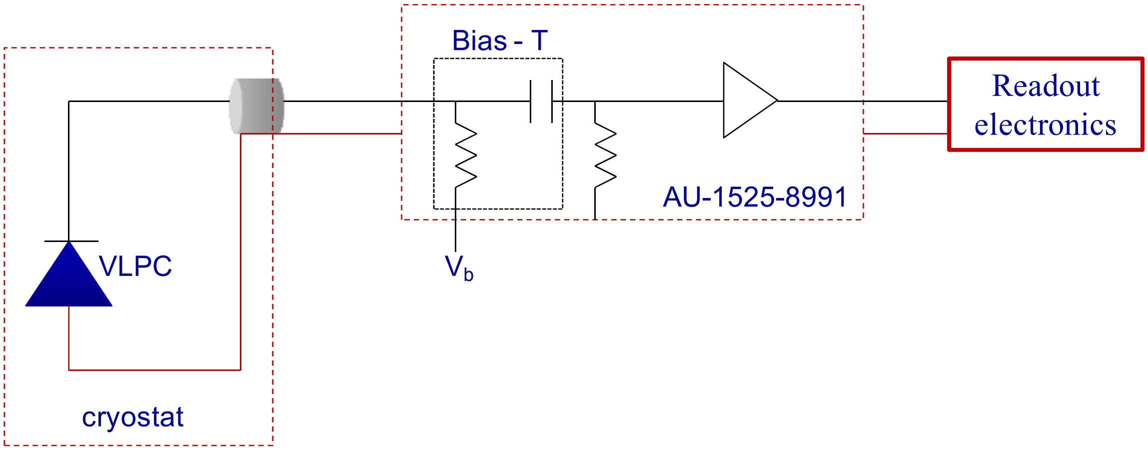

Figure 7-6: Schematics of VLPC connections. Ground connections are shown in red.

---

[79] Not surprisingly, a twisted pair's susceptibility to electromagnetic interference drastically depends on the twisting staying intact during installation. As a result, twisted-pair cables usually have stringent requirements for maximum pulling tension as well as minimum bend radius. Thus, for sensitive setups like ours we strongly recommend buying pre-twisted pairs (e.g., Duo-Twist from Lakeshore) as opposed to constructing one by twisting two wires together. Also, note that when nearby pairs have equal twist rates, the same conductors of the different pairs may repeatedly lie next to each other, partially undoing the benefits of common-mode noise suppresion. For this reason we suggest using pairs with different twist rates if possible.

[80] Grounding is an extremely important issue when it comes to detector setups. *Ground loops*, often created by poor design or installation, are a major cause of noise and interference. Thus, any equipment or conductor (including optical tables and transfer lines) that makes electrical contact with the ground must do so only because it is intentionally designed to be the ground. Along the same lines, all equipment must be connected to the same power socket, usually facilitated via power strips. Different power sockets, even if in the same room, can be connected to different earth grounds, leading to voltage fluctuations exceeding 200 mV.

[81] EESeal silicone filters are also available for D-sub connectors, but currently they are ten times more expensive (~$150) than the standard D-sub filter adapter.

Amplifier noise can significantly affect PNR by effectively decreasing the ENF and, hence, low-noise high-gain amplifiers are required. We have tested several low-noise room-temperature amplifiers and, thus far, found the Miteq Au-1525-8891, with a gain of ~60 dB and a noise figure of ~1 dB, to be the most suitable for our application,. Figure 7-6 shows a schematic of the electrical connections to the detector housed inside a cryostat. In this configuration, designed for use with the in-built bias "T"[82] on the AU-1525-8991, the bias pad on the detector packaging is grounded and a positive bias[83] is applied to the signal pad.

To reduce the noise further, we could incorporate cryogenic preamplifiers to enhance the signal before it travels through lossy cables. Cryogenic preamplifiers must be chosen with care; not only do they need to have low noise but they cannot be silicon based (silicon carriers freeze out around 40K), which the majority of commercially available ones are. GaAs amplifiers, however, can be used at very low temperatures. Unfortunately, nearly all commercially available low-noise GaAs amplifiers are designed at high frequencies with narrow bandwidths common in wireless applications. For instance, the Agilent MGA-81563 is a low-noise amplifier offering 14 dB of gain at frequencies between 0.9 and 6 GHz. We have tested a preamplifier circuit, developed by Agilent[84], that lowers the operating frequency range and expands the bandwidth of the MGA-81563, which could be incorporated in future designs. More details on the cryogenic preamplifier, including circuit design, can be found in Appendix C.

Once the external noise has been suppressed (<~80 mV) and the detectors are cooled to ~7 K, they can be biased for operation. Figure 7-7 shows the oscilloscope trace of a one-photon detection event from a VLPC biased at 7 V at 7 K. This 150-mV ultrafast pulse that only comes on when the detectors are biased above a certain temperature-dependent threshold voltage (~5 V) signifies a working detection system, which can then be characterized in detail and optimized for performance. The next chapter discusses the operational behavior of VLPCs, including efficiency and PNR measurements, in great detail.

---

[82] The bias "T" allows the detector to be biased via the signal line. Its purpose here is two-fold: 1. It reduces the number of wires entering the cryostat, thereby reducing the number of noise sources. 2. It is an excellent AC noise-filter for the bias voltage. We highly recommend this configuration for its noise-minimizing characteristics and easy setup.

[83] Note that the detectors must be reverse-biased, which can be accomplished by applying either a negative voltage to the bias pad relative to the grounded signal (detector) pad, or by grounding the bias pad and applying a positive voltage to the detector.

[84] The circuit is based on Agilent design tip # G0004, titled "Extending the Low Frequency Response of the MGA-81563 and MGA-82563 RFIC Amplifiers", authored by Bob Myers. It can be found at: http://avagotech.kr/docs/Design_Tip_G004.

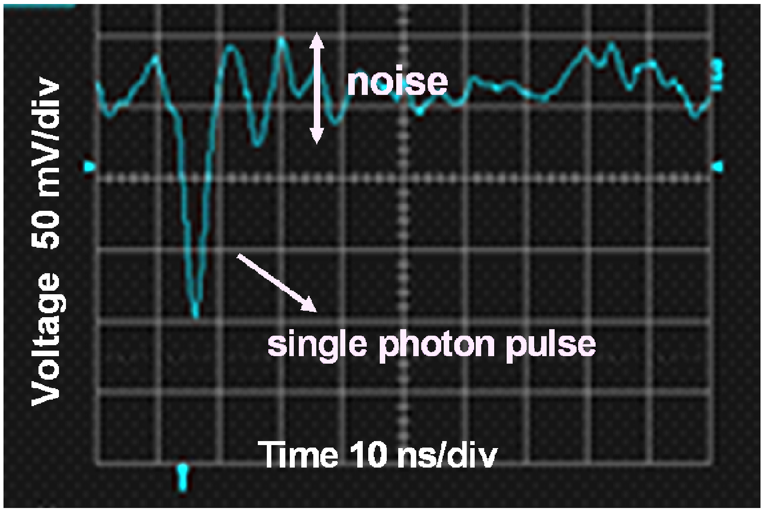

Figure 7-7: Oscilloscope trace of a single-photon detection event from a VLPC at 7 K, biased at 7 V (cf. Figure 7-6).

Chapter 8
Detector Characterization

It's not what you look at that matters, it's what you see.
-Henry David Thoreau

The VLPCs are estimated to have an intrinsic QE of 95% ± 5% (at 694 nm [33]), but the highest observed *overall* detection efficiency is only 88% ± 5%. The SSPMs also have a very high inferred intrinsic QE, 96% ± 3% (at 660 nm [32-33]), but again the measured overall detection efficiency has been limited to ~86% ± 5% . Moreover, both the detectors have demonstrated PNR – the VLPCs have been shown to distinguish >5 incident photons [83, 88]. Further, theoretically they can resolve up to 30 photons (limited only by their very low ENF). In fact, when compared with every other type of single-photon detectors, only the superconducting transition-edge sensors (TES) surpass VLPCs and SSPMs in measured QE (95% ± 2% at 1556 nm) and PNR capability (up to 7 photons) [89]. However, not only do the TES require a sophisticated cryogenic system because of their ~100 mK operating temperate (compare to ~7 K, achievable with a simple helium Dewar, for VLPCs) but also have a ~800-ns recovery time (VLPCs effectively have zero dead time[85]), and suffer from a ~100-ns timing jitter[86] (compared to ~250 ps for VLPCs). Superconducting nanowire detectors have extremely low timing jitter <30 ps, but thus far their QE < 25% [91]. Detector dead times inherently limit detector speeds, and timing jitter directly affects the time-correlated single-photon measurements, as well as more general optical quantum logic gates. Thus, VLPCs and SSPMs offer truly exciting possibilities for OQIP by enabling high clock-rate quantum communication protocols, high-efficiency PNR for metrology, e.g., with "NOON" states [92], and opportunities for never-before possible tests of quantum mechanics, e.g., a truly loophole-free test of Bell's inequalities (discussed in Section 9.3).

In spite of their extremely high QE, the actual measured efficiencies of these detectors were limited to <88% due to losses in the coupling optics, dominated by the reflection losses at the detector surface itself, suboptimal fiber coupling of the input photons into the device, and likely transmission losses in the

---

[85] VLPCs can be considered to have a zero dead time because a single photon detection "consumes" ~ a 4-μm diameter of the detector surface (1-mm diameter) during the avalanche process (see Section 7.1), leaving 99.9% of the detector operational for another photon detection. However, it is possible for the second photon to hit the first ~4-μm region; it takes ~3.5 ms for the initial avalanche area to recover [90].

[86] Timing jitter is the uncertainty in the response time of the detector (measured from when the photon hits the detector to the output of the electronic signal).

(plastic) fibers themselves. The previous chapter discussed the interdependent cryogenic, optical, and ultra-fast electronic challenges one has to solve to operate these detectors, as well as the improvements to the light-detector coupling and the readout electronics for complete optimization of the extremely high efficiency and PNR capability of VLPCs. In this chapter, with the low-noise electronics, noise-shielding and stable cryogenic operation in place, we discuss the characterization, current status and limitations of both (QE and PNR) crucial measurements.

8.1 **Efficiency Measurements**

We use the free-space version of the vacuum constant-flow cryostat system to characterize the QE of VLPCs. Light from a 635-nm laser diode was attenuated with neutral density filters and directly focused onto the VLPC from outside the cryostat through a glass window and a cold PMMA block (the center of which is at ~40 K). For a given average power P of the diode laser measured after the focusing lens, the number of incident photons per second can be estimated per second as

$$N_{in} = \frac{\alpha P \lambda}{ch}, \qquad 8.1$$

where λ is the wavelength, c is the speed of light, h is Plank's constant, and α is the net transmission of the system, obtained by multiplying the individual transmission of all neutral density filters[87]; this is the rate of photons incident outside the cryostat. The detectors display intrinsic noise – "dark counts" – caused by thermal excitations, which are indistinguishable from the actual single-photon counts. The total detection efficiency ε can then be calculated from the number of pulses N_{pulses} at the output of the amplifier as

$$\varepsilon = \frac{N_{pulses} - N_d}{N_{in}} \qquad 8.2$$

The dark counts N_d increase nearly exponentially with bias voltage while the intrinsic quantum efficiency also increases with bias voltage. Hence, there occurs a natural trade-off resulting in an optimum bias voltage at a given temperature (within the operational range 6-10 K), at which the highest efficiency can be achieved. Figure 8-1 shows the overall (from source to detector) efficiency at 635 nm as a function of the applied bias voltage at several different temperatures. As the temperature is decreased,

---

[87] Note that stacked reflective neutral density filters can result in measuring higher-than-actual efficiencies because of multiple reflections between the stacks. In this regard, absorptive neutral density filters are better. Additionally, the filters could be tilted to completely avoid the effects of reflective beams; in this case, care must be taken to measure the attenuation at that orientation for accurate results.

the peak of the quantum efficiency curve shifts to the right (higher bias). This is because the device (particularly the gain layer) acts like a series resistor, with increasing resistance for lower temperatures, thereby reducing the effective voltage seen in the gain layer. The highest overall detection efficiency of 56% was observed with a bias voltage of 6.8 V at 8 K. For a given temperature, as the bias voltage is increased, saturation effects begin to dominate, explaining the decrease in the system efficiency. Increasing the bias voltage beyond this point results in breakdown, where a huge current[88] begins to flow. Thus, both temperature and voltage have to be optimized to obtain the best detector performance. Note that for these measurements, the coupling optics are not optimized. We can estimate the intrinsic QE of the detectors by accounting for the optical losses still present in the system. The transmission through the optical cryostat windows and the PMMA block was measured to be only ~ 79.6%, which includes the reflection losses at all four surfaces. Fresnel reflections alone account for ~4% losses at each of the two surfaces of the cryostat glass window and another 4% loss at the front and back surfaces of the PMMA block. These could be greatly reduced using AR coatings. For the relatively short thickness of the PMMA block (1.8 mm), the intrinsic bulk transmission is above 97%. The detector surface itself has a ~22% reflection loss at 654 nm (discussed Section 7.3). Thus, the inferred intrinsic peak efficiency for the detectors is 90.2 ± 6%[89]. Additionally, the spot size of the beam at the detector needs to be optimized[90]. By incorporating our optimized AR coated detectors and coupling optics, we therefore anticipate actual detection efficiencies in excess of 90%.

We also characterized the operation of the detectors in the dunking probe system in cryostat 4 (Section 7.4) – with a Nd-Yag laser at 532 nm, pulsed at 40,000 Hz, and attenuated to the single-photon level. Detection efficiency measurements yield an overall efficiency of 18% at 7.2 V and 7 K. Most of the loss is currently due to poor coupling efficiency from the end of the fiber to the detector, which can be improved. Additionally, the fibers themselves represent a significant loss. To shield from room-temperature thermal photons, we use plastic (PMMA) fibers, which have very high attenuation in the

---

[88] Breakdown mode signifies the direct tunneling of electrons from the bound As impurity atoms, which initiate avalanches, causing a huge current to flow through the device. During operation, once breakdown is observed we recommend lowering the voltage such that the device is turned off. Measurements can then be resumed starting at a lower voltage.

[89] Power measurements were made using Newport 1936-C power meter combined with a 818 detector head, which together had ~4% uncertainty. There was an additional ~1% uncertainty in the measurement of α.

[90] If the spot size is too big, then the photons in the tail of the transverse spatial mode miss the sensitive area of the detector. If the spot size is too small, then saturation effects begin to dominate and the observed counts starts to decrease. Note that saturation effects are a function of the input *intensity*; therefore, the spot size needs to be optimized for significant variations in the beam intensities. Saturation effects can be easily estimated by modeling the avalanche area as a ~4-μm diameter independent detector with a ~3.5 ms dead time. We find that the input intensities should be kept below ~25 Hz/μm^2 to avoid reducing the efficiency by more than 1%.

infrared. However, these 120-cm long fibers have a sizable attenuation, with a measured 85% transmission at our test wavelength of 532 nm, including an expected 4% reflectivity at each interface.

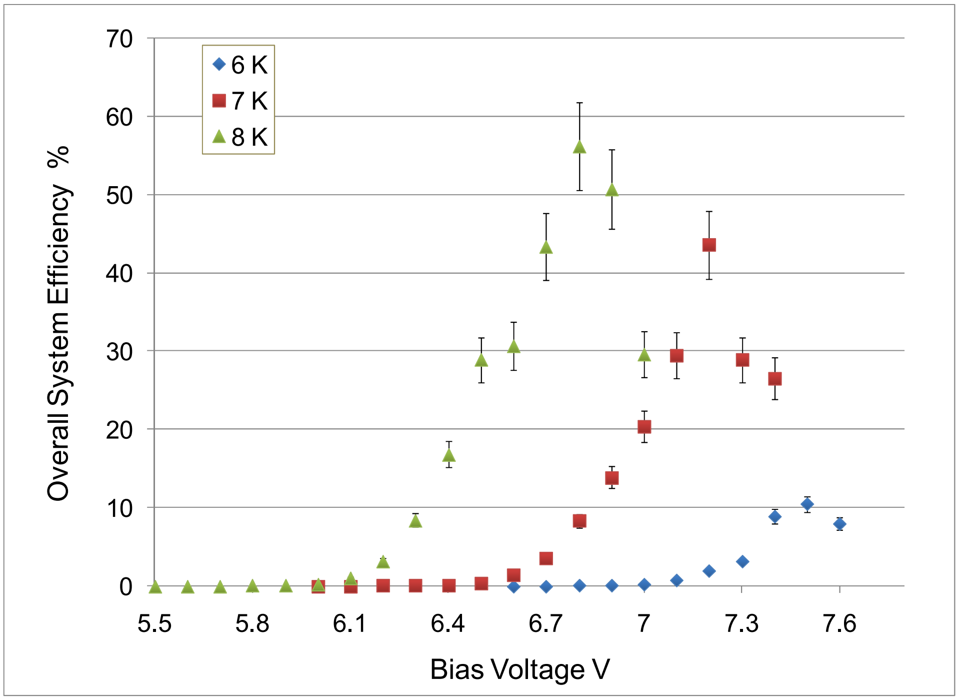

Figure 8-1: VLPC efficiency as a function of the bias voltage. Data taken at 6 K (blue diamonds), 7 K (red squares) and 8 K (red squares) with the free-space version of the constant-flow cryostat 2.

8.2 PNR Measurements[91]

VLPCs facilitate PNR because the output pulse heights are proportional to the input incident photon number (for up to ~30 photons). Therefore, one of the key requirements is the ability to perform a pulse height analysis on the ultrafast small-amplitude pulses from the VLPCs. Most commercially available electronics cannot resolve ultrafast (< 5 ns) pulses especially if the pulses are < 500 mV. Standard off-the shelf pulse analyzers (e.g., the Ortec Maestro MCA), cannot resolve shorter than ~50 ns pulses. Thus, we use a custom-built four-channel analyzer (FCA), which is a modified version of the FCA used in [88] to analyze fast pulses. A schematic of the custom FCA is shown in Figure 8-2. The circuit contains four digitally-controlled potentiometers which are used to set voltage thresholds with approximately 2-mV

---

[91] This work was done in collaboration with Kevin Zielnicki.

precision. A comparator circuit compares the pulse from the post-detector amplifiers to each threshold and triggers a digital logic (TTL[92]) output pulse on the appropriate channel. There is no output pulse if the input is below the first threshold, while a pulse on channel 1 indicates the pulse was between the first two thresholds, channel 2 between the second and third, and channel 3 between the third and fourth, with channel 4 representing a pulse higher than the fourth threshold.

The analyzer is primarily used in one of two modes. In the first mode, the voltage thresholds are set such that single-photon detections register on channel 1, two-photon events on channel 2, and so on. This is useful when the system is fully calibrated, but unfortunately the appropriate voltage thresholds can vary significantly with detector temperature and bias voltage. In the second mode, an automated program sets the thresholds at small regular intervals and slowly increments them, building up a histogram plot of counts relative to voltage level, used for analyzing pulse heights.

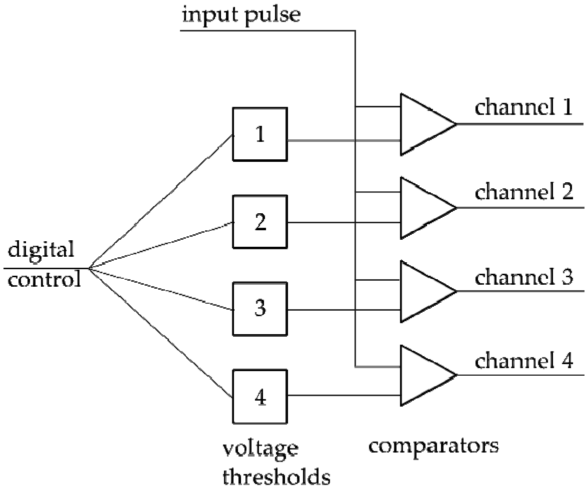

Figure 8-2: Rough schematic of four channel analyzer. Boxes 1-4 represent a circuit that uses a digital potentiometer to set a reference voltage. The comparator circuits check whether the input pulse exceeds the reference voltage levels and output a TTL pulse accordingly.

Figure 8-3a shows the oscilloscope trace of observed detector pulses showing one-and two-photon peaks[93]. The VLPCs register multiple photons as a single detection event, required for PNR, only when the photon arrival times of the photons are all well within the timing resolution of the device, i.e., the

---

[92] TTL, or a transistor-transistor logic pulse is archetypical of a certain class of digital circuits. TTL signals must meet an input/output voltage and current specification, and a rise/fall time specification (maximum ~50 ns). For any given hardware, the signal must also have a minimum pulse width (~5 -10 ns). The high (H) and low (L) output voltage and current specifications are: $V_L = 0.4$ V, $V_H = 2.4$ V, $I_L = 16$ mA, $I_H = 400$ μA.

[93] This data was taken using an attenuated 635-nm pulsed diode laser with optical pulse widths > 4 ns.

incident pulse width ideally should be << 1 ns. Thus, in order to characterize the PNR of these detectors, we use an attenuated frequency-doubled Nd-Yag laser at 532 nm, with an expected pulse width ~600 ps[94] and a repetition rate of ~40,000 Hz. The FCA is triggered using an electronic signal from the Nd-Yag to reduce dark counts by only allowing actual signals to be registered. Using such a source, we are able to detect 1-5 simultaneous photons as shown in Figure 8-3b. The pulse-height plot is constructed as follows: we select a narrow voltage bin using the FCA, and then count all input pulses that fall within that bin. A histogram of the pulse height distribution is then obtained by scanning the voltage bin over the desired voltage range. The bin size of the FCA is tunable and a small bin size enables us to obtain a high resolution image of the pulse height distribution (at the cost of longer data acquisition times), facilitating easy comparison with theoretical predictions of the characteristics of the distribution. The center of each peak in the distribution corresponds to the mean peak height of an n-photon detection event (n = 1,2,3…) for a laser pulse with a set average number of photons per pulse n_{avg}. The first peak at ~170 mV is the typical height of a pulse produced by a single photon (for a device with similar gain characteristics), the second peak at ~315 mV is the expected height for two simultaneous photons, and so on. The width of the peaks – i.e., the range of voltages – is determined by both the intrinsic noise of the VLPC and the electronic noise of the system. Figure 8-3b also shows a curve fit consisting of a sum of Gaussian peaks, constructed with all available theoretical constraints. The area of each peak is determined from a Poisson distribution with $n_{avg} = 2.8$. Ideally, the center of each peak would be located at an integer multiple of the first peak. However, the estimated ~600 ps duration of laser pulses is a sizable fraction of the ~1 ns VLPC pulse width. Therefore, when two photons arrive at the detector slightly offset in time, the resulting pulse is slightly shorter and broader than when they arrive simultaneously, causing peaks beyond the first to be at a lower voltage than originally expected. This effect is significant, reducing the second peak to 93% of its expected value. A calculation of this shift is included in the fit in Figure 8-3b. The program used to model this fit is shown in Appendix C.

---

[94] This is the pulse width before doubling, as specified in the Nd-Yag laser manual.

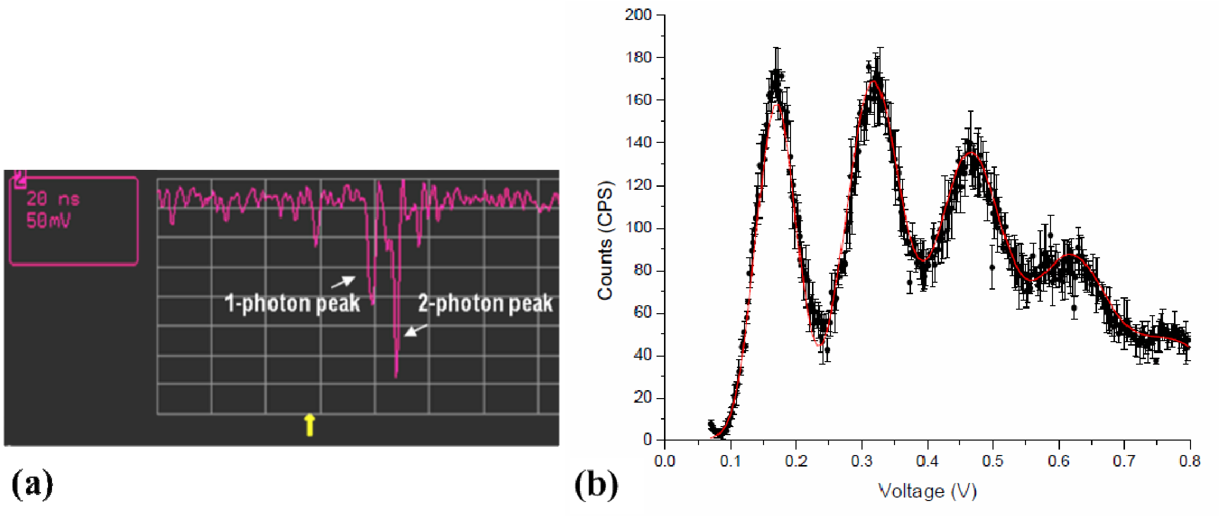

Figure 8-3: Observed detector pulses. (a) Oscilloscope trace showing 1-photon and 2-photon peaks. (b) Typical pulse height distribution plot showing multi-photon-detection, taken with the dunking probe setup of cryostat 4. The peaks correspond to laser pulses containing 1-5 detected photons.

8.3 Gain Variation[95]

The VLPCs we have been working with were supplied by Dr. Alan Bross of Fermilab. They were deemed to be “rejects” although the mode of failure was communicated to be complete failure of maximum two detectors on a chip of eight, which the remaining detectors operating normally. Unfortunately, in course of the past five years, we have learned that several of the developmental challenges we have been seeing are intrinsic to the devices we have been working with. In fact, one of the most profound discoveries made during the course of detector development is identification of the wide variation in the detector gain between devices. The external electronic noise in the system is fixed, so, any gain variation manifests as a spread in the signal-to-noise of the system, which makes it extremely hard to isolate the root cause thereof. Additionally, because the external ultrafast electronics are sensitive to pulse amplitudes and SNR, and because device characterization relies on multiple, interdependent variables, intrinsic gain variation resulted in significant difficulties and drastic inconsistencies, originally thought to arise from the instabilities in *our* system. Out of the ~25 reject VLPC chips we received (each with eight detectors), only three even work at all – with signal to noise ratios of 2.5:1, 1:5:1, and 1:5:1, respectively (all significantly lower than the devices which were studied in previous works by other groups). Since then, we have obtained another chip with 6 working detectors on them from Duke University; these have a 3:1 SNR. During our tests, we have found that the gain variation occurs mostly from chip to chip, i.e., individual devices on the chip do not exhibit significant gain variation. Since this discovery, DRS

---

[95] This work was done in collaboration with Kevin Zielnicki.

Technologies, the original manufacturer, has confirmed that gain variation is a significant problem in their first generation devices[96], of which our devices are examples of, and has been solved in their next generation[97]. To combat these problems, it might be necessary to fabricate an entirely new batch of devices.

8.4 Outlook

Despite the significant progress made in our development and understanding of the operation of VLPCs and SSPMs, limitations of the current systems leave much room for improvement on several fronts. We have observed intrinsic efficiencies and PNR consistent with previous measurements; however, stable operation of the detection systems is still currently a challenge, e.g., thermal cycling effects on any of the parts can give rise to electronic noise or high dark counts. Although most of the problems that arise can be isolated and fixed typically within ~ 2 days, overall the detectors have not yet been incorporated into a complete turn-key system and, in fact, require a specialist for device operation. Obtaining high gain devices that work would definitely help make the system less sensitive. Below, we discuss some other future areas of improvement for detector development.

Improved Ultrafast electronics: One of the difficulties with the custom-designed FCA we currently use for counting the fast pulses is that because of the varying characteristics of the comparators, the voltage thresholds have an error of about 10 mV, limiting the accuracy of data obtained. The FCA could instead be replaced with a fast integrator circuit similar to the one constructed by NIST[98], shown to be much more robust to pulse-amplitude fluctuations, thereby allowing superior photon-number resolution. An integrator would provide the pulse height of each detected pulse automatically, rather than requiring a histogram approach to determine the pulse-height distribution. This should lead to faster and more accurate processing of photon detection. However, note that the device developed at NIST was designed for considerably slower pulses. A similar device with the capability to handle our short pulses would need to be designed and constructed.

Closed-cycle cryostat: The cost of using liquid helium to cool the detectors to their operating temperature of around 7K quickly adds up. To overcome such rising costs, one could develop a single self-contained closed-cycle cryostat[99]. Unlike traditional cryostats, closed-cycle cryostats have a built-in compressor and do not require an external liquid helium Dewar to reach cryogenic temperatures. This

---

[96] Henry Hogue, private communication.

[97] There have been at least two generations of VLPCs thus far.

[98] http://physics.nist.gov/Divisions/Div844/FPGA/fpga.html (last accessed March 16, 2010).

[99] Likely vendors for the closed-cycle cryostat include Janis Research and Cryo Industries.Currently, a 4-K system costs roughly ~$55,000.

would have the advantage of being a self-contained system that in the long term would pay for itself by offsetting liquid helium costs.

Improvements requiring fabrication: Given that high-gain low-noise working devices are currently not very readily available, a new order of custom fabricated devices might be necessary. Apart from incorporating optimized AR coatings during the device fabrication, as discussed in Section 7.3, other features that could be improved are:

1. New low-noise small-area detectors - One challenge to obtaining accurate measurements with the VLPCs is the issue of dark counts. Dark counts are indistinguishable from true photon detection events, and thus skew photon detection results. Since the number of dark counts is proportional to the detector surface area, reducing the detector diameter by a factor of 10 should also reduce dark counts by a factor of 100. The dark count rate for the current 1-mm diameter detectors is around 10,000 counts per second (at ~7.2V, 7K), so by moving to 100-μm diameter detectors, we should be able to achieve a level of only 100 dark counts per second, comparable to current Si APDs. However, there is a limit to how small of a detector would be desirable. Since a photon detection temporarily "uses up" a certain region of the detector surface (estimated to be ~30 μm in diameter), if two incident photons arrive with too little spatial separation, they will not be registered as separate events. As shown in Figure 8-4, the associated loss relative to a 1-mm diameter detector is negligible for two simultaneous photons and acceptable for higher numbers of simultaneous photons. It should also be noted that the saturation point would also be reduced proportional to the area, due to the ~3-ms recovery time of an avalanched region [90]. Since the detectors currently saturate at around ~10^6 counts per second, these small-area detectors would limit detection events to ~10^4 counts per second.

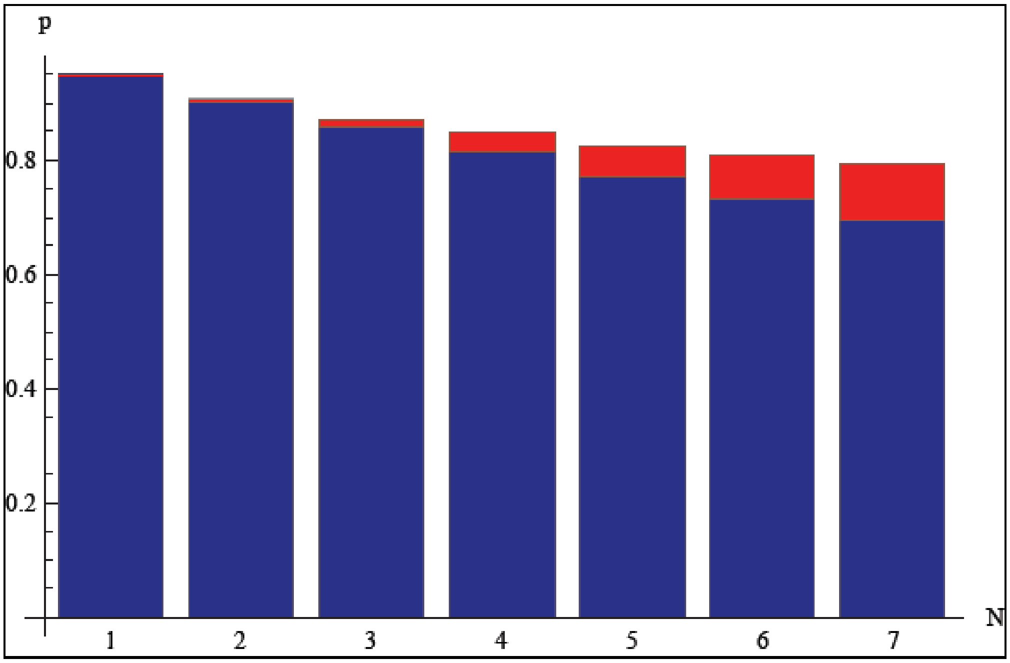

Figure 8-4: The calculated ideal probability of detecting N photons for a 100-micron diameter detector (blue) compared to 1 mm (red), assuming a 95% detection efficiency and a 12 μm^2 filament area (corresponding to a 4 μm diameter) .

Detector array: An additional advantage of smaller detectors is that it would be more practical to build a detector array consisting of a larger number of detectors. Currently, the VLPC detector arrays contain 8 detectors. By increasing this to 32 detectors, we would have a much more flexible system in a similarly sized package. This could open up the detectors to possible additional applications, such as spatially resolved detection. However, there are difficulties with having a large number of detectors as well. Each additional detector requires an additional wire—and for fiber-optic in-coupling, an additional fiber—to be run through the cryostat. For very large detector arrays, this could become cumbersome and impractical, but should be manageable for a 32-detector array.

In summary, VLPCs and SSPMs have extremely desirable characteristics for OQIP. They feature intrinsic efficiencies >90% and perhaps >95%, and have a low timing jitter of ~ 250 ps. Further, both detectors display photon-number resolving capabilities (theoretically limited to ~30 and experimentally seen up to 7 photons). They saturate around 10 MHz, require cryogenic 7 K operation and have dark counts ~10 kHz (at 7.2 V, 7K). As discussed in this thesis, we have in the course of these investigations started from the scratch and developed an expertise in building and operating VLPCs, and have laid the foundation for developing an extremely high-efficiency turn-key detector system. These high-efficiency photon-number resolving detectors are truly an enabling technology with applications in fundamental physics and scalable quantum information, such as a loophole-free test of Bells' inequality [38], single-photon sources [30, 92], quantum key distribution [93], quantum repeaters [94], optical quantum computing [1], and entangled-state metrology [31, 95]. In the next chapter, we highlight the advantages of such optimized detector as well as source technologies by explicitly discussing their role in two different OQIP protocols – teleportation and quantum fingerprinting.

Chapter 9

Improved Source and Detector Technology: Proposed Applications

I spy far far worlds with moons all rocky,
(and) when this piece 's all done –
you beam me up, Scotty!

There are laws we defied –
well, some were too shoddy,
once we rig this gear up –
you just beam me up, Scotty!

To a land …
Where we can
Fight the dark (and) save daring men
For all me and mine,
to see the white and light attain.

I long for these skies and for them I device,
A rig so techy –
so you could beam me up Scotty!
–Envisioned soundtrack to the teleportation experiment.

Indistinguishable photon-pair sources and high-efficiency PNR detectors can be easily incorporated into several OQIP applications to make them more scalable and efficient, to facilitate new protocols, and even to further fundamental studies. Here we exemplify the technological benefits of these improved sources and detectors via two quantum communications protocols – teleportation and fingerprinting. Combined, the optimized source and detector technologies signify a 10^5–fold brightness enhancement and a 50% efficiency increase for quantum teleportation and fingerprinting, making these communication protocols more scalable. Additionally, we propose a novel protocol, quantum hyper-fingerprinting, where one can communicate up to seven messages using one hyper-entangled [37] qubit. Finally, we outline their implications for fundamental studies by briefly discussing a long-awaited definitive test of quantum nonlocality – a 'loophole-free' test of Bell's inequality [38].

9.1 **Teleportation**

Not to be confused with its pop culture significance, "teleportation" [52]refers to an actual quantum communication protocol, involving the faithful transfer of unknown quantum states from a sender, Alice, to a distant receiver, Bob, who share an entangled state. Faithful quantum communication and distributed quantum computation protocols require the ability to perform high-fidelity quantum teleportation. However, the highest reported fidelity is only ~89%, with a four-fold coincidence rate of ~0.04 counts/second [3]. High teleportation fidelities are not only indicative of true non-locality, but are imperative for long distance quantum communication, currently limited to ~100 km in fibers due to the exponential decrease of the fidelity with channel length [93]. Further, quantum repeater and quantum relay protocols proposed to overcome these photon losses are also based on quantum teleportation. High coincidence counts mean faster protocols as well as practical scalability. Here, we discuss how incorporating the indistinguishable photon-pair source and the high-efficiency photon-number resolving detectors lead to efficient high-fidelity high-count-rate teleportation.

The Protocol: Figure 9-1 shows the schematics of the teleportation protocol [53], which works as follows. Alice and Bob initially share a maximally entangled 2-qubit *Bell* state. Alice has the photon 1 in the unknown to-be-teleported state, $\left|X\right\rangle_1 = \alpha\left|0\right\rangle_1 + \beta\left|1\right\rangle_1$[100]. Her other photon (2) is entangled with Bob's photon (3) together they are initially in the Bell state ψ^-_{23}. Thus, the initial state of the system can be give by

$$\left|\phi\right\rangle_{123} = \left|X\right\rangle_1 \left|\psi^-\right\rangle_{23} = \left(\alpha\left|0\right\rangle_1 + \beta\left|1\right\rangle_1\right)\left(\left(\left|0_2 1_3\right\rangle - \left|1_2 0_3\right\rangle\right)/\sqrt{2}\right) \quad , \qquad 9.1$$

which with some algebra can be written as:

$$\begin{aligned} = \frac{1}{2}\Big[& \left|\psi^-\right\rangle_{12}\left(-\alpha\left|0\right\rangle_3 - \beta\left|1\right\rangle_3\right) + \left|\psi^+\right\rangle_{12}\left(-\alpha\left|0\right\rangle_3 + \beta\left|1\right\rangle_3\right) \\ & + \left|\varphi^-\right\rangle_{12}\left(\alpha\left|1\right\rangle_3 + \beta\left|0\right\rangle_3\right) + \left|\varphi^+\right\rangle_{12}\left(\alpha\left|1\right\rangle_3 - \beta\left|0\right\rangle_3\right)\Big]. \end{aligned} \qquad 9.2$$

Next, Alice performs a joint measurement on photons 1 and 2, projecting them onto any of the four Bell states, $\varphi^{\pm} = \left(\left|00\right\rangle \pm \left|11\right\rangle\right)/\sqrt{2}$ and $\psi^{\pm} = \left(\left|01\right\rangle \pm \left|10\right\rangle\right)/\sqrt{2}$. Such a projection of an arbitrary two-photon state onto the Bell basis (consisting of the four Bell states) is called a Bell-state measurement (BSM).

---

[100] Here, the qubits are presented in terms of their generalized basis states $\left|0\right\rangle$ and $\left|1\right\rangle$ to broaden our scope; we have thus far referred to them via a polarization encoding, i.e., $\left|0\right\rangle \leftrightarrow \left|H\right\rangle ; \left|1\right\rangle \leftrightarrow \left|V\right\rangle$. Other possible encodings include spatial mode, frequency, etc.

When photons 1 and 2 are projected into, say, the ψ_{12}^{-} Bell state, photon 3 at Bob's location is "instantly" projected onto the initial state of photon 1(ignoring an irrelevant global phase) because of the entanglement between 2 and 3. Bob thus acquires the initial unknown state $|\psi\rangle_3 = \alpha|0\rangle_3 + \beta|1\rangle_3$. Alice's BSM could have equally likely projected the state into any of the other three Bell states. In such a case, Bob can retrieve the initial unknown state by an appropriate unitary transformation, based on the results of Alice's BSM, which she communicates to him via a classical channel. Note that during teleportation of the quantum state to Bob, Alice will destroy the quantum state at hand so that neither party obtains any information about the unknown state.

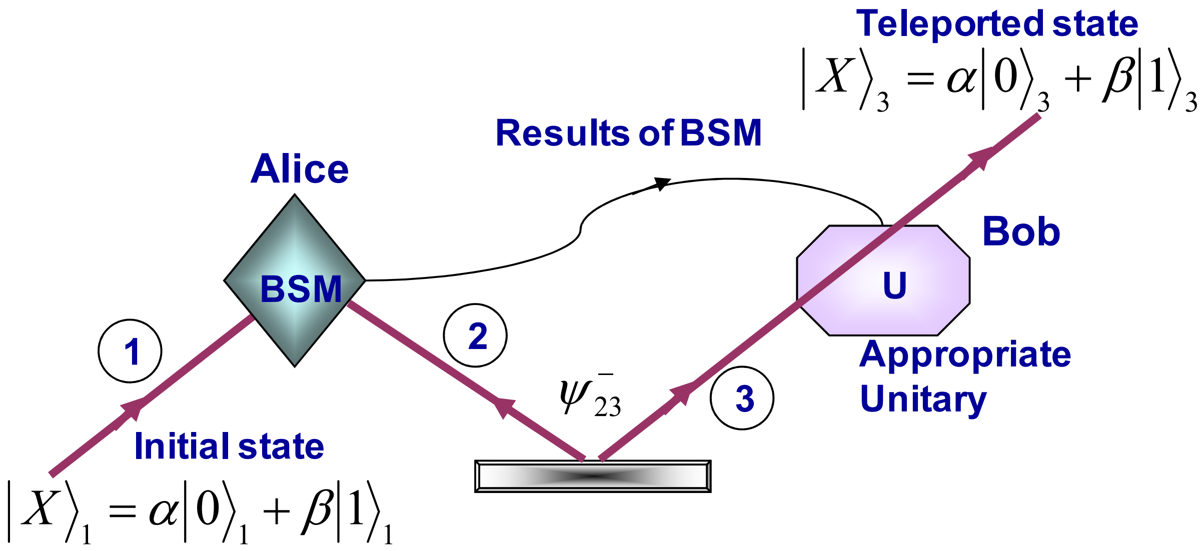

Figure 9-1: Schematic of quantum teleportation of an unknown quantum state from Alice to Bob using a Bell state measurement (BSM) and unitary transformations (U).

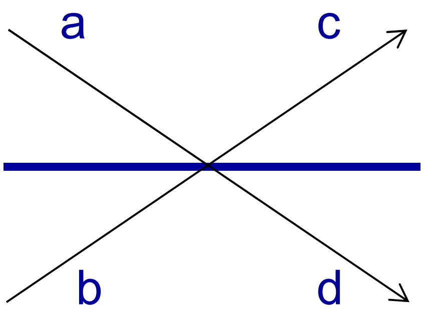

Figure 9-2: A HOM interferometer as part of a BSM.

The BSM: The protocol relies on Alice's capability to efficiently perform a BSM, i.e., the ability to differentiate the four Bell states. Experimentally, the BSM consists of a HOM interferometer (discussed in Section 1.1.1). To see how a HOM interferometer can help distinguish the input Bell state, we show the results of propagating each Bell state through an ideal 50-50 beam splitter (with a $\pi / 2$ phase shift on reflection), as shown in Figure 9-2:

$$\left|\psi^-\right\rangle = \frac{1}{\sqrt{2}}\left(\left|0_a 1_b\right\rangle - \left|1_a 0_b\right\rangle\right) \xrightarrow{\text{beam splitter}} \frac{1}{\sqrt{2}}\left(\left|0_c 1_d\right\rangle - \left|1_c 0_d\right\rangle\right), \qquad 9.3$$

$$\left|\psi^+\right\rangle = \frac{1}{\sqrt{2}}\left(\left|0_a 1_b\right\rangle + \left|1_a 0_b\right\rangle\right) \xrightarrow{\text{beam splitter}} \frac{i}{\sqrt{2}}\left(\left|1_c 0_c\right\rangle + \left|1_d 0_d\right\rangle\right), \qquad 9.4$$

$$\left|\phi^\pm\right\rangle = \frac{1}{\sqrt{2}}\left(\left|0_a 0_b\right\rangle \pm \left|1_a 1_b\right\rangle\right) \xrightarrow{\text{beam splitter}} \frac{i}{\sqrt{2}}\left(\left|0_c 0_c\right\rangle + i\left|0_d 0_d\right\rangle\right) \pm \frac{i}{\sqrt{2}}\left(\left|1_c 1_c\right\rangle + i\left|1_d 1_d\right\rangle\right) . \qquad 9.5$$

$\left|\psi^-\right\rangle$ is immediately distinguishable because it is the only state for which the photons leave via separate ports, i.e., this is the only state that results in a coincidence dip. By having polarizing beam spitters in *c* and *d,* $\left|\psi^+\right\rangle$ can also be distinguished. However, the two remaining states $\left|\phi^\pm\right\rangle$ will give the same experimental signature. In fact is has been *proved that* using only linear optics, only two out of four Bell states can be distinguished with 100% efficiency[101,102] [97-98]. However, when photon-number resolving detectors are available and with $\left|\phi^\pm\right\rangle$ grouped as one set, three basis states can be unambiguously distinguished, yielding higher teleportation efficiencies. Additionally, because the engineered source can generate ultra-bright indistinguishable photon pairs, they greatly enhance the efficiency of a HOM interferometer, the BSM, and the teleportation protocol itself. Hence, our optimized source should enable the possibility of high-fidelity high-count-rate teleportation – currently a challenge [3]. E.g., even the quasi-optimized engineered source is predicted to have a coincidence rate improvement of ~250, compared to present systems. Because teleportation (as well as the entanglement-swapping protocol briefly discussed below) require *double* pairs of photons, this implies a net gain of nearly 5 orders of magnitude in the rate, while maintaining a visibility >90%. Figure 9-3 shows the schematics of the envisioned experimental setup using the indistinguishable-photon source. Note that these brightness improvements drastically reduce the data collection times in typical teleportation experiments.

Similar brightness and efficiency advantages can be expected for a related OQIP protocol, entanglement swapping [99-100]. Entanglement swapping works analogous to teleportation; here, the

---

[101] Note that all four polarization Bell states can be distinguished if the photons are simultaneously entangled in another degree of freedom [96]. However, this technique will not work with independent photons, e.g., Alice's photon 1 and 2.

[102] As discussed in Section 1.1.1, the HOM interference relies on the indistinguishability of the photons.

unknown state to be teleported is actually part of another Bell state, i.e., photon 1 is entangled with photon 4. Implementing the teleportation protocol entangles Bob's particle with 4, thereby effectively transferring quantum entanglement.

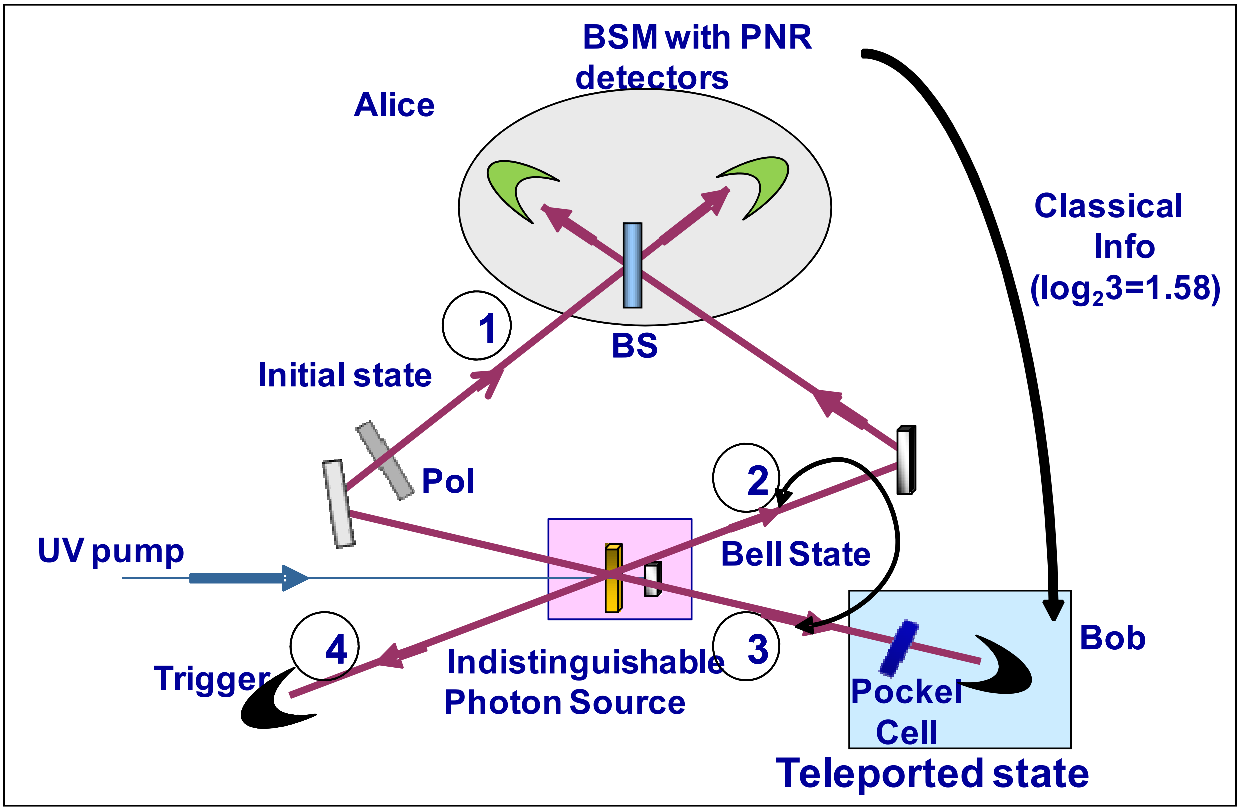

Figure 9-3: Quantum teleportation using the indistinguishable photon source that employs a double pump-pass setup. BS: beam splitters, BSM: bell state measurement, PNR: photon-number resolving, Pol: polarizers, UV: ultraviolet.

9.2 (Hyper)fingerprinting

Introduction to fingerprinting: Fingerprinting is an extremely useful technique in communication complexity, in which comparisons between two large and distributed sets of data are made using much smaller fingerprints of the original messages. The protocol, shown in Figure 9-4, involves a distant supplier, Sapna, who sends a pair of messages to Alice and Bob, who cannot communicate with each other but want to verify the equality of their messages. They can instead send "fingerprints", smaller data sets, to a referee, Roger, who checks whether their messages are the same via their fingerprints [101]. Hence, fingerprinting is an efficient way of verifying whether large distributed databases are identical without checking the entire database. Quantum fingerprinting, where (only) the fingerprints are qubits instead of bits, offers an exponential advantage in resources: for messages of length N, fingerprints of length O(√N) bits are required classically for low error probability, whereas only O(log N) *qubits* are required [101-102]. Further, when Alice and Bob are allowed to share an entangled resource and implement a one-sided error protocol[103], quantum fingerprinting offers an even more impressive advantage: classically impossible error-free protocols may be realized in certain cases, e.g., when a set of *n* messages each of length N can be grouped into *m* equal size groups ($m<n$ and $n=2N$) [102].

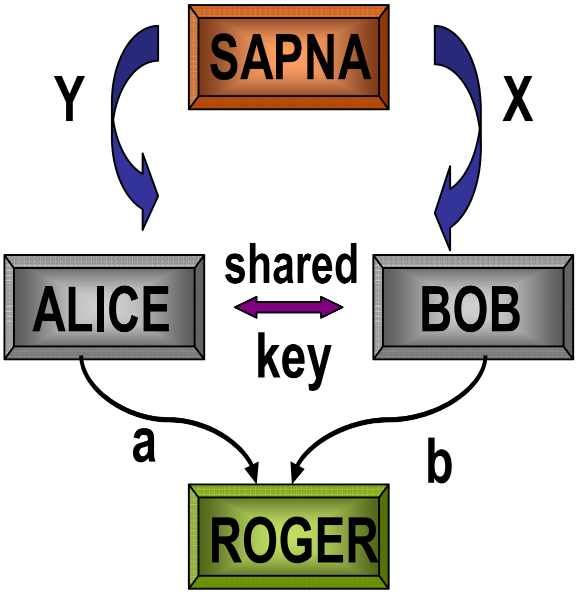

Figure 9-4: Communication flowchart for the fingerprinting scheme.

Proposed schemes and improvements: Fingerprinting is typically evaluated in the worst case scenario (WCS), in which Sapna sends pairs of messages for which Roger's error probability, P_{err}^{wcs}, for false negatives[103] is maximized. When Alice and Bob have no shared key and the set of allowed fingerprints is smaller than that of the possible original messages, it can be shown that Sapna, who is aware of the protocol, can always come up with a pair of identical messages that would generate fingerprints, which would result in a false negative [103]. In fact, no matter what fingerprinting protocol is used, classically the worst case scenario error is 100%, i.e., $P_{C\_err}^{wcs}=1$. Quantum fingerprinting can improve the reliability of fingerprinting by reducing $P_{Q\_err}^{wcs}$ to 2/3, in the case of fingerprinting four different messages (each of

---

[103] In the one-sided error protocol, only false negatives are allowed, i.e., Roger incorrectly believes Alice's and Bob's messages to be different.

length *log₂4=2* bits). In quantum fingerprinting, like the classical scenario, Alice and Bob possess no shared key (i.e., no entangled pair, random strings, etc.) but use *qubits* for the fingerprints. Ideally, the protocol has only one-sided errors and theoretically, false positives (fp, i.e., Roger incorrectly believes Alice's and Bob's messages to be the same) never occur.

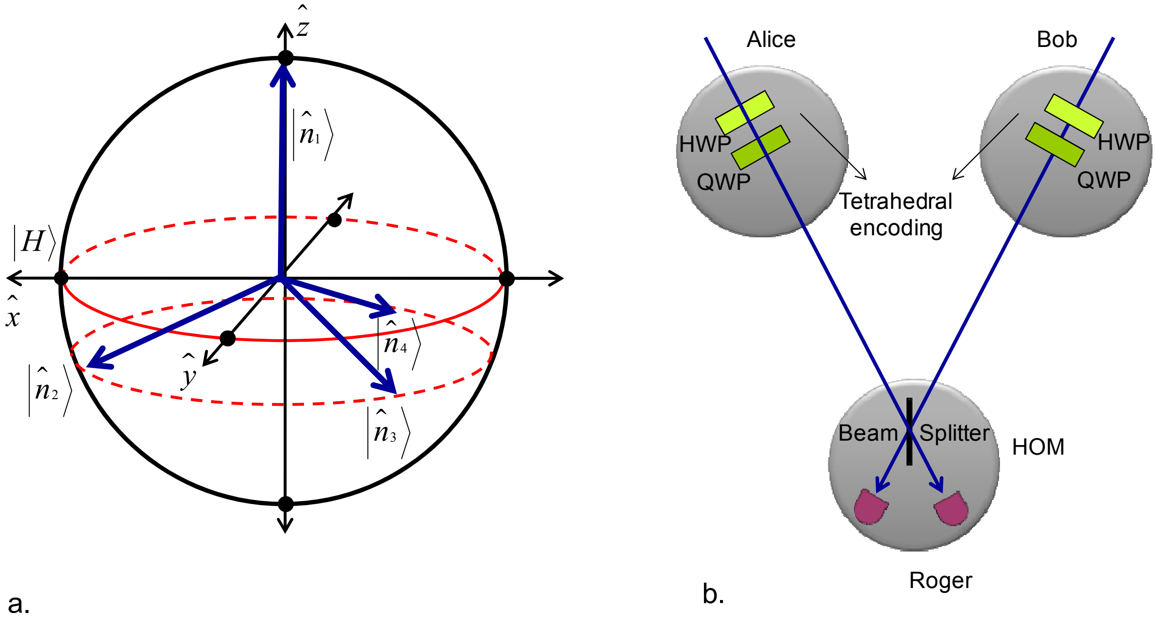

Figure 9-5: Linear optical implementation of the quantum fingerprinting protocol without shared resources. a. Tetrahedral states, $\hat{n}_1, \hat{n}_2, \hat{n}_3, \hat{n}_4$, on the Poincaré sphere. b. Alice and Bob construct fingerprints using the tetrahedral encoding on their input photons. Roger performs a HOM interference to verify their equality.

Horn et al.[2] have recently demonstrated single-qubit optical quantum fingerprinting, achieving $P^{wcs}_{Q\_err}$<72% and $P^{fp}_{Q\_err}$~6%. Here, Alice's and Bob's messages were encoded into *tetrahedral states*, states which form a tetrahedron on the Poincaré sphere[104] as shown in Figure 9-5a, generated via type-I SPDC to create a unique fingerprint. Specifically, for any message (out of the larger set of four total messages) that Alice and Bob receive, they create a unique tetrahedral state as a fingerprint. It is assumed that Alice and Bob use the same mapping, i.e., $x = y \Leftrightarrow |\hat{n}_x\rangle = |\hat{n}_y\rangle$, where x and y refer to different messages and $|\hat{n}_{x,y}\rangle$ to their tetrahedral fingerprints. Alice and Bob would each then send their

---

[104] The Poincaré sphere is the polarization equivalent of the Bloch sphere, a geometrical representation of the pure state space of a two-level quantum mechanical system.

polarization-encoded qubits to Roger, who performs a HOM interference to infer whether the messages are the same (Figure 9-5b). Note that this polarization encoding can be extended to fingerprint larger message sets, but the distinguishability of these distinct states diminishes as the number increases. For the specific case of fingerprinting a four-message dataset, tetrahedral states were chosen specifically because they have a minimal overlap $\left|\langle \hat{n}_i | \hat{n}_j \rangle\right|^2$ $(i, j = 1,2,3,4; i \neq j)$ with each other of 1/3.

We propose an improved protocol using high-efficiency photon-number resolving detectors, which can distinguish no-coincidence events from those in which one photon was lost, leading to a considerable efficiency gain. Further, one could encode Sapna's messages into higher-dimensional states encoded in both polarization and spatial mode. Such an encoding would lead to lower errors and facilitate fingerprinting of larger messages. Next, error-free quantum fingerprinting with shared entanglement as proposed by Horn *et* al. [2] could be implemented for the very first time. According to the scheme, Alice and Bob share the singlet state $|\psi^-\rangle$, and depending on the message each receives from Sapna, they apply certain Pauli operations. If they both perform the same operations, then the state remains the same (except for a global phase). Hence, Roger infers whether Alice and Bob received the same message by performing a Bell state measurement on the fingerprint qubits to determine if they are in the $|\psi^-\rangle$ state. Using such an entangled resource scheme, one can encode 4 messages. Obviously, there is a close analogy with the quantum dense coding protocol [104]. Note that since Roger uses a BSM to verify the equality of the fingerprints, drastic advantages are expected from incorporating the indistinguishable photon-pair source and high-efficiency photon-number resolving detectors (as discussed in Section 9.1) .

Hyper-fingerprinting via hyper-entanglement: We have also theoretically investigated the potential of quantum *hyper-fingerprinting*, a protocol where Alice and Bob share hyper-entangled resources [37], and found that it facilitates theoretically error-free fingerprinting of up to 7 messages. Conservation of orbital angular momentum (OAM) of light results in entanglement of spatial modes. By optimizing SPDC parameters for both polarization and spatial mode entanglement, the following hyper-entangled state (a state entangled in all DOF) can be produced using the two-crystal scheme (discussed in Section 2.4)

$$|\psi\rangle = \underbrace{\left(\cos\theta_p |HH\rangle + e^{i\varphi}\sin\theta_p |VV\rangle\right)}_{polarization} \otimes \underbrace{\left(|rl\rangle + \alpha|gg\rangle + |lr\rangle\right)}_{spatial\,\mathrm{mod}\,e} \otimes \underbrace{\left(|ss\rangle + |ff\rangle\right)}_{energy-time} \qquad 9.6$$

Here, $|l\rangle$, $|g\rangle$ and $|r\rangle$ represent the spatial modes in the Laguerre-Gauss basis, which carry $-\hbar$,0 and $\hbar$ OAM, respectively; α determines their relative contributions, and the last term represents entanglement in energy-time with $|s\rangle$, $|f\rangle$ labeling two distinct emission times [37]. With hyper-entangled states, 100%-efficient BSM with LOCC is attainable [96]. Moreover, using hyper-entanglement and photon-number resolving detectors, seven out of sixteen *hyper-Bell* states, created from polarization and spatial-mode Bell states, can be unambiguously distinguished. Shows a schematic of the hyper-BSM setup [105]. Hence, quantum hyper-fingerprinting allows for theoretically error-free fingerprinting of 7 messages. Alternatively, Alice and Bob can use the extra qubits as redundant fingerprints making the scheme more robust, i.e., instead of fingerprinting 7 messages, Alice and Bob restrict their protocol to a smaller message set (say 4 messages) and use the additional (three) qubits to fingerprint part (three) of the messages again.

9.3 Loophole-free Test of Quantum Nonlocality

While the above two applications emphasize the need for optimized sources and detectors in quantum information tasks, there is also much interest in using these technologies for fundamental tests of physics, e.g., to demonstrate quantum nonlocality. Although there have now been numerous tests of nonlocality [106-107], the vast majority of which agree with quantum mechanical predictions, in fact no experiment to date has incontrovertibly ruled out local realism – there has not yet been a single unambiguous test. This is because all experiments thus far possess at least one of two loopholes arising from auxiliary experimental assumptions: the so-called "detection" and "rapid switching" loopholes[105]. The extremely high-efficiency detectors and the optimized source developed here truly enable a completely "loophole-free" test of Bell's theory to unambiguously resolve the Einstein–Podolsky–Rosen paradox.

In particular, the BiBO source generates ultra-bright high-quality polarization-entangled photons, thereby providing an optimal source for the loophole-free test – predicted to be 3-fold brighter than the source discussed in [64]. Moreover, in order to close the detection loophole, one must have extremely efficient single-photon detectors; an overall detection efficiency of ~85%, including all optical losses between entanglement sources and detectors, is required [38][106]. The optimized VLPCs relax the experimental constraints – their expected 95% QE allow for reasonable losses in the intervening optics, and their PNR capability permits exclusion of higher-order events.

---

[105] The loopholes have been closed independently in two separate experiments. A lossy photon experiment closed the timing loophole [107] and a trapped ion experiment closed the detection loophole [106]. Because of the nature of these systems, neither could close both loopholes simultaneously.

[106] To close the timing loophole, the photons need to be transported some distance away from each other, to account for the latency of the random number generators and the switching speed of the Pockel cells used to set the polarization basis. It has been previously estimated that (for setups similar to ones discussed here) the photon analysis systems should be ~30 m (~100 ns) distant from the entanglement source and also at least that same distance from each other.

As elaborated in the three above examples – quantum teleportation, hyper-fingerprinting and a loophole-free test of Bell's inequalities – incorporating both optimized sources and high-efficiency detector technologies discussed in this thesis offers striking advantages and novel prospects for fundamental physics and for OQIP.

Chapter 10
Conclusions

Come writers and critics who prophesize with your pen
And keep your eyes wide, the chance won't come again
And don't speak too soon, for the wheel's still in spin
And there's no telling who that it's namin'
Oh the loser now will be later to win
For the times, they are a changin'.
-Excerpt from The Times They Are a-Changin', Bob Dylan (1964).

Less than ten years ago, the main focus of the field of quantum information was to demonstrate proof-of-principle experiments. Now as we are beginning to move towards bigger systems, there is a need for these systems to be well-engineered. In fact, the recent focus on technology development, in itself, signifies a dramatic outward shift in the quantum information processing ideology – on top of using quantum mechanics to understand fundamental science and demonstrate possibilities, we now talk of *engineering* optimized turn-key devices – moving from the pedestal of fascinating science towards the possibility of building exciting gadgets[107].

The overarching goal motivating our own research is to have two black boxes – the world's best entanglement source and world's best photon detector – completely optimized for optical quantum information processing as we understand it today. While we do not yet have these ultimate prototypes, the source and detector development discussed here *paves the way to scale quantum computation and quantum communications towards a more practical technology*. The immediate challenges are low-brightness low-fidelity sources and inefficient detectors that require in-depth understanding for device operation and optimization. Combined, these current technologies result in extremely long data-acquisition times, thereby impeding large-scale quantum information systems and complex protocols[108]; current teleportation (four-fold) coincidence rates are ~144 *counts per hour* with 89% fidelity [3] and

---

[107] Quantum cryptography is leading the way in technology commercialization (compared to other quantum information technology) – currently, there are at least two quantum cryptography companies: MagiQ (based in the US) and idQuantique (based in Switzerland). There is at present one quantum computing company, D-Wave Systems (the scientific jury is still out on them) but with no commercial products as of now.

[108] Long data-acquisition time is an especially serious issue since most of the quantum information protocols require interferometric stability over the *entire* measurement; thus, their overall scope (e.g., the number of input qubits to a quantum computer or the number of messages communicated) is drastically limited.

state-of-the-art one-way quantum computers feature six-fold coincidence rates of ~40 *counts per hour* with <60% fidelity. Ultra-bright truly indistinguishable-photon sources, implemented by either extending the downconversion-optimization approach presented here or via other techniques, such as four-wave mixing in photonic-crystal fibers or even solid-state implementations like quantum dots, would result in teleportation rates many orders of magnitude beyond the current "glacial" implementations. Additionally, super high-efficiency photon-number resolving detectors can improve communication protocol efficiencies by at least 50% and facilitate generation of extremely large Schrödinger-cat states *("Schrödinger-tigers"?),* required for scaling optical quantum computers. VLPCs offer a viable option since the device design has mostly been optimized and they are commercially available (although not easily affordable). With the continued improvement in speeds, efficiency and costs of cryo-coolers, transition-edge sensors [89] and superconducting nanowire detectors [91] appear promising as well. Nevertheless, the devices need to be extremely reliable and robust, as well as easily available and affordable. In short, a stable turn-key system is needed. Such optimized photonic technologies would expedite drastic improvement in a range of other quantum information processes as well, including entanglement swapping and coupling to atomic-memories. In turn, *quantum repeaters* [108] (that integrate entanglement swapping and atomic memories) that have only recently been preliminarily demonstrated [109], could become more practical, thereby enabling realistic long-distance quantum communication (presently limited to ~100 km, mainly due to inevitable photon loss in the transmission channel).

The trend of improving computing performance by reducing transistor sizes cannot continue for much longer without eventually including quantum mechanical effects in some form. At the same time, it has been more than 15 years since the discovery of Shor's factoring algorithm [110]. Thus, while the timing is about right for a new technology to surface and push the bounds of computing further forwards, it is still too early to predict its physical platform or even its fundamental paradigm. While many quantum systems hold promise, two specific avenues appear truly exciting: *integrated-optics* that implement "bulk-optics" circuits in compact solid-state systems, and *atom chips*, micro-fabricated circuits, which can confine, control and manipulate cold atoms[109]. Nevertheless, presently it is difficult to envision anything *better* than a photonic network for long-distance quantum communications. Thus, by optimizing what appear to be essential components, such as photonic sources and detectors, we hope to shape quantum technology into a strong contender for the next grand revolution in information processing.

---

[109] Note that both of these fields build on two well-developed technologies. Integrated optics, in fact, combines two mature technologies: optics and solid-state systems. The atom chip, on the other hand, combines cold atoms – a relatively new but very well controllable quantum system – with the immense technological capabilities of micro (nano)fabrication.

Appendix A
Entanglement Source Simulation

Here we present the algorithm for our type-I polarization-entanglement source simulation code, used for the theoretical predictions in Chapter 3. The code can be used to predict expected spatial phase maps, calculate entangled-state properties (fidelity, tangle, etc), and design temporal and spatial compensation crystals, etc., in any uniaxial or biaxial crystal. The complete simulation package can be found on our website – http://research.physics.illinois.edu/QI/photonics/phase_compensation.html – along with an example simulation and a *read-me* file with details on using the code. The main output is a 4x4 density matrix representing the two-photon polarization state of the system, and a phasemap of the signal-side iris. The calculation takes into account the phases acquired by the pump, signal and idler photons as they propagate through the down-conversion and compensation crystals (if present). Explicit calculations for the temporal and spatial decoherence/compensation are presented in Section 3.3. Overall, the sequence of the simulation is as follows:

1. Choose a signal photon having a wavelength passed by the frequency filter and a momentum vector $\vec{k}$ that falls inside the collection iris (i.e., the geometrical ray along $\vec{k}$ lies within the solid angle subtended by the iris, with respect to the center of the downconversion crystal).

2. If the distribution of idler photon k-vectors associated with this signal photon (determined by the k-vector content of the pump beam) is large relative to spacing between points on the computational grid spanning the idler iris, then pick any idler k-vector and frequency that fall in the idler iris, filter range and satisfies energy conservation. If the idler distribution is small (i.e., narrow angular range), then find the idler direction corresponding to the signal photon by conservation of momentum.

3. Propagate the pump through the precompensation crystal (if present) to find the phases it acquires. Find the polarization modes, k-vectors, and Poynting vectors of signal and idler photons in the first and second down-conversion crystals.

4. Find the phase acquired by each photon in the crystals in the two possible processes: (1) down-conversion in the first crystal and (2) down-conversion in the second crystal.

5. Propagate signal and idler photons through any phase-compensation crystals, as in steps 3-4, by finding polarization modes, k-vectors, Poynting vectors and phases.

6. By taking a superposition of the two down-conversion processes, find the pure polarization state that describes the signal and idler photons.

7. Repeat the above procedure for all k-vectors and wavelengths that are collected by the irises and filters. The total number of loops (i.e., the range integration over frequencies, iris points, etc.) can be independently set in the program.

8. Incoherently sum all of the resulting pure density matrices to obtain the overall density matrix.

KEY ASSUMPTIONS/APPROXIMATIONS MADE IN THE SIMULATION:

- Type-I down-conversion is a fast → slow + slow process (fast photon downconverts into two slow photons); for a uniaxial SPDC crystal this would be *negative* uniaxial crystal. See Boeuf et al. [75] for more details.
- Pump beam is modeled as a Gaussian.
- The down-conversion crystals are thin enough such that the two down-conversion processes can be considered indistinguishable.
- The down-conversion and compensation crystals are not wedged, and their surfaces are all parallel to each other (and normal to the pump k-vector).
- The signal and idler frequency filters have 100% transmission for wavelengths that fall in the passband, and no transmission outside the passband.
- Loss due to Fresnel reflections at crystal surfaces is ignored.

Appendix B
Birefringent Focusing

Here we present a simplified derivation of the polarization-dependent beam-waist location when focusing through a birefringent crystal with the optic axis at an arbitrary angle. The analysis is similar to case of a 90° optic axis cut, considered by Park et al. [77], and is calculates the shift in the location of the focused spot because of refraction and spatial walkoff in a birefringent crystal (Figure B-1).

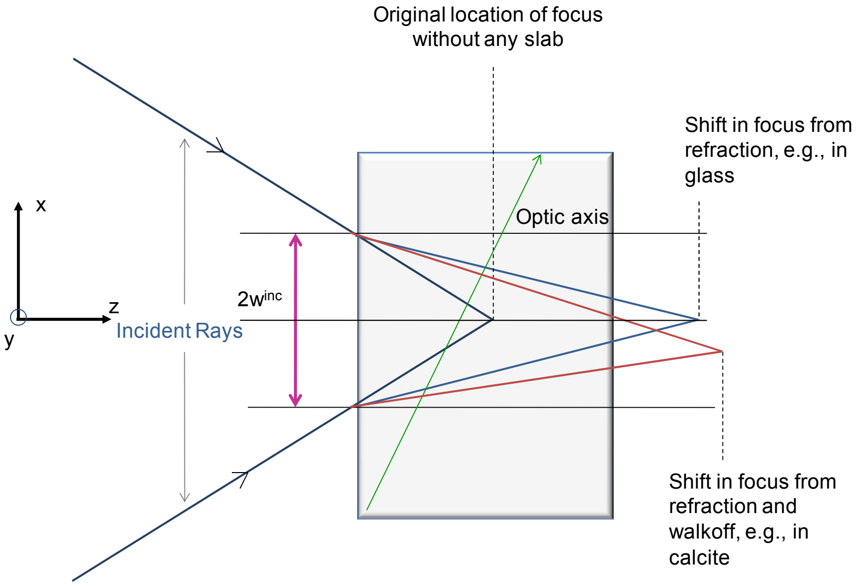

Figure B-1: Shift in the position of the focused spot caused by refraction and spatial walkoff.

Similar to the approach shown in [77], we consider three independent cases: ordinary polarization, extraordinary polarization incident in the vertical plane, and finally, extraordinary polarization incident in the horizontal plane. When the crystal optic axis is no longer cut at 90°, the refractive index of both the vertically and horizontally incident extraordinary polarization varies according to the ray propagation directions; since in general none of these rays is perpendicular to the optic axis of the crystal. Additionally, these rays experience Poynting vector walkoff in different directions. Thus, the beam waists of the extraordinary rays are elliptical spots, which occur at distinguishable longitudinal locations depending on their plane of incidence. Additionally, because of spatial walkoff, the waists are also

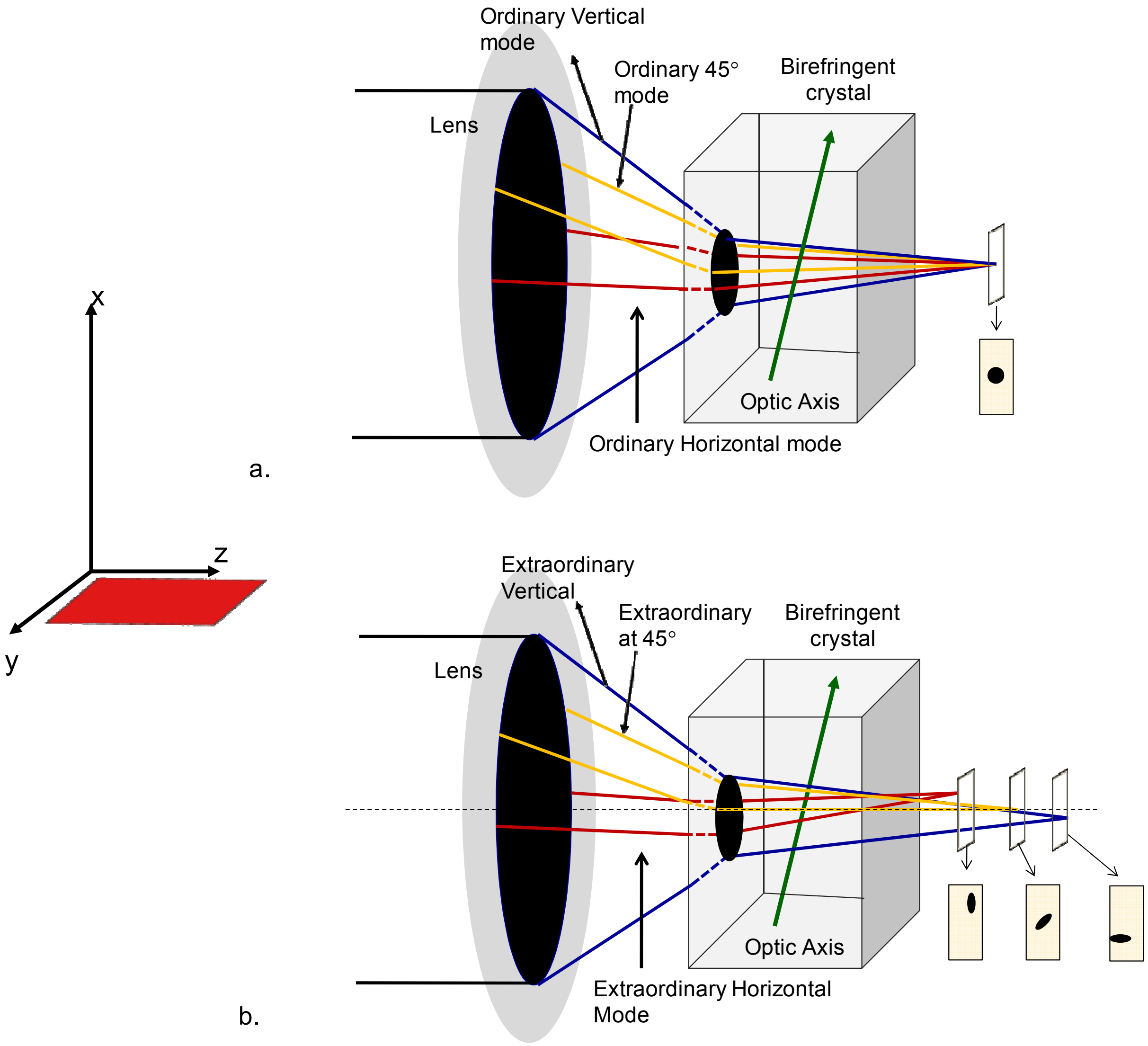

Figure B-2: Schematic showing the focusing of the ordinary (**a**) and extraordinary (**b**) polarization, using a lens and a birefringent crystal with the optic axis cut at an arbitrary angle, for rays in the horizontal (red), vertical (blue) and 45° plane of incidence (yellow). **a**. The ordinary beam results in a symmetric focused spot for all spatial modes. **b.** The extraordinary beam results in an elongated blurred spot; the extreme spots are caused by the extraordinary ray in the horizontal plane and the extraordinary ray in the vertical plane. Both the horizontal (in the y-z plane) and the vertical components experience an angle-dependent index. A ray in between the two extreme cases, e.g., the in the 45° plane, focuses in between. Note that the extraordinary polarization results in an elongated, blurred and displaced spot along *x, y* and *z* due to incident-direction dependence of the refractive index and spatial walkoff (the vertical components walk off along the *x* axis and the horizontal components walk off along the *y* axis).

displaced in the transverse plane (*x* and *y*). Thus, the extraordinary polarization results in a blurred focus in z that is displaced in x and y, due to incident-direction dependence of the refractive index as well as spatial walkoff of the vertically incident components (x-axis) and the horizontally incident components (y-axis), as shown in Figure B-2. The ordinary polarization focuses into a symmetric spot similar to the 90° optic axis cut, also shown in Figure B-2. Here, we use a simplified theory to derive the specific location of each of the beam waists for each of these cases. A more detailed and complete analysis based on propagating Gaussians would give the behavior of the entire extraordinary-polarized focused beam at any location.

B. 1 **Ordinary Polarization**

The simplest case is that of ordinary polarization, for which the birefringent crystal behaves identically to a regular glass slab. These rays thus experience a constant refractive index n_o in the birefringent slab of thickness d. We assume they are focused to an image point by a lens with focal length f. Using Snell's law and ray transfer matrices, the shift Δz_o in the focus of the ordinary polarization caused by the birefringent slab, can be written as:

$$\Delta z_o = d\left(1-\frac{1}{n_o}\right). \qquad \text{B.1}$$

Note that, as expected, the shift is always positive, and goes to zero as $n_0 \rightarrow 1$.

B.2 Extraordinary Polarization: Vertical Plane

For extraordinary polarization, the effective refractive index depends on the angle Φ between the direction of propagation in the medium and the crystal cut, i.e., the orientation of the optic axis. The effective angle-dependent refractive index $n(\Phi)$, can be given by

$$n_\mathrm{e}(\Phi) = \frac{n_\mathrm{o} n_\mathrm{e}}{\sqrt{n_\mathrm{o}^2 \sin^2(\Phi) + n_\mathrm{e}^2 \cos^2(\Phi)}} \quad . \qquad \text{B.2}$$

Φ is the direction between the propagation direction and the optic axis [41]. Since these rays are extraordinary, the actual direction of energy propagation is given by the Poynting vector, which walks off from the wave vector inside a birefringent medium. Hence, to find the beam-waist location for extraordinary polarization, we first solve for the angle of refraction and then calculate the walkoff inside the crystal. From Snell's law the incidence angle determines the direction of a refracted ray. Thus, we consider the two extreme incidence angles – the upper-most (UEPV) and lower-most (LEPV) – of the extraordinary-polarized rays in the vertical plane, and calculate the refraction angle of these wave vectors separately. Figure B-3 shows the geometry of the system, including the UEPV and LEPV rays.

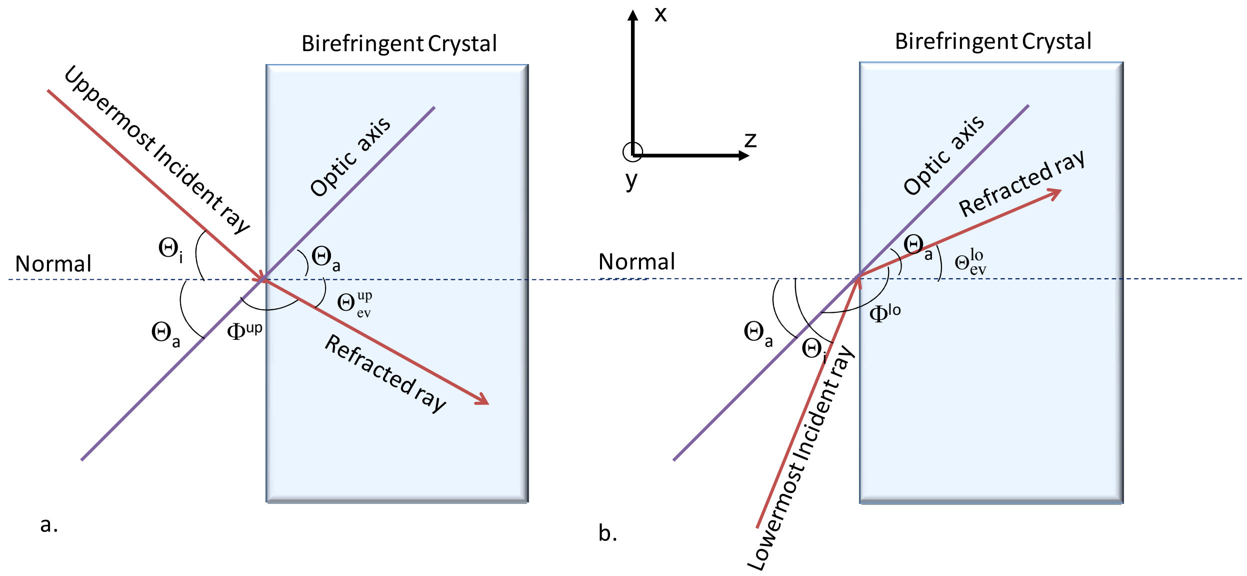

Figure B-3: Relevant angles for the (**a**) uppermost (UEPV) and (**b**) lowermost (LEPV) incident rays with extraordinary polarization in the vertical plane.

Refraction of the upper vertical ray: The first step is to solve for the refraction angle $\Theta_{\text{ev}}^{\text{up}}$ of the UEPV ray, in terms of the system parameters. Figure B-3a shows the relevant angles for the UEPV beam. Let Θ_{i} represent the angle of the incident UEPV beam with respect to the surface normal, Θ_{a} the crystal optic axis angle, and $\Theta_{\text{ev}}^{\text{up}}$ the angle of the refracted wave vector $\vec{k}$. The angle Φ^{up} between $\vec{k}$ and the optic axis is given by

$$\Phi^{\text{up}} = \pi - \left(\Theta_{\text{a}} + \Theta_{\text{ev}}^{\text{up}}\right), \qquad \text{B.3}$$

$$\Rightarrow \cos\Phi^{\text{up}} = -\cos(\Theta_{\text{a}} + \Theta_{\text{ev}}^{\text{up}}), \qquad \text{B.4}$$

$$\sin\Phi^{\text{up}} = \sin(\Theta_{\text{a}} + \Theta_{\text{ev}}^{\text{up}}), \qquad \text{B.5}$$

$$\tan\Phi^{\text{up}} = -\tan(\Theta_{\text{a}} + \Theta_{\text{ev}}^{\text{up}}). \qquad \text{B.6}$$

From Snell’s law and Eqn. 5.5,

$$\frac{\sin\Theta_{\text{i}}}{\sin\Theta_{\text{ev}}^{\text{up}}} = n_{\text{ev}}^{\text{up}}(\Phi^{\text{up}}), \qquad \text{B.7}$$

$$\Rightarrow \sin\Theta_{\mathrm{i}} = \frac{n_{\mathrm{o}} n_{\mathrm{e}} \sin(\Theta_{\mathrm{ev}}^{\mathrm{up}})}{\sqrt{n_{\mathrm{o}}^2 \sin^2(\Theta_{\mathrm{a}} + \Theta_{\mathrm{ev}}^{\mathrm{up}}) + n_{\mathrm{e}}^2 \cos^2(\Theta_{\mathrm{a}} + \Theta_{\mathrm{ev}}^{\mathrm{up}})}}\,, \tag{B.8}$$

$$\Rightarrow \sin(\Theta_{\mathrm{ev}}^{\mathrm{up}}) = \frac{\sin(\Theta_{\mathrm{i}})}{n_{\mathrm{o}} n_{\mathrm{e}}} \sqrt{n_{\mathrm{o}}^2 \sin^2\left(\Theta_{\mathrm{a}} + \Theta_{\mathrm{ev}}^{\mathrm{up}}\right) + n_{\mathrm{e}}^2 \cos^2\left(\Theta_{\mathrm{a}} + \Theta_{\mathrm{ev}}^{\mathrm{up}}\right)}\ , \tag{B.9}$$

$$= \sin(\Theta_{\mathrm{i}}) \sqrt{\frac{1}{n_{\mathrm{e}}^2} \sin^2\left(\Theta_{\mathrm{a}} + \Theta_{\mathrm{ev}}^{\mathrm{up}}\right) + \frac{1}{n_{\mathrm{o}}^2} \cos^2\left(\Theta_{\mathrm{a}} + \Theta_{\mathrm{ev}}^{\mathrm{up}}\right)}\ . \tag{B.10}$$

At this point, we can simplify using the following trigonometric identities:

$$\sin(\Theta_{\mathrm{a}} + \Theta_{\mathrm{ev}}^{\mathrm{up}}) = \sin(\Theta_{\mathrm{a}}) \cos(\Theta_{\mathrm{ev}}^{\mathrm{up}}) + \cos(\Theta_{\mathrm{a}}) \sin(\Theta_{\mathrm{ev}}^{\mathrm{up}}) \text{ and} \tag{B.11}$$

$$\cos(\Theta_{\mathrm{a}} + \Theta_{\mathrm{ev}}^{\mathrm{up}}) = \cos(\Theta_{\mathrm{a}}) \cos(\Theta_{\mathrm{ev}}^{\mathrm{up}}) - \sin(\Theta_{\mathrm{a}}) \sin(\Theta_{\mathrm{ev}}^{\mathrm{up}})\ . \tag{B.12}$$

Further, if we consider only small refraction angles, such that $\sin(\Theta_{\mathrm{ev}}^{\mathrm{up}}) \approx \Theta_{\mathrm{ev}}^{\mathrm{up}}$ and $\cos(\Theta_{\mathrm{ev}}^{\mathrm{up}}) \approx 1$, we can solve for $\Theta_{\mathrm{ev}}^{\mathrm{up}}$:

$$\Theta_{\mathrm{ev}}^{\mathrm{up}} = \sin(\Theta_{\mathrm{i}}) \times$$

$$\sqrt{\underbrace{\frac{\sin^2(\Theta_{\mathrm{a}})}{n_{\mathrm{e}}^2} + \frac{\cos^2(\Theta_{\mathrm{a}})}{n_{\mathrm{o}}^2}}_{\equiv 1/n_{\mathrm{e}}^2(\Theta_{\mathrm{a}})} + 2\sin(\Theta_{\mathrm{a}})\cos(\Theta_{\mathrm{a}}) \left(\underbrace{\frac{1}{n_{\mathrm{e}}^2} - \frac{1}{n_{\mathrm{o}}^2}}_{\equiv \eta^-} \right) \Theta_{\mathrm{ev}}^{\mathrm{up}} + \left(\underbrace{\frac{\sin^2\left(\Theta_{\mathrm{a}}\right)}{n_{\mathrm{o}}^2} + \frac{\cos^2\left(\Theta_{\mathrm{a}}\right)}{n_{\mathrm{e}}^2}}_{\equiv 1/n_{\mathrm{inv,e}}^2\left(\Theta_{\mathrm{a}}\right)} \right) \left(\Theta_{\mathrm{ev}}^{\mathrm{up}}\right)^2}\ ,$$

$$\Rightarrow \Theta_{\mathrm{ev}}^{\mathrm{up}} = \sin(\Theta_{\mathrm{i}}) \sqrt{\frac{1}{n_{\mathrm{e}}^2(\Theta_{\mathrm{a}})} + \left(2\sin(\Theta_{\mathrm{a}})\cos(\Theta_{\mathrm{a}})\eta^-\right)\Theta_{\mathrm{ev}}^{\mathrm{up}} + \frac{1}{n_{\mathrm{inv,e}}^2\left(\Theta_{\mathrm{a}}\right)}\left(\Theta_{\mathrm{ev}}^{\mathrm{up}}\right)^2}\,. \tag{B.13}$$

This equation can be solved for $\Theta_{\mathrm{ev}}^{\mathrm{up}}$:

$$\Theta_{\mathrm{ev}}^{\mathrm{up}} = \sqrt{\frac{\sin^2\left(\Theta_{\mathrm{i}}\right)}{n_{\mathrm{e}}^2\left(\Theta_{\mathrm{a}}\right)\left(1 - \dfrac{\sin^2\left(\Theta_{\mathrm{i}}\right)}{n_{\mathrm{e,inv}}^2\left(\Theta_{\mathrm{a}}\right)}\right)} + \left(\frac{\sin^2\left(\Theta_{\mathrm{i}}\right)\sin\left(\Theta_{\mathrm{a}}\right)\cos\left(\Theta_{\mathrm{a}}\right)\eta^-}{1 - \dfrac{\sin^2\left(\Theta_{\mathrm{i}}\right)}{n_{\mathrm{e,inv}}^2\left(\Theta_{\mathrm{a}}\right)}}\right)^2} + \frac{\sin^2\left(\Theta_{\mathrm{i}}\right)\sin\left(\Theta_{\mathrm{a}}\right)\cos\left(\Theta_{\mathrm{a}}\right)\eta^-}{1 - \dfrac{\sin^2\left(\Theta_{\mathrm{i}}\right)}{n_{\mathrm{e,inv}}^2\left(\Theta_{\mathrm{a}}\right)}}\,. \tag{B.14}$$

From this equation, we can derive the result for the special case $\Theta_{\mathrm{a}} = \frac{\pi}{2}$,

$$\Theta_{\mathrm{ev}}^{\mathrm{up}} = \sqrt{\frac{\sin^2\left(\Theta_{\mathrm{i}}\right)/n_{\mathrm{e}}^2}{1 - \sin^2\left(\Theta_{\mathrm{i}}\right)/n_{\mathrm{o}}^2}}\qquad , \tag{B.15}$$

which matches exactly what Park et al. [77] derive for the special case of a perpendicular optic axis cut.

Refraction of the lower vertical ray: The refracted angle $\Theta_{\mathrm{ev}}^{\mathrm{lo}}$ for the lowermost extraordinary polarized ray in the vertical plane can be derived similarly. Figure B-3b defines the corresponding angles for this case. Once again, Θ_{i} represents the angle of the incident beam with respect to the normal to the surface, and Θ_{a} is the cut of the crystal's optic axis. The angle Θ^{lo} between the refracted k -vector and the optic axis is given by

$$\Phi^{\mathrm{lo}} = \pi - \left(\Theta_{\mathrm{a}} - \Theta_{\mathrm{ev}}^{\mathrm{lo}}\right), \qquad \text{B.16}$$

$$\Rightarrow \cos\Phi^{\mathrm{lo}} = -\cos(\Theta_{\mathrm{a}} - \Theta_{\mathrm{ev}}^{\mathrm{lo}}), \qquad \text{B.17}$$

$$\sin\Phi^{\mathrm{lo}} = \sin(\Theta_{\mathrm{a}} - \Theta_{\mathrm{ev}}^{\mathrm{lo}}), \qquad \text{B.18}$$

$$\tan\Phi^{\mathrm{lo}} = -\tan(\Theta_{\mathrm{a}} - \Theta_{\mathrm{ev}}^{\mathrm{lo}}). \qquad \text{B.19}$$

An analytical expression for $\Theta_{\mathrm{ev}}^{\mathrm{lo}}$ can be derived similar to Eqns. B.7 to B.14.

$$\Theta_{\mathrm{ev}}^{\mathrm{lo}} = \sin(\Theta_{\mathrm{i}})\sqrt{\frac{1}{n_{\mathrm{e}}^2(\Theta_{\mathrm{a}})} - \left(2\sin(\Theta_{\mathrm{a}})\cos(\Theta_{\mathrm{a}})\eta^-\right)\Theta_{\mathrm{ev}}^{\mathrm{lo}} + \frac{1}{n_{\mathrm{inv,e}}^2\left(\Theta_{\mathrm{a}}\right)}\left(\Theta_{\mathrm{ev}}^{\mathrm{lo}}\right)^2}\ , \qquad \text{B.20}$$

$$\Theta_{\mathrm{ev}}^{\mathrm{lo}} = \sqrt{\frac{\sin^2\left(\Theta_{\mathrm{i}}\right)}{n_{\mathrm{e}}^2\left(\Theta_{\mathrm{a}}\right)\left(1-\dfrac{\sin^2\left(\Theta_{\mathrm{i}}\right)}{n_{\mathrm{e,inv}}^2\left(\Theta_{\mathrm{a}}\right)}\right)} + \left(\frac{\sin^2\left(\Theta_{\mathrm{i}}\right)\sin\left(\Theta_{\mathrm{a}}\right)\cos\left(\Theta_{\mathrm{a}}\right)\eta^-}{1-\dfrac{\sin^2\left(\Theta_{\mathrm{i}}\right)}{n_{\mathrm{e,inv}}^2\left(\Theta_{\mathrm{a}}\right)}}\right)^2} - \frac{\sin^2\left(\Theta_{\mathrm{i}}\right)\sin\left(\Theta_{\mathrm{a}}\right)\cos\left(\Theta_{\mathrm{a}}\right)\eta^-}{1-\dfrac{\sin^2\left(\Theta_{\mathrm{i}}\right)}{n_{\mathrm{e,inv}}^2\left(\Theta_{\mathrm{a}}\right)}} \qquad \text{B.21}$$

$$= \sqrt{\frac{\sin^2\left(\Theta_{\mathrm{i}}\right)/n_{\mathrm{e}}^2}{1-\sin^2\left(\Theta_{\mathrm{i}}\right)/n_{\mathrm{o}}^2}}, \text{ for } \Theta_{\mathrm{a}} = \frac{\pi}{2} \text{ (again in agreement with Park et al).}$$

With the directions of the refracted rays, we move to the second step, which is to calculate the amount of spatial (Poynting-vector) walkoff inside the birefringent crystal.

Direction of Poyting-vector walkoff: The Poynting vector (and therefore the walkoff) for a *negative* uniaxial crystal, such as BBO, can be calculated as follows [111]. If ρ is the relative angle between the refracted k-vector and the Poynting vector in the crystal (note that Φ is angle between the k-vector and the optic axis), as shown in Figure B-4a, then

$$\rho(\Phi) = \arctan\left(\left(\frac{n_{\mathrm{o}}}{n_{\mathrm{e}}}\right)^2 \tan(\Phi)\right) - \Phi\,. \qquad \text{B.22}$$

However, the upper and the lower vertical extraordinary rays have different relative angles Φ^{up} and Φ^{lo} between the refracted rays and the optic axis. Thus,

$$\rho(\Phi^{\mathrm{up}}) = \arctan\left(\left(\frac{n_{\mathrm{o}}}{n_{\mathrm{e}}}\right)^2 \tan(\Theta_{\mathrm{a}} + \Theta_{\mathrm{ev}}^{\mathrm{up}})\right) - \left(\Theta_{\mathrm{a}} + \Theta_{\mathrm{ev}}^{\mathrm{up}}\right) \text{ and} \qquad \text{B.23}$$

$$\rho(\Phi^{\mathrm{lo}}) = \arctan\left(\left(\frac{n_{\mathrm{o}}}{n_{\mathrm{e}}}\right)^2 \tan(\Theta_{\mathrm{a}} - \Theta_{\mathrm{ev}}^{\mathrm{lo}})\right) - \left(\Theta_{\mathrm{a}} - \Theta_{\mathrm{ev}}^{\mathrm{lo}}\right), \qquad \text{B.24}$$

are the respective walkoffs for the upper and lower vertical rays. This gives us the total walkoff angle. However, we are mainly interested in the overall deviation of the vertical rays with respect to the center-ray (the center of the beam waist) at the exit plane of the crystal. Therefore, we define new walkoff angles ρ'^{up} and ρ'^{lo}, (note that ρ is measured relative to the refracted k-vector) measured relative to the horizontal axis (see Figure B-4a):

$$\rho'^{\mathrm{up}} = \rho(\Phi^{\mathrm{up}}) + \Theta_{\mathrm{ev}}^{\mathrm{up}}, \qquad \text{B.25}$$

$$\rho'^{\mathrm{lo}} = \Theta_{\mathrm{ev}}^{\mathrm{lo}} - \rho(\Phi^{\mathrm{lo}}). \qquad \text{B.26}$$

Finally, as the last step, we can calculate the position of the beam waist for the extraordinary rays in the vertical plane.

Beam-waist location of the vertical rays: We need to calculate the beam waist for vertical rays in the exit-plane with respect to the center-ray. Figure B-5 shows the simple geometric relationships needed for this derivation. The walkoff of the center-ray is given by

$$\Delta x_{\mathrm{e}}^{\mathrm{ce}} = d \cdot \tan \rho(\Theta_{\mathrm{a}}) \ . \qquad \text{B.27}$$

If w^{inc} is the beam waist in the plane of incidence, the beam width in the exit plane is the difference between the walkoff for an extraordinary ray relative to the walkoff of the center ray. For the uppermost and the lowermost extraordinary vertical rays in the exit plane, their respective beam widths w'^{up} and w'^{lo} are:

$$w'^{\mathrm{up}} = w^{\mathrm{inc}} - d\left(\tan\rho'^{\mathrm{up}} - \tan\rho\left(\Theta_a\right)\right), \qquad \text{B.28}$$

$$w'^{\mathrm{lo}} = +w^{\mathrm{inc}} - d\left(\tan\rho\left(\Theta_{\mathrm{a}}\right) + \tan\rho'^{\mathrm{lo}}\right). \qquad \text{B.29}$$

The average beam-waist location for extraordinary polarization in the vertical plane can then be written as

$$\Delta z_{\text{ev}} = \frac{w'^{\text{up}} + w'^{\text{lo}}}{2\cdot\tan\Theta_{\text{i}}} \quad . \qquad \text{B.30}$$

To see the origin of this equation consider a simple non-birefringent slab (e.g., glass) with no spatial walkoff. As shown in Figure B-5, the shift in the location of the focus can be given by $\Delta z_{new} = \delta x / \tan\Theta_{\text{i}}$. In the presence of walkoff, the average δ_x can be given by $w'^{\text{up}} + w'^{\text{lo}} / 2$, thereby resulting in Eqn. B.30.

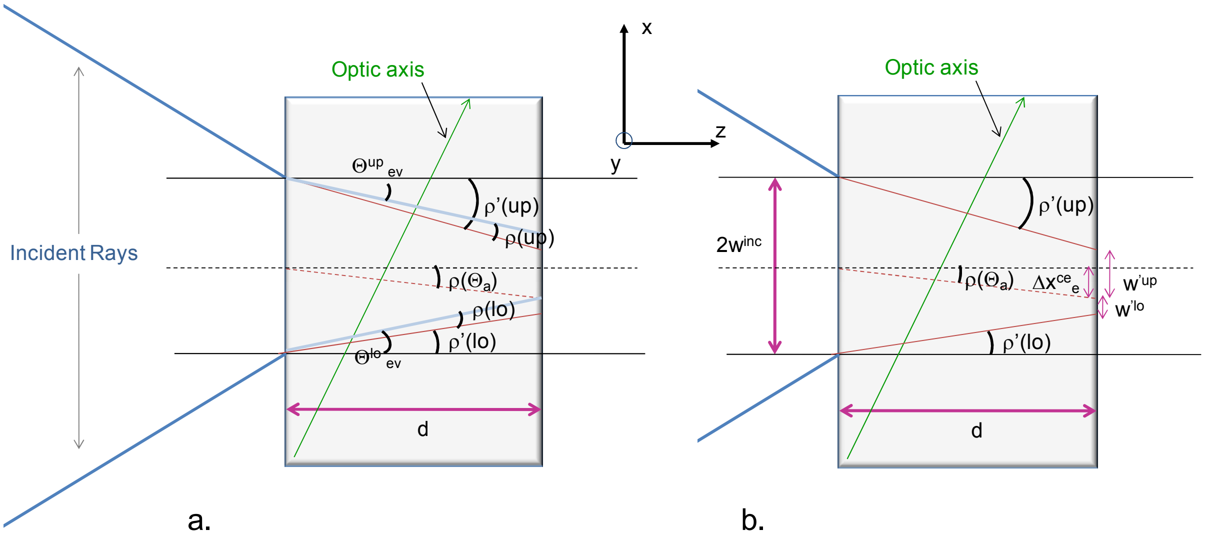

Figure B-4: Schematic showing (**a**) the refracted and walkoff rays and (**b**) the resulting change in the incident beam waist in the exit plane of a negative uniaxial crystal, for extraordinary polarized rays in the vertical plane.

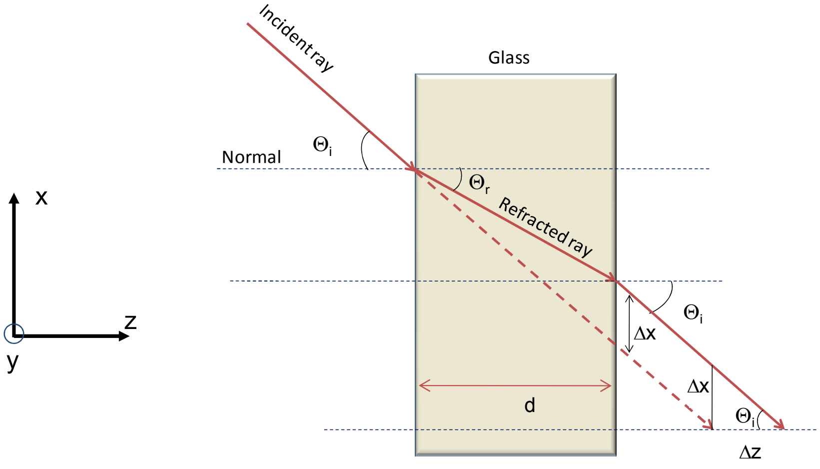

Figure B-5: The shift in the location of the focused spot because of refraction. The simple case for the shift in the position of the focus caused by a non-birefringent slab with no walkoff is shown here.

B.3 Extraordinary Polarization: Horizontal Plane

For extraordinary polarization incident in the horizontal plane (see [76]), the Poynting vector walkoff does occur in same incidence plane; the walkoff is along a plane containing the refracted ray and the optic axis. Figure B-6 shows the orientation of the optical axis $\overrightarrow{OA}$, the direction of the refracted ray $\overrightarrow{RR}$ and the Poynting vector $\vec{s}$ with respect to the horizontal plane (Figure B-2b shows the relative orientation of the optic axis and the horizontally incident beam with respect to the horizontal plane). Thus, for calculations in this section it is easier to use vector algebra. Similar to the rays in the vertical plane, we first determine the refraction angle Θ_{eh}. Because the incident focused beam is spherically symmetric, the angle between the extreme ray incident in the horizontal plane and the optic axis is the same as that for the upper-most incident ray in the vertical plane. Hence, the refractive index can be written as

$$n\left(\Theta_{\mathrm{a}}+\Theta_{\mathrm{eh}}\right)=n\left(\Theta_{\mathrm{a}}+\Theta_{\mathrm{ev}}^{\mathrm{up}}\right). \qquad \text{B.31}$$

We can define the direction of the optic axis and the refracted vector as:

$$\overrightarrow{OA}=\begin{pmatrix}0\\ -\sin(\Theta_{\mathrm{a}})\\ -\cos(\Theta_{\mathrm{a}})\end{pmatrix} \quad \text{and} \quad \overrightarrow{RR}=\begin{pmatrix}\sin(\Theta_{\mathrm{eh}})\\ 0\\ \cos(\Theta_{\mathrm{eh}})\end{pmatrix}. \qquad \text{B.32}$$

The Poynting vector $\vec{s}$ of the horizontal refracted extraordinary light walks off and is located in the plane containing $\overrightarrow{OA}$ and $\overrightarrow{RR}$. Therefore, $\vec{s}$ can be described by a rotation of $\overrightarrow{RR}$ about a vector normal $\vec{n}$ to the $\overrightarrow{OA}-\overrightarrow{RR}$ plane (shown in Figure B-6):

$$\vec{n}=\overrightarrow{OA}\times\overrightarrow{RR}=\sum_i \epsilon_{ijk}(OA)_j(RR)_k\hat{e}_i=\begin{pmatrix}-\sin(\Theta_{\mathrm{a}})\cos(\Theta_{\mathrm{eh}})\\ -\cos(\Theta_{\mathrm{a}})\sin(\Theta_{\mathrm{eh}})\\ \sin(\Theta_{\mathrm{a}})\sin(\Theta_{\mathrm{eh}})\end{pmatrix}. \qquad \text{B.33}$$

The unit normal vector $\hat{e}_{\mathrm{n}}$ can be obtained by normalizing $\vec{n}$:

$$\hat{e}_{\mathrm{n}}=\underbrace{\frac{1}{\sqrt{\sin^2(\Theta_{\mathrm{a}})+\cos^2(\Theta_{\mathrm{a}})\sin^2(\Theta_{\mathrm{eh}})}}}_{1/L}\begin{pmatrix}-\sin(\Theta_{\mathrm{a}})\cos(\Theta_{\mathrm{eh}})\\ -\cos(\Theta_{\mathrm{a}})\sin(\Theta_{\mathrm{eh}})\\ \sin(\Theta_{\mathrm{a}})\sin(\Theta_{\mathrm{eh}})\end{pmatrix}. \qquad \text{B.34}$$

The walkoff-angle $\rho=\rho(\Phi^{\mathrm{up}})$ can now be given by a rotation about the unit normal vector. The rotation matrix $\overleftrightarrow{M}$ can be written as

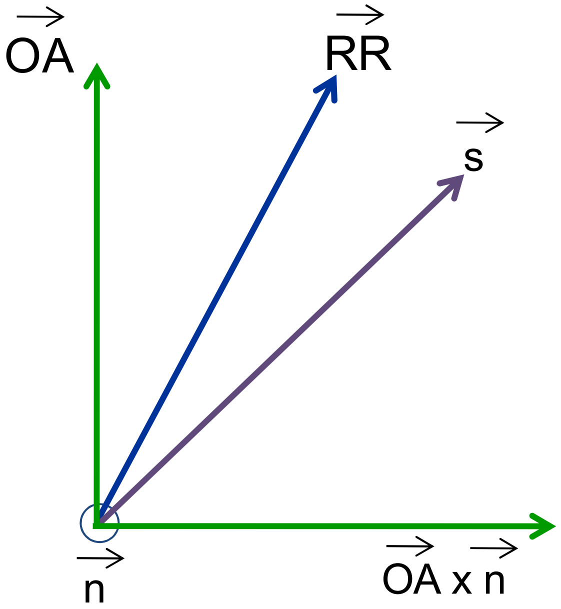

Figure B-6: Plane containing the optic axis $\overrightarrow{OA}$, refracted ray $\overrightarrow{RR}$, normal vector $\vec{n}$ and walkoff vector $\vec{s}$ for the extraordinary polarization incident in the horizontal plane of incidence.

$$\overleftrightarrow{M} = \begin{pmatrix} \cos(\rho)+e_1^2(1-\cos(\rho)) & e_1e_2(1-\cos(\rho))-e_3\sin(\rho) & e_1e_3(1-\cos(\rho))+e_2\sin(\rho) \\ e_2e_1(1-\cos(\rho))+e_3\sin(\rho) & \cos(\rho)+e_2^2(1-\cos(\rho)) & e_2e_3(1-\cos(\rho))-e_1\sin(\rho) \\ e_3e_1(1-\cos(\rho))-e_2\sin(\rho) & e_3e_2(1-\cos(\rho))+e_1\sin(\rho) & \cos(\rho)+e_3^2(1-\cos(\rho)) \end{pmatrix}.$$

We find the direction of the Poynting vector by applying the rotation matrix $\overleftrightarrow{M}$ on the refracted ray $\overrightarrow{RR}$:

$$\begin{aligned} \hat{s} &= \overleftrightarrow{M}\cdot\overrightarrow{RR} \\ &= \frac{1}{L}\begin{pmatrix} -\sin(\Theta_{\text{eh}})\cos(\Theta_{\text{eh}})\cos(\Theta_{\text{a}})\sin(\Theta_{\text{a}}) \\ \sin(\Theta_{\text{a}}) \\ \sin^2(\Theta_{\text{eh}})\cos(\Theta_{\text{a}}) \end{pmatrix}\sin(\rho) + \begin{pmatrix} \sin(\Theta_{\text{eh}}) \\ 0 \\ \cos(\Theta_{\text{eh}}) \end{pmatrix}\cos(\rho)\,, \end{aligned} \qquad \text{B.35}$$

where L is defined in Eqn. B.34, $\Theta_{\text{eh}} = \Theta_{\text{ev}}^{\text{up}}$ is given by Eqn. B.14, and $\rho=\rho\left(\Phi^{\text{up}}\right)$ is given by Eqn. B.23. The transverse walkoff (side view of the plane containing the optic axis and walkoff is shown in Figure B-7) of the extraordinary polarization in the horizontal plane is

$$\Delta y_{\text{h}} = d\cdot\frac{s_y}{s_z} = d\cdot\frac{\sin(\Theta_a)\sin(\rho)}{\sin^2(\Theta_{\text{eh}})\cos(\Theta_{\text{a}})\sin(\rho)+L\cos(\Theta_{\text{eh}})\cos(\rho)}. \qquad \text{B.36}$$

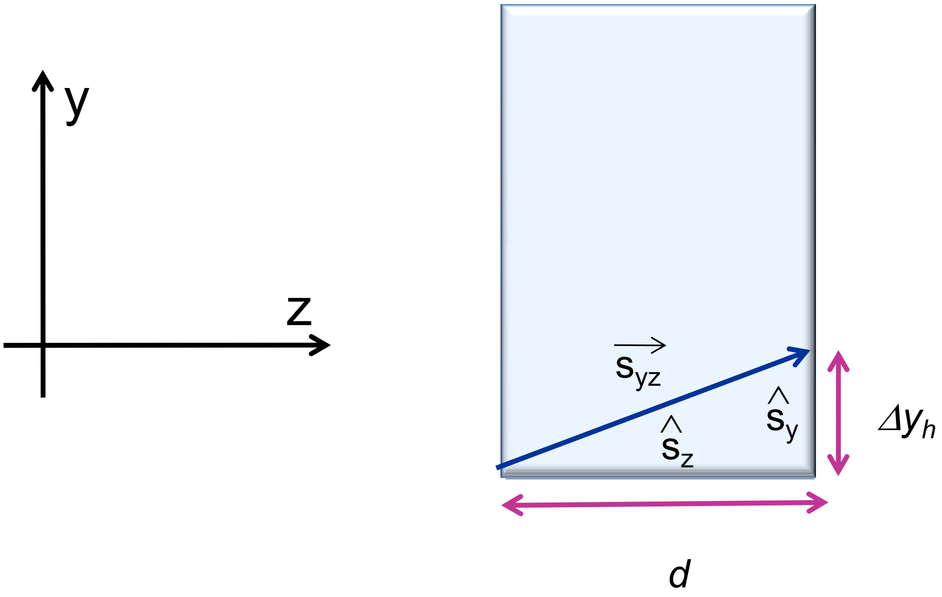

Figure B-7: Side view showing the projection of the walkoff vector on the yz plane.

Beam-waist location of the horizontal rays: The beam waist of the extraordinary rays incident in the horizontal plane can be calculated relative to w^{inc}, as shown in Figure B-8, as

$$\begin{aligned} w'_{eh} &= w^{inc} - d\frac{s_\mathrm{x}}{s_\mathrm{z}} \\ &= w^{inc} - d\left(\frac{-\sin(\Theta_\mathrm{eh})\cos(\Theta_\mathrm{eh})\cos(\Theta_\mathrm{a})\sin(\rho) + L\sin(\Theta_\mathrm{eh})\cos(\rho)}{\sin^2(\Theta_\mathrm{eh})\cos(\Theta_\mathrm{a})\sin(\rho) + L\cos(\Theta_\mathrm{eh})\cos(\rho)}\right). \end{aligned} \tag{B.37}$$

The location of the beam waist of the extraordinary rays in the horizontal plane is given by z_eh as

$$z_\mathrm{eh} = \frac{w'_\mathrm{eh}}{\tan\Theta_\mathrm{i}} \ . \tag{B.38}$$

Thus, Eqns. B.1, B.30 and B.38 give us the locations for the three focused spots of the ordinary polarization, and extraordinary polarization incident in the vertical and horizontal plane respectively. The separation between the two extreme extraordinary foci Δz_e is given by

$$\Delta z_\mathrm{e} = z_\mathrm{eh} - z_\mathrm{ev} = \frac{w'_\mathrm{eh}}{\tan\Theta_\mathrm{i}} - \frac{w'^{\mathrm{up}}_\mathrm{ev} + w'^{\mathrm{lo}}_\mathrm{ev}}{2\cdot\tan\Theta_\mathrm{i}} \ . \tag{B.39}$$

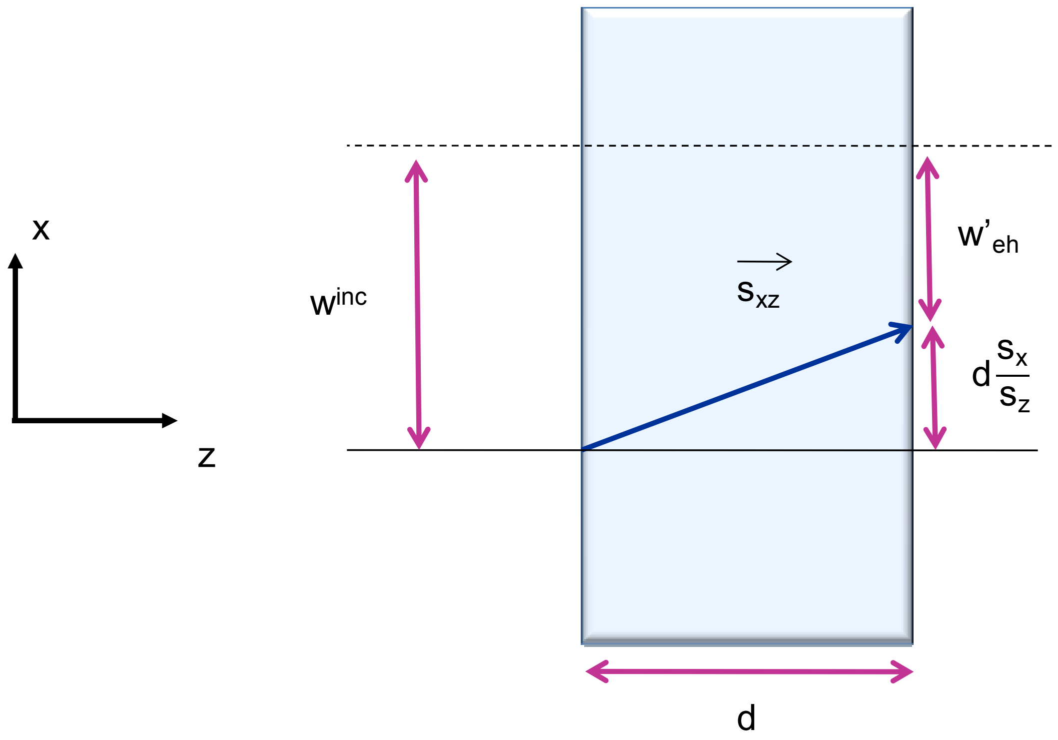

Figure B-8: The beam waist of the extraordinary rays in the horizontal plane relative to the incident beam waist (i.e., before the focusing lens).

Appendix C
Detector Development

C.1 Anti-reflection coatings

Details on the characterization, modeling and deposition of in-house anti-reflection (AR) coating of the VLPC detectors are presented here. The simplest interference AR coating consists of a single quarter-wave layer of transparent material with refractive index $n_{AR} = \sqrt{n_1 n_2}$, where n_1, n_2 are the indices of the two media. In the case of detectors, typically, $n_1 = n_{air} = 1.0$ and n_2 is the effective refractive index of the detector surface, which includes any preexisting coatings. Theoretically, such an ideal quarter-wave layer gives zero reflectance at the center wavelength and decreased reflectance for wavelengths in a broad band around the center. In the absence of the ideal thin-film material, a multilayer coating, consisting of alternating layers of high- and low-index materials, can be used to decrease reflection losses to <0.1%. In general, multilayer coatings are more sensitive to incident angle, wavelength, and cryogenic thermal cycling. To decrease the latter, we recommend minimizing the number of thin-film layers (e.g., we used a SiO_2 and a SiN layer, in addition to the preexisting SiO_2 layer) and moreover using a stress-free deposition process such as reactive low voltage ion plating (RLVIP). Due to the unavailability of RLVIP equipment at our in-house facilities, we used plasma-enhanced chemical vapor deposition (PECVD) and thermal evaporation (TE) for our in-house coatings. RLVIP is available at certain commercial vendors (e.g., INO, Canada). Note that even in the case of outsourcing detector coatings, existing layers have to be characterized and modeled. Moreover, care has to be taken to mask the mounted detectors to ensure that the gold contact pads on the ceramic mount will not be covered by the insulating dielectric coating layers[110]. Alternatively, we recommend desoldering the detector chip from the ceramic chip before coating the detectors; this allows for a higher-temperature coating process – the indium solder used to mount the detector chip onto the ceramic melts at ~180° C – thereby enabling higher quality coatings. Tips on (un)soldering the detector chip (from) onto the ceramic substrate are presented in Section C-2.

---

[110] Note that in the process of handling the detectors, the extremely delicate gold wire bonds are easily destroyed. While these can be wire bonded again, this process can only be repeated ~10 times on the same detector because of two main reasons: there is only a limited amount of space on the gold contact pads on the detector chip, and the "*ball of metal*" made by ball bonds are not easily removable. For this reason we recommend using wedge bonds. Note also that it should be possible to etch existing "used-up" contact pads and re-fabricate new gold contact layers on the detector chip (if need be) using standard lithographic techniques. Possible contact issues might arise when attempting to do this on AR-coated detectors.

The overall procedure for custom-coating detectors is as follows. For each of the experimental steps, it is crucial to ensure that the surface of the detector is extremely clean.

Step 1 - Calibration: Measure the wavelength-dependent reflectivity of the detector surface, and estimate the index and thickness of the existing coating on the detector surface using a visible-range ellipsometer (e.g., *J. A. Woollam Vase or the Rudolph FE- III Focus*).

Step 2 – Modeling detector surface: Confirm the index and thickness of the existing coatings on the detector surface by modeling the expected wavelength-dependent reflectivity using the programs presented below and matching the theoretical curves to the experimentally obtained reflectivity (from Step 1).

Step 3 – Modeling new coatings: Model the additional coatings to be deposited, based on the operating wavelength and the approximate refractive indices n of available materials (e.g., at 710 nm, n =1.48 for Silicon oxide SiO_2 and n =1.98 for SiN). Note that the programs given here can be easily modified to include any other thin films. One could also estimate the ideal index needed to minimize the reflection losses in order to find the closest available match.

Step 4 - Coatings: The currently available in-house dielectric deposition equipment is not optimized for high-quality precise AR coatings (e.g., layer thicknesses and indices are not reproducible after a few days, even for identical system settings). Thus, given the sensitivity of the reflection losses to thickness of the deposited layers, we highly recommend the following *model-calibrate-coat-measure-repeat* procedure for repeatable extremely low-reflection coatings:

a. Model the optimized (first) coating layer using the coating programs presented here.
b. Calibrate the first deposition system (e.g., PECVD of SiO_2) using an epitaxial-quality silicon chip (NOT THE DETECTORS), or preferably a silicon chip deposited with coatings[111] similar to the existing high-reflectivity detector.
c. Estimate the thickness and index of the deposited layer using an ellipsometer.
d. Coat the masked/un-mounted detector with the first layer immediately after system calibration.
e. Measure the thickness and index of the deposited layer using an ellipsometer. The actual deposition rates might have changed because the detector geometry and structure differs from that of the calibration chip.
f. Repeat a-e for each additional layer.

---

[111] The author recognizes the Gödelian implications of such a procedure. To break free of the self-referential chain, start by using in-built calibration tool (e.g., crystal monitors or deposition rates) available for most equipment.

Step 5 - Measure: Measure the wavelength-dependent reflectivity of the AR-coated detector surface. Model the expected dependence for the measured index and thickness of the deposited layers and confirm agreement.

C.1.1 Coating Programs (in Matlab)

Fresnel.m: This modified program calculates the Fresnel reflection coefficient for a dielectric stack at wavelength (lambda in microns). Theta is the angle in radian of the k-vector with respect to the surface normal in free space (n=1). Films are specified as an array of the following structure:

film = [n0 -;

n1 d1; reflectivity_theta ( )

n2 d2;

n3 d3;

n_f -;];

where n_i is the index of the ith layer, and d_i is its thickness. The thicknesses of the first and last layer are ignored. This program also takes into account the reduced intensities of the incident beam for different surfaces. Note that the reflection dependence on wavelength and incident angle for any device (film) structure can be easily modeled using this function, by simply looping through the desired range of parameters.

```
function [rs,rp]=fresnel(film, theta, lambda)
rs=0;
rp=0;
Rs=[];
Rp=[];
Ts=[];Tp=[];Ts (1)=1;Tp (1)=1;
R_S=0; R_P=0;
n = size (film, 1);
phase = 0;
st = sin (theta);
for j=2:n
  n1 = film (j-1,1);
  n2 = film (j,1);
  theta1 = asin (st/n1);
  theta2 = asin (st/n2);
```

```
  if (theta > 0)
    r1 = -sin(theta1 - theta2)/sin(theta1+theta2);
    r2 = tan (theta1-theta2)/tan(theta1+theta2);
  else
    r1 = (n2-n1)/(n2+n1);
    r2 = r1;
  end
  Rs (j) =Ts (j-1)*r1*exp (i*2*phase);
  Rp (j) = Tp (j-1)*r2*exp (i*2*phase);
  phase = phase+2*pi*film (j,2)*n2/(lambda*cos (theta2));
  Ts (j)=Ts (j-1)-abs (Rs (j))^2;
  Tp (j)=Tp (j-1)-abs (Rp (j))^2;
  R_S=R_S + Rs (j);
  R_P=R_P + Rp (j);
end
  rs=R_S;
  rp=R_P;
(abs (rs^2)+abs (rp)^2)/2
```

Optimized_thickness.m: This program calculates optimal dual-layer coating. Note that the existing film structure needs to be manually changed in the program, depending on the device structure one is trying to optimize. Use this to calculate the optimized thickness for a given material with a specific refractive index. Note that index of silicon varies greatly with wavelength (use the silicon index program shown next).

```
function   [Sinthick,SiO2thick,R]=   optimized_thickness(theta,Si_index,
lambda)
R=1 ;
Sinthick=0;
SiO2thick=0;
t2=0.093;
for t=0.001:0.001:0.1
  for t2=0.093:0.001:0.3
    [rs,rp]=fresnel([1 0;1.98 t;1.48 t2;Si_index 0], theta, lambda) ;
    R1=( abs (rs)^2+abs (rp)^2)/2;
    if (R1 < R)
        R=R1;
```

```
        Sinthick = t;
        SiO2thick = t2;
    end
  end
end
```

Si_index.m: This function returns the index of silicon for a wavelength specified in microns. Si index values are unfortunately easy to come by but hardly consistent. The two formulae presented here are based on a Sellmeier-type dispersion formula obtained from the Handbook of Optical Constants of Solids [112]. Comparing these two formulae with http://luxpop.com/ and the measured data, the second formula is more consistent with our measurements. Both formulae are provided here for the sake of completeness.

```
function Si_index (lambda)

%First formula
% n=sqrt (11.6858 + (0.939816/lambda^2) + \
((8.10461e-3*1.1071^2)/(lambda^2-1.1071^2)))

l=1/(lambda^2-0.028);
A=3.41906;
B=1.23172E-1;
C=2.65456E-2;
D=-2.66511E-8;
E=5.45852E-14;

%Second Formula (use this)
n=A+ B*l + C*l^2 + D*lambda^2 + E*lambda^4
```

C.2 Mounting/Unmounting the VLPCs from the ceramic substrate

The VLPC silicon chips typically come mounted on a ceramic substrate with gold contact pads, which are electrically connected via gold wire bonds to the eight detectors and the bias on the chip. The chips are soldered onto the ceramic substrate using indium solder (99.99% pure indium), which melts ~180° C. Thus, any post-mount processing temperature has to be below 180° C. However, the detector chip can be desoldered from the ceramic substrate and easily soldered back on. Here are some guidelines for desoldering/soldering the VLPCs:

Desoldering: Firmly and completely pull out the wire bonds with the help of a good tweezers. Place the detectors on a piece of silicon and place the silicon on a hot plate heated to 200° C. Once the indium solder has melted (~2 minutes) hold the ceramic chip down (using a pair of tweezers) and firmly pull the detectors straight up. You can test whether the solder has melted by carefully pushing on the edge of the detectors to see if they move relative to the ceramic chip. Let the detector chip cool completely by placing it on an unheated piece of silicon. Most of the indium solder will be left behind on the ceramic substrate.

Soldering: Place the ceramic chip on a piece of silicon and place the silicon on a hot plate heated to 200° C. Place a small amount of indium on the ceramic mount if needed[112]. Once the indium solder has melted (~2 minutes) hold the ceramic chip down (using a pair of tweezers) and place the detectors on the melted solder. Take care not to exert any force on the detectors when the solder is still hot, as the detectors can easily become misaligned. Carefully remove the silicon piece (with the mounted detectors on it) from the hot plate and let cool completely. The detectors will be firmly soldered onto the ceramic chip. Wire-bond the detectors onto the contact pads on the ceramic chip using wedge (preferable) or ball bonding and gold or aluminum wires.

C.3 Cryogenic preamplifier

We have successfully tested a low-noise cryogenic preamplifier in conjunction with the VLPCs (in cryostat #2). The preamplifier circuit employs an Agilent (now Avago) Technologies GaAs amplifier MGA-81563, a low-noise amplifier offering 14 dB of gain at frequencies between 0.9 and 6 GHz. The circuit is based on a design modification[113] provided by Agilent for lowering the frequency range and expanding the bandwidth of the amplifier. By employing an external resistance-capacitance (RC) feedback circuit, shown in Figure C-1, the bandwidth of the amplifier was extended to 1-500 MHz at the cost of a lower gain (~7 dB). The DC blocking capacitors protect the amplifier from any DC components and were designed to provide a low impedance (1 – 5 ohms) at the lowest frequency of operation (1 MHz). We chose a capacitance value of 68 nF, resulting in a resistance of 2.5 Ω at 1 MHz, thereby minimizing the 1/f noise of GaAs amplifiers. The AC components of the bias signal are filtered by the bypass capacitors and the RF choke filter. Without these, AC components would lead to fluctuations in the amplifier bias, resulting in inconsistent gain and additional noise. The RF choke was designed to provide high impedance at the lowest frequency of operation and the bypass capacitors are similar to the

---

[112] Avoid using excess indium – it can easily overflow and ruin the detector surface. Once indium gets on the detector surface, there is no easy way to remove the solder without destroying the detector surface. In case of doubt, first try soldering without *any* extra indium solder, i.e., use any leftover indium solder on the ceramic chip.

[113] Agilent design tip # G0004 titled "Extending the Low Frequency Response of the MGA-81563 and MGA-82563 RFIC Amplifiers", authored by Bob Myers, can be found at: http://avagotech.kr/docs/Design_Tip_G004. We acknowledge Kyle McKay and Prof. Jungsang Kim at Duke University for help designing the low-noise cryogenic preamplifier.

DC blocking capacitors. A resistance value of 250 Ω and a capacitance value of 1000 pF were used. Using these values, an average gain of 6-7 dB was observed over a bandwidth of 500 MHz.

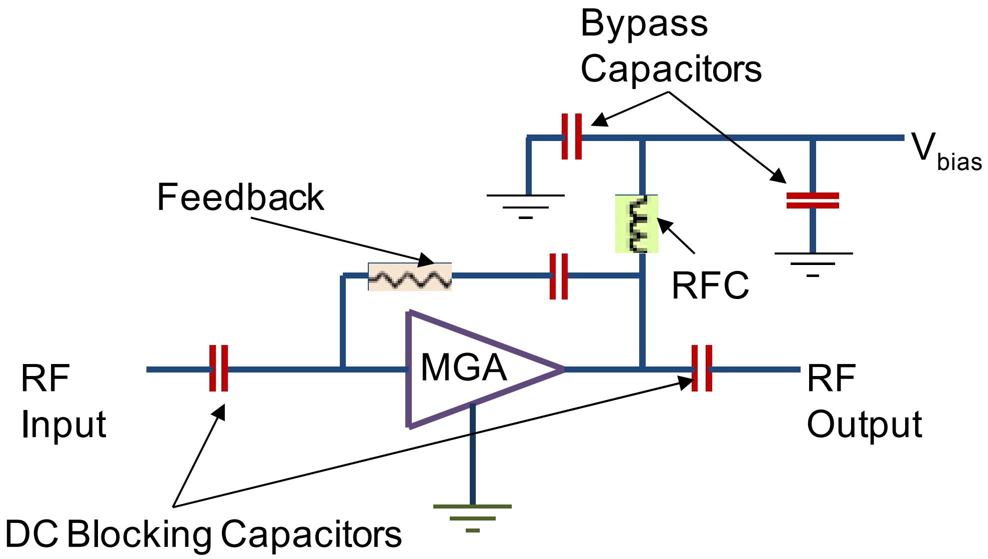

Figure C-1: Cryogenic preamplifier circuit, using the Agilent MGA 81563 GaAs amplifier.

C.4 Fitting PNR curves [114]

When the laser pulse duration is comparable to the VLPC output pulse width, then the expected peak height for 2-photon and higher-order events is reduced. The Mathematica functions presented here were used to account for this effect when fitting the photon-number resolution curve shown in Figure 8-3b. In the functions below, *width* is the incident laser pulse width divided by the VLPC output pulse width. The larger the value of *width*, the greater is the reduction in the expected peak height. Statements enclosed in (*…*) below are comments explaining the function of the code immediately following them.

```
(* PctReduction returns how much smaller the 2-photon peak will be for
a given pulse width *)
PctReduction[width_]:=(peak1=width     RandomReal[]-width/2;peak2=width
RandomReal[]-width/2;(2 PDF[NormalDistribution[0,0.5`],0]
Maximize[PDF[NormalDistribution[peak1,0.5`],x]+PDF[NormalDistribution[
peak2,0.5`],x],{x}][[1]])/(2 PDF[NormalDistribution[0,0.5`],0]))
(* For example, when the laser pulse is twice as big as the VLPC
pulse, the 2-photon peak will be reduced by a factor of ~0.46 *)
```

---

[114] This program was written by Kevin Zielnicki.

```
PctReduction[2]
0.463346

(* AvgPctReduction performs the above function for a specified # of
trials *)
AvgPctReduction[width_,trials_]:=(
data=Table[PctReduction[width],{trials}];
{Mean[data],StandardDeviation[data]/Sqrt[Length[data]]})
(* For example, when the laser pulse width is the same as the VLPC
output pulse, the pulse height reduces by a factor of ~0.1 - obtained
by averaging over 100 trials. *)
AvgPctReduction[1,100]
{0.0971961,0.0098885}


(* PctCorrection is the same as PctReduction, but generalized for more
than 2 peaks *)
PctCorrection[width_,peaks_]:=(
peakHeights=Table[Random[NormalDistribution[0,width/2.35482]],{peaks}]
;
peakFunctions[x_] :=PDF[NormalDistribution[#,0.5],x] &/@peakHeights;
peakSum[x_]:=Total[peakFunctions[x]];
Maximize[peakSum[x],{x}][[1]]/(peaks*PDF[NormalDistribution[0,0.5],0])
)
 (* AvgPctCorrection averages the generalized peak correction function
over a specified # of trials *)
AvgPctCorrection[width_,peaks_,trials_]:=(data=Table[PctCorrection[wid
th,peaks],{trials}];{Mean[data],StandardDeviation[data]/Sqrt[Length[da
ta]]})
(* For example, when width =0.07, the fifth peak reduces by a factor
of 0.99 with a standard deviation of 3x10^-5 , obtained by averaging
over 1000 trials)
AvgPctCorrection[.07,5,1000]
{0.998573,0.0000314845}
```

References

[1] E. Knill, R. Laflamme, and G. J. Milburn, Nature **409**, 46 (2001).
[2] R. T. Horn *et al.*, Physical Review Letters **95**, 150502 (2005).
[3] J.-W. Pan *et al.*, Physical Review Letters **86**, 4435 (2001).
[4] C. Bennett, and G. Brassard, in Proceedings of {IEEE} International Conference on Computers, Systems, and Signal Processing, edited by Ieee1984), pp. 175.
[5] V. Giovannetti, S. Lloyd, and L. Maccone, Physical Review Letters **96**, 010401 (2006).
[6] K. Pieter, L. B. Samuel, and P. D. Jonathan, Journal of Optics B: Quantum and Semiclassical Optics, S811 (2004).
[7] C.-Y. Lu *et al.*, Nat Phys **3**, 91 (2007).
[8] M. Varnava, D. E. Browne, and T. Rudolph, Physical Review Letters **100**, 060502 (2008).
[9] M. Nielsen, and I. Chuang, *Quantum Computation and Quantum Information* (Cambridge University Press, 2000).
[10] P. Kok *et al.*, Reviews of Modern Physics **79**, 135 (2007).
[11] C. K. Hong, Z. Y. Ou, and L. Mandel, Physical Review Letters **59**, 2044 (1987).
[12] M. O. Scully, and M. S. Zubairy, *Quantum Optics* (Cambridge University Press, 1997), p. 652.
[13] L. Mandel, and E. Wolf, *Optical Coherence and Quantum Optics* ({Cambridge University Press}, 1995).
[14] G. Di Giuseppe *et al.*, Physical Review A **68**, 063817 (2003).
[15] A. B. U'Ren *et al.*, Laser Physics **15** (2005).
[16] C. Santori *et al.*, Nature **419**, 594 (2002).
[17] C. Kurtsiefer *et al.*, Physical Review Letters **85**, 290 (2000).
[18] D. C. Burnham, and D. L. Weinberg, Physical Review Letters **25**, 84 (1970).
[19] M. Fiorentino *et al.*, Physical Review A **69**, 041801 (2004).
[20] R. Boyd, *Nonlinear Optics, Second Edition* (Academic Press, 2003).
[21] L. E. Vincent *et al.*, to be published.
[22] A. URen, K. Banaszek, and I. Walmsley, Journal of Quantum Information and Computation **3**, 480 (2003).
[23] K. B. A. B. U'Ren, I. A. Walmsley, Quantum Information and Computation **3**, 480 (2003).
[24] P. G. Kwiat *et al.*, Physical Review A **60**, R773 (1999).
[25] A. Valencia *et al.*, Physical Review Letters **99**, 243601 (2007).
[26] O. Kuzucu *et al.*, Physical Review Letters **94**, 083601 (2005).
[27] W. P. Grice, A. B. U'Ren, and I. A. Walmsley, Physical Review A **64**, 063815 (2001).
[28] P. J. Mosley *et al.*, Physical Review Letters **100**, 133601 (2008).
[29] O. Cohen *et al.*, Physical Review Letters **102**, 123603 (2009).
[30] N. A. Peters *et al.*, in Quantum Communications and Quantum Imaging IV (Proceedings of the SPIE, 2006), p. 630507.
[31] M. W. Mitchell, J. S. Lundeen, and A. M. Steinberg, Nature **429**, 161 (2004).
[32] P. Kwiat *et al.*, Applied Optics **33**, 1844 (1994).
[33] S. Takeuchi *et al.*, Applied Physics Letters **74**, 1063 (1999).
[34] J. Kim *et al.*, Applied Physics Letters **74**, 902 (1999).
[35] M. D. Petroff, M. G. Stapelbroek, and W. A. Kleinhans, Applied Physics Letters **51**, 406 (1987).
[36] P. Eberhard, P. Kwiat, and M. Petroff, in *Applications of Photonic Technology* (Plenum Press, New York, 1995).

[37] J. T. Barreiro *et al.*, Physical Review Letters **95**, 260501 (2005).
[38] P. H. Eberhard, Physical Review A **47**, R747 (1993).
[39] P. T. Juan, M.-T. Gabriel, and T. Lluis, Journal of Optics B: Quantum and Semiclassical Optics, 235 (2005).
[40] C. I. Osorio *et al.*, Opt. Express **15**, 14636 (2007).
[41] G. G. Gurzadian, V. G. Dmitriev, and D. N. Nikogosian, *Handbook of nonlinear optical crystals* (Springer-Verlag, Berlin ; New York :, 1991).
[42] W. Wasilewski *et al.*, Opt. Lett. **31**, 1130 (2006).
[43] M. Avenhaus *et al.*, Opt. Lett. **34**, 2873 (2009).
[44] S. Quabis *et al.*, Applied Physics B: Lasers and Optics **72**, 109 (2001).
[45] K. Chen *et al.*, Physical Review Letters **99**, 120503 (2007).
[46] S. P. Walborn *et al.*, Nature **440**, 1022 (2006).
[47] R. Jozsa, Journal of Modern Optics **41**, 2315 (1994).
[48] W. K. Wootters, Physical Review Letters **80**, 2245 (1998).
[49] D. F. V. James *et al.*, Physical Review A **64**, 052312 (2001).
[50] J. B. Altepeter *et al.*, in *Advances In Atomic, Molecular, and Optical Physics* (Academic Press, 2005), pp. 105.
[51] D. Branning *et al.*, Physical Review Letters **83**, 955 (1999).
[52] C. H. Bennett *et al.*, Physical Review Letters **70**, 1895 (1993).
[53] D. Bouwmeester *et al.*, Nature **390**, 575 (1997).
[54] P. Walther *et al.*, Nature **434**, 169 (2005).
[55] M. Barbieri *et al.*, Physical Review Letters **92**, 177901 (2004).
[56] J. F. Hodelin, G. Khoury, and D. Bouwmeester, Physical Review A **74**, 013802 (2006).
[57] Y.-H. Kim *et al.*, Physical Review A **67**, 010301 (2003).
[58] O. Kuzucu, and F. N. C. Wong, Physical Review A **77**, 032314 (2008).
[59] B.-S. Shi, and A. Tomita, Physical Review A **69**, 013803 (2004).
[60] P. G. Kwiat *et al.*, Physical Review Letters **75**, 4337 (1995).
[61] D. Dehlinger, and M. W. Mitchell, American Journal of Physics **70**, 903 (2002).
[62] B. R. Gadway, E. J. Galvez, and F. D. Zela, 2009), p. 015503.
[63] Y. Nambu *et al.*, Physical Review A **66**, 033816 (2002).
[64] J. Altepeter, E. Jeffrey, and P. Kwiat, Opt. Express **13**, 8951 (2005).
[65] S. Cialdi *et al.*, Appl. Opt. **47**, 1832 (2008).
[66] P. Trojek, and H. Weinfurter, Applied Physics Letters **92**, 211103 (2008).
[67] C. E. Kuklewicz *et al.*, Physical Review A **69**, 013807 (2004).
[68] P. Becker, J. Liebertz, and L. Bohatý, Journal of Crystal Growth **203**, 149 (1999).
[69] M. Ghotbi, and M. Ebrahim-Zadeh, Opt. Express **12**, 6002 (2004).
[70] H. Hellwig, J. Liebertz, and L. Bohaty, Journal of Applied Physics **88**, 240 (2000).
[71] M. Ghotbi *et al.*, Opt. Lett. **29**, 2530 (2004).
[72] A. G. White *et al.*, Physical Review Letters **83**, 3103 (1999).
[73] A. Joobeur *et al.*, Physical Review A **53**, 4360 (1996).
[74] T. E. Keller, and M. H. Rubin, Physical Review A **56**, 1534 (1997).
[75] N. Boeuf *et al.*, Optical Engineering **39**, 1016 (2000).
[76] A. Migdall, J. Opt. Soc. Am. B **14**, 1093 (1997).
[77] J.-H. Park *et al.*, Opt. Express **11**, 1862 (2003).
[78] T. J. Herzog *et al.*, Physical Review Letters **72**, 629 (1994).
[79] T. J. Herzog *et al.*, Physical Review Letters **75**, 3034 (1995).
[80] A. Lamas-Linares, J. C. Howell, and D. Bouwmeester, Nature **412**, 887 (2001).
[81] P. Kolenderski, W. Wasilewski, and K. Banaszek, Physical Review A **80**, 013811 (2009).
[82] A. B. U'Ren *et al.*, Physical Review Letters **97**, 223602 (2006).
[83] E. Waks *et al.*, arXiv:quant-ph/0308054 (2003).
[84] F. S. Isaac *et al.*, Review of Scientific Instruments **73**, 2108 (2002).

[85] J. Ekin, *Experimental Techniques for Low-temperature Measurements: Cryostat Design, Material Properties and Superconductor Critical-current Testing* (OUP Oxford, 2006).
[86] E. R. I. Abraham, and E. A. Cornell, Appl. Opt. **37**, 1762 (1998).
[87] P. Michel *et al.*, edited by A. Claude, K. Norbert, and H. A. Macleod (SPIE, 2004), pp. 471.
[88] G. Khoury, in *Physics* (University of California, Santa Barbara, 2006), p. 184.
[89] A. E. Lita, A. J. Miller, and S. W. Nam, Opt. Express **16**, 3032 (2008).
[90] A. Bross *et al.*, Applied Physics Letters **85**, 6025 (2004).
[91] E. A. Dauler *et al.*, Journal of Modern Optics **56**, 364 (2009).
[92] K. T. McCusker, and P. G. Kwiat, Physical Review Letters **103**, 163602 (2009).
[93] C. Gobby, Z. L. Yuan, and A. J. Shields, Applied Physics Letters **84**, 3762 (2004).
[94] H. J. Briegel *et al.*, Physical Review Letters **81**, 5932 (1998).
[95] B. S. L. Kok P, and J. P. Dowling, **6**, 811 (2004).
[96] P. G. Kwiat, and H. Weinfurter, Physical Review A **58**, R2623 (1998).
[97] N. Lütkenhaus, J. Calsamiglia, and K. A. Suominen, Physical Review A **59**, 3295 (1999).
[98] L. Vaidman, and N. Yoran, Physical Review A **59**, 116 (1999).
[99] J.-W. Pan *et al.*, Physical Review Letters **80**, 3891 (1998).
[100] M. Żukowski *et al.*, Physical Review Letters **71**, 4287 (1993).
[101] H. Buhrman *et al.*, Physical Review Letters **87**, 167902 (2001).
[102] R. T. Horn *et al.*, Quantum Inf. Comput. **5**, 596 (2005).
[103] J. N. de Beaudrap, Physical Review A **69**, 022307 (2004).
[104] K. Mattle *et al.*, Physical Review Letters **76**, 4656 (1996).
[105] T.-C. Wei, J. T. Barreiro, and P. G. Kwiat, Physical Review A (Atomic, Molecular, and Optical Physics) **75**, 060305 (2007).
[106] M. A. Rowe *et al.*, Nature **409**, 791 (2001).
[107] G. Weihs *et al.*, Physical Review Letters **81**, 5039 (1998).
[108] H. J. Briegel *et al.*, Physical Review Letters **81**, 5932 (1998).
[109] Z.-S. Yuan *et al.*, Nature **454**, 1098 (2008).
[110] P. W. Shor, SIAM J. Comput. **26**, 1484 (1997).
[111] P. G. Kryukov, Quantum Electronics, 749 (1997).
[112] E. Palik, *Handbook of optical constants of solids II* (Academic Press, 1991).